AES 2018 in Marseille - France

The 6th Advanced Electromagnetics Symposium

Proceedings

AES 2018 in Marseille - France

The 6th Advanced Electromagnetics Symposium

Share your comments, photos & videos!

facebook   https ://www.facebook.com/aes.symposium

twitter   @aes_contact

CONTENTS

ABOUT AES

The Advanced Electromagnetics Symposium (AES) serves as an international multidisciplinary forum for deliberations on recent advances and developments in the entire broad field of electromagnetics, Antennas and Propagation. Included in this wide-ranging subject, pertinent to both researchers and industry professionals, are all aspects of electromagnetics, and all frequency ranges from static to optics. Of special interest are :

- Electromagnetic Theory
- Antennas
- Propagation theory, modelling and simulation
- Microwave and Millimeter Circuits and Systems
- Scattering, diffraction and RCS
- Electromagnetic Compatibility
- Computational Electromagnetics
- Optimization Techniques
- Coupled Field Problems
- Optics and Photonics
- Remote Sensing, Inverse Problems, Imaging Radar
- Electromagnetic and photonic Materials
- Bioeffects of EM fields, Biological Media, Medical electromagnetics
- Techniques and tools for RF material characterisation
- EMI/EMC/PIM chambers, instrumentation and measurements
- Educational Electromagnetics

Additionally, through its unique from-Conference-to-Journal-Publication concept, AES offers a rare opportunity for authors to submit papers to Advanced Electromagnetic (AEM) journal and then be considered for journal publication.

Following a now well-established tradition AES takes place in unique locations around the world.

Year	Organizers	Venue
2017	Junsuk Rho, Said Zouhdi	Incheon, Korea
2016	Enrique Márquez Segura, Eva Rajo-Iglesias, Said Zouhdi	Torremolinos (Malaga), Spain
2014	Lingling Sun, Ke Wu, Said Zouhdi	Hangzhou, China
2013	Hamid M. K. Al-Naimiy, Said Zouhdi	Sharjah-Dubai, United Arab Emirates
2012	Xavier Begaud, Said Zouhdi	Paris, France

AES 2017 ORGANIZATION

Said Zouhdi, General Chair
Paris–Sud University, France

INTERNATIONAL ADVISORY COMMITTEE

Yahia Antar, Canada
Jean Chazelas, France
Wen-Shan Chen, Taiwan
Christos Christopoulos, UK
Tie Jun Cui, China
Peter de Maagt, Netherlands
Apostolos Georgiadis, Spain
Dave V. Giri, USA
Xun Gong, USA

Lixin Guo, China
Yang Hao, United Kingdom
Nathan Ida, USA
Koichi Ito, Japan
Andrzej Karwowski, Poland
Kwai Man Luk, Hong Kong
Adel Razek, France
Alain Sibille, France
Ari Sihvola, Finland

Paul Smith, Australia
C-K Clive Tzuang, China
J(Yiannis) C. Vardaxoglou, UK
Junhong Wang, China
Yong-Jun Xie, China
Yu Zhang, China

TECHNICAL PROGRAM COMMITTEE

Christos Argyropoulos, USA
Silvio Ernesto Barbin, Brazil
Muhammad Bawa'aneh, Jordan
Xavier Begaud, France
Pai-Yen Chen, USA
Qin Chen, China
Christophe Craeye, Belgium
Laurent Daniel, France
Salvador Gonzalez Garcia, Spain
Brahim Guizal, France
Tian Sen Jason Horng, Taiwan
Zhirun Hu, UK
Laure Huitema, France
Ruey-Bing Hwang, Taiwan
Mohd Faizal Jamlos, Malaysia
Sungtek Kahng, Korea

Ali Khenchaf, France
Ahmed Kishk, Canada
Ken-ichi Kitayama, Japan
Maciej Krawczyk, Poland
Sebastien Lallechere, France
Allen M. Larar, USA
Howard Lee, USA
Jean-Claude Levy, France
Jensen Li, UK
Jean-Marc Lopez, France
Andrea Massa, Italy
Ozlem Ozgun, Turkey
Oscar Quevedo-Teruel, Sweden
Eva Rajo-Iglesias, Spain
Blaise Ravelo, France
Junsuk Rho, Korea

Thomas Schneider, Germany
Josaphat Tetuko Sri Sumantyo, Japan
Mohamed Swillam, Egypt
Van Yem Vu, Viet Nam
Konstantin Vytovtov, Russia
Steve Hang Wong, Hong Kong
Amir I. Zaghloul, USA
Kuang Zhang, China
Qi-Jun Zhang, Canada
Linjie Zhou, China
Tao Zhou, China
Arkady Zhukov, Spain

SPECIAL SESSIONS ORGANIZERS

Kodo Kawase, Japan
Xianshu Luo, Singapore

Yury Shestopalov, Sweden
Masayoshi Tonouchi, Japan

Linjie Zhou, China

AES 2018 VENUE

AES 2018 will be held aboard the dream-class cruise ship Costa Diadema as a round-trip Marseille cruise from 24 June to 1st July 2018.

GETTING TO THE CRUISE PORT/TERMINAL

The departure port is located :

Porte 4, Port de Marseille, Chemin du Littoral
13015 Marseille
France

Get driving directions and arrange for transfers from your airport or hotel ahead of time. If you are flying in, don't forget to claim your luggage at the airline's baggage claim area.

From "Marseille Provence" Airport

Marseille Provence Airport is located around 27 km / 17 ml (1/2 hour drive distance) northwest of the cruise port and 9 km (5,6 ml) from the city centre.

- ☐ **By Taxi**

    The easiest way to reach the cruise port is to take a taxi straight from the airport, the price is around €50.

- ☐ **By Bus and Taxi**

    Shuttle bus lines run every 20 min from the airport to the St Charles train station daily (between 5 am - 11 pm). Drive distance is approx 30 min. A taxi from from the train station to the cruise ship terminals costs about €20. Occasionally, the port also provides a free shuttle bus line to the city.

Travelling by Car

To reach terminal car parking, take exit 5 off the A55 if you are heading for the cruise terminal area at Porte 4 (Gate 4). You should find a large cruise passengers' car-park, or parking croisieristes, at the end of the Mole Leon Gourret near the Marseille-Provence Cruise Terminal. Be advised that the charges for this car-park are fairly steep.

CRUISE ITINERARY

7 Days Mediterranean-West

Costa Diadema is setting sail on Sunday, 24 June 2018, for 7 nights departing from Marseille and visiting Palma de Mallorca ; Cagliari ; Civitavecchia ; Savona ; Marseille.

Embarkation Time

Embarkation time is when you should arrive at the cruise terminal. In Marseille we will procced with the conference registration before embarking (from **12 :00** to **15 :30**). This will give you enough time to complete your check-in at the cruise terminal before boarding.
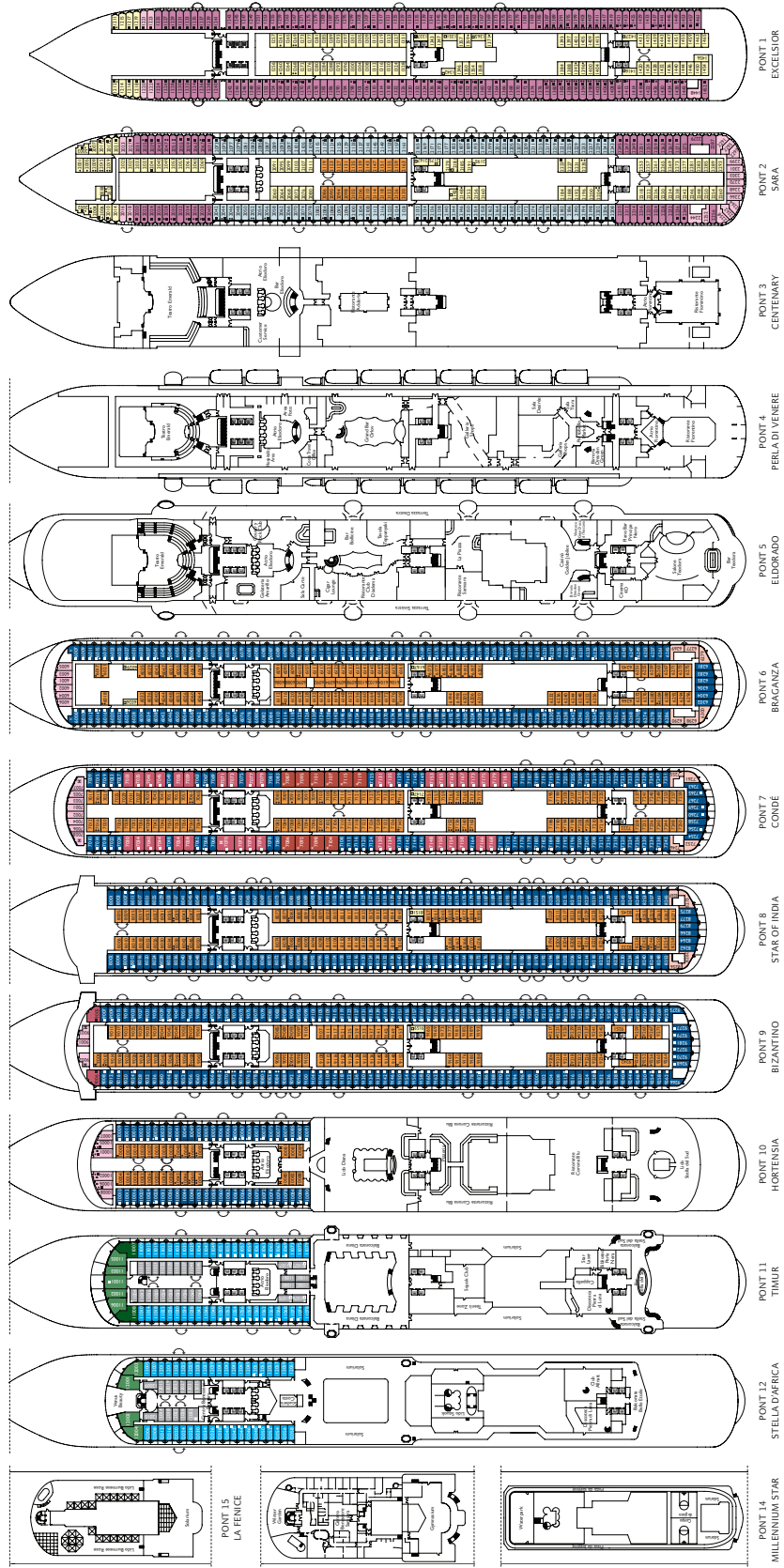
In the other stopover ports (Barcelona, Palma de Mallorca, Cagliari, Civitavecchia and Savona) we highly encourage you to board no later than one hour prior to the departure time (gates close 30mn before depar-
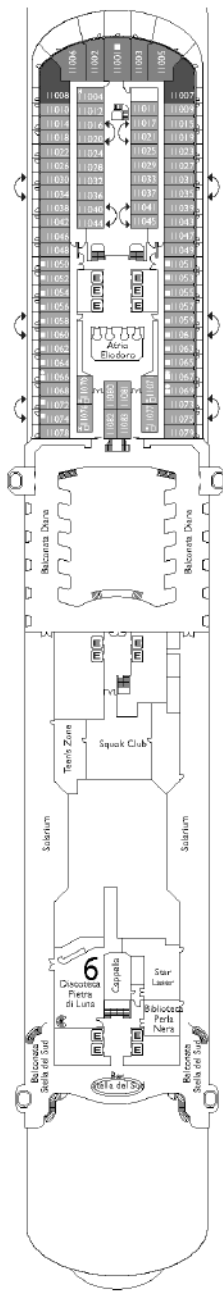
ture).

Ports of Call

Day	Port	Arrival	Departure
1	Marseille	-	17:00
2	Barcelona	9:00	19:00
3	Palma de Mallorca	9:00	-
4	Palma de Mallorca	-	1:00
5	Cagliari, Sardinia	8:00	17:00
6	Civitavecchia	8:00	19:00
7	Savona, Italy	7:00	17:00
8	Marseille	8:00	-

COSTA DIADEMA DECK PLANS

PONT 1 EXCELSIOR

PONT 2 SARA

PONT 3 CENTENARY

PONT 4 PERLA DI VENERE

PONT 5 ELDORADO

PONT 6 BRAGANZA

PONT 7 CONDÉ

PONT 8 STAR OF INDIA

PONT 9 BIZANTINO

PONT 10 HORTENSIA

PONT 11 TIMUR

PONT 12 STELLA D'AFRICA
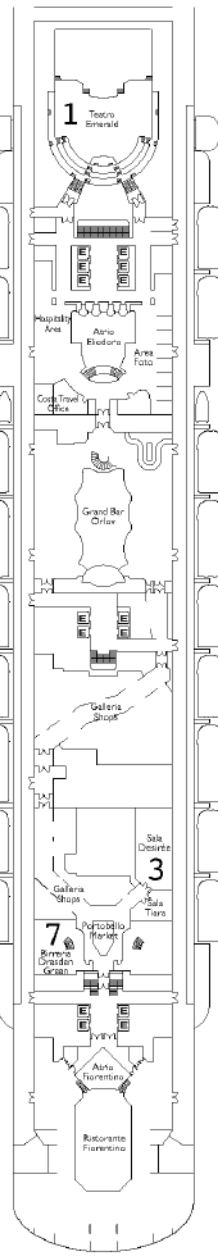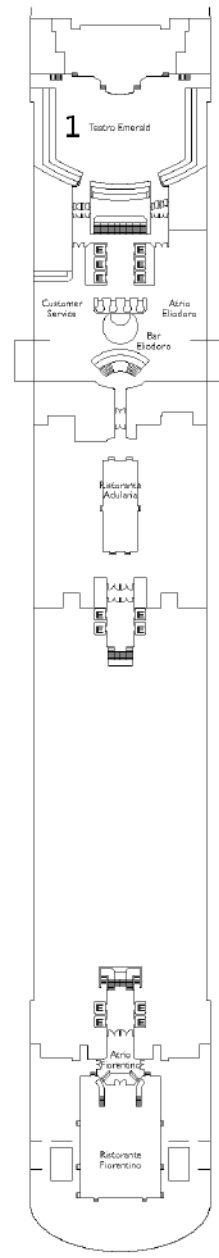
PONT 15 LA FENICE

PONT 14 MILLENNIUM STAR

FLOOR PLANS

PONT 11
TIMUR

PONT 5
ELDORADO

PONT 4
PERLA DI VENERE

PONT 3
CENTENARY

1 : Teatro Emerald
2 : Salone Teodora
3 : Sala Desirée
4 : Piano Bar Principe Nero
5 : Country Rock Club
6 : Discoteca Pietra di Luna
7 : Birreria Dresden Green

GUIDELINES FOR PRESENTERS

ORAL PRESENTATIONS

Each session room is equipped with a stationary computer connected to a LCD projector. Presenters must load their presentation files in advance onto the session computer. Technician personnel will be available to assist you.

Scheduled time slots for oral presentations are 15 mn for regular, 20 mn for invited presentations, 30 mn for keynote talks and 35 mn for plenary talks, including questions and discussions. Presenters are required to report to their session room and to their session Chair at least 15 minutes prior to the start of their session.

The session chair must be present in the session room at least 15 minutes before the start of the session and must strictly observe the starting time and time limit of each paper.

POSTER PRESENTATIONS

Presenters are requested to stand by their posters during their session. One poster board, A0 size (118.9 x 84.1 cm), in portrait orientation, will be available for each poster (there are no specific templates for posters). Pins or thumbtacks are provided to mount your posters on the board. All presenters are required to mount their papers 30mn before the session and remove them at the end of their sessions. Posters must prepared using the standard AES poster template (available on the symposium website).

TABLE OF CONTENTS

Terahertz Science and Technology

Waves in heterogeneous and nonlinear media: direct and inverse problems, recent advancesâ€

Photonic integration from devices to sub-systems

Electromagnetics

Antenna and Propagation

Terahertz Science and Technology

Multi wavelength injection-seeded THz parametric generator

Kosuke Murate[1], Kazuki Maeda[1], Guo Yunzhuo[1], Kodo Kawase[1]

[1]Department of Electronics, Nagoya University, Nagoya, Japan
*corresponding author, E-mail: kodo@nagoya-u.jp

Abstract

In 2003, we reported the first-ever development of a spectral imaging system using THz-wave parametric oscillator (TPO) [1]. At that time, the TPO had a dynamic range below four orders of magnitude, which enables it to identify reagents only through thin (0.2mm^t) envelopes using spectral imaging.

Recently, we have succeeded in the development of high power and high sensitivity THz wave spectral imaging system using injection-seeded THz parametric generation (is-TPG) and detection [2] as shown in Fig. 1. A dynamic range of 100 dB has been obtained, which is much higher than that of the 2003 TPO. The peak output power of is-TPG

approached 50 kW by introducing a microchip YAG laser with shorter pulse width of 420ps. In the detection section of our system, THz-wave was converted back into near infrared beam by nonlinear optical wavelength conversion. We have realized ten orders of dynamic range using commercially available near infrared photo detector. Now we can detect drugs under much thicker obstacles than before using is-TPG spectroscopic imaging system as shown in Fig. 2 [3,4]. Further, our evolved multi-wavelength is-TPG system [5] has potential applications in fast spectroscopic sensing and imaging of chemicals through obstacles and non-destructive CT imaging of plastic/ceramic products. We have also compared our is-TPG spectrometer and TDS (THz Time Domain Spectroscopy) for the purpose of drug detection through thick envelopes.

Fig.1. Experimental set up for THz spectrometer using is-TPG
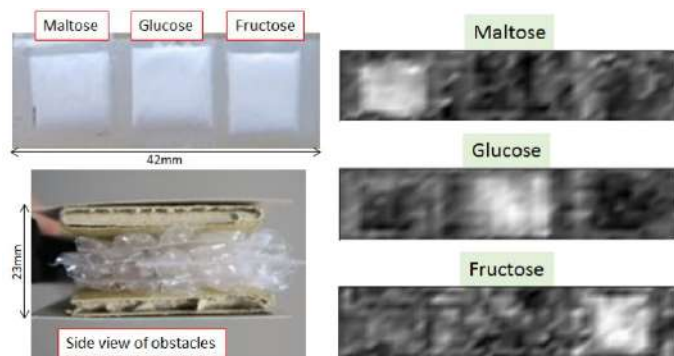
Fig. 2 THz spectroscopic imaging of powder samples in two cardboards + four bubble wraps + two corrugated boards.

References

[1] K. Kawase, Y. Ogawa, Y. Watanabe and H. Inoue, "Non-destructive terahertz imaging of illicit drugs using spectral fingerprints," Optics Express, vol. 11, no. 20, pp. 2549-2554 (2003).

[2] S. Hayashi, K. Nawata, T. Taira, J. Shikata, K. Kawase, H. Minamide "Ultrabright continuously tunable terahertz-wave generation at room temperature," Scientific Reports, Vol. 4, Article number 5045 (2014).

[3] M. Kato, S. R. Tripathi, K. Murate, K. Imayama and K. Kawase, "Non-destructive drug inspection in covering materials using a terahertz spectral imaging system with injection-seeded terahertz parametric generation and detection," Optics Express, 24, 6425-6432 (2016).

[4] S. Tripathi, Y. Sugiyama, K. Murate, K. Imayama, K. Kawase, "Terahertz wave three-dimensional computed tomography based on injection-seeded terahertz wave parametric emitter and detector," Optics Express, 24(6), 6433-6440 (2016).

[5] K. Murate, S. Hayashi, K. Kawase, "Multiwavelength terahertz-wave parametric generator for one-pulse spectroscopy", Applied Physics Express, vol. 10, No. 3, pp. 032401 (2017).

Femtosecond Acoustics and Terahertz Ultrasonics

Chi-Kuang Sun[1*]

[1]Graduate Institute of Photonics and Optoelectronics and Department of Electrical Engineering, National Taiwan University, Taipei, Taiwan
*corresponding author, E-mail: sun@ntu.edu.tw

Abstract

Taking advantage of the slow sound velocity in materials, here we show that femtosecond-time-resolved acoustic measurement, with a terahertz bandwidth, is capable to explore the material heat transport properties and to noninvasively monitor *in situ* an interface and sub-surface area under atmospheric conditions with sub-atomic layer sensitivity.

1. Introduction

Sound wave is one of the nature-chosen tools for communication and imaging. Combined with excitation laser light, photoacoustic tomography employs ultrasounic detection to image optical absorption contrast with a micrometer to sub-micron spatial resolution deep inside tissues [1,2]. For even higher spatial resolution, picosecond ultrasonics [3] and nanoultrasonics [4] generate sub-THz to THz acoustic waves by using picosecond and femtosecond laser pulses, so as to achieve sub-surface ultrasonic imaging with a spatial resolution up to a few nanometers. It is thus highly desirable to extend the laser ultrasonic techniques even further with an atomic or even sub-atomic layer resolution, which is critical for in situ noninvasive monitoring of chemical reactioins at a solid water interface.

In this presentation, we show that femtosecond acoustics [5,6], a technique based on the time-domain analysis with femtosecond acoustic pulses, is capable to noninvasively monitor *in situ* the chemical reactions occurring at a solid/liquid-water interface and sub-surface area under atmospheric conditions while providing sub-atomic layer sensitivity. We will also discuss the topic of THz ultrasonics, which is to provide a tool to explore the coherent acoustic phonon spectra with a terahertz bandwidth for the first time, with the capability to resolve the un-resolved phonon mysteries like the Boson peak problem, Kapitza anamoly, and the collisionless transport in crystals.

2. Methods and results

By converting a femtosecond optical pulse into a femtosecond acoustic pulse, one can take advantage of the ultraslow sound velocity, which is usually on the order of 3000 m/s and the ultrahigh temporal resolution which is usually on the order of 100 fs. It can be noted that within 100 fs, a femtosecond acoustic pulse travels only a distance of 3 angstroms, assuming a 3000 m/s velocity. Femtosecond time-resolved sound propagation imaging can thus provide a spatial resolution down to 1.5 angstroms assuming an acoustic round trip path. By generating femtosecond acoustic pulses using a piezoelectric nanolayer (3nm InGaN in our case) under excitation of a femtosecond optical pulse (400 nm femtosecond optical pulse) and by femtosecond time-resolved acoustic echo imaging, this acoustic pulse then travelled towards a solid-liquid interface, got reflected by the multiple interfaces and was finally femtosecond-time-resolved by an optical probe pulse when it reached the piezo-transducer again. To study the performance of femtosecond acoustics applied on *in situ* monitoring a chemical reaction at a solid/liquid interface, the well-known anode-oxidation process occurring during the GaN-based photo-electro-chemical (PEC) water splitting was taken as our model. An n-GaN thin film was used as the un-protected photoanode and a platinum wire was used as the counter electrode. On top of the n-GaN cap layer, we deposited a microfluidic channel, which allows a better control of the water thickness with much improved imaging stability during the experiments.

Figure 1 shows the resulted M-mode femtosecond acoustics image of the depth profile across the n-GaN-water interface over the accumulated PEC reaction time [6]. From this unprocessed data, a nanolayer of Gallium oxide can be observed to grow between GaN and water with time. Two echo peaks can be clearly observed starting from 21 mins. The peak to peak temporal differences for the 21-min and the 24-min traces are 0.57 ps and 0.60 ps, respectively, indicating a system temporal resolution better than 0.57 ps, and our acoustic pulsewidth should be shorter than 0.57 ps. With further deconvolution analysis, based on the acoustic traces before the PEC reaction as well as at a later time, our analysis shows a resolution as high as 2 angstroms, which is half of the effective atomic layer thickness of gallium oxide. Our study indicated that femtosecond acoustics can indeed noninvasively monitor the dynamic changes of physical structures at a solid/water interface and sub-surface area with an sub-atomic-level resolution, thus providing the capability to reveal key physical information on reactions occurring at solid/liquid interfaces, ideal for next generation energy conversion and electrochemical energy storage device developments as well as for the study of early-stage corrosion or oxidation processes.
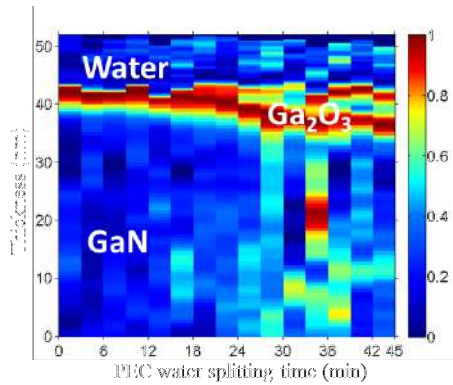
Figure 1: A color-coded M-mode femtosecond acoustics Image [6] showing the depth profile across the GaN-water interface over the PEC water splitting time.

3. Discussion & conclusions

Solid/liquid-water interface plays a critical role in various natural phenomena, such as catalytic process, wetting of surfaces, metal corrosion, and protein folding. Having a nondestructive sub-surface imaging technique with an atomic resolution and the capability of *in situ* monitoring a solid/liquid interface can help to reveal the mysterious dynamics. *In situ* imaging a chemical reaction at a solid/liquid interface has been reported by few researchers. These previous efforts including scanning tunneling microscopy, transmission and scanning electron microscopy either provide limited spatial resolution or face experimental restrictions. In this presentation, we will show more details regarding the technique called femtosecond acoustics, a technique based on the time-domain analysis with femtosecond acoustic pulses. By generating femtosecond acoustic pulses using a piezoelectric nanolayer and by femtosecond time-resolved acoustic echo imaging, also known as nanoultrasonics scan [4], our study indicates that femtosecond acoustics can indeed noninvasively monitor the dynamic changes of physical structures longitudinally at a solid/water interface [6] and the sub-surface area [5,6] with an sub-atomic-level resolution, thus providing the capability to reveal key physical information on reactions occurring at solid/liquid interfaces, ideal for next generation energy conversion and electrochemical energy storage device developments as well as for the study of early-stage corrosion or oxidation processes. Furthermore, whenever the to-be-monitored layer thickness equals an integral number of the effective atomic layer thickness, the measured acoustic echo will show a higher signal-to-noise ratio [5], indicating not only the discrete quantum behavior of this coherent-phonon-based technique, but also providing justification of the applicability of the impedance-matching-layer model even down to a single atomic layer regime. In our presentation we will also report the observation of the "speckle" noise in the quantum regime [5] and will discuss the physical meaning of non-integer atomic layer thickness for ultrasonic imaging, especially when in this study we

push the ultrasonic imaging to its ultimate resolution limitation.

References

[1] L. V. Wang and S. Hu, Photoacoustic tomography: in vivo imaging from organelles to organs, *Science* **335**, 1458 (2012).

[2] S.-Y. Lee, Y.-H. Lai, K.-C. Huang, Y.-H. Cheng, T.-F. Tseng, and C.-K. Sun, In vivo sub-femtoliter resolution photoacoustic microscopy with higher frame rates, *Scientific Reports* **5**, 15421 (2015)..

[3] C. Thomsen, J. Strait, Z. Vardeny, H. J. Maris, J. Tauc, and J. J. Hauser, Coherent Phonon Generation and Detection by Picosecond Light Pulses, *Phys. Rev. Lett.* **53**, 989 (1984).

[4] K.-H. Lin, C.-M. Lai, C.-C. Pan, J.-I. Chyi, J.-W. Shi, S.-Z. Sun, C.-F. Chang, and C.-K. Sun, Spatial Manipulation of Nanoacoustic waves with a Nanoscale Spot Size, *Nature Nanotech.* **2**, 704 (2007).

[5] H.-Y. Chen, Y.-R. Huang, H.-Y. Shih, M.-J. Chen, J.-K. Sheu, and C.-K. Sun, Extracting elastic properties of an atomically-thin interfacial layer by time-domain analysis of femtosecond acoustics, *Appl. Phys. Lett.* **111**, 213101 (2017).

[6] C.-C. Shen, M.-Y. Weng, J.-K. Sheu, Y.-T. Yao, and C.-K. Sun, In situ monitoring of chemical reactions at a solid-water interface by femtosecond acoustics, *J. Phys. Chem. Lett.* **8**, 5430 (2017).

Linear and nonlinear optics of switchable terahertz metasurfaces

N. Karl[1], G. R. Keiser[1], M. S. Heimbeck[2], H. O. Everitt[2], H.-T. Chen[3], A. J. Taylor[3], I. Brener[4], J. L. Reno[4], and D. M. Mittleman[1*]

[1]School of Engineering, Brown University, Providence, RI USA
[2]US Army AMRDEC, Redstone Arsenal, Huntsville, AL USA
[3]Center for Integrated Nanotechnologies, Los Alamos National Laboratory, Los Alamos, New Mexico USA
[4]Center for Integrated Nanotechnologies, Sandia National Laboratories, Albuquerque, New Mexico USA
*corresponding author, E-mail: `daniel_mittleman@brown.edu`

Abstract

We present experimental studies of the linear and nonlinear optical response of switchable terahertz metasurfaces, using terahertz ellipsometry and nonlinear transmission spectroscopy with intense THz pulses.

1. Introduction

In the terahertz region of the electromagnetic spectrum, there has been a long-standing interest in the development of devices and components to manipulate free-space beams. Metamaterials offer a promising strategy for enabling many capabilities that are otherwise challenging, such as filtering and modulation. In most cases, these structures are realized as two-dimensional meta-surfaces, a class of metamaterials where the scattering elements are arranged in a planar array. Because the elements are deposited on a dielectric surface, the optical properties can be modulated by actively modifying the properties of the surface. This general approach has revealed a wealth of new phenomena, opening up many possibilities for both linear and non-linear optical interactions in the terahertz range. Here, we discuss the characterization of such a switchable metasurface, using both ellipsometry and nonlinear transmission spectroscopy with intense THz pulses.

2. Metasurface design

Our device consists of a planar array of split-ring resonators (SRRs) fabricated on n-doped GaAs. The inset in figure 1 shows the geometry of the MM unit cell. The length of the SRR is L = 66 μm, the linewidth is w = 6 μm, and the capacitive gap width is g = 2 μm. These dimensions are chosen such that the first transmission resonance falls at a frequency of 0.4 THz. The SRR elements are arranged in a square array with a periodicity of 88 μm, composing the metasurface over a 2 cm by 2 cm area. The SRRs are connected with metallic wires to a contact pad for electrical modulation. The resonance amplitude varies with applied bias by about a factor of 2, consistent with previous reports [1,2].

3. Characterization: linear response

The experimental data was obtained on a variable angle spectroscopic ellipsometry (VASE) system [3], in two frequency regions of 330 – 515 GHz and 660 GHz – 1 THz. Spectra were collected at each angle of incidence, θ, which was varied from 30° to 70° for each value of DC bias applied to the sample. Ellipsometry data is given in terms of the ellipsometric parameter ρ which is defined as the ratio of the complex Fresnel reflection coefficients R_p/R_s.

To extract characteristic results from our experimental data, we must first construct a model for the metasurface. We use generalized sheet transition conditions (GSTCs) [4], which employ surface susceptibility parameters to relate the fields around the surface to the surface polarizations and magnetizations induced in the surface. The surface susceptibility parameters of a metasurface array depend on the characteristics (polarizabilities) of its constituent elements and on the layout of the array due to element-element interaction of the metallic elements [5].

The polarizability tensors of a single eSRR element are calculated through finite element (FEM) simulations via the charges and currents excited in the element by an incident plane wave. This method has the advantage that it allows the recovery of the full polarizability matrix of scattering
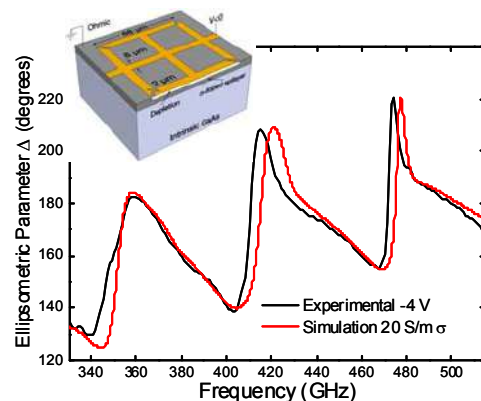
Fig. 1 – A comparison of measured and simulated ellipsometry data, illustrating the good agreement. The inset shows a single element of the SRR array [5].

elements including the substrate. The polarizability matrix is in general a 6x6 matrix that contains co- and cross-coupling terms of the electric and magnetic fields along each axis. Importantly this allows for the inclusion of interesting effects such as substrate-induced-bianisotropy (SIB). The intra-planar interaction matrix which depends on the details of the array such as the element periodicities a, and b is also in general a 6x6 matrix with co- and cross-field terms. The interaction matrix can be analytically calculated with the dyadic Green's functions as described in [5].

The final step for the characterization of the device is to solve the inverse problem of modeling the experimental data to estimate the values of the susceptibilities that produce results predicted from the model that best fit the experimental data. The voltage dependence of the susceptibilities are determined through this inverse process, by fitting to the experimental data at each value of applied bias. This procedure enables us to extract voltage-dependent surface susceptibilities which can be used for *a priori* predictions of the performance of metasurfaces. Our results shows that the ellipsometry data matches the simulations [6], as indicated by the comparison in figure 1. In addition, we find that the voltage dependence can be modeled as a tuning of the conductivity of the epilayer.

4. Characterization: nonlinear response

To experimentally characterize the metamaterial's nonlinear response at varying applied voltage, THz pulses with field strength between 20 and 50kV/cm were generated using the tilted pulse front technique in $LiNbO_3$ and focused onto the metasurface at normal incidence. The transmitted pulse was then used to perform time-domain spectroscopy to obtain transmission spectra for the metasurface.

The nonlinear response of the metasurface arises from two separate effects [7]. At lower fields, intervalley scattering lowers the carrier mobility, and is induced by the interaction of charge carriers with the *incident* THz field. At higher field strengths, impact ionization increases the carrier concentration and thus the GaAs conductivity, and results from the interaction of charge carriers with the *resonant* THz fields localized in the SRR capacitive gap.

Figure 2a shows the response for the metasurface with 0V applied bias. For low fields (blue curve), the conductivity of the GaAs shorts the SRRs and no resonance is seen. For 20 kV/cm incident fields (red curve), inter-valley scattering decreases the carrier mobility in the GaAs, turning on the SRR 'LC' mode at 0.4 THz. For 50 kV/cm peak fields (yellow curve), impact ionization generates carriers in the GaAs substrate, shorting the SRR capacitive gaps again, decreasing the resonance strength. Figure 2b shows the effects of applying a 15V bias to the MM array. The bias depletes carriers from the n-doped layer, and the resonance is now visible at low fields. (blue curve) The bias also allows for impact ionization at lower fields, resulting in a weaker resonance for 20 kV/cm fields (red curve). The 50 kV/cm spectrum (yellow curve) remains largely unchanged by the applied voltage. This is because the resonance is already largely suppressed by impact ionization even at zero bias [8].
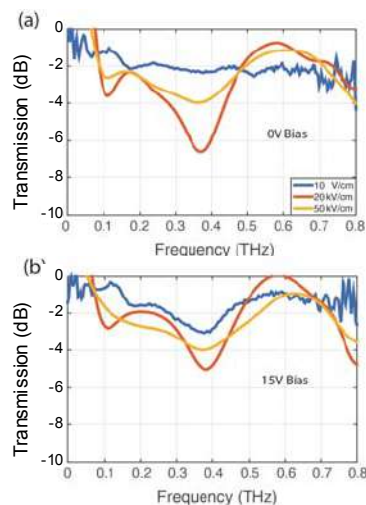
Fig. 2 – Transmission spectra at low field (blue curves) and higher fields (red and yellow curves) for two different values of the DC bias: (a) 0 volts; (b) 15 volts. These results illustrate the competing effects which determine the nonlinear response of the switchable metasurface [7].

References

[1] H.-T. Chen, et al., "Active terahertz metamaterial devices" *Nature* **444**, 597 (2006).

[2] N. Karl, et al., "An electrically driven terahertz metamaterial diffractive modulator with more than 20 dB of dynamic range" *Appl. Phys. Lett.* **104**, 091115 (2014).

[3] T. Hofmann, C. M. Herzinger, A. Boosalis, T. E. Tiwald, J. A. Woollam, and M. Schubert, "Variable-wavelength frequency-domain terahertz ellipsometry," *Rev. Sci. Instrum.*, 81, 023101 (2010).

[4] E. F. Kuester, et al. "Averaged transition conditions for electromagnetic fields at a metafilm" *IEEE Trans. Antennas Propag.* **51**, 2641–2651 (2003).

[5] A. D. Scher, "Boundary effects in the electromagnetic response of a metamaterial using the point-dipole interaction model", Ph.D. thesis, University of Colorado at Boulder, (2008).

[6] N. Karl, et al. "Characterization of an active metasurface using terahertz ellipsometry" *Appl. Phys. Lett.* **111**, 191101 (2017).

[7] K. Fan, et al. "Nonlinear Terahertz Metamaterials via Field-Enhanced Carrier Dynamics in GaAs" *Phys. Rev. Lett.*, **110**, 217404 (2013).

[8] G. R. Keiser, et al. "Nonlinear terahertz metamaterials with active electrical control" *Appl. Phys. Lett.* **111**, 121101 (2017).

Recent progress in terahertz applications in industry

Philip F. Taday

TeraView Limited, Platinum Building, St John's Innovation Park, Cambridge CB4 0DS, UK

*corresponding author, E-mail: `philip.taday@teraview.com`

Abstract

In this presentation we discuss the recent progress in the application of terahertz pulses to industry. A common theme with these applications is that the thickness of the coating of the order of the wavelength of light and the final products have high commercial value.

1. Introduction

Over the past twenty years everyone in the terahertz community has been looking for the so-called "killer" application. The so-called application that will drive terahertz application into the main stream. There have been many potential applications this paper will concentrate on just one – the pharmaceutical industry.

2. Pharmaceutical industry

Figure 1: Photograph showing a TeraPulse 4000 in the background and a six-axis robot used to analysis pharmaceutical coatings.

After a number of years there is still considerable interest in using terahertz pulses in understanding the thickness of coating on pharmaceutical products. Figure 1 shows TeraPulse 4000 with a six-axis robotic system. The operation of this system has been well described before by Zeilter *et al.* *(1)*. Unlike traditional microscopy measurements, the terahertz method provides the advantage of non-destructive assessment of coating thickness and other properties, preserving the tablet for subsequent dissolution testing. In 2008 the US FDA (Spencer *et al.* (2)) used terahertz pulsed imaging (TPI) to measure the coating thickness on mesalamine tablets. The tablets in this study were later destroyed in destructive dissolution tests to provide the mean dissolution time of these tablets. Spencer *et al.* showed a correlation between the coating thickness and the mean dissolution time. Lo *et al.* (3, 4, 5) showed in a series of papers that it was possible to correlate not only the coating thickness but also the density of the coating. In later work Lo *et al.* also used the raw terahertz pulse and chemometrics to predict the dissolution of substained release pharmaceutical product (5). An example of correlation between the thickness on an enteric coated tablet and the dissolution is shown in Figure 2. The outliners from the straight lines are due to imperfections in the tablet coating.
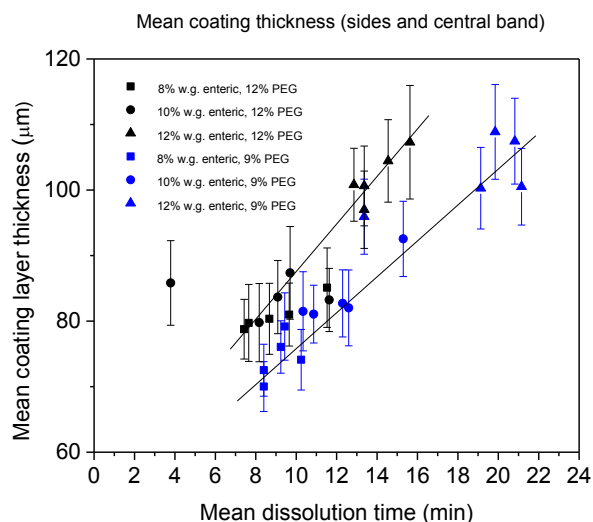
Figure 2: The coating thickness of enteric coated tablets is derived from terahertz pulsed measurements are correlated against the mean dissolution time for different coating weighs and levels of polymer (PEG). The black points have 12% PEG while the blue points have a PEG level of 9%. The outliner at x=4 minutes was due to a crack in the coating of the tablet.

In a recent paper by May *et al.* the authors showed a good correlation between the refractive index measured by terahertz pulsed imaging and the crushing force measured from in compression tests was found using a set of tablets that were compacted at various compression forces and this was found to be relate to tablet hardness (6). The same group used a terahertz sensor inside a coating pan to follow the build-up of a pharmaceutical coating on a tablet (7). An example of where terahertz sensors are being used in industrial applications. One of the potential applications as process analytical tool (PAT) is the monitoring of push–pull osmotic systems (8). In this paper we will review recent progress in the osmotic systems.

2.1. Measurements

Osmotic tablets are being developed to control the release of an active pharmaceutical compound by coating a bilayer tablet with a semipermeable membrane. Swelling of the internal tablet core drives the discharge of active through a port in the apex of the tablet's cap. Many factors control the rate of release, with one of them being the thickness of the semipermeable membrane which can be measured using terahertz pulsed imaging. In this paper number of tablets from different development batches were measured with terahertz imaging and the coating thickness was determined. Dissolution testing was then performed on these tablets to obtain the release rate of each tablet. Subsequently, chemometric analysis was used to develop a predictive model yielding the release rate of the active as a function of coating thickness.
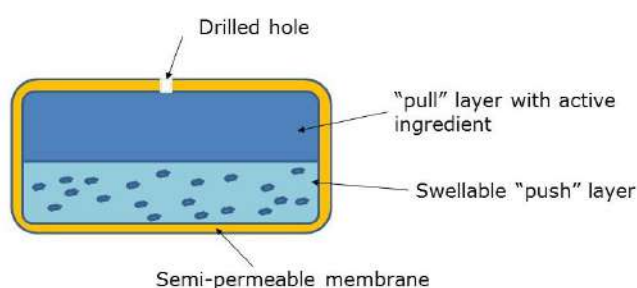
Figure 3: Schematic diagram of osmotic tablet.

2.2 Results

Figure 4 shows typical waveforms from the osmotic tablet. The first strong reflection is from the tablet surface the later reflection is from the coating core interface. The direction of this peak depends on the change in refractive index from the coating to the tablet core and the strength depends on the magnitude of that change.
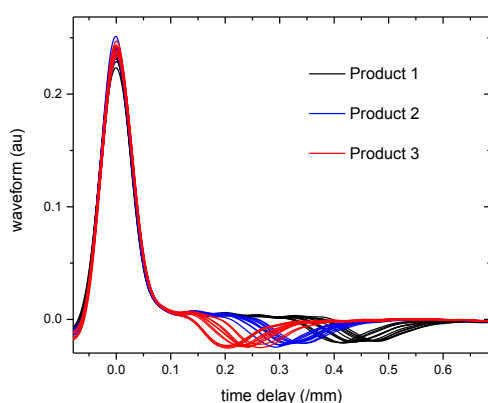
As terahertz pulsed imaging is a time-of-flight technique we can calculate the thickness of coating of each of these products. Subsequent to terahertz test the tablets are destroyed in dissolution testing where the amount of drug released with respect to time is measured. These osmotic tablets have a long release time – several hours and

measuring the thickness of the semi-permeable membrane allows prediction of the dissolution properties of these products using chemometric analysis.

3. Conclusions

Terahertz pulsed imaging was used to measure the coating thickness of long release pharmaceutical products. The thickness of these coatings could be correlated to drug release of these products. With this correlation it maybe possible to a terahertz sensor within the coating process as a PAT tool to determine the end-point of the coating process rather than the weight gain normally employed within the industry.

References

1. J Axel Zeitler, Y. C. Shen, C. Baker, P. F. Taday, Michael Pepper and Thomas Rades, "Analysis of Coating Structures and Interfaces in Solid Oral Dosage Forms by Three Dimensional Terahertz Pulsed Imaging", *J. Pharmaceutical Science, 96(2),* 330-340 (2007).
2. John A. Spencer, Zongming Gao, Terry Moore, Lucinda F. Buhse, Philip Taday, David A. Newnham, Yaochun Shen, Alessia Portieri, Ajaz Husain, "Delayed Release Tablet Dissolution Related to Coating Thickness by Terahertz Pulsed Image Mapping" J. Pharmaceutical Science 97(4), 1543-1550 (2008).
3. Ho L, Müller R, Römer M, Gordon KC, Heinämäki J, Kleinebudde P, Pepper M, Rades T, Shen YC, Strachan CJ, Taday PF, Zeitler JA., "Analysis of sustained-release tablet film coats using terahertz pulsed imaging", J Control Release. 119(3):253-61 (2007).
4. Ho L, Müller R, Gordon KC, Kleinebudde P, Pepper M, Rades T, Shen Y, Taday PF, Zeitler JA, "Terahertz pulsed imaging as an analytical tool for sustained-release tablet film coating", Eur J Pharm Biopharm. 71(1):117-23 (2009).
5. Ho L, Müller R, Gordon KC, Kleinebudde P, Pepper M, Rades T, Shen Y, Taday PF, Zeitler JA "Monitoring the film coating unit operation and predicting drug dissolution using terahertz pulsed imaging" J Pharm Sci.;98(12):4866-76 (2009).
6. May RK, Evans MJ, Zhong S, Warr I, Gladden LF, Shen Y, Zeitler JA, "Terahertz in-line sensor for direct coating thickness measurement of individual tablets during film coating in real-time" J Pharm Sci. 2010 Oct 18 DOI: 10.1002/jps.22359
7. Lin, H., May, R. K., Evans, M. J., Zhong, S., Gladden, L. F., Shen, Y., & Zeitler, J. A. (2015). Impact of Processing Conditions on Inter-tablet Coating Thickness Variations Measured by Terahertz In-Line Sensing. Journal of pharmaceutical sciences.
8. Malaterre, V., Pedersen, M., Ogorka, J., Gurny, R., Loggia, N., & Taday, P. F. (2010). Terahertz pulsed imaging, a novel process analytical tool to investigate the coating characteristics of push–pull osmotic systems. *European Journal of Pharmaceutics and Biopharmaceutics*, *74*(1), 21-25

Nonlinear THz Spectroscopy of Two-Dimensional Systems

Manfred Helm*[1,2], Jacob König-Otto[1,2], Johannes Schmidt[1,2], Emmanouil Dimakis[1], Stephan Winnerl[1], and Harald Schneider[1]

[1]Helmholtz-Zentrum Dresden-Rossendorf, Bautzner Landstr. 400, 01328 Dresden, Germany
[2]TU Dresden, 01062 Dresden, Germany
*corresponding author, E-mail: `m.helm@hzdr.de`

Abstract

Nonlinear THz experiments using a free-electron laser are presented on Landau quantized graphene as well as on intersubband transitions in a single GaAs quantum well.

1. Introduction

Owing to the development of powerful THz sources, both table-top and accelerator-based, highly nonlinear THz investigations of materials are possible today. Here we will present two recent examples of nonlinear spectroscopy on two-dimensional material systems: resonant four-wave mixing in graphene under a magnetic field, and nonlinear THz spectroscopy of intersubband transitions in a semiconductor quantum well.

2. Results

2.1. Four-wave mixing in Landau-quantized graphene

Graphene is predicted to be a highly nonlinear material due to its linear dispersion. Clear experimental observations are relatively scarce, however. In a magnetic field, the band structure splits up into non-equidistant Landau levels, giving rise to resonant behavior of the optical properties. We demonstrate resonantly enhanced four-wave-mixing (FWM) at a photon energy of 78 meV (19 THz), resonant at a magnetic field of B = 4.5 T. The $\chi^{(3)}$ character is clearly demonstrated by the power dependence of the four-wave-mixing signal and the narrower line shape as compared to the linear absorption. The FWM signal, proportional to the induced microscopic polarization, decays faster than the also measured pump-probe signal, beyond the time resolution of the experiment (~4 ps) [1].

2.2. Dressing intersubband transitions in quantum wells

Intersubband transitions in quantum wells, due to their similarities to atomic transitions, have been a playground for many fundamental optical and quantum mechanical effects as well as for novel devices for three decades [2]. Nonlinear or quantum optical effects such as dressed states or electromagnetically induced transparency (EIT) were demonstrated, however, only in the mid-infrared range [3] or probed in the near infrared [4]. Here we employ our THz free-electron laser in combination with THz time-domain spectroscopy to realize a true narrow-band pump – broadband probe experiment: While pumping the 2-3 intersubband transition in a single GaAs/AlGaAs quantum well (at 3.5 THz = 15 meV), we probe the entire THz absorption up to 4 THz (including 1-2 and 2-3 transitions). The experiment allows one to extract the transmission change vs pump-probe time delay as well as the complete spectral shape of the transmission change at a specific time delay. We will discuss the observed spectra, including indications for the Autler-Townes splitting on the 1-2 transition.

References

[1] J. C. König-Otto, Yongrui Wang, A. Belyanin, C. Berger, W. A. de Heer, M. Orlita, A. Pashkin, H. Schneider, M. Helm, S. Winnerl, Four-Wave Mixing in Landau-Quantized Graphene, *Nano Lett.* 17: 2184-2188, 2017.

[2] M. Helm, The basic physics of intersubband transitions, *Semiconductors and Semimetals* 62: 1-99, 2000.

[3] J. F. Dynes, M. D. Frogley, M. Beck, J. Faist, C. C. Phillips, ac Stark Splitting and Quantum Interference with Intersubband Transitions in Quantum Wells, *Phys. Rev. Lett.* 94: 157403, 2005.

[4] S. G. Carter, V. Birkedal, C. S. Wang, L. A. Coldren, A. V. Maslov, D. S. Citrin, M. S. Sherwin, Quantum Coherence in an Optical Modulator, *Science* 310: 651-653, 2005.

Ultrastrong light-matter coupling beyond unity coupling strength

C. Lange, A. Bayer, Marcel Pozimski, Simon Schambeck, Dieter Schuh,
Rupert Huber, and Dominique Bougeard

Department of Physics, University of Regensburg, 93040 Regensburg, Germany

We introduce a paradigm change in the design of THz light-matter coupled systems by treating the electronic and photonic components on equal footing instead of optimizing them separately. Exploiting both cavity and electronic excitation to confine the vacuum mode, we achieve $\Omega_R/\omega_c = 1.43$ for cyclotron resonances ultrastrongly coupled to metamaterials. Under this condition, the vacuum ground state exhibits a record population of 0.37 virtual photons per resonator, massively facilitating the envisaged detection of quantum vacuum radiation by diabatic switching of Ω_R/ω_c.

Sensing and Control of Methylation of Cancer DNA by Terahertz Radiation

Hwayeong Cheon[1] and Joo-Hiuk Son[1,2,*]

[1]Department of Physics, University of Seoul, Seoul, Korea
[2]iNexus, Inc., Gyeonggi-do, Korea
*corresponding author, E-mail: joohiuk@uos.ac.kr

Abstract

By canceration, there is a chemical change in DNA which is a rearrangement of 5-methylcytidine distribution called methylation. This chemical change of methylation is directly observed with terahertz time-domain spectroscopy, showing a resonance at 1.6 THz for various types of cancer. The resonance peak is reduced or controlled by illuminating high-intensity terahertz pulses and it is proved to be resonant process by applying a filter around the frequency.

1. Introduction

Cancer is defined as a genetic and epigenetic disease involving the chemical and structural alteration of DNA. An epigenetic modification is the aberrant DNA methylation, which are a well-known carcinogenic mechanism [1, 2] and a common chemical and structural modification of DNA that does not change the DNA sequence. Terahertz electromagnetic waves can be utilized to observe such modification to DNA because the characteristic energies of biomolecules occur in the terahertz region. We have found resonance fingerprints of methylation in cancer DNA using improved terahertz spectroscopic methods [3]. The degree of resonance is also controlled and reduced by irradiating high-intensity terahertz electromagnetic waves at the resonant frequency.

2. Results

The terahertz characteristics of methylated cytidine, a nucleoside, were a clue to observe the resonance fingerprints of DNA methylation (see the inset of Fig. 1). In aqueous solutions, we tracked and observed the molecular resonance of genomic DNA from two control (293T, M-293T) and five cancer (PC3; prostate cancer, A431; skin cancer, A549; lung cancer, MCF-7; breast cancer, SNU-1; gastric cancer) cell lines, using freezing technique and baseline correction, as shown in Fig. 1 [3]. The amplitudes of the resonance signals were dependent on the types of cancer cells the DNA had come from. These signals could be quantified to identify cancer cell types, and the results were similar to those of biological quantification method called ELISA-like reaction.

The resonance peak was reduced by irradiating high-intensity terahertz waves from a LiNbO$_3$ crystal driven by 1-kHz regenerative amplifier with a filter around 1.6 THz.
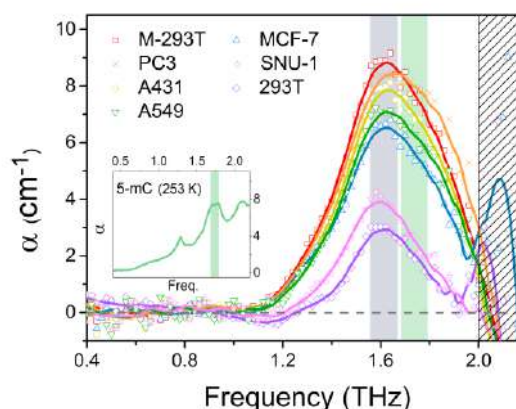
Figure 1: Resonant peaks of normal and cancer DNAs [3].

3. Conclusions

The result demonstrates that the molecular resonance of cancer DNAs exists in the terahertz region. This can be utilized to diagnose early cancer at the molecular level and to provide a potential cancer biomarker. The degree of resonance is also controlled and reduced which could lead to the demethylation of cancer DNA.

References

[1] P.A. Jones, DNA methylation and cancer. Oncogene **21**, 5358–5360 (2002).

[2] P.W. Laird, The power and the promise of DNA methylation markers. Nat. Rev. Cancer **3**, 253–266 (2003).

[3] H. Cheon, et al., Terahertz molecular resonance of cancer DNA. Scientific Reports **6**, 37103 (2016).

Terahertz Microfluidic Devices coupled with Meta Atoms

Masayoshi Tonouchi

Institute of Laser Engineering, Osaka University, Osaka, Japan
E-mail: tonouchi@ile.osaka-u.ac.jp

Abstract

We present a nonlinear optical crystal (NLOC)-based terahertz (THz) microfluidic chip with a few arrays of split ring resonators (SRRs) for ultra-trace and quantitative measurements of liquid solutions. Using this chip, we have succeeded in observing the 31.8 femtomol of ion concentration in actual amount of 318 picoliter water solutions This technique opens the door to microanalysis of biological samples with THz waves and accelerates development of THz lab-on-chip devices.

1. Introduction

Microfluidic devices are now essential for medical diagnosis and biological analysis. Terahertz (THz) diagnostic technology has also opened a variety of possibilities in bioscience applications [1]. Thus a combination of those such as a THz micro-total analysis system (THz-µTAS) would provide a powerful tool for future bioscience. THz time domain spectroscopy has been expected to be indispensable for such bio application, which provides the important information to clarify biological reaction dynamics such as hydrogen bonds and hydrophobic interactions. However, there still remain some major hurdles for real world application. One of the weak points is poor sensitivity of liquid samples. Since the THz beam diameter is rather large and thus THz intensity is low, which requires a large amount of the sample solution. Recently we have developed a rapid laser scanning THz near field imaging system which utilizes nonlinear crystal as a sample holding plate, emitting THz beam locally, and is proven to have excellent performance as a THz imaging system with high sensitivity, high resolution and high speed [2-5]. In the present work, we propose the sensitivity enhanced THz-µTAS with a few of arrays of meta-atoms [6,7], and demonstrate detection of trace amount of minerals in commercial water.

2. Experimental

Figure 1 shows a schematic drawing of the concept of the THz microfluidic chip. The chip consists of a THz radiation point source, a single microchannel and a few arrays of meta-atoms, elementary units of metamaterials. The THz radiation is generated by optical rectification in a nonlinear optical crystal (NLOC, GaAs in the present work) close underneath the microchannel, and couples to the meta-

atoms. The chip then determines the solution concentrations based on changes in the resonant frequency and peak attenuation of the THz transmission spectrum. The THz measurement system is similar to a conventional THz-TDS with a fiber-coupled fs laser source at a wavelength of 1560 nm [3].

To evaluate the sensitivity of the chip, we employed distilled water (0 mg/L of minerals) and commercial mineral water (Contrex, 1468 mg/L of minerals) with different hardness as liquid solutions and measured their resonance characteristics. To avoid the effect of the ion composition change, we chose 1 mineral water and prepared 5 kinds of sample solutions with different hardness by diluting with the distilled water such as 10, 40, 200, 600, and 1000 mg/L. In the measurement, the channel was covered by a 580-μ m-thick quartz plate to prevent drying of the liquid sample and the liquid solutions with ~50 nL was dripped with a micro syringe (0.5BR-7BV: World Precision Instruments, Inc.) manually at a water storage area that is fabricated at both sides of the channel. Then it was automatically installed into the micro-fluid channel by capillarity phenomenon. Note that the actual amounts of the liquid solution that interact with the SRRs were about 318 picoliter.
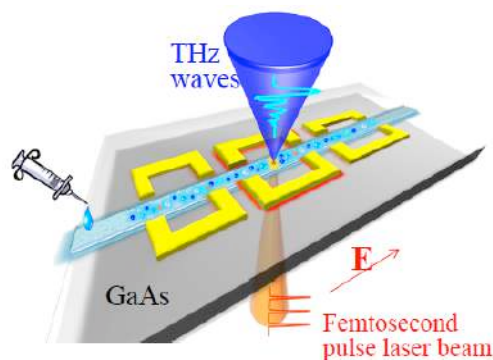
Figure 1: Resonance frequency as a function of the mole number of mineral water.

3. Results and Discussion

Figure 2 show a plot of the frequency shift as a function of the mole number, and that the resonance frequency is shifted to higher frequency with an increase of the amount of minerals in the mineral water. Here, the mole number

was calculated by using the molar mass of $CaCO_3$ (100.087 g/mol: World Health Organization standard) and the volume of the channel being in contact with SRR arrays.

The results indicate that the minute change of the minerals of 10 mg/L is sensitively detected, which corresponds to 31.8 femtomol according to the calculation as referred to above.
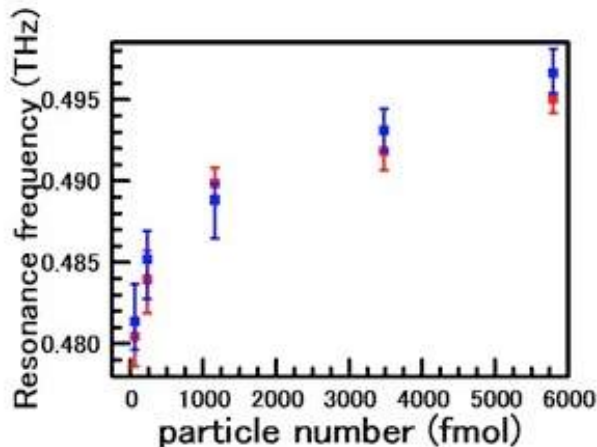
Figure 2: Resonance frequency as a function of the mole number of mineral water.

4. Conclusions

In conclusion, we fabricated and demonstrated a NLOC based THz microfluidic chip with a few arrays of meta-atoms for microanalysis, high-sensitive and label-free measurements of biological samples. The microfluidic chip was evaluated by using distilled water and commercial mineral water with different hardness, and we were able to detect 31.8 femtomol of the mineral in a 318 picoliter solution.

References

[1] M. Tonouchi, Nature Photon. 1, 97 (2007).

[2] H. Murakami, K. Serita, Y. Maekawa, S. Fujiwara, E. Matsuda, S. Kim, I. Kawayama, and M. Tonouchi, J. Phys. D: Appl. Phys. 47, 374007 (2014).

[3] K. Serita, S. Mizuno, H. Murakami, I. Kawayama, Y. Takahashi, M. Yoshimura, Y. Mori. J. Darmo, and M. Tonouchi, Opt. Express 20, 12959 (2012).

[4] W. Withayachumnankul, H. Lin, K. Serita, C. Shah, S. Sriram, M. Bhaskaran, M. Tonouchi, C. Fumeaux, and D. Abbott, Opt. Express 20, 3345 (2012).

[5] C. Fumeaux, H. Lin, K. Serita, W. Withayachumnankul, T. Kaufmann, M. Tonouchi, and D. Abbott, Opt. Express 20, 18397 (2012).

[6] K. Serite, J. Darmo, I. Kawayama. H. Murakami, and M. Tonouchi, J. Infrared Milli. Terahz. Waves 38, 1107 (2017).

[7] K.Serita, E. Matsuda, K. Okada, H. Murakami, I. Kawayama, and M. Tonouchi. APL Photonics 3, 051603 (2018).

Extreme Nonlinear Optics in Transition Metal Dichalcogenide Monolayers

Koichiro Tanaka[1,2]

[1]Department of Physics, Kyoto University, Oiwake-cho, Kitashirakawa, Sakyo, Kyoto, 606-8502 Japan
[2]Institute for Integrated Cell-Material Sciences (iCeMS), Kyoto University, Yoshida-honmachi, Sakyo, Kyoto, 606-8501 Japan
*corresponding author E-mail: kochan@scphys.kyoto-u.ac.jp

Abstract

Nonlinear optical phenomena under extremely high optical field have been studied in transition metal dichalcogenide monolayers with 60 THz excitation. High-harmonic generation is clearly observed and enhanced around the absorption band due to van Hove singularity of the joint density of states.

1. Introduction

Observation of higher-order harmonic generation (HHG) in solids [1, 2, 3, 4, 5] has opened a new platform for investigating the ultrafast electron dynamics in the multi-terahertz region, because it clearly reflects the electron motion driven by the intense sub-cycle laser fields. The mechanism of HHG is fundamentally different from that in atomic gases because of the higher density of the atoms and their periodic structure. In particular, recent reports have revealed that HHG is sensitive to the orientation of the electric field relative to the crystal axis [1, 2, 3, 4]. They demonstrated that HHG is a good tool for exploring the nature of the electron systems in crystals in terms of the symmetry of the electronic band structure [2], inter-atomic bonding [3], and the material's Berry curvature [4].

While this interesting property of HHG clearly reflects the diversity of solids, it may obscure the universal nature of HHG in solids. Among these materials, a monolayer of the transition metal dichalcogenide (TMDC) is one of the simplest crystalline materials to show the origin of HHG. In Ref.[4], even orders of HHG are observed in MoS_2 with the perpendicular polarization to the polarization of the excitation pulse.

In this work, we show the enhancement of the even-orders of HHG around the band-nesting frequency in various TMDCs and propose the origin of the enhancement.

2. Experimental

We used monolayer TMDC crystals grown by CVD method on sapphire substrates. To generate HHG, mid-infrared (MIR) femtosecond laser pulses with 0.26 eV photon energy (60 THz) are generated using a differential frequency generation (DFG) from signal and idler pulses from an optical parametric amplifier (OPA) pumped by a Ti:sapphire based regenerative amplifier (800 nm center wavelength, 35 fs pulse duration, 1 kHz repetition rate, and 1 mJ pulse en-
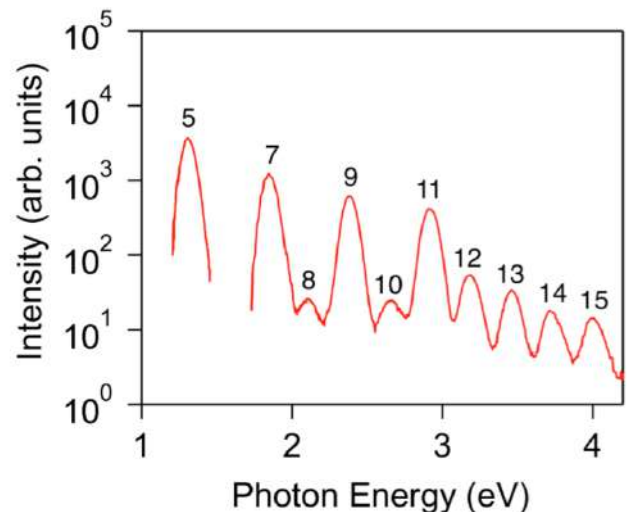
Figure 1: High-harmonic generation spectrum from monolayer MoS_2 under excitation of 60 THz light with 35 fs in pulse width.

ergy). The MIR pulses were focused on the sample by a ZnSe lens of 62.5 mm focal length down to a spot about 30 μm in diameter. The maximum intensity of the pump pulse at the sample was 1 TW/cm^2. The generated HHG was measured by a grating spectrometer (iHR320, Horiba) equipped with a Peltier-cooled charge-coupled device camera (Syncerity CCD, Horiba). All spectra were corrected for the grating efficiency and the quantum efficiency of the detector.

3. Results and Discussions

Typical HHG spectrum in monolayer MoS_2 is shown in Fig.1. We set the polarization of the MIR pulse in parallel with Mo-Mo direction. We observed the even and odd harmonic generation up to 15th harmonics in near-infrared to ultraviolet spectral region. The spectrum is almost the same as that reported in Ref.[4]. The excitation power dependence of the harmonic intensity shows the deviation from the perturbative nonlinear process, indicating a non-perturbative feature of the HHG in MoS_2. We also confirmed even orders of HHG are polarized in perdendicular with the excitation light. The intensity of the 12th harmonics is larger than 8th, 10th, and 14th as shown in Fig. 2,
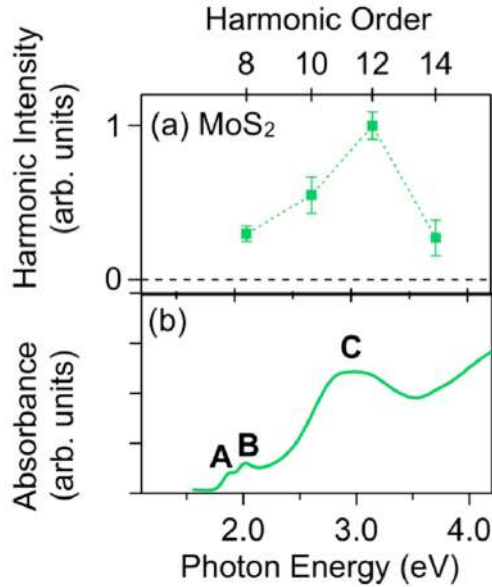
Figure 2: (a) Intensities of even orders of high harmonics in MoS_2. (b) Absorption spectrum of monolayer MoS_2 at room temperature.

4. Conclusions

We clearly demonstrated high-harmonic generation in in transition metal dichalcogenide monolayers with mid-infrared excitation. High-harmonic generation is clearly enhanced around the band-nesting absorption band (van Hove singularity). This suggests that the driving process in k-space with keeping valley-polarization should play an important role in HHG generation process.

Acknowledgement

References

[1] S. Ghimire, A. D. DiChiara, E. Sistrunk, P. Agostini, L. F. DiMauro, and D. A. Reis, "Observation of high-order harmonic generation in a bulk crystal", Nature Phys. **7**, 138 (2010).

[2] F. Langer, M. Hohenleutner, C. P. Schmid, C. Poellmann, P. Nagler, T. Korn, C. Schuller, W .S. Sherwin, U. Huttner, J. T. Steiner, S. W. Koch, M. Kira, R. Huber, "Lightwave-driven quasiparticle collisions on a subcycle timescale", Nature **533**, 255 (2016).

[3] Y. S. You, D. A. Reis and S. Ghimire, "Anisotropic high-harmonic generation in bulk crystals", Nature Phys. **13**, 345 (2017).

[4] H. Liu, Y. Li, Y. S. You, S. Ghimire, T. F. Heinz, and D. A. Reis, "High-harmonic generation from an atomically thin semiconductor", Nature Phys. **13**, 262 (2016).

[5] N. Yoshikawa, T. Tamaya, and K. Tanaka, "High-harmonic generation in graphene enhanced by elliptically polarized light excitation", Science **356**, 736 (2017).

while the intensity of odd orders monotonically decrease with increasing harmonic order. Interestingly, the energy position of the 12th harmonics is almost coincides with the absorption peak **C** that is the van Hove singularity in the joint density of states in the band structure (band nesting). This is not the case only in MoS_2. We made the same experiments in $MoSe_2$, WS_2, and WSe_2 and confirmed the enhancement around the band nesting as well.

In order to account for the enhancement, we carefully consider the driving process in k-space under excitation of the strong MIR pulse. With the linearly polarized excitation, electron-hole polarizations are created in K and K' valleys. The polarization should be described by the sum of two valley-polarized states $|r>$ and $|l>$. The driving effects for $|r>$ and $|l>$ are different from each other under excitation with linear polarization in parallel with Mo-Mo direction: In a phase when $|r>$ state moves from K to the K' direction, $|l>$ state moves from K' to the Γ direction. In turn, as the field direction is reversed, $|r>$ state drives from K to the Γ direction and $|l>$ state drives from K' to the K' direction. Only when the wave-function moves to the Γ direction, it reaches to the band-nesting resonance region with keeping valley polarization. It is noteworthy that $K \to \Gamma$ or $K' \to \Gamma$ motion occurs alternately in every half cycle and should contribute to the perpendicularly polarized even orders of HHG.

THz Pulse Radiation with GHz Repetition Rate in Silicon

M. Mahdi Assefzadeh and Aydin Babakhani*

Electrical and Computer Engineering, UCLA
*Corresponding Author E-mail: aydinbabakhani@ucla.edu

Abstract

In this paper, we report a single-chip array of THz pulse radiators with the ability to produce and radiate 5.4psec pulses. Elements of a 2x4 array radiate the picosecond pulses coherently with a jitter of 270fsec. Picosecond pulse radiation is achieved using a fully electronic laser-free scheme based on the technique of Direct-digital-to-Impulse (D2I) radiation. The chip is fabricated in 90nm SiGe BiCMOS process technology.

1. Introduction

There is a significant demand for producing high-power THz impulses with picosecond duration and GHz repetition rate for imaging, spectroscopy, and wireless communication. Traditionally, photoconductive antennas activated by femtosecond laser pulses are used to radiate picosecond impulses in the THz regime. Unfortunately, these systems are expensive, bulky, and suffer from the low repetition rate of the laser (100MHz or below). These limitations prevent the use of THz systems in applications that demand high volume and low cost. These include smart phones, handheld spectrometers, and portable 3D imaging systems.

In this article, we report a laser-free fully-electronic THz impulse radiating chip that produces high-power picosecond pulses with repetition rates up to 5GHz. The chip consists of an array of 4×2 impulse radiators. Each radiator is equipped with a programmable delay controller that shifts the trigger signal with a resolution step of 300fsec.

2. Circuit Architecture

Fig. 1 shows the architecture of a 4×2 impulse-radiating array that is based on direct digital to impulse radiation [1-2]. In this design, DC magnetic energy is stored on an on-chip slot-bow-tie antenna by passing a DC current through the antenna. This current flows through a high-speed cascode pair of bipolar transistors, which are placed in series with the antenna. Then an external digital trigger signal with a rise-time of 150psec is fed to the chip. This trigger signal passes through multiple edge sharpening amplifiers that reduce the rise/fall time to less than 6psec. The new sharp signal then turns off the pair of cascode transistors and interrupts the DC current of the antenna. This procedure converts the stored DC magnetic energy to a

picosecond impulse radiation. In this method the timing of radiation is locked to the arrival time of the trigger signal at the base of the lower transistor in the cascode pair (Fig. 1).

This timing can be controlled by a programmable delay at the location of each radiator. In this chip, an array of 4×2 radiators are integrated on a single chip.

The external trigger signal is distributed by an H-Tree network and fed to the input of the programmable delay at each element. This architecture allows the chip to align the pulses radiated from 8 elements in space to maximize the peak radiated power.
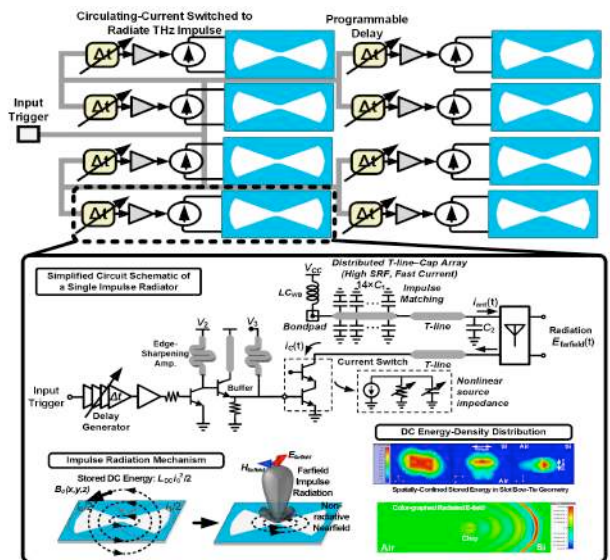
Figure 1 Architecture of the 4×2 impulse-radiating array

3. Measurement Results

Fig. 2 shows the time-domain waveform measured by an optical sampling system. The measured FWHM of the impulse is 5.4psec. This figure also shows that the delay generator can delay the radiated impulse by a step resolution of 300fsec.

In order to measure peak EIRP and jitter of the radiated impulse train, a wideband custom PCB-based impulse receiver antenna with an Agilent DCA86100 with sampling head 86118A is used.

Based on a 3-GHz repetition rate, a peak EIRP of 30dBm is measured. The measured timing jitter of the radiated

impulse is about 270fsec with 64 times averaging. The micrograph of the array chip as well as the zoomed photo of a single element are shown in Fig. 3. The zoomed figure shows the location of the impulse antenna, impulse matching network, edge sharpening amplifier, and the current switch. The entire 4×2 array occupies an area of 1.6mm by 1.5mm including the pads. The chip is fabricated in IBM 90nm SiGe BiCMOS process technology and consumes 710mW.
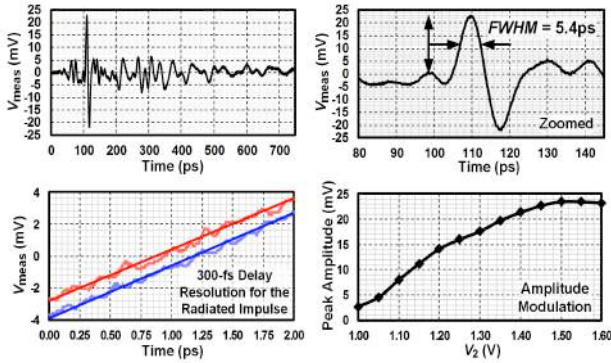
Figure 2 Time-domain measurement results
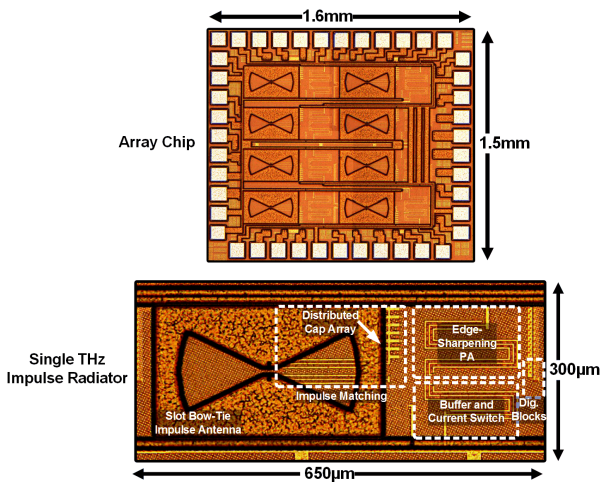
Figure 3 Micrograph of the 4×2 array Chip

4.   Conclusions

In this paper, we reported a laser-free technique for producing and radiating high-power picosecond pulses. The technique relies on storing a magnetic energy on a broadband impulse slot-bow-tie antenna and then releasing it by an external digital trigger. This mechanism results in radiation of a picosecond impulse. To demonstrate this concept, an array of 4×2 impulse radiators is designed, fabricated, and successfully tested.

Acknowledgements

References

[1] M. Assefzadeh and A. Babakhani, "Broadband THz Spectroscopic Imaging based on a Fully Integrated 4x2 Digital-to-Impulse Radiating Array with a Full-Spectrum of 0.03-1.03THz in Silicon," in IEEE Symposia on VLSI Technology and Circuits, Jun. 2016.

[2] M. Assefzadeh and A. Babakhani, " Broadband Oscillator-Free THz Pulse Generation and Radiation Based on Direct Digital-to-Impulse Architecture," in IEEE Journal of Solid-State Circuits, Vol. 52, No. 11, pp. 2905-2919, Nov. 2017.

Terahertz Spectroscopy of Semiconductors and Semiconductor Nanostructures

Coleen T. Nemes[1], Kevin P. Regan[1],
John R. Swierk[1], and Charles A. Schmuttenmaer[1],*

[1]Department of Chemistry, and Yale Energy Sciences Institute, Yale University, New Haven, CT 06520-8107, United States
*corresponding author, E-mail: `charles.schmuttenmaer@yale.edu`

Abstract

Terahertz spectroscopy has proven itself to be an excellent noncontact probe of charge injection and conductivity with subpicosecond time resolution. One may exploit this capability to study a variety of materials, such as transient photoconductivity of wide band gap metal oxides such as TiO2, SnO_2, and WO_3. Our particular interest is the characterization and dynamics of the photoinduced carriers that are required for efficient oxidation at the metal oxide/electrolyte interface, as well as in situ probing of functioning photoelectrochemical devices.

1. Introduction

Photoelectrochemical cells (PECs) convert solar energy into either electrical power or into a fuel, and their development is a promising pathway toward achieving a renewable energy source. Metal oxide semiconductors have been widely studied for their application in water splitting cells due to their favorable structural and electronic properties. Tungsten oxide (WO_3) is of particular interest because it possesses a relatively small band gap energy of 2.6 eV (corresponding to a wavelength of 475 nm), enabling it to absorb light in the visible spectrum without the need for sensitizer dyes. Its electrochemical properties and spectroscopic properties, including transient absorption and time-resolved microwave spectroscopy, have been studied previously. However, the ultrafast charge dynamics on the picosecond timescale have not yet been investigated. Our particular interests lie in the characterization and dynamics of the nascent photoinduced carriers that are required for efficient oxidation at the metal oxide/electrolyte interface.

2. Results and Discussion

2.1 Tungsten oxide particles

Time-resolved THz spectroscopy and open circuit photovoltage measurements have been employed to examine the size-dependent charge carrier dynamics of WO_3 particles. Specifically, films of commercially available WO_3 nanoparticles (NPs) and granular particles (GPs) with diameters of 77 ± 34 nm and 390 ± 260 nm, respectively, were examined in air and also while immersed in 0.1 M

Na2SO4 electrolyte. See Figure 1 for a SEM images of the two particle types. Examination of the frequency-dependent transient photoconductivity at short and long timescales indicates the presence of high mobility photoinduced charge carriers at early times, and in some cases low mobility ones at later times with comparable carrier densities. The presence of long-lived photoinduced charge carriers that contribute to surface chemistry are not detectable until the high-mobility carriers are trapped.
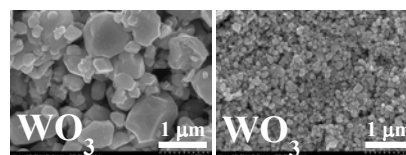
Figure 1. Comparison of GPs (left) and NPs (right).

Ultrafast optical pump – THz probe spectroscopy (OPTP) [1] was employed to determine the photoinduced mobile charge carrier lifetime in WO_3 [2]. THz radiation is sensitive to the product of concentration and mobility of electrons and holes, i.e., the sample's conductivity. The arrival of the THz probe pulse is delayed with respect to the arrival of the 400 nm optical pump pulse over a range of -5 ps to 900 ps. The THz probe pulse is attenuated by mobile charge carriers in the valence and conduction bands of the WO_3, which enables measurement of the rate and magnitude of carrier generation and trapping upon photoexcitation.

OPTP measurements were performed under open circuit conditions in air and 0.1 M Na2SO4 (pH = 2) electrolyte used for photoelectrochemical measurements. The introduction of electrolyte allows for the determination of carrier trapping dynamics under circumstances similar to operating conditions. The overall conductivity decay dynamics due to filling of trap states at grain boundaries and the metal oxide/dielectric interface was measured and the results are shown in Figure 2. We find that long-lived charge carriers may exist in the NPs for 900 ps or longer, and these long-lived photoinduced carriers manifest as an offset in the OPTP trace. On the other hand, grain
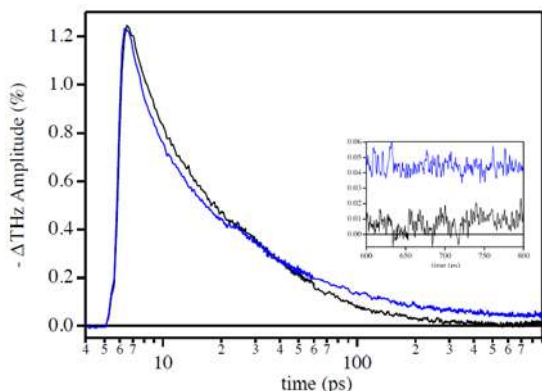
Figure 2. OPTP measurements of WO_3 NP (blue) and GP (black) films. The residual conductivity at 600 ps and beyond is significantly higher for the NPs compared to the GPs.

boundaries in the polycrystalline GPs fully trap the carriers by 500 ps.

2.1 Probing photoelectrochemical cells

In addition, we have recently shown that it is possible to probe a fully functioning dye-sensitized solar cell by using patterned transparent conductive oxide (TCO) electrodes. [3] The standard TCO electrodes transmit visible light, but reflect THz light, and are in fact often used as dichroic mirrors in THz experiments. Our results show that it is possible to probe a DSSC while applying a bias voltage and/or under steady state illumination.
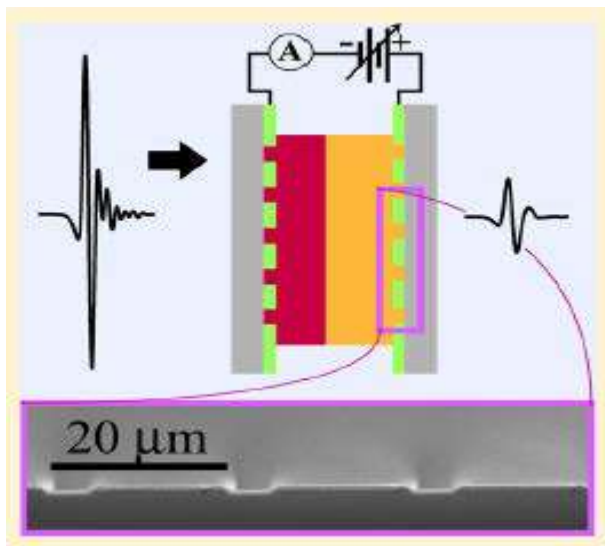
Figure 3. Schematic diagram of a functioning dye-sensitized solar cell probed with THz spectroscopy.

References

[1] M. Beard, G.M. Turner, C.A. Schmuttenmaer, Transient photoconductivity in GaAs as measured by time-resolved terahertz spectroscopy, *Phys. Rev. B*, 62: 15764-15777, 2000.

[2] K.P. Regan, S.W. Sheehan, C. Koenigsmann, C.A. Schmuttenmaer, Size-dependent ultrafast charge carrier dynamics of WO_3 for photoelectrochemical oxidation reactions, *J. Phys. Chem. C*, 120: 14926 – 14933, 2016.

[3] C. T. Nemes, C. Koenigsmann, C. A. Schmuttenmaer, Functioning photoelectrochemical devices studied with time-resolved terahertz spectroscopy, *J. Phys. Chem. Lett.*, 6: 3257 – 3262, 2015.

Nanoscale Laser Terahertz Emission Microscopy

Pernille Klarskov[1,2], Angela Pizzuto[1], & Daniel Mittleman[1]

[1]School of Engineering, Brown University, Providence, RI 02912, USA
[2]DTU Fotonik - Department of Photonics Engineering, Technical University of Denmark, DK-2800 Kgs. Lyngby, Denmark
*corresponding author, E-mail: `pernilleklarskov@gmail.com`

Abstract

We implement Laser Terahertz Emission Microscopy (LTEM) in a near-field microscopy configuration where we simultaneously perform THz nanoscopy. By studying the approach curves of the two methods we obtain a similar spatial confinement on the order of a few 10s of nanometers emphasizing LTEM's potential as a nanoscale imaging technique.

1. Introduction

With the aim of beating the diffraction limit for optical imaging, scattering-type scanning near-field optical microscopy (s-SNOM) has been capable of providing a spatial resolution of 10s of nanometers by taking advantage the ability to scatter light off a sharp, metallic tip when it is in the proximity of a surface [1,2]. Using s-SNOM for imaging with terahertz (THz) beams enables sensing of material parameters such as the carrier concentration on a nanometer scale [3], and recently the s-SNOM technique was developed further into an optical-pump THz-probe configuration for studies of carrier dynamics in nanostructures [4].

Laser Terahertz Emission Microscopy (LTEM) is an alternative method for THz imaging with an improved resolution [5]. Relying on the fact that most semiconductors are capable of emitting THz pulses after being photo-excited by femtosecond (fs) pulses due to a build-in surface field or an externally applied bias, the spatial resolution is determined by the diffraction limit of the fs pulses rather than the THz beam. With this, it has been possible to image current flow in an integrated circuit chip with a spatial resolution of 1 μm [6]. Here, we present an implementation of LTEM in an s-SNOM configuration in order to push the spatial resolution further down to the nanoscale. In the same configuration, we also perform THz time-domain nanoscopy enabling us to compare the two methods back-to-back. We measure the approach curves from both methods and demonstrate how we observe a slightly better near-field confinement for nano-resolved LTEM than for THz nanoscopy. In relation to our recently published results where a gold nanorod was imaged with nanoscale LTEM [7], this study confirms that LTEM can provide a similar spatial resolution as for THz nanoscopy while the two techniques provide complementary information.
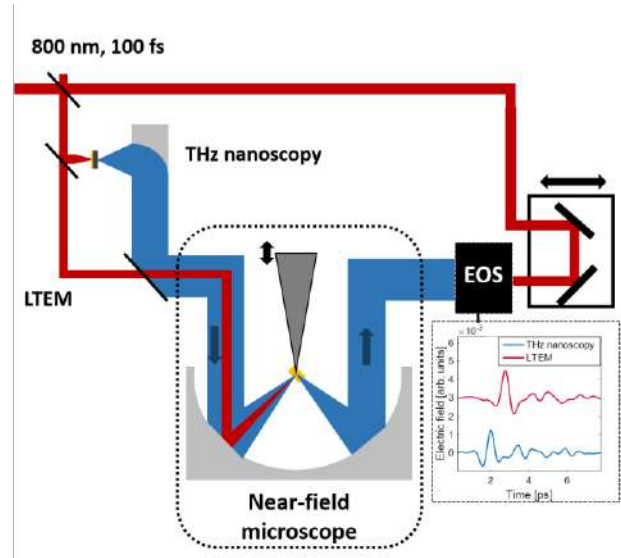
Figure 1: Schematic of the setup.

2. Experiment

The experimental setup is sketched in Figure 1. Femtosecond laser pulses (repetition rate: 80 MHz, center wavelength: 820 nm, pulse duration: 100 fs) are used both to photo-excite the sample directly for LTEM, to generate THz pulses from a photoconductive antenna for performing THz nanoscopy and for detecting the THz pulses in the far-field with electro-optic sampling (EOS). The fs laser pulses and the THz pulses are coupled to a commercial tapping mode atomic force microscopy (AFM) based near-field microscope (neaSNOM, Neaspec) using an ITO coated beam splitter transmitting the laser beam but reflecting the THz beam. The THz field scattered off the tip of the AFM probe is detected by performing lock-in detection of the EOS signal referenced to a harmonic of the AFM probe's oscillation frequency. The inset in Fig. 1 shows the THz pulses for LTEM and THz nanoscopy measured when locking to the 1st harmonic of the tapping frequency. It is seen that the magnitude of the LTEM signal is observed to be slightly higher than the magnitude of the THz nanoscopy signal.

3. Results

In order to study the spatial confinement of the THz near-fields for LTEM and THz nanoscopy, we obtain approach curves where the THz peak field is measured for varied tip-sample distances (z) which are shown in Fig. 2. The sample used in this experiment is a p-doped InAs wafer which is known to be a strong THz emitter [8]. For both THz nanoscopy and LTEM we observe the expected exponential decays of the THz peak field with increasing z-values and for each harmonic of the tapping oscillation, the solid lines indicate the exponential fits to the recorded data. The near-field confinement is defined as the 1/e-width of the exponential decay which is indicated as the dashed line on the plots and estimated in the table below. In general, it is seen that we find a better confinement for the LTEM signal in this experiment which is ranging from 45 nm to 12 nm when recording the signals referenced to the 1st and up to the 5th harmonic of the tip tapping frequency. We note that the confinement of the LTEM signal measured here is significantly better here than in [7] where a gold nanorod still was resolved despite the higher 1/e-width of the LTEM signal.

4. Conclusions and outlook

We have demonstrated a setup combining LTEM and THz nanoscopy in an s-SNOM configuration enabling a direct comparison of the two methods. We show that we achieve a slightly better confinement for LTEM with a 1/e width of the approach curve of 12 nm for the 5th harmonic. We believe that this highly confined LTEM near-field is essential for achieving a high spatial resolution for future imaging of nanostructures and devices.

Harmonic	1	2	3	4	5
THz nanoscopy 1/e width (nm)	83	42	27	24	-
LTEM 1/e width (nm)	45	28	22	15	12

Figure 2: Approach curves for THz nanoscopy and LTEM for signals referenced from the 1st to the 5th harmonic of the tapping oscillation. The solid lines are exponential fits and the dashed line indicates the 1/e value. The table below indicates the estimated 1/e widths.

References

[1] A. Lewis, M. Isaacson, A. Harootunian, and A. Muray, Development of a 500 Å spatial resolution light microscope: I. light is efficiently transmitted through λ/16 diameter apertures, Ultramicroscopy 13, 227-231 (1984).

[2] J. M. Atkin, S. Berweger, A. C. Jones, and M. B. Raschke, Nano-optical imaging and spectroscopy of order, phases, and domains in complex solids, Adv. Phys. 61, 745-842 (2012).

[3] A. J. Huber, F. Keilmann, J. Wittborn, J. Aizpurua, and R. Hillenbrand, Terahertz near-field nanoscopy of mobile carriers in single semiconductor nanodevices, Nano Lett. 8, 3766-3770 (2008).

[4] M. Eisele, T. L. Cocker, M. A. Huber, M. Plankl, L. Viti, D. Ercolani, L. Sorba, M. S. Vitiello, and R. Huber, Ultrafast multi-terahertz nano-spectroscopy with sub-cycle temporal resolution, Nature Photon. 8, 841-845 (2014).

[5] H. Murakami and M. Tonouchi, Laser terahertz emission microscopy, C. R. Phys. 9, 169-183 (2008).

[6] T. Kiwa, M. Tonouchi, M. Yamashita, and K. Kawase, Laser terahertz-emission microscope for inspecting electrical faults in integrated circuits, Opt. Lett. 28, 2058-2060 (2003).

[7] P. Klarskov, H. Kim, V. L. Colvin, and D. M. Mittleman, Nanoscale Laser Terahertz Emission Microscopy, ACS Photonics 4, 2676-2680 (2017).

[8] P. Gu, M. Tani, S. Kono, K. Sakai, and X. C. Zhang, Study of terahertz radiation from InAs and InSb, J. Appl. Phys. 91, 5533-5537 (2002).

Broadband Terahertz Wave Generation from "Liquid-like" media

Alexei1 Balakin1[1,2]**, Vladimir2 Makarov2**[1]**, Nikolay3 Kuzechkin3**[1,2]
Igor4 Kotelnikov4[3,4]**, Peter5 Solyankin5**[2,1]**, and Alexander6 Shkurinov6**[1,2*]

[1]Faculty of Physics & International Laser Center, Lomonosov Moscow State University, Moscow, Russia
[2]Institute on Laser and Information Technologies of RAS, Shatura, Russia
[3]Budker Institute of Nuclear Physics, Novosibirsk, Russia
[4]Novosibirsk State University, Novosibirsk, Russia.
*corresponding author, E-mail: `ashkurinov@physics.msu.ru`

Abstract

We present results of the research on generation of THz radiation in liquid like media under irradiating them with high-intensity femtosecond optical pulses: gas clusters and liquid nitrogen. We used a dual-frequency scheme when emissions of the main laser frequency and its second harmonic are mixed in the same medium. To interpret the observed effects we developed a simple theoretical model of liquid like media ionization which predicts level of ionization, electron temperature in the medium and then the THz wave properties.

1. Introduction

Similar to the existence of four concepts: earth, water, air and fire, the history of human induced terahertz radiation can be traced by using these forms of matter. It was first observed with the help of iron shotgun pellets. Next it was observed in fire. Later THz radiation was found in air and very recently it was obtained from water and other liquids. Time has come to extract it from cold. We present the results of research carried out for the first time, the on generation of terahertz radiation under the action of high power femtosecond laser pulses on liquid like media - gas clusters in supersonic jet and the liquid gas - liquid nitrogen (LN). Our experimental results supported by careful theoretical interpretation, showed clearly that under femtosecond laser radiation, pure liquid, cluster jet and air emit THz waves in a very different way. We assumed that the mobility of ions and electrons in these media can play an essential role, forming a quasi-static electric field by means of ambipolar diffusion mechanism. The role of the diffusion of the electrons in the THz wave generation process is also discussed. The research showed, that energy and polarization properties of THz radiation, which we observed in liquid like media, are determined by coherent superposition of contributions described both as multiwave mixing, liquid-ionization theories and the ionization dynamics. In our work we observed for the first time the nonlinear optical effect: the rotation of the polarization ellipse under the propagation of THz radiation in LN. The source of electromagnetic radiation in the THz band on the basis of laser spark was firstly presented in [1]. An experiment in which a liquid, namely, water was used for the conversion of femtosecond radiation into the THz one is described in [2]. Water is a polar liquid which has high absorption in the THz frequency range and the authors of previously published works have to use for the experiments the very thin water films. Unlike water, considerable absorption both in THz and NIR ranges is absent in LN.

2. Experimental Setup

2.1. Setup for Terahertz Generation and Detection

In our work we made use of two types of femtosecond laser systems, which enabled the study of energy dependencies of the generated THz radiation on the laser pulse energy from 0.5 mJ up to 40 mJ per pulse and the pulse repetition rates from 10 Hz to 1 kHz.

The laser system of the first type uses laser radiation from Ti: Sapphire regenerative amplifier (Spectra Physics Spitfire) with the energy up to 2.5 mJ per pulse, minimal pulse duration 30 fs, wavelength 797 nm and 1 kHz repetition rate. Pulse duration is tuned in the range of $30 \div 300$ fs by chirping the laser pulse in internal grating compressor of the Spectra Physics Spitfire regenerative amplifier.

The laser system of the second type uses CPA laser system based on a femtosecond Ti:Sapphire laser with multipass amplifier. This laser system provides pulses with the energy up to 40 mJ at the repetition rate of 10 Hz, 810-nm central wavelength. Pulse duration is tuned in the range of $50 \div 800$ fs by chirping the laser pulse in an external vacuum grating compressor.

2.2. LN materials and the cluster preparation

LN used in our experiments was obtained by the use of an ordinary membrane system of nitrogen separation from compressed air. The system provides nitrogen purity of around 98 % of the feed compressed air.

For cluster production we applied well-known technique of adiabatic expansion of the gas flow into vacuum through a special nozzle. We used a supersonic conical nozzle with input diameter d_{in} = 0.7 mm, output diameter d_{out} = 4.7 mm, half opening angle α = 5○, and 24.7 mm length. The nozzle is connected to a high-pressure cham-
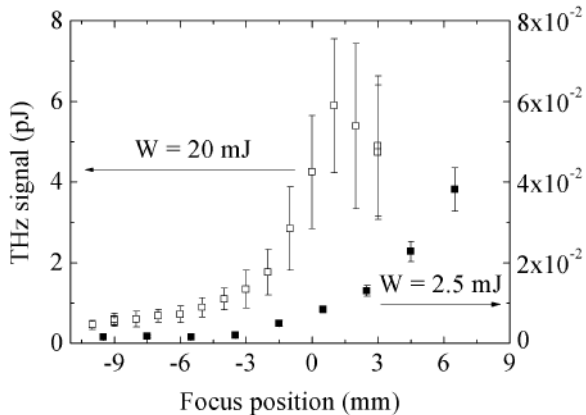
Figure 1: Dependence of THz pulse energy on the lens focus position regarding the surface level of the liquid nitrogen. "black squares" indicate THz signal with 2.5 mJ pumping energy; "open squares" indicate THz signal with 20 mJ pumping energy.

ber with a pulsed electromagnetic valve, which operates at repetition rate of 1.25 Hz and synchronized with the laser pulses. Time delay between laser pulse and moment of the valve opening is controlled with timing module to provide ability to manage and optimize the process of clusters formation. Pure argon gas was used for clusters production. Maximum value of the gas backing pressure that we used was 2 MPa and working pressure in the vacuum chamber did not exceed 5 mTorr

3. Experimental results

3.1. THz wave generation in LN

First of all, we obtained the THz radiation with the use of a dual frequency scheme in an experimental set-up without liquid nitrogen, from a routine optical air breakout. After that, the laser beams on the fundamental and the second harmonic was focused into LN and the THz radiation was also observed. Figure 1 shows the dependences of the THz pulse energy on the lens focus position regarding the surface of liquid nitrogen (the laser beam waist is located inside the liquid if z < 0 and in the air if z > 0). The intensity of the generation changes exponentially as the beam-waist position varies and a and a leap in the level is observed when the level of the surface is passed.

Also we have studied how THz yield scales with laser pulse duration and its energy, angle of rotation of the BBO crystal and measured spectra of the THz radiation.

3.2. THz wave generation in gas cluster medium

We have found that yield of THz and X-Ray radiation from argon cluster beam, excited by high-intensity femtosecond laser pulses, differently depends on the laser pulse duration. THz yield strongly decreases when laser pulse duration is the shortest whereas X-Ray yield is maximal under these

conditions.

The difference in the optimal laser pulse duration for efficient generation of X-ray and THz radiation can be explained by the different times required for formation of electron subsystems in argon cluster. The population of outer electrons rises quickly during the first 50 femtoseconds and they are responsible for the generation of X-ray, that explains the maximal X-ray yield at the minimal pulse duration in our experiments. Whereas the inner electrons of the cluster are responsible for the generation of THz radiation. The inner electrons multiply slowly and their population reachs maximum at the time scale of about hundreds femtosecond, that can be attributed to the enhancement of THz yield at $\tau \approx 250$ fs in our experiments. At the later stages the population of outer electrons begins to rise again that may cause the decrease in THz signal. Usage of two-color excitation scheme results in enhancement of the THz yield and does not change yield of the X-Ray radiation.

4. Conclusions

With respect to the case of THz wave generation from air-plasma, the bandwidth of THz wave generated from water film was somewhat narrower, but the intensity was more than one or two orders of magnitude stronger. In contrast to THz generation from air-plasma, for the single beam laser excitation of the water film, THz generation was more efficient for longer pulse duration. The experimental data from [2] supports the dipole approximation interpretation for normal incident and for the large angles of incident. For thin films of water after laser ionization such effect can be described by the model of micro-plasma for the case of deep focusing of radiation, which leads to formation of very small volume of highly ionized plasma. It is this volume that has to emit THz radiation under large conical angles. At the same time, under the one-color laser excitation forward radiation is also possible, if the volume of highly dense plasma has clear boundaries. Such mechanism was predicted theoretically earlier, however, it has not yet been proved experimentally.

References

[1] H. Hamster, A. Sullivan, S. Gordon, W. White, and R. W.Falcone, Subpicosecond, electromagnetic pulses from intense laser-plasma interaction, *Phys. Rev. Lett.* 71: 2725-2728, 1993 .

[2] [2] Q. Jin, Y. E, K. Williams, J. Dai, and X.-C. Zhang, Observation of broadband terahertz wave generation from liquid water, *App. Phys. Lett* 111: 071103, 2017.

Photonic engineering of continuous wave THz quantum cascade resonators

Miriam Serena Vitiello

[1]NEST, CNR - Istituto Nanoscienze and Scuola Normale Superiore, Piazza San Silvestro 12, 56127, Pisa, Italy

*corresponding author, E-mail: Miriam.vitiello@sns.it

Abstract

The talk will provide an overview of our recent technological developments of miniaturized Terahertz quantum cascade lasers (QCLs) operating in continuous wave (CW) with state of the art performances, controlled and directional beam profiles and fine control of the spectral bandwidth.

1. Introduction

Quantum cascade lasers (QCLs) operating at THz frequencies have undergone rapid development since their first demonstration.[1] Typically, continuous-wave (CW) operation is required to target application needs, combined with a low divergent spatial profile in the far-field, and a fine spectral control of the emitted radiation.[2] This, however, is very difficult to achieve in practice both when single-mode emission and multimode emission are required. Here we report on the development of THz QCLs exploiting a novel lithographic configurations to address simultaneously the need for: i) low divergence; ii) single-mode emission; iii) high power; iv) high wall-plug efficiency; v) continuous wave operation.[3]

We devised a set of in-plane emitting 1D-wire lasers exploiting a corrugated wire laser cavities, employing a feedback grating provided by the sinusoidal lateral corrugation, weakly coupled into free-space. In this latter case, holes with diameters (10 μm), significantly smaller than the emitted radiation wavelength, have been periodically patterned onto the top surface with a periodicity equal to the extraction wave-vector k_{ex}, to allow efficient point-like isotropic vertical extraction (Figs.1a,b). This new architecture overcomes all the present technological limits in optimizing the performance of THz QCLs, and has led to the achievement of low-divergent beams (10˚) (Fig.1c), single-mode emission, very high slope-efficiencies (250 mW/A), and stable CW operation.[3]

Simultaneously, we also devised novel broadband coherent light sources: quasi crystal[4,5] or random[6] THz laser embedding a QCL heterostructure (Fig. 1d) capable to produce coherent broadband radiation with up to 10 spectral lines around a central frequency of 3.1 THz combined with an almost diffraction limited far-field emission profile and ~ 80 mW of optical power (Fig.1e).

Acknowledgements
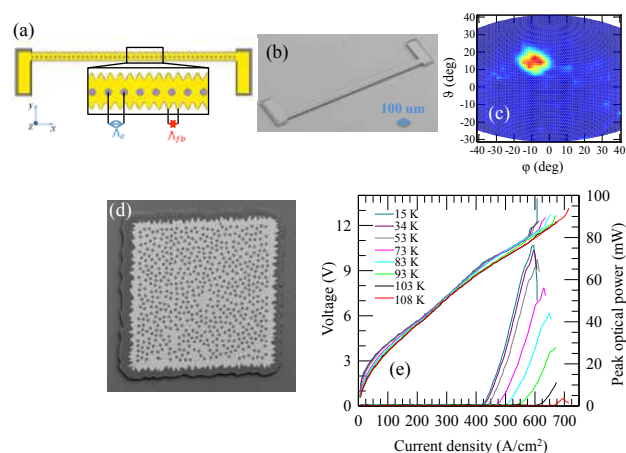
References

[1] M.S. Vitiello, G. Scalari, B.S. Williams, P. De Natale, **Optics Express** 23, 5167 (2015).

[2] F. Castellano, S. Zanotto, L. H. Li, A. Pitanti, A. Tredicucci, E. H. Linfield, A. G. Davies and M. S. Vitiello, ***Appl. Phys. Lett.*** 106, 011103, (2015).

[3] S. Biasco, K. Garrasi, F. Castellano, L. Li, H. H. Beere, D. A. Ritchie, E. H. Linfield, A. G. Davies and M. S. Vitiello, ***Nature Communication*** (2018), in press.

[4] M.S. Vitiello, M. Nobile, A. Ronzani, A. Tredicucci, F. Castellano, A. Talora, L.H.Li, E.H. Linfield, A.G. Davies ***Nature Communications*** 5, 5884 (2014).

[5] S. Biasco, L. Li, E. H. Linfield, A. G. Davies and M. S. Vitiello, ***Photonics*** 3, 32 (2016).

[6] S. Biasco, L. Li, E. H. Linfield, A. G. Davies and M. S. Vitiello, *manuscript in preparation.*

Waves in heterogeneous and nonlinear media: direct and inverse problems, recent advances…

Waves in Metal-Dielectric Waveguides filled with Nonlinear Inhomogeneous Media

Yuri Shestopalov[1], Eugene Smolkin[2*], Maxim Snegur[1]

[1]University of Gävle, Gävle, Sweden
[2]Penza State University, Penza, Russia
*corresponding author, E-mail: e.g.smolkin@hotmail.com

Abstract

The propagation of monochromatic electromagnetic waves in a cylindrical waveguide filled with nonlinear inhomogeneous media is considered. The physical problem is reduced to solving a transmission eigenvalue problem for a system of ordinary differential equations. Spectral parameters of the problem are propagation constants of the waveguide. For the numerical solution, a method is proposed based on solving an auxiliary Cauchy problem (a version of the shooting method). As a result of comprehensive numerical modeling, new propagation regimes are discovered.

1. Introduction

Theory of propagation of electromagnetic waves in circular dielectric waveguide is well elaborated in the linear case, i.e. when the waveguide is filled with linear isotropic homogeneous medium [1, 2]. It is well-known that there are two types of azimuthal-symmetric electromagnetic polarized waves: TE- and TM-waves.

In this work we consider a circular metal-dielectric waveguide filled with nonlinear isotropic inhomogeneous medium. We will assume that medium in the waveguide is described by the Kerr law. In this case two types of azimuthally-symmetric electromagnetic polarized TE- and TM-waves also exist (see [3] for TE-waves and [4] for TM-waves).

A numerical method proposed for the determination of the propagation constants for TE and TM cases (see [5, 6, 7]) can be applied for numerical study of the propagation of hybrid waves.

2. Statement of the problem

Consider three-dimensional space $\mathbb{R}^3$ with the cylindrical coordinate system $O\rho\varphi z$. A circular cylindrical waveguide placed in $\mathbb{R}^3$ along Oz-axis is filled with isotropic nonmagnetic medium and has the cross section $\Sigma := \{(\rho, \varphi, z) : r_0 \leq \rho < r, 0 \leq \varphi < 2\pi\}$. We assume $\mu = \mu_0$, where $\mu_0 > 0$ is the permeability of vacuum. The waveguide is unlimitedly continued in the z direction.

We assume that the fields $\tilde{\mathbf{E}}$, $\tilde{\mathbf{H}}$ depend harmonically on time [8]. It is obvious that $|\mathbf{E}e^{-i\omega t}| = |\mathbf{E}|$. This allows us to rewrite Maxwells equations for the complex amplitudes $\mathbf{E}, \mathbf{H}$:

$$\begin{cases} \operatorname{rot} \mathbf{H} = -i\omega\varepsilon\mathbf{E}, \\ \operatorname{rot} \mathbf{E} = i\omega\mu_0\mathbf{H}. \end{cases} \quad (1)$$

Complex amplitudes of electromagnetic field $\mathbf{E}, \mathbf{H}$ satisfy the Maxwell equations (1); the tangential components of the electric field vanish on the perfectly conducting surfaces $\rho = r_0$ and $\rho = r$.

Waves propagating along the boundary depend on z as $e^{i\gamma z}$, where γ is unknown spectral parameter (propagation constant). We will assume that γ is real. Obviously, $|\mathbf{E}e^{i\gamma z}| = |\mathbf{E}|$ does not depend on z. Thus, the components $E_\rho, E_\varphi, E_z, H_\rho, H_\varphi, H_z$ have the following form:

$$\widetilde{E}_\rho \equiv E_\rho(\rho)e^{i\gamma z}, \quad \widetilde{E}_\varphi \equiv E_\varphi(\rho)e^{i\gamma z}, \quad \widetilde{E}_z \equiv E_z(\rho)e^{i\gamma z},$$
$$\widetilde{H}_\rho \equiv H_\rho(\rho)e^{i\gamma z}, \quad \widetilde{H}_\varphi \equiv H_\varphi(\rho)e^{i\gamma z}, \quad \widetilde{H}_z \equiv H_z(\rho)e^{i\gamma z},$$

and fields $\tilde{\mathbf{E}}, \tilde{\mathbf{H}}$ can be represented as

$$\tilde{\mathbf{E}} = \operatorname{Re}\left\{\left(E_\rho e^{i(\gamma z - \omega t)}, E_\varphi e^{i(\gamma z - \omega t)}, E_z e^{i(\gamma z - \omega t)}\right)^T\right\},$$
$$\tilde{\mathbf{H}} = \operatorname{Re}\left\{\left(H_\rho e^{i(\gamma z - \omega t)}, H_\varphi e^{i(\gamma z - \omega t)}, H_z e^{i(\gamma z - \omega t)}\right)^T\right\}.$$

We suppose that permittivity inside the waveguide Σ has the form

$$\varepsilon = \varepsilon_0\left(\varepsilon(\rho) + \alpha\left(|\mathrm{E}_\rho|^2 + |\mathrm{E}_\varphi|^2 + |\mathrm{E}_z|^2\right)\right), \quad (2)$$

where $\varepsilon(\rho)$ is a smooth function and $\alpha > 0$ is a real constant.

Rewrite system (1) in the expanded form and after simple transformations we get

$$\begin{cases} \gamma^2 u_1 + \gamma u_3' = k_0^2\varepsilon u_1, \\ \left(\rho^{-1}(\rho u_2)'\right)' - \gamma^2 u_2 = -k_0^2\varepsilon u_2, \\ \gamma\rho^{-1}(\rho u_1)' + \rho^{-1}(\rho u_3')' = -k_0^2\varepsilon u_3, \end{cases} \quad (3)$$

where $k_0^2 = \omega^2\mu_0\varepsilon_0 > 0$, k_0 is the wavenumber of free space, and

$$u_1(\rho) := E_\rho(\rho), \ u_2(\rho) := E_\varphi(\rho), \ u_3(\rho) := iE_z(\rho).$$

Formulate *Problem P_H: find real values γ such that there are functions u_1, u_2, and u_3 such that: $|\mathbf{u}|^2 \not\equiv 0$, u_1, u_2, and u_3 are the solutions of equations (3) and functions u_2 and u_3 vanish at $\rho = r_0$ and $\rho = r$.*

3. Numerical method and results

The method under consideration makes it possible to find (normalized) propagation constant γ. Consider the Cauchy problem for the system of equations (3) with the following initial conditions

$$u_1(r) := C_1, \; u_2(r) := 0, \; u_2'(r) := C_2, \; u_3(r) := 0.$$

Represent functions u_2 and u_3 on the boundary $\rho = r$ as the following expression

$$u_1(r) = C \cos\theta, \; u_2'(r) = C \sin\theta, \qquad (4)$$

where constant $C > 0$ (value of field on the boundary) is supposed to be known and parameter $\theta \in [0, 2\pi]$. We choose condition (4) to relate the constants C_1 and C_2.

Using the transmission condition on the boundary r_0 we obtain the following system of dispersion equations

$$\begin{cases} \Delta_E(\gamma) := u_2(r_0; \gamma, \theta) = 0, \\ \Delta_M(\gamma) := u_3(r_0; \gamma, \theta) = 0, \end{cases} \qquad (5)$$

where quantities $u_2(r_0)$ and $u_3(r_0)$ are obtained from the solution to the Cauchy problem.

Choosing the value of constant C and variate the values of angular parameter θ, we can determine (numerically) the solutions of the equations $\Delta_E = 0$ and $\Delta_M = 0$.

For the numerical solution of Problem P_H a method based on the solution to the auxiliary Cauchy problem is proposed (see [9]). The following values of parameters are used for calculations: $C = 1$, $r_0 = 2$, $r = 5$, $\varepsilon = 4$, $\alpha = 0.1$.

In Fig. 1 the dependence $\gamma(\omega)$ is plotted. We call $\gamma(\omega)$ the dispersion curve (DC). Red line corresponds to the nonlinear hybrid wave, green and blue curves correspond to the linear TE- and TM-waves, respectively. A grey dashed angle is the domain where the linear problems have a solution. The vertical dotted black line corresponds to the circular frequency $\omega = 1$. Eigenvalues of a particular problem are points of intersections of this dotted line with the DCs;
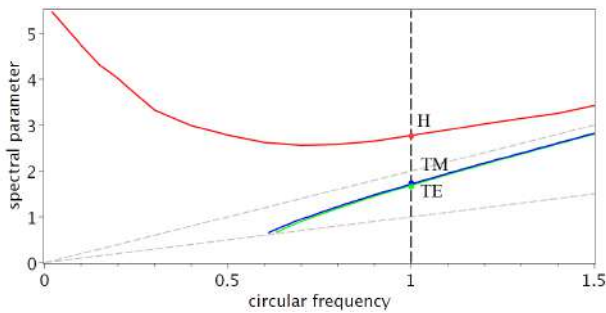
Figure 1: DCs for linear TE, TM and nonlinear hybrid waves. Marked eigenvalues: linear TE eigenvalue $\gamma \approx 1.674$ (green dot); linear TM eigenvalue $\gamma \approx 1.719$ (blue dot); nonlinear hybrid eigenvalue $\gamma \approx 2.761$ (red dot).

4. Conclusion

Numerical results which predict the existence of non-polarized azimuthal-symmetric waves in a metal-dielectric waveguide are presented. An interesting fact is that these waves do not correspond to nonlinear TE and TM polarized waves. Natural question that arises is to check experimentally existence of nonlinear hybrid waves.

References

[1] A.W. Snyder, J. Love, *Optical waveguide theory,* Springer, 1983.

[2] M.J. Adams, *An Introduction to Optical Waveguides,* New York: Wiley, 1951.

[3] Y.G. Sminov, H. W. Schürmann and Y. V. Shestopalov, *Integral equation approach for the propagation of TE-waves in a nonlinear dielectric cylindrical waveguide,* J. Nonlinear Math. Phys. No. 11, pp. 9256–268, 2004.

[4] Y. G. Smirnov, D. V. Valovik, *ElectromagneticWave Propagation in Nonlinear Layered Waveguide Structures,* Penza: Penza State Univ. 2011.

[5] Yu.G. Smirnov, E.Yu. Smolkin, D.V. Valovik, *Nonlinear Double-Layer Bragg Waveguide: Analytical and Numerical Approaches to Investigate Waveguiding Problem*, Advances in Numerical Analysis, Vol. 2014, pp. 1–11, 2014;

[6] E.Yu. Smolkin and D.V. Valovik *Guided Electromagnetic Waves Propagating in a Two-Layer Cylindrical Dielectric Waveguide with Inhomogeneous Nonlinear Permittivity*, Advances in Mathematical Physics. Vol. 2015, pp. 1-11, 2015

[7] E. Smolkin and Yu. Shestopalov *Nonlinear Goubau line: analyticalnumerical approaches and new propagation regimes*, Journal of Electromagnetic Waves and Applications. Vol. 31, pp. 781-797, 2017

[8] P. N. Eleonskii, L. G. Oganesyants, and V. P. Silin, *Cylindrical nonlinear waveguides,* Soviet Physics JETP, Vol. 35, 44–47, 1972.

[9] Eugene Smolkin, *The Azimuthal Symmetric Hybrid Waves in Nonlinear Cylindrical Waveguide,* Progress In Electromagnetics Research Symposium Proceedings, pp. 1–6, 2017.

Resonant States and Unique Permittivity Reconstruction of Layered Dielectrics

Yury Shestopalov

Faculty of Engineering and Sustainable Development, University of Gävle, Gävle, Sweden
*corresponding author, E-mail: `yuyshv@hig.se`

Abstract

Proceeding from the discovery of complex singularities of the scattering matrix of a multi-layered parallel-plane dielectric inclusion in a waveguide of rectangular cross section, a method is proposed for justifying unique reconstruction of the layer permittivities. The technique is extended to the analysis of more complicated dielectric inclusions placed in waveguides of arbitrary cross section.

1. Introduction

Consider the scattering of a normal waveguide mode by a multi-layered parallel-plane dielectric inclusion placed in a waveguide of rectangular cross section (Fig. 1). Recent discovery [1] of complex singularities of the transmission coefficient for this structure significantly impacts upon the methodology of solving the inverse problem of reconstructing layer permittivities. The case of one layer constitutes here an in-demand inverse waveguide problem that finds applications in many standard devices and experimental setups (see e.g. [2] and references therein). Construction of techniques that guarantee non-ambiguous reconstruction of the layer permittivity from the measured transmission/reflection coefficients is an urgent task. In this study we develop an approach [3] aimed at justification of a reconstruction technique that employs information about singularities and extrema of the scattering matrix elements in the complex domain.
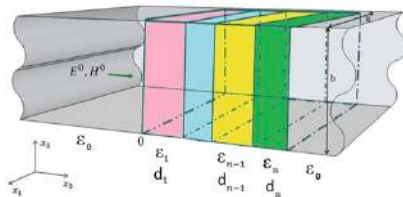
Figure 1: Multi-layered parallel-plane dielectric inclusion in a waveguide of rectangular cross section.

2. Singularities of the transmission coefficient

2.1. Single-layer case

The case of one layer constitutes a canonical setting. For the established time-harmonic ($\sim e^{-i\omega t}$) solution of the Maxwell's equation in the waveguide with a one-layer inclusion, the transmission coefficient acquires an explicit form [4]

$$F = F(z) = \frac{\exp(ist)}{g(z)}, \qquad g(z) = \cos tz + iZ(z)\sin tz, \qquad (1)$$

$$Z(z) = \frac{1}{2}(\frac{z}{s} + \frac{s}{z}), \qquad z = z(\varepsilon_1; f) = (\varepsilon_1 - \pi^2/(k_0 a)^2)^{1/2},$$

$s = s(f) = (1 - \pi^2/(k_0 a)^2)^{1/2}$, $t = k_0 d_1$, ε_1 is the inclusion permittivity, a is the waveguide width, $k_0 = \frac{\omega}{c}$ is the free-space wavenumber, $\omega = 2\pi f$, c is the speed of light in vacuum, and f is the frequency. For the functions in (1), the following statements are valid [1, 4]:

- $|g(z)| \geq 1, |F(z)| \leq 1$ for $\operatorname{Im} z \leq 0, \operatorname{Im} t = 0$;
- $|g(z_m^{*(i)})|' = 0$, $z_m^{*(1)} = \pi m / t$, $z_m^{*(2)} \in (z_m^{*(1)}, z_{m+1}^{*(1)})$, $m = 1, 2, \ldots$;
- $|F(z)|$ has alternating minima at $z_m^{*(2)}$ and maxima at $z_m^{*(1)}$ where $|g(z_m^{*(1)})| = |F(z_m^{*(1)})| = 1$

These properties of the transmission coefficient follow from the statements partially proved in [2, 3]: functions $g(z)$ and $g'(z)$ have each infinitely many complex zeros, all with nonzero imaginary part, forming infinite countable sets

$$S^{(j)} = S^{(j)+} \bigcup S^{(j)-}, S^{(1)\pm} = \{\xi_m^\pm\}_{m=1,2},$$

where $S^{(j)+}$, $S^{(j)-}$ are situated in the first and third quadrants of the complex z-plane, $j = 1,2$ correspond, respectively, to $g(z)$ and $g'(z)$, and $\operatorname{Re} \xi_m^\pm$ asymptotically approach $\pm\pi m$ as $m \to \infty$ (see Fig. 2). Consequently, $F(z)$ is a meromorphic function with a set of poles $S^{(1)}$ having neither zeros nor real singularities.

2.2. Multi-layered inclusions

Using perturbation theory and small-parameter method, one can generalize the results of Section 2 and show [1, 3] that for any number n of layers in a multi-layered dielectric inclusion (diaphragm) the transmission coefficient considered w.r.t. longitudinal wavenumber of each particular layer (denoted by z in the single-layer case) has infinitely many complex poles. In view of this, one can state that in a multi-layer diaphragm each layer L_p generates [4] its own

singularity set which forms a hypersurface $S_p^{(j)}$ continuous w.r.t. the problem parameters such as frequency f and layer
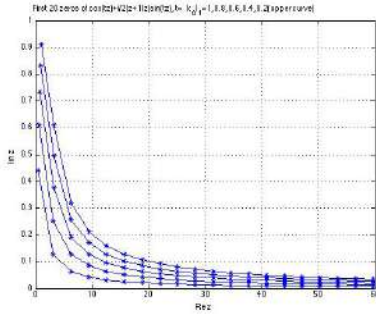
Figure 2: Typical hyperbola-like distribution on the complex plane z of the first 20 poles of the transmission coefficient for a single-layer parallel-plane dielectric inclusion in a waveguide of rectangular cross section at five values of $t = k_0 d_1 = 1, 0.8, 0.6, 0.4, 0.2$ (upper curve: $t = 0.2$).

widths $d_p, p = 1, 2, \ldots, n$, the total singularity set being a union of all sets $S_p^{(j)}$.

3. Analysis of unique solvability

3.1. Permittivity reconstruction for one layer of a multi-layered diaphragm

Permittivity ε_p of a pth layer of an n-layer diaphragm is obtained by solving the equation

$$F(z_p(\varepsilon_p); f; P) = T, \quad z_p = (\varepsilon_p - \pi^2 / (k_0 a)^2)^{1/2}, \quad (2)$$

w.r.t. z_p, where T is the (measured) transmission data, P is a vector comprising all problem parameters (given in measurements), and F is determined explicitly using a recursion [4]; equation (2) defines $\varepsilon_p = \varepsilon_p(f; P)$ as an implicit function. For a single-layer case F is given by (1). The information about the location of singularity and 'extremal' sets of F allows one to justify correct determination of real or complex permittivity by specifying domains in the complex ε_p- or z_p-plane where F is one-to-one; that is, the domains free from the singularities of F.

3.2. The case of real permittivity

Finding real permittivity from (2) is incorrect [3] (already for the exact data T) because for a specified frequency interval, T must belong to the range of $F(z_p(\varepsilon_p); f; P)$ considered on the given interval $I_{apr} = (\varepsilon_{apr}^* < \varepsilon_p < \varepsilon_{apr}^{**})$ of the *a-priori* known permittivity values; this range forms a curve on the complex plane F (a set of measure zero); equation (2) becomes overdetermined, so that additional conditions must be imposed on its right-hand side to guarantee the solvability; and small perturbation of data T (occurring when the data is noisy) removes it from the 'permitted' set (a signature curve) so that the frequency interval must be changed and adjusted in

order to provide unique solvability of (2). It can be shown, following [3, 5], that in the single-layer case, $F(z(\varepsilon_1); f; P)$ is one-to-one w.r.t. real permittivity on the frequency-dependent intervals

$$I_k^* = (\varepsilon_{2k}^*(f), \varepsilon_{2k+2}^*(f)), \quad (3)$$
$$\varepsilon_n^*(f) = (c/2)^2(1/a^2 + n^2/d_1^2)/f, \quad n = 0, 1, \ldots,$$

where unique permittivity reconstruction is possible, and for complex permittivities belonging to the rectangles $D_{F,n} = \{\varepsilon_{2n}^* < \operatorname{Re}\varepsilon_1 < \varepsilon_{2n+2}^*, -\infty < \operatorname{Im}\varepsilon_1 < \varepsilon_{im}^{*\max}\}$, $n = 0, 1, \ldots$ for a certain $\varepsilon_{\max}^{*im} > 0$.

3.3. Generalization to the *n*-layer structure

The results of Section 3 concerning unique solvability are generalized to the case of n-layer diaphragms in terms of the analysis of corresponding equation (2). The generalization employs the multi-parameter setting [3] when the sought permittivities of one or several layers of an n-layer inclusion are determined from (2) as implicit vector-functions of several complex variables. The singularity sets are obtained in the form of hypersurfaces using a version of the Cauchy-Kowalevski theorem.

4. Conclusions

A justification is proposed for the unique reconstruction of permittivities of multi-layered parallel-plane dielectric inclusion in a rectangular waveguide from the measured transmission data which may be noisy. The justification technique employs the knowledge about the location of complex singularities of the transmission coefficient and can be extended to more complicated dielectric inclusions and waveguides of arbitrary cross section.

References

[1] Y. Shestopalov, Resonant states in waveguide transmission problems, *PIER B* 64: 119-143, 2015.
[2] D. L. Faircloth, M. Baginsky, S. M. Wentworth, Complex permittivity and permeability extraction for multilayered samples using S-parameter waveguide measurements, *IEEE Trans. MTT* 54: 1201-1209, 2006.
[3] Y. Shestopalov, On unique solvability of multi-parameter waveguide inverse problems, *Proc. ICEAA 2017*, Verona, Italy, pp. 372-376, 2017.
[4] Y. Smirnov, Y. Shestopalov, and E. Derevyanchuk, Permittivity reconstruction of layered dielectrics in a rectangular waveguide from the transmission coefficient at different frequencies, *Springer Proc. Math. Stat.* 52: 169–181, 2013.
[5] E. Sheina, A. Smirnov, and Y. Shestopalov, Optimization of the boundary conditions and computational parameters for the FDTD solution of the inverse problem of reconstructing permittivity of a dielectric inclusion in a waveguide, *Proc. PIERS 2016*, Shanghai, China, pp. 211-216, 2016.

Iteration Methods for 3D Electromagnetic Scattering Problems

Alexander Samokhin[1*], Anna Samokhina[2], Yury Shestopalov[3]

[1]Institute of Information Technologies, Moscow Technological University, Moscow, Russia
[2]Institute of Control Sciences, Russian Academy of Sciences, Moscow, Russia
[3]Faculty of Engineering and Sustainable Development, University of Gävle, Gävle, Sweden
*corresponding author, E-mail: `absamokhin.yandex.ru`

Abstract

We consider iteration methods which can be used for numerical solution of volume singular integral equations (VSIEs) describing many classes of 3D electromagnetic scattering problems.

1. Introduction

To solve the integral equation numerically, one reduce it to a system of linear algebraic equations (SLAE). It is clear that we must apply only iteration methods [1]. Number T of arithmetic operations that guarantees the required accuracy of solution and memory volume M required for the implementation of the algorithm are the main efficiency criteria for any numerical algorithm. Multiplication of matrix SLAE by vector is the most laborious operation of the iteration method. Therefore, the number of multiplications for the implementation of a particular algorithm will be called the number of iterations.

2. Iteration methods

We consider two classes of iteration methods. Usually, the integral equations under study are solved by the iteration algorithm called generalized minimal residual algorithm (GMRES) and its various modifications. When this method is applied the iteration parameters are determined in the course of calculations and depend on the current iteration index. Such methods may be called nonstationary iteration algorithms. There is another family of iteration methods called stationary iteration algorithms for which the iteration parameters are determined before the iteration procedure.

2.1. Nonstationary algorithms

By using Poynting theorem, we prove that GMRES algorithms may be applied for numerical solution considered VSIEs [1, 2]. However, their implementation requires comparatively large amount of computer memory. We also present other nonstationary algorithm – iteration method of gradient descent. Unlike the majority of iteration techniques, the proposed iteration procedure does not require any additional conditions, apart from the requirement that the initial SLAE is uniquely solvable for any right-hand side, i.e. the system determinant is nonzero.

However, the convergence of iterations is not so high as for GMRES algorithms.

2.2. Stationary algorithms

We present two stationary algorithms – generalized method of simple iteration and generalized Chebyshev iteration method [3]. These techniques demand knowledge of the spectrum localization on the complex plane. It is not possible to obtain this information for the majority of considered problems. However, one can do it a number of important particular cases. For low-frequency problems we show the spectrum localization on the complex plane in general case [3, 4]. Therefore, above-mentioned stationary methods can be effectively used for numerical solution of VSIEs in low-frequency case.

3. Conclusions

We present iteration methods which can be used for numerical solution of VSIEs of electromagnetics. We also demonstrate some numerical results concerning convergence iterations to solution for the considered methods.

References

[1] A-B. Samokhin, *Integral equations and iteration methods in electromagnetic scattering,* VSP, Utrecht, 2001.

[2] A.B. Samokhin, Volume singular integral equations for problems of scattering on 3D dielectric structures, *Differential equations* 9: 1201-1216, 2014.

[3] A.B. Samokhin, Y.V. Shestopalov, K. Kobayashi, Stationary iteration methods for solving 3D electromagnetic scattering problems, *Applied mathematics and computations* 222: 107-122, 2013.

[4] N.V. Budko, A.B. Samokhin, Spectrum of the volume integral operator of electromagnetic scattering, *SIAM sci. comput.* 28: 682-700, 2006.

Problems of Electromagnetic Scattering on 3D Dielectric and Perfectly Conducting Structures

Alexander Samokhin[1*], Anna Samokhina[2], Yury Shestopalov[3]

[1]Institute of Information Technologies, Moscow Technological University, Moscow, Russia
[2]Institute of Control Sciences, Russian Academy of Sciences, Moscow, Russia
[3]Faculty of Engineering and Sustainable Development, University of Gävle, Gävle, Sweden
*corresponding author, E-mail: `absamokhin.yandex.ru`

Abstract

By using integral equations, we consider the problems of electromagnetic scattering on 3D inhomogeneous dielectric objects in presence of perfectly conducting surfaces. We also present method for the numerical solution of these problems.

1. Introduction

We consider the following class of 3D electromagnetic scattering problems. The medium in a finite domain Q is characterized the permittivity tensor-function. Outside the domain Q, the medium parameters are constant and isotropic. There is a bounded perfectly conducting surface (or a system of surfaces) S outside Q. The problem is to determine the electromagnetic field excited in the medium by a given external field.

2. Analysis of the problems

We formally reduce (with unknown Green tensor function) these problems to the volume singular integral equations (VSIEs) with respect of electric field in domain Q [1]. Then, we see that the singular part of considered VSIEs is the same as for VSIEs describing the electromagnetic scattering problems without perfectly conducting surface S [2, 4, 5]. By using the theory of singular integral equations [3] and taking into account the above-mentioned assertion, we obtain the statements relating to uniqueness and solvability considered problems.

3. Numerical results

To construct a method for solving our problems we reduce the problems to the system of integral equations: VSIEs in the domain Q and hypersingular integral equations on the surface S [1]. The unknown functions in the equations are the electric field in the domain Q and the electric current on the surface S. We introduce functional space W consisting of square integrable functions for the electric field and functions for the current satisfying the conditions: currents belong to square integrable functions; divergence of the currents also belong to square integrable functions. We use the Galerkin method to solve system of integral equations numerically. Let H belonging to W be a finite-dimensional space describing the solution of our system with sufficient accuracy. We define a basis of this space and seek an approximate solution of the system of integral equations as superposition of the basis functions with unknown coefficients. By using Galerkin method, we obtain the system of linear algebraic equations (SLAE) with respect of unknown coefficients. We prove that for any real parameters of the medium in Q and nonclosed surface (or surfaces) S there exists a unique solution of SLAE [1].

4. Conclusions

We reduce problems on scattering of electromagnetic waves on 3D dielectric structures in presence of bounded perfectly conducting surfaces to system of integral equations. We use results of theory of singular integral equations to study these problems mathematically and suggest numerical method.

References

[1] A.B. Samokhin, A.S. Samokhina, Y.V. Shestopalov, Analysis and solution method for problems of electromagnetic wave scattering on dielectric and perfectly conducting structures, *Differential equations* 53: 1165-1173, 2017.

[2] A-B. Samokhin, *Integral equations and iteration methods in electromagnetic scattering,* VSP, Utrecht, 2001.

[3] S.G. Michlin, S. Prosdorf, *Singular integral equations,* Akademie-Verlag, New York, 1986.

[4] A.B. Samokhin, Volume singular integral equations for problems of scattering on 3D dielectric structures, *Differential equations* 50: 1201-1216, 2014.

[5] A.B. Samokhin, A.S. Samokhina, Volume singular integral equations for transparent structures over an ideally conducting surface, *Differential equations* 51: 1219-1224, 2015.

Synthesis of an anisotropic impedance plane for the incidence of two orthogonally polarized waves

Yury V. Yukhanov[1], Tatiana Y. Privalova[2], Egor E. Privalov[2],
Timur Amirokov[1]

[1]Institute of radio engineering systems and management, Southern Federal University, Taganrog, Russia
[2]Faculty of Physics, Southern Federal University, Rostov on Don, Russia
*corresponding author, E-mail: `yu_yukhanov@mail.ru`

Abstract

Solved the problem of synthesis of an inhomogeneous anisotropic impedance plane, on which two uniform plane waves of orthogonal polarizations fall from different directions. The synthesized plane reflects these waves in a given direction with the required transformation of the plane of polarization. Obtained the reflection coefficients. Formulated the limitations on the class of scattering diagrams implemented using a dense array of orthogonal reactant strips. Numerical results are presented.

1.   Introduction

In systems of communication, telemetry data transfer, radio astronomy [1], [2] it is often necessary to have a reflector antenna radiating an electromagnetic wave in one direction by means of two spaced apart irradiators. In this case, the isolation between the irradiators should be maximized, for example, due to their work on orthogonal polarizations. The mirror in this case must sum up the incident irradiator fields in a given direction with the corresponding polarization transformation (acting as a polarizer). For example, for incidence of two waves of orthogonal linear polarizations, they are transformed into a linear polarized wave rotated by a given angle or into a wave of rotating polarization. The coefficient of use of the aperture of the antenna reflector should be at the maximum. It is possible to implement such a reflector by means of an impedance non-specular reflecting surface with inhomogeneous anisotropic impedance. The effectiveness of controlling the characteristics of scattering and radiation was demonstrated in papers [3] ÷ [6].
The design of reflectors that provide simultaneous reflection in a given direction with transformation of the plane of polarization requires the solution of the problem of synthesis of an anisotropic inhomogeneous electrodynamic structure. For highly directional antennas with reflectors of large electrical dimensions, the solution of such problems can be obtained approximately, for example, by the method of physical optics. In this case, it is necessary to know the reflection coefficients of an anisotropic inhomogeneous plane.

At present, the papers [3]÷[6] are known in which the synthesis problems of inhomogeneous isotropic and anisotropic scatterers have been solved in a given direction of the reflected beam on the coherent [7], [9]÷[13] and cross [14], [15] polarizations. There are also known papers [16], [17], devoted to the development of polarization converters of the reflective type. In [18], the two-dimensional problem of synthesis of an isotropic impedance surface of an arbitrary normal cross section, excited by a finite number of irradiators located at given points of space, is solved for the required direction of maximum radiation. With two separate irradiators, at each point of the impedance plane, there are two incident beams, which it must reflect in the given direction with a polarization transformation. The reflection coefficients for such cases are unknown in the literature.
Therefore, the goal of this paper is: the solution of the problem of synthesis of an inhomogeneous anisotropic plane onto which two plane waves of orthogonal polarizations incident from different directions; search for the distribution law of a purely reactive impedance over a given direction of wave reflection with the required transformation of the plane of polarization; determination of reflection coefficients and constraints on the class of implemented scattering diagrams.

2.   Formulation of inverse problem

Suppose that on the surface S (y=0) (fig.1,a,b) the impedance boundary conditions of Leontovich are met:

$$[\mathbf{n}, \mathbf{E}] = -\hat{Z}[\mathbf{n}[\mathbf{n}, \mathbf{H}]]. \tag{1}$$

Surface impedance is implemented using a dense array of orthogonal bands oriented at an angle α to the axis z (fig.1,b) with a diagonal tensor $\hat{Z}$:

$$\hat{Z} = \begin{vmatrix} Z_E & 0 \\ 0 & Z_M \end{vmatrix}, \tag{2}$$

where

$$E_u = -Z_E H_v; \quad E_v = Z_M H_u. \tag{3}$$
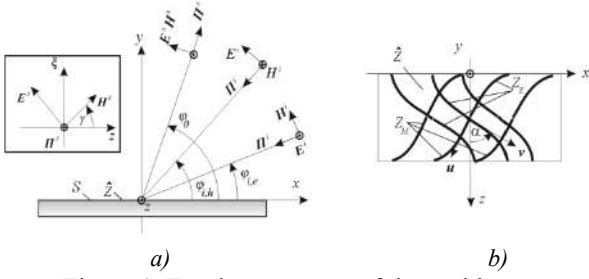
a)   *b)*

Figure 1: For the statement of the problem.

Along the z axis, the system is homogeneous – the problem is two-dimensional.

Plane E-polarized wave incidents onto the surface S (fig.1) from the direction $\varphi_{i,e}$

$$E_z^i = E_0^i e^{ikx \cos \varphi_{i,e}}; \quad H_x^i = -\sin \varphi_{i,e} E_z^i, \qquad (4)$$

and from the direction φ_{ih} - plane H-polarized wave

$$H_z^i = H_0^i e^{ikx \cos \varphi_{i,h}}; \quad E_x^i = \sin \varphi_{i,h} H_z^i, \qquad (5)$$

where $k = 2\pi/\lambda$; λ is the incident wave's length.

Let's find the components

$$Z_E(x) = iX_E(x) \ (ReZ_E = 0);$$
$$Z_M(x) = iX_M(x) \ (ReZ_M = 0) \qquad (6)$$

of the tensor (2) of reactant structure and the orientation of the strips of the system $\alpha(x)$, providing reflection of the wave E^s, H^s from the plane y=0 in the given direction φ_0 with the required polarization:

$$H_z^s = H_0 e^{i\Psi_0} e^{-ikx \cos \varphi_0}; \quad E_z^s = E_0 e^{i\Phi_0} e^{-ikx \cos \varphi_0}, \ (7)$$

where $E_0 = Y H_0$ and Φ_0, Ψ_0 are given amplitudes and phases of the orthogonal components of the reflected field, which determine the polarization of the reflected wave.

The components of the impedance tensor and the electric field strength vector are normalized to the characteristic impedance of the free space $W = 120\pi$ Ohm.

3. Basic layout features Reflection coefficients of an inhomogeneous impedance plane

We introduce the reflection coefficients as follows:

$$E_z^s = P_{11} E_z^i + P_{12} H_z^i; \quad H_z^s = P_{21} E_z^i + P_{22} H_z^i. \qquad (8)$$

Expressions for reflection coefficients for a plane with a system of orthogonal strips Z_M, Z_E (see fig.1b) we obtain, using the impedance boundary conditions (3) and relations (4), (5), (7):

$$P_{11} = \frac{\sin \varphi_{i,e} Z_E Z_M - \sin \varphi_0 + \sin \varphi_0 \sin \varphi_{i,e} Z_{22} - Z_{11}}{\Delta};$$

$$P_{22} = \frac{\sin \varphi_{i,h} - \sin \varphi_0 Z_M Z_E + \sin \varphi_0 \sin \varphi_{i,h} Z_{22} - Z_{11}}{\Delta};$$

$$P_{12} = \sin \alpha \cos \alpha \frac{(\sin \varphi_0 + \sin \varphi_{i,h})(Z_M - Z_E)}{\Delta};$$

$$P_{21} = \sin \alpha \cos \alpha \frac{(\sin \varphi_0 + \sin \varphi_{i,e})(Z_E - Z_M)}{\Delta} \qquad (9)$$

where $Z_{11} = \cos^2 \alpha \, Z_E + \sin^2 \alpha \, Z_M$; $Z_{22} = \sin^2 \alpha \, Z_E + \cos^2 \alpha \, Z_M$; $\Delta = \{\cos^2 \alpha \, (\sin \varphi_0 + Z_E)(\sin \varphi_0 \, Z_M + 1) + \sin^2 \alpha \, (\sin \varphi_0 + Z_M)(1 + \sin \varphi_0 \, Z_E)\}$;

Formulas (8) for a homogeneous impedance plane ($Z_E(x) = $ cons и $Z_M(x) = $ const), when $\varphi_0 = \pi - \varphi_i$, turn into well-known ones [6]. The resulting reflection coefficients (9) allow us to find the scattered fields of anisotropic impedance structures, including those of arbitrary shapes and large electrical dimensions, by the method of physical optics.

4. Scattering diagrams

Expressions for scattering diagrams in E- and H-planes ($F_E(\varphi)$ and $F_H(\varphi)$) taking into account (4), (5), (7) and (8) will take form:

$$E_z^s(p) = H_0^{(2)}(kr) F_e(\varphi); \quad H_z^s(p) = H_0^{(2)}(kr) F_h(\varphi),$$

where

$$F_e(\varphi) = \frac{k}{4} \int_{x'=-\infty}^{\infty} \{(\sin \varphi - \sin \varphi_{i,e} + (\sin \varphi_0 + \sin \varphi)P_{11})E_z^i + (\sin \varphi_0 + \sin \varphi)P_{12}H_z^i\} e^{ikx' \cos \varphi} dx'; \ (10)$$

$$F_h(\varphi) = \frac{k}{4} \int_{x'=-\infty}^{\infty} \{(\sin \varphi - \sin \varphi_{i,h} + (\sin \varphi_0 + \sin \varphi)P_{22})H_z^i + (\sin \varphi_0 + \sin \varphi)P_{21}E_z^i\} e^{ikx' \cos \varphi} dx' \ (11)$$

The first summands in the integrands (10) and (11) determine the shadow scattered field, which is equal to the scattering field of the «black» body model according to Kirchhoff [19]. When calculating the scattering fields of the reflector in the frontal hemisphere, they can be neglected.

5. Synthesis of the reactant plane

The required laws for the distribution of impedance or reactance can be obtained directly from (10) and (11) by setting:

$$\begin{cases} \{P_{22}H_z^i + P_{21}E_z^i\} e^{ikx' \cos \varphi_0} = H_0 e^{i\Psi_0}; \\ \{P_{11}E_z^i + P_{12}H_z^i\} e^{ikx' \cos \varphi_0} = E_0 e^{i\Phi_0}. \end{cases}$$

However, knowing the analytical representation of the incident and given reflected fields (4) ÷ (7), the required impedance distribution law is easier to obtain directly from the boundary conditions (2).

Taking into account (3) for the components of the impedance tensor $Z_E(x), Z_M(x)$ we get:

$$Z_E = \frac{E_x \cos \alpha - E_z \sin \alpha}{H_x \sin \alpha + H_z \cos \alpha}; \quad Z_M = \frac{E_x \sin \alpha + E_z \cos \alpha}{-H_x \cos \alpha + H_z \sin \alpha}. \qquad (12)$$

Separating (12) into real and imaginary parts, we obtain conditions

$$Re\{\dot{H}_z E_x - \dot{H}_x E_z\} = 0; \quad \tan 2\alpha = \frac{Re[\dot{H}_z E_x + \dot{H}_x E_z]}{Re[\dot{H}_z E_z - \dot{H}_x E_x]}, \qquad (13)$$

which are constraints on the class of realized scattering diagrams with the help of the reactant structure (6) and determine the achievable values of the given reflection directions φ_0 of a wave and the possibility of transforming its polarization E_0, H_0 and Φ_0, Ψ_0. Studies show that the

reactance plane, in addition to the given one in the direction of φ_0 invariably produces beams [15]:

$$H_z^z = H_0^z e^{ikx \cos \varphi_{i,h}}, \; E_z^z = E_0^z e^{ikx \cos \varphi_{i,e}},$$

specular to the incident ones.

As a result, it is possible to obtain amplitudes of the reflected fields H_0, H_0^z and E_0^z from (13) through the incident and given type of polarization of the main beam:

$$H_0^z = -\frac{\sin \varphi_0 - \sin \varphi_{i,h}}{\sin \varphi_0 + \sin \varphi_{i,h}} H_0^i; \; E_0^z = -\frac{\sin \varphi_0 - \sin \varphi_{i,e}}{\sin \varphi_0 + \sin \varphi_{i,e}} E_0^i.$$

$$H_0 = \sqrt{\frac{\left(\frac{2 \sin \varphi_{i,h}}{\sin \varphi_0 + \sin \varphi_{i,h}} H_0^i\right)^2 + \left(\frac{2 \sin \varphi_{i,e}}{\sin \varphi_0 + \sin \varphi_{i,e}} E_0^i\right)^2}{1 + \Upsilon^2}}. \quad (14)$$

Angle of strip orientation $\alpha(x)$ turns out also to be (as shown in [13] ÷ [17]) a variable, the behavior of which is determined by the ratio of the angles $\varphi_{i,h}$, $\varphi_{i,e}$, φ_0 and the polarization of the reflected wave - E_0, H_0 and Φ_0, Ψ_0.

6. Calculation results

As an example, consider the incidence of E- and H-polarized plane waves from directions $\varphi_{i,e} = 30^0$ and $\varphi_{i,h} = 60^0$ onto the reactant structure. The synthesized reactance (12) reflects them in the direction $\varphi_0 = 90^0$, transforming into a circularly polarized wave ($\Upsilon = 1, \Delta\Psi = \Phi_0 - \Psi_0 = 90^0$). The distribution of reactances and the orientation of the strips are shown in fig. 2 and fig. 3 Scattering diagrams for a fragment of a plane $L = 6\lambda$ with such structure (see fig.1) are shown in fig.4. Here the red curve corresponds to the diagram $Fh(\varphi)$, and blue one – to $Fe(\varphi)$.
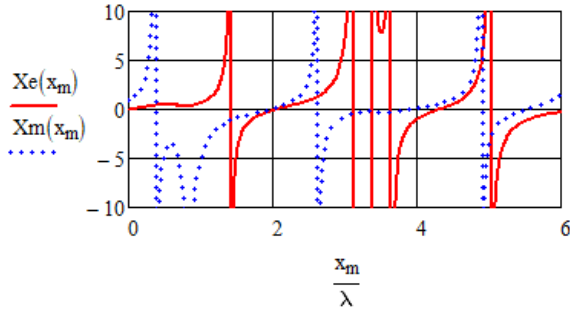
Figure 2: Law of distribution of reactances of strips .
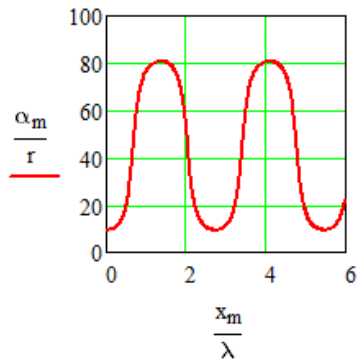
Figure 3: The law of changing the orientation angle of reactant.
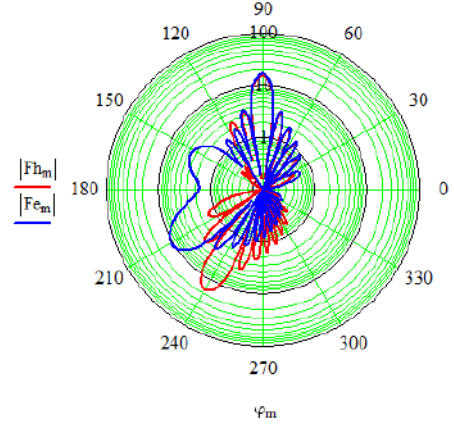
Figure 4: Scattering diagrams of a structure with parameters $\varphi_{i,e} = 30^0$, $\varphi_{i,h} = 60^0$, $\varphi_0 = 90^0$ and $\Upsilon = 1, \Delta\Psi = 90^0$.

Figures 5-8 show the results of the synthesis of the fragment of the plane $L = 6\lambda$ with given angles $\varphi_{i,e} = 30^0$ and $\varphi_{i,h} = 60^0$, creating in the direction $\varphi_0 = 45^0$ circular polarization field ($\Upsilon = 1, \Delta\Psi = \Phi_0 - \Psi_0 = 90^0$).
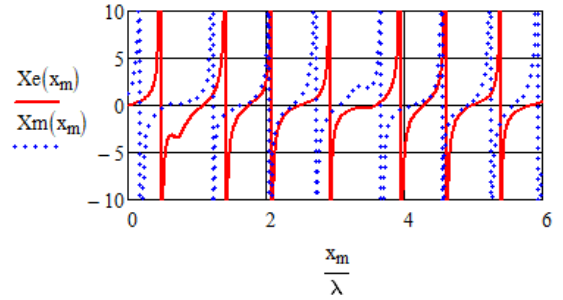
Figure 5: Law of distribution of reactances of strips .
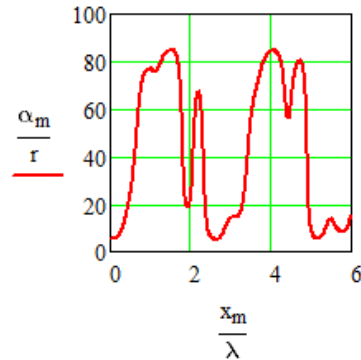
Figure 6: The law of changing the orientation angle of reactant.
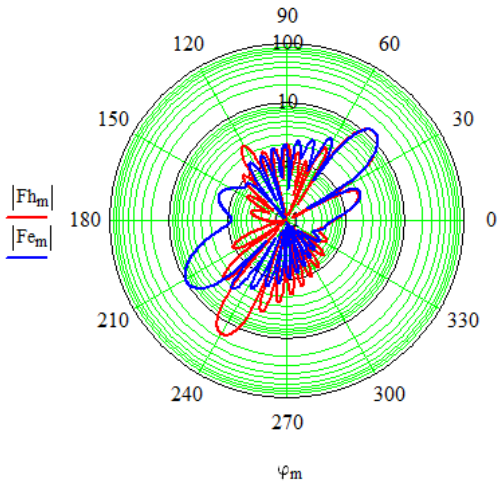
Figure 7: Scattering diagrams of a structure with parameters $\varphi_{i,e} = 30^0$, $\varphi_{i,h} = 60^0$, $\varphi_0 = 45^0$ and $\Upsilon = 1, \Delta\Psi = 90^0$.

Numerical studies have shown that in all the cases considered, the orientation of the reactance bands is of a significantly variable nature (see fig.3 and fig.6). Fixing the angle $\alpha = const$ leads to a substantial distortion of the scattering diagrams.

And only for $\varphi_0 = 90^0$ and symmetric with respect to the angle of maximum scattering, the orientation angle of the reactant structure is a constant $\alpha = 45^0$.

To illustrate what has been said, Fig. 8 and Fig. 9 show the results of synthesis of the fragment of the reactant plane $L = 6\lambda$ of fixed orientation $\alpha = 45^0$ with given angles $\varphi_{i,e} = 30^0$ and $\varphi_{i,h} = 120^0$, creating in the direction $\varphi_0 = 90^0$ circular polarization field ($\Upsilon = 1, \Delta\Psi = \Phi_0 - \Psi_0 = 90^0$).
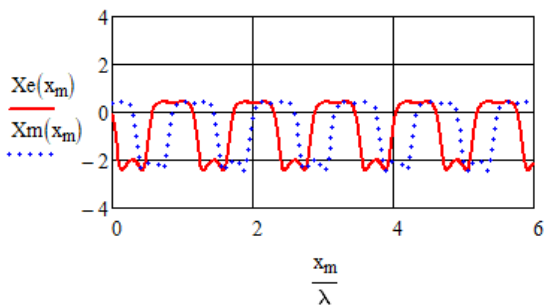
Figure 8: Law of distribution of reactances of strips
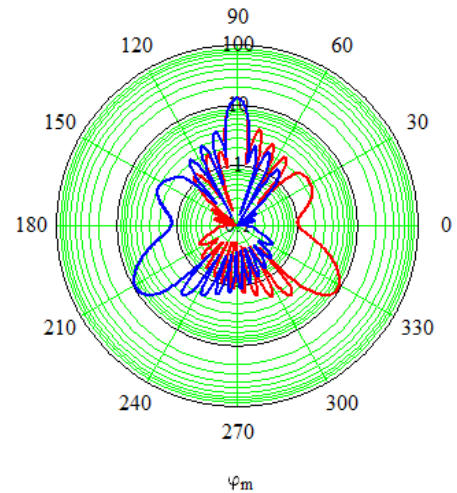
Figure 9: Scattering diagrams of a structure with parameters $\varphi_{i,e} = 30^0$, $\varphi_{i,h} = 120^0$, $\varphi_0 = 90^0$ and $\Upsilon = 1, \Delta\Psi = 90^0$.

Scattering diagrams (see fig. 4, fig. 7 and fig. 9) were calculated strictly, by solving integral equations on a fragment of an anisotropic reactant strip with width $L = 6\lambda$ relative to the orthogonal components of the total fields E_z and H_z. In all the considered cases, as expected, the scattering diagrams of synthesized structures have specular lobes, and, the more the angles $\varphi_{i,e}$, and $\varphi_{i,h}$, differ from φ_0, the higher is their level, which corresponds to formulas (14).

7. Conclusions

Thus, in this paper we solve the problem of synthesis of an anisotropic reactant structure that reflects the incident plane waves of orthogonal linear polarizations in a given direction with the required polarization. Expressions for the reflection coefficients were obtained. Expressions for the reactances of orthogonal bands Z_E (x),Z_M (x) of anisotropic impedance and angle of their orientation (x) were obtained explicitly. Found the class of scattering diagrams implemented using the reactant structure. The results of explicit numerical calculations confirmed the validity of the obtained formulas.

Acknowledgements

References

[1]. Frolov O.P., Wald V.P. Mirror antennas for satellite earth stations. - Moscow: Hot line - Telecom, 2008. - 496 p.

4

[2]. Shishlov A.V. Theory and technique of multi-reflector antennas. - The Journal of Antennas, 2009, Issue 7 (146), pp. 14-29. UDC 621.396.67.

[3]. Miller M.A., Talanov V.I. "Use of concept of a superficial impedance in the theory of superficial electromagnetic waves," Radiophysics, 1961. vol. 4. № 5. C. 795-830.

[4]. Lawrie R.E. "The control of echo area of ogives by cutoff corrugated surfaces," IEEE Trans.- 1966, vol.AP-17, №3.

[5]. Short I., Chen K.M. "Backscattering from an impedance loaded slotted cylinder," IEEE Trans.- 1969, vol.AP-14, №6.

[6]. Kurushin E.P., Nefedov E.I., Fialkovski A.T. "Diffraction of electromagnetic waves on anisotropic structures", - M.: Nauka, 1975. - 196 p.

[7]. Petrov B.M., Yukhanov Yu.V. The inverse scattering problem for an impedance cylinder of arbitrary cross section, Izv. High Schools of Radioelectronics. - 1980.-T.23.-№9.-P.78-81.

[8]. Petrov B.M., Sharvarko V.G. Approximate solution of the inverse scattering problem for a circular impedance cylinder // Scattering of electromagnetic waves. - Taganrog, 1976. Issue 41. - C.11-24.

[9]. Petrov B.M., Yukhanov Yu.V. Synthesis of a two-dimensional reactive reflector. Izv. High Schools of Radioelectronics. - 1980.-T.23.-№9.-P.59-63.

[10]. Yukhanov Y.V. Analysis and synthesis of an impedance plane// Radiotekhnika and Elektronika. 2000. Pp. 404-409.

[11]. Whites K.W., Mittra R. "A systematic study of the impedance boundary condition (EM scattering)". Antennas and Propagation Society International Symposium, 1990. AP-S. Merging Technologies for the 90's. Digest. 1990, pp. 870 - 873 vol.2, DOI: 10.1109/APS.1990.115246.

[12]. Smith P. D., Rawlins A. D. "Diffraction from structures with an impedance boundary". 2013 International Conference on Electromagnetics in Advanced Applications (ICEAA), pp. 1297 - 1300, DOI: 10.1109/ICEAA.2013.6632459.

[13]. Yukhanov Y.V., Privalova T.Y. "Synthesis of Nonstationary Plane by a Given Frequency Spectrum of the Reflected Field". 2015 International Conference on Electromagnetics in Advanced Applications (ICEAA). Year: 2015, pp. 521 - 524,DOI: 10.1109/ICEAA.2015.7297169.

[14]. Yukhanov Y. V. "Synthesis of anisotropic impedance plane"., 4th International Conference on Antenna Theory and Techniques (Cat. No.03EX699)Volume: 1.pp. 121 – 124.
vol.1, DOI: 10.1109/ICATT.2003.1239164.

[15]. Yukhanov Y. V., Privalova T.Y. "Synthesis of Impedance of Axisymmetric Body". 2013 Asia-Pacific Microwave Conference Proceedings (APMC). Year: 2013/ pp. 582 - 584, DOI: 10.1109/APMC.2013.6694871.

[16]. Yukhanov Y.V., Privalova T.Y. Synthesis of impedance reflection type polarizer". 2016 24th Telecommunications Forum (TELFOR). Year: 2016, pp. 1- 4,DOI: 10.1109/TELFOR.2016.7818848.

[17]. Privalova T.Yu. "Synthesis of Impedance Polarization Rotator of Reflective Type"//Proceedings of 2016 IEEE 5th Asia-Pacific Conference on Antennas and Propagation (APCAP) July 26-29, 2016 in Kaohsiung, Taiwan// http://apcap2016.org/callforpapers.html/ pp.233-234.

[18]. Yukhanov Y. V., Privalova T. Y. Synthesis of impedance surface excited by irradiators system//2015 International Conference on Antenna Theory and Techniques (ICATT). DOI: 10.1109/ICATT.2015.7136784.Year: 2015.Pages: 1 – 4.

[19]. Zakharyev LN, Lemansky AA Scattering of waves by "black" bodies. Moscow: Sov. Radio. 1972.-288c.

Synthesis of Anisotropic Impedance Metasurface as Substrate of Cylindrical Phased Antenna Array on the Given Polarization of Radiation Field

Andrey I. Semenikhin[1], Diana V. Semenikhina[1], Yury Yu. Yukhanov[1*], Artem I. Chernokolpakov[1]

[1] Institute of Radio Engineering Systems and Management, Southern Federal University
Taganrog, Russia
*corresponding author, E-mail: yu_yukhanov@mail.ru

Abstract

Inverse problem for homogeneous anisotropic cylindrical impedance metasurface (MS) as substrate of conformal cylindrical antenna array is formulated and solved. Cylindrical phased antenna array model made of ribbons with traveling waves of longitudinal electric and magnetic currents. On MS, an input anisotropic thin-layered covering is placed. Radiation fields of an antenna array for linear co-polarizations and cross-polarizations are found with eigen function method. The impedance tensor of MS is found, which ensures a given polarization of the radiation field of the antenna array for all observation angles.

1. Introduction

To construct of conformal phased antenna arrays (PAAs), impedance substrates, coverings and metasurfaces (MSs) are used [1-5]. Such impedance structures allow broadening functional capability of PAA and improving radiation characteristics, allow reducing return losses and radar cross section, allow improving weight and size characteristics (to create low profile, conformal arrays). In [2], the flat anisotropic impedance metasurface was suggested to control the polarization of the radiated field. Conformal input covers located on the external surface of the antennas can be used to control the scattering characteristics of antennas in higher frequency ranges.

In many cases, carriers of PAAs are objects of cylindrical form. Therefore, solutions of direct and inverse problems of wave excitation by antenna arrays located near impedance cylindrical MSs with input coatings are timely. The anisotropy of a cylindrical metasurface is also used to control the polarization characteristics of a phased array. The PAA itself can consist of simpler elements with linear polarization of radiation in free space. This can simplify the design and feed network of lattice elements.

In [3], the two-dimensional problem of controlling the radiation pattern of a current filament is considered using a homogeneous isotropic cylindrical metasurface by changing the surface impedance of the MS. In [6, 7], the synthesis

problems of an anisotropic impedance cylindrical surface were solved for a given polarization of the scattered field.

In the paper, the inverse problem of impedance cylindrical metasurface as substrate of conformal cylindrical antenna array is considered. A PAA model is given in the form of ribbons of longitudinal electric and magnetic currents. A homogeneous impedance tensor MS from the deviator class, which provides a given polarization of the radiation field of the antenna array for all observation angles is found.

2. Formulation of inverse problem

Let the cylindrical MS infinite in the z-axis has a radius $r=a$ (Fig. 1) and is described by a normalized tensor (on 120π Ohm) of equivalent surface impedance with the components Z_{pq}; $p,q=1,2$.
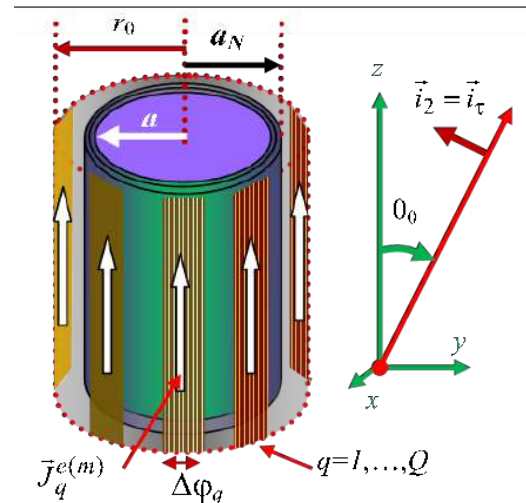

Figure 1: The model of a cylindrical antenna array in the form of ribbons of currents near a metasurface with a coating.

On the external surface of the MS there is an input anisotropic thin-layered piecewise homogeneous coating. It has a total thickness δ and consists of N layers, each layer is of thickness δ_n, $n = 1,\ldots, N$. Each coating layer is described by tensors of permittivity and permeability:

$$\hat{\varepsilon}^{(n)} = \left\| \varepsilon_{ij}^{(n)} \right\|, \quad \hat{\mu}^{(n)} = \left\| \mu_{ij}^{(n)} \right\|, \quad i,j = 1,2,3. \quad (1)$$

The effect of the coating is taken into account approximately by means of two-sided boundary conditions [8] at the outer boundary $r = a+\delta = a_N$ of the metasurface with a coating:

$$E_\varphi = \frac{1}{ik(a+\delta)} \frac{\partial}{\partial \varphi} (D_0 E_r - D_1 E_\varphi - D_2 E_z) +$$
$$W_0[(Z_{12} - M_{21})H_\varphi - (Z_{11} + M_{22})H_z - M_2 H_r];$$
$$E_z = \frac{1}{ik} \frac{\partial}{\partial z} (D_0 E_r - D_1 E_\varphi - D_2 E_z) + \quad (2)$$
$$W_0[(Z_{22} + M_{11})H_\varphi - (Z_{21} - M_{12})H_z + M_1 H_r],$$

where $k = 2\pi/\lambda$ is the wave number of free space; D_o, D_p, M_p, M_{pq} are the averaged parameters of the thin-layer coating:

$$D_0 = ik \sum_{n=1}^{N} \delta_n / \varepsilon_{33}^{(n)}; \quad D_p = ik \sum_{n=1}^{N} \delta_n \varepsilon_{3p}^{(n)} / \varepsilon_{33}^{(n)};$$

$$M_p = ik \sum_{n=1}^{N} \delta_n \mu_{p3}^{(n)} / \mu_{33}^{(n)};$$

$$M_{pq} = ik \sum_{n=1}^{N} \delta_n \left(\mu_{pq}^{(n)} - \mu_{p3}^{(n)} \mu_{3q}^{(n)} / \mu_{33}^{(n)} \right). \quad (3)$$

The model of a circular antenna array of infinite ribbons of electric and magnetic longitudinal currents is located on a circle of radius $r_0 \geq a_N$ and is given by the angular coordinates of the midpoints of the ribbons φ_q and the angular width of the ribbons $\Delta\varphi_q$, $q = 1,\ldots, Q$ (Fig. 1).

The current densities vary along the ribbons according to the traveling wave law with the phase coefficient $h_1 = k\cos\theta_0$. The angle $0 < \theta_0 < \pi$ characterizes the direction of the beam phasing and is reckoned from the longitudinal axis z of the lattice. In the transverse azimuth direction (along the width of the ribbons), the current densities can vary according to known laws [5]:

$$\vec{j}^{e(m)} = \vec{i}_z \delta(r' - r_0) e^{-ih_1 z'} \sum_{q=1}^{Q} J_{0z}^{e(m)} f_{zq}(\varphi'), \quad (4)$$

$$f_{zq}(\varphi') = \begin{cases} f_{zq}(\varphi'), & \varphi' \in [\varphi_q - \Delta\varphi_q/2; \; \varphi_q + \Delta\varphi_q/2]; \\ 0, & \varphi' \notin [\varphi_q - \Delta\varphi_q/2; \; \varphi_q + \Delta\varphi_q/2], \end{cases} \quad (5)$$

where $f_{zq}(\varphi')$ is the amplitude-phase angular distribution of the current density along the width of the q-th ribbon, normalized to complex current amplitudes $J_{0z}^{e(m)}$.

Let us find the MS impedance tensor providing a predetermined PAA radiation field polarization which the same for all angles of observation in the far zone. We will seek the solution of the inverse problem for homogeneous impedance MSs from the deviators' class [6, 7]:

$$Z_{11} = Z_{22} = 0, \; Z_{12} = -Z_{21}^* = D\exp(i\psi),$$
$$|D| \in [0,\infty], \; \psi \in (-\pi, \pi]. \quad (6)$$

3. Far field of the spatial wave of the PAA model

The solution of the problem of exciting of the metasurface and covering by currents (4) is obtained by the method of eigenfunctions [9]. The required field must satisfy the Maxwell equations for $r > a_N$, the boundary conditions (2) for $r = a_N$ and the radiation conditions at infinity for $r \to \infty$. At the observation point of the total far field for $r > r_0$ we introduce a linearly orthogonal left (with respect to the direction on the MS) polarization base. We direct the base unit vectors perpendicular to the direction of the phasing of the beam (Fig. 1):

$$\vec{i}_1 = \vec{i}_\varphi, \quad \vec{i}_2 = \vec{i}_\tau = \vec{i}_z \sin\theta_0 - \vec{i}_r \cos\theta_0. \quad (7)$$

The solution of the problem gives the following expressions for the projections of the total field of the PAA to the base vectors in the spherical coordinate system ($\theta \neq 0^\circ$) in the matrix form:

$$\left\| \begin{matrix} E_\varphi \\ E_\tau \end{matrix} \right\| = \sqrt{\frac{2i}{\pi v_1 r}} \frac{v_1 r_0}{4} e^{-iv_1 r - ih_1 z} \left\| \begin{matrix} g_{11}(\varphi) & g_{12}(\varphi) \\ g_{21}(\varphi) & g_{22}(\varphi) \end{matrix} \right\| \left\| \begin{matrix} J_{0z}^m \\ J_{0z}^e W_0 \end{matrix} \right\|, \quad (8)$$

where the matrix $\hat{G}(\varphi) = \| g_{pq}(\varphi) \|, p, q = 1;2$ is equal to

$$\hat{G}(\varphi) = \sum_{n=-\infty}^{\infty} i^n \zeta_{zn} e^{-in\varphi} \times$$

$$\times \left\| \begin{matrix} J_n(v_1 r_0) + f_{11} H_n^{(2)}(v_1 r_0) & f_{12} H_n^{(2)}(v_1 r_0) \\ -f_{21} H_n^{(2)}(v_1 r_0) & -J_n(v_1 r_0) - f_{22} H_n^{(2)}(v_1 r_0) \end{matrix} \right\|. \quad (9)$$

Here $J_n(v_1 r_0)$ are the Bessel functions of order n; $H_n^{(2)}(v_1 r)$ are the Hankel functions of order n of the second kind; $v_1 = k\sin\theta_0$.

Elements of the matrix $\hat{G}(\varphi)$ in expression (9) determine radiation patterns of the antenna array in the azimuthal plane on linear co- and cross-polarizations taking into account the effect of MS and the input coating. Functions $g_{11}(\varphi)$ and $g_{21}(\varphi)$ determine radiation patterns of the magnetic ribbon array in E-plane for linear co- and cross-polarization, respectively. Radiation patterns of electric ribbon array in the H-plane on linear co- and cross-

polarizations are described by the functions $g_{22}(\varphi)$ and $g_{12}(\varphi)$, respectively. Here the cross-polarizations as well as the E- and H-planes are indicated relative to the polarization of the primary field of the PAA. The complex coefficients in formula (9) take into account the angular distributions of the current densities on the ribbons and are equal [10]:

$$\zeta_{zn}= \sum_{q=1}^{Q} \int_{\varphi_q-\Delta\varphi_q/2}^{\varphi_q+\Delta\varphi_q/2} f_{zq}(\varphi')\exp(in\varphi')d\varphi'. \quad (10)$$

In the case when $f_{zq}(\varphi')= f_{zq}= $ const:

$$\zeta_{zn}= \sum_{q=1}^{Q} \frac{2}{n}\sin(\frac{n\Delta\varphi_q}{2})f_{zq}e^{in\varphi_q}. \quad (11)$$

For a model of PAA elements in the form of lattices of filaments, when $\Delta\varphi_q \to 0$, the surface currents in the formula (4) are replaced by linear currents [10]:

$$J_{0z}^{e(m)}r_0 \Delta\varphi_q \to I_{0z}^{e(m)}, \qquad \zeta_{zn} = \sum_{q=1}^{Q} f_{zq}e^{in\varphi_q}. \quad (12)$$

Matrix $\hat{F} = \| f_{pq} \|$ of the scattering coefficients of E- and H-waves on the metasurface in formula (9) is determined in an explicit form:

$$\hat{F} = [\hat{X} H_n^{(2)}(v_1 a_N) + \hat{Y} H_n'^{(2)}(v_1 a_N)]^{-1} \times$$
$$[-\hat{X} J_n(v_1 a_N) - \hat{Y} J_n'(v_1 a_N)], \quad (13)$$

where the prime ('') at the Bessel and Hankel functions indicates a derivative;

$$\hat{X} = \| x_{pq} \|; \qquad \hat{Y} = \| y_{pq} \|; \quad (14)$$

$x_{11}=i[n^2 a_N^{-2}D_0- nh a_N^{-1}(Z_{12}-M_{21}) - v^2(Z_{11}+M_{22})]/k^2;$

$x_{12}=in[h-nhD_1/(ka_N)+v^2 D_2/k-kM_2]/(k^2 a_N);$

$x_{21}=[-nh a_N^{-1}D_0+ nh a_N^{-1}(Z_{22}+M_{11})+v^2(Z_{21}-M_{12})]/k^2;$

$x_{22}=[v^2 + nh^2 D_1/(ka_N) - hv^2 D_2/k - nkM_1/a_N]/k^2;$

$y_{11}= v(k- na_N^{-1}D_1 - hM_2)/k^2;$

$y_{12}= v[-nhk^{-2}a_N^{-1}D_0+(Z_{12}-M_{21})]/k;$

$y_{21}= ihv(-D_1 + M_1)/k^2;$

$y_{22}= iv[-k^{-2}h^2 D_0+(Z_{22}+M_{11})]/k;$
$v= v_1= k\sin\theta_0; \quad h = h_1 = k\cos\theta_0.$

4. The solution of the problem of synthesis of the impedance tensor of an MS

Let's use the representation (8), (9), (13) spatial wave field of PAA to solve the inverse problem. Let's find the impedance MS, which provides a given polarization of the radiation field of the phased array for all observation angles in the far zone.

The specified polarization of the radiation field of the PAA is described on the complete complex plane by means of a phasor

$$p^r = E_\tau / E_\varphi = p_0 e^{i\xi_0}. \quad (15)$$

We represent the phasor (15) with allowance for the expression (8):

$$p^r(\varphi) = \frac{g_{21}(\varphi)J_{0z}^m + g_{22}(\varphi)J_{0z}^e W_0}{g_{11}(\varphi)J_{0z}^m + g_{12}(\varphi)J_{0z}^e W_0}. \quad (16)$$

Analysis of expression (16) shows that the condition for the independence of the phasor p^r from the angles of observation of the far field can be satisfied for $r_0 = a$. The ribbons of the currents should be located on the metasurface. The electrical thickness of the input coating in the operating frequency range of the PAA should be negligible.

Then we can prove the following polarization property of the radiation field of the model of the PAA, which is conformally located on a cylindrical anisotropic metasurface with impedance (6).

The phasor p^r of the radiation field of a phased array in the form of ribbons with traveling waves of longitudinal electric and magnetic currents on a cylindrical metasurface is determined only by the impedance of the metasurface

$$p^r = -D\exp(-i\psi). \quad (17)$$

The phasor (17) does not depend on the angles of observation of the radiation field and the conditions for exciting the PAA.

Finally, it follows from (15), (17) that the given PAA polarization, which is the same for all observation angles, is realized for the following parameters D, ψ of the MS impedance tensor:

$$D = p_0; \qquad \psi = \pi - \xi_0. \quad (18)$$

Let us consider a special case of realization of the circular polarization of the PAA radiation field $p_0 = 1$, $\xi_0 = \pm\pi/2$ for all observation angles. It follows from (18) that right or left circular polarization is realized for PAA substrates in the form of mutual metasurfaces with a normalized impedance tensor (6), when:

$D = 1, \quad \psi = +\pi/2$ for right circular polarization;

$D = 1, \quad \psi = -\pi/2$ for left circular polarization. (19)

5. Conclusions

In the work with help of the eigenfunction method, the inverse problem of wave excitation by the PAA model in the presence of cylindrical anisotropic impedance metasurface with a thin-layered anisotropic coating has been solved. The model of a cylindrical PAA from ribbons with traveling waves of longitudinal electric and magnetic

3

currents was considered. The MS impedance tensor was found that provides a predetermined polarization of the radiation field of the PAA model on the cylindrical MS provided that the polarization does not depend on the angles of observation.

Acknowledgements

References

[1] C.L. Holloway, E.F. Kuester, J.A. Gordon, J. O'Hara, J. Booth, and D.R. Smith, "An overview of the theory and applications of metasurfaces: The two-dimensional equivalents of metamaterials," IEEE Antennas and Propagation Magazine, vol. 54, no. 2, pp. 10–35, 2012.

[2] R. Quarfoth, and D. Sievenpiper, "Broadband unit-cell design for highly anisotropic impedance surfaces," IEEE Trans. on Antennas and Propagat., vol. 62, no. 8, pp. 4143–4152, 2014.

[3] F. Yang, Z.L. Mei, and T.J. Cui, "Control of the Radiation Patterns Using Homogeneous and Isotropic Impedance Metasurface," Intern. Journal of Antennas and Propagat., vol. 2015, ID 917829, http://dx.doi.org/10.1155/2015/917829.

[4] Y.R. Padooru, A.B. Yakovlev, P.-Y. Chen, and A. Alù, "Line-source excitation of realistic conformal metasurface cloaks," J. Appl. Phys., vol. 112, 104902, 2012.

[5] D.D. Gabriel'yan, and M.Yu. Zvezdina, "The influence of impedance surface of a circular cylinder on the dipole pattern," Proc. of 3rd Int. Conf. Antenna Theory and Techniq, Sevastopol, Ukraine, 1999, pp. 113-115.

[6] D.V. Semenikhina, A.I. Semenikhin and Y.V. Yukhanov, "Synthesis of the Anisotropic Impedance Cylinder on the Given Polarization of the Scattered Field", 22nd Telecommunications forum (TELFOR), Belgrade, Serbia, 25-27 Nov. 2014, pp .830-833. DOI: 10.1109/TELFOR.2014.7034535.

[7] A.I. Semenikhin, D.V. Semenikhina, and Y.V. Yukhanov, "Synthesis of the Anisotropic Impedance Cylinder on the Given Polarization of the Scattered Field Independent on the Angle of Incidence and Polarization of Incidence Field", 26th Intern. Conf. Radioelektronika (RADIOELEKTRONIKA), Kosice, Slovakia, pp. 486-489, 2016.

[8] N.A. Kuzmin, "Approximate Boundary Conditions in the Electrodynamics of Stratified Tensor Media," Radio Sci., vol. 4, no. 8, pp. 703-708, 1969.

[9] G.T. Markov, and A.F. Chaplin, *Vozbuzhdenie elektromagnitnykh voln* [Electromagnetic Waves Excitation]. Moscow, Radio I Svyaz', 1983.

[10] A.F. Chaplin, *Analiz i sintez antennykh reshotok* [Analysis and Synthesis of Antenna Arrays]. L'vov, Vishcha Shkola, Ukraine, 1987.

Analysis of 3D problems of magnetic cloaking using optimization method

Gennady Alekseev[1,2], Yuliya Spivak[1,2], Aleksey Lobanov[1], and Elizaveta Paklina[2]

[1]Institute of Applied Mathematics FEB RAS, Vladivostok, Russia
[2]Far Eastern Federal University, Vladivostok, Russia
*corresponding author, E-mail: alekseev@iam.dvo.ru

Abstract

We consider the control problems for the 3D model of magnetic scattering by a permeable isotropic obstacle having the form of a spherical bilayer. These problems arise while developing the design technologies of magnetic cloaking devices using the optimization method for solving the corresponding inverse problems. The solvability of direct and optimization problems for the magnetic scattering model under study is proved. The optimality system which describes the necessary conditions of extremum is derived. Based on its analysis the sufficient conditions to the data are established which provide local uniqueness and stability of optimal solutions. Also numerical aspects of applying the optimization approach for solving problems of designing magnetic cloaking devices are discussed.

1. Introduction

In the last few years, devices for cloaking material objects have attracted the rapid attention in the research fields of invisibility and metamaterials. The first works in the mentioned fields were the articles [1, 2, 3, 4]. These were the start of development of different methods, schemes and techniques of solving problems when cloaking electromagnetic waves, acoustic waves [5, 6], magnetic, electric, thermal and other static fields [7, 8, 9, 10, 11, 12, 13]. It should be noted that the solutions obtained in these papers possess several drawbacks. In particular, some components of spatially dependent parameter tensors of ideal cloak are required to have infinite or zero values at the inner boundary of the cloak [2] which are very difficult to implement.

One of approaches of overcoming these difficulties consists of replacing "exact" singular solutions of cloaking problems under study by approximate non-singular solutions and designing cloaking devices based on these approximations (see., e.g., [14, 15, 16, 17]). Alternative approach is based on using the optimization method of solving inverse problems. This method is based on replacing initial cloaking problem by minimization problem of a suitable tracking-type cost functional which corresponds to inverse problem under consideration. The method to which one should referred to as inverse design method [18, 19] was applied in [20, 21, 22] devoted to the numerical analysis of 2D problems of designing layered cloaking shells. Also, it was applied in [23]–[29] when studying theoretically electromagnetic or acoustic cloaking problems. Pa-

pers [30, 31] are devoted to studying invisibility problem in X-ray tomography.

The goal of this paper is theoretical analysis of the cloaking problem for the 3D model of magnetic scattering by a layer shell using the optimization method. The plan of our paper is as follows. Firstly, the unique solvability of the direct problem of magnetic scattering by a permeable isotropic obstacle having the form of a spherical layer $a < r < b$ surrounded by another spherical layer $a < r < c$ with different variable permeabilities $\mu_k, k = 1, 2$ in every layer is proved. Then control problems are formulated. These problems arise while using optimization method for solving corresponding inverse problems for the magnetic scattering model under study. The solvability of these control problems is proved, the optimality system is derived which describes the necessary conditions of the extremum. Based on analysis of the optimality system the local uniqueness and stability of optimal solutions are established. Also numerical aspects of applying the optimization approach for solving the magnetic cloaking problems under study are discussed.

2. Statement and analysis of direct magnetic scattering problem

We consider the domain Ω in the space $\mathbb{R}^3$ having in spherical coordinates (r, θ, φ) the form of spherical layer $\Omega_1 = \{\mathbf{x} \in \mathbb{R}^3 : a < r = |\mathbf{x}| < b\}$ surrounded by another spherical layer $\Omega_2 = \{\mathbf{x} \in \mathbb{R}^3 : b < r = |\mathbf{x}| < c\}$, where a, b and c are positive constants. Denote by Ω_i and Ω_e^∞ the interior and exterior of the domain Ω. We will assume that the domains Ω_i and Ω_e^∞ are filled by homogeneous isotropic media with permeabilities μ_i and μ_e, respectively, while Ω_1 and Ω_2 are filled by inhomogeneous isotropic media with permeabilities μ_1 and μ_2, respectively.

Denote by B_R the ball $|\mathbf{x}| < R$, where $R > c$, containing domains Ω_i, Ω_1 and Ω_2. We will assume that there are sources outside B_R, which generate externally applied magnetic field $\mathbf{H}_a = -\text{grad}\Phi_a$ corresponding to potential Φ_a (see Fig. 1). Due to the absence of free currents in cloaking shell, magnetic field in the space $\mathbb{R}^3$ can be expressed by means of a magnetic scalar potential Φ in the form $\mathbf{H} = -\text{grad}\Phi$, where the potential Φ is a solution of equation

$$-\text{div}(\tilde{\mu}\mathbf{H}) = \text{div}(\tilde{\mu}\text{grad}\Phi) = 0.$$
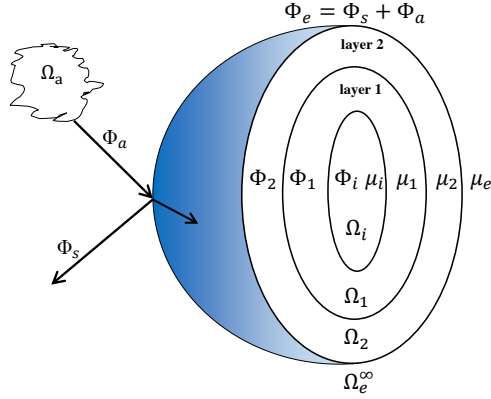
Figure 1: Layout of external sources and spherical bilayer cloak

Here $\tilde{\mu}$ is a given function satisfying the conditions $\tilde{\mu} = \mu_i$ in Ω_i, $\tilde{\mu} = \mu_k$ in Ω_k, $k = 1, 2$ and $\tilde{\mu} = \mu_e$ in Ω_e^∞. Denote by $\Phi_i, \Phi_1, \Phi_2, \Phi_e$ the restrictions of potential Φ to the domains $\Omega_i, \Omega_1, \Omega_2$ and Ω_e^∞, respectively. We set $\Phi_s = \Phi_e - \Phi_a$ and note that the fields Φ_i, Φ_1, Φ_2 and $\Phi_e = \Phi_a + \Phi_s$ are the solution of the following magnetic scattering problem [19, Ch. 3]:

$$\mu_i \Delta \Phi_i = 0 \text{ in } \Omega_i, \ \operatorname{div}(\mu_1 \nabla \Phi_1) = 0 \text{ in } \Omega_1,$$

$$\operatorname{div}(\mu_2 \nabla \Phi_2) = 0 \text{ in } \Omega_2, \ \mu_e \Delta \Phi_e = 0 \text{ in } \Omega_e^\infty, \quad (1)$$

$$\Phi_i = \Phi_1, \ \ \mu_i \frac{\partial \Phi_i}{\partial r} = \mu_1 \frac{\partial \Phi_1}{\partial r} \text{ at } r = a,$$

$$\Phi_1 = \Phi_2, \ \ \mu_1 \frac{\partial \Phi_1}{\partial r} = \mu_2 \frac{\partial \Phi_2}{\partial r} \text{ at } r = b,$$

$$\Phi_2 = \Phi_a + \Phi_s, \ \ \mu_2 \frac{\partial \Phi_2}{\partial r} = \mu_e \frac{\partial(\Phi_a + \Phi_s)}{\partial r} \text{ at } r = c, \ (2)$$

$$\Phi_s(\mathbf{x}) = o(1) \text{ as } r = |\mathbf{x}| \to \infty. \quad (3)$$

In the particular case, when μ_1 and μ_2 are nonnegative constants and, besides, the field $\mathbf{H}_a$ is uniform, the direct problem (1)–(3) admits an exact solution which can be found using Fourier's method (see [15, 16]).

Now, consider the case when the external field $\mathbf{H}_a$ is inhomogeneous and therefore it is not possible to apply Fourier's method for finding an exact solution of the problem (1)–(3). A number of functional spaces will be used while studying the direct problem (1)–(3) and respective control problems. Let $\Omega_e = \Omega_e^\infty \cap B_R$. We will use the space $H^1(D)$, where D is one of domains $B_R, \Omega_i, \Omega_1, \Omega_2$, Ω_e, and also spaces $L^\infty(\Omega_k)$, $H^s(\Omega_k)$, $s > 0$, $k = 1, 2$, $L^2(Q)$, $H^{1/2}(\Gamma_R)$ and $H^{-1/2}(\Gamma_R)$. Here $Q \subset B_R$ is an arbitrary open subset of B_R, Γ_R is a boundary of B_R (see Fig. 2). The norms and scalar products in $H^1(D)$, $H^s(\Omega_k)$, $L^2(Q)$, $H^{1/2}(\Gamma_R)$ and $H^{-1/2}(\Gamma_R)$ will be denoted by $\|\cdot\|_{1,D}, (\cdot,\cdot)_{1,D}, \|\cdot\|_{s,\Omega_k}, (\cdot,\cdot)_{s,\Omega_k}, \|\cdot\|_Q, (\cdot,\cdot)_Q, \|\cdot\|_{1/2,\Gamma_R}$ and $\|\cdot\|_{-1/2,\Gamma_R}$. We set $L_{\lambda_0}^\infty(\Omega_k) = \{\lambda \in L^\infty(\Omega_k) : \lambda(\mathbf{x}) \geq \lambda_0\}$, $H_{\lambda_0}^s(\Omega_k) = \{\lambda \in H^s(\Omega_k) : \lambda(\mathbf{x}) \geq \lambda_0\}$,

$\lambda_0 = \text{const} > 0$, $k = 1, 2$. It is well known by the embedding theorem that the continuous and compact embedding $H^s(\Omega_k) \subset L^\infty(\Omega_k)$ at $s > 3/2$, $k = 1, 2$, holds and the following estimate takes place:

$$\|\lambda\|_{L^\infty(\Omega_k)} \leq C_s \|\lambda\|_{s,\Omega_k} \ \forall \lambda \in H^s(\Omega_k), s > 3/2, k = 1, 2. \quad (4)$$

Here C_s is a constant depending on $s > 3/2$ and Ω_1, Ω_2. We need also a subspace $H(\Omega_e) = \{\Phi \in H^1(\Omega_e) : \Delta\Phi = 0$ in $\Omega_e\}$, equipped with the norm $\|\cdot\|_{1,\Omega_e} \equiv \|\cdot\|_{H^1(\Omega_e)}$. The space $H(\Omega_e)$ will be served for describing restrictions of externally applied field Φ_a to the domain Ω_e.
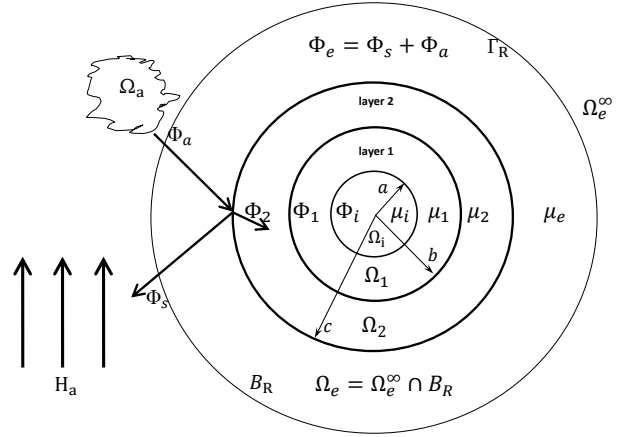
Figure 2: Schematic layout of artificial boundary Γ_R

It should be noted that by the trace theorem there exists a trace $\Phi|_{\Gamma_R} \in H^{1/2}(\Gamma_R)$ for any function $\Phi \in H^1(B_R)$ while for any function $\Phi^e \in H(\Omega_e)$ there exists a normal trace $\partial\Phi^e/\partial n|_{\Gamma_R} \in H^{-1/2}(\Gamma_R)$ and the following estimates hold:

$$\|\Phi\|_{1/2,\Gamma_R} \leq C_R \|\Phi\|_X \ \ \forall \Phi \in H^1(B_R), \quad (5)$$

$$\|\partial\Phi^e/\partial n\|_{-1/2,\Gamma_R} \leq C_R' \|\Phi^e\|_{1,\Omega_e} \ \ \forall \Phi^e \in H(\Omega_e). \quad (6)$$

Here C_R, C_R' are constants depending on Ω_e and R but are independent of $\Phi \in X$ and $\Phi^e \in H(\Omega_e)$.

We assume below that the following conditions take place:

(i) $\mu_1 \in L_{\mu_1^0}^\infty(\Omega_1)$, $\mu_2 \in L_{\mu_2^0}^\infty(\Omega_2)$, $\mu_1 \geq \mu_1^0, \mu_2 \geq \mu_2^0$, $\mu_1^0 = \text{const} > 0$, $\mu_2^0 = \text{const} > 0$;

(ii) $\Phi^e \equiv \Phi_a|_{\Omega_e} \in H(\Omega_e)$.

As the potential Φ is determined up to an additive constant we will not distinguish functions of the space $H^1(B_R)$ which differ from each other by an additive constant. Thus the main role below will be played by the following quotient-space $X = H^1(B_R) \setminus \mathbb{R}$ with the norm:

$$\|\Phi\|_X^2 = \|\nabla\Phi\|_{\Omega_i}^2 + \|\nabla\Phi\|_{\Omega_1}^2 + \|\nabla\Phi\|_{\Omega_2}^2 + \|\nabla\Phi\|_{\Omega_e}^2. \ (7)$$

One can show that the space $X = H^1(B_R) \setminus \mathbb{R}$ is Hilbert for this norm and, besides, the following analogue of Poincaré-Friedrichs inequality holds:

$$\|\Phi\|_{B_R} \leq C_P \|\Phi\|_X \ \ \forall \Phi \in X. \quad (8)$$

Here C_P is a constant which is independent of $\Phi \in X$.

We begin our analysis with defining weak formulation and weak solution of direct problem (1)–(3). Preliminarily we reduce problem (1)–(3) to an equivalent boundary problem considered in the bounded domain (ball) B_R. To this end we introduce as in [27] the Dirichlet-to-Neumann operator $T : H^{1/2}(\Gamma_R) \to H^{-1/2}(\Gamma_R)$ which maps every function $h \in H^{1/2}(\Gamma_R)$ to the function $\partial\tilde{\Phi}/\partial\nu \in H^{-1/2}(\Gamma_R)$. Here $\tilde{\Phi}$ is a solution of the external Dirichlet problem for equation $\Delta\tilde{\Phi} = 0$ in $\Omega_e^\infty \backslash B_R$ with the boundary condition $\tilde{\Phi}|_{\Gamma_R} = h$ satisfying the condition $\tilde{\Phi}(\mathbf{x}) = o(1)$ as $r = |\mathbf{x}| \to \infty$. We note that problem (1)–(3) considered in $\mathbb{R}^3$ is equivalent to boundary value problem (1), (2) considered in the ball B_R under the following additional condition for Φ_s on Γ_R:

$$\partial\Phi_s/\partial n = T\Phi_s \text{ on } \Gamma_R. \quad (9)$$

For brevity we will refer below to the problem (1), (2), (9) as Problem 1.

Based on the space X we derive now the weak formulation of Problem 1. Let $S \in X$ be a test function. We multiply every of equations in (1) considered in domains $\Omega_i, \Omega_1, \Omega_2$ and Ω_e by S, integrate over $\Omega_i, \Omega_1, \Omega_2$ or Ω_e, respectively, and apply Green formulae. Adding the obtained identities and using the boundary conditions in (2) and (9) we arrive at the following identity for the quadruple $\Phi = (\Phi_i, \Phi_1, \Phi_2, \Phi_e) \in X$:

$$a_\mu(\Phi, S) \equiv a_0(\Phi, S) + a(\mu_1, \mu_2; \Phi, S) = \langle F, S \rangle \ \forall S \in X. \quad (10)$$

Here and below μ denotes the pair (μ_1, μ_2) while $a_0(\cdot, \cdot), a(\mu_1, \mu_2; \cdot, \cdot)$ and F are bilinear and linear forms defined by

$$a_0(\Phi, S) = \mu_i \int_{\Omega_i} \nabla\Phi \cdot \nabla S d\mathbf{x} + \mu_e \int_{\Omega_e} \nabla\Phi \cdot \nabla S d\mathbf{x} -$$

$$- \int_{\Gamma_R} (T\Phi) S d\sigma, \quad (11)$$

$$a(\mu_1, \mu_2; \Phi, S) = a_1(\mu_1; \Phi, S) + a_2(\mu_2; \Phi, S), \quad (12)$$

$$a_1(\mu_1; \Phi, S) = \int_{\Omega_1} \mu_1 \nabla\Phi \cdot \nabla S d\mathbf{x}, \quad (13)$$

$$a_2(\mu_2; \Phi, S) = \int_{\Omega_2} \mu_2 \nabla\Phi \cdot \nabla S d\mathbf{x}, \quad (14)$$

$$\langle F, S \rangle = - \int_{\Gamma_R} T\Phi^e S d\sigma + \int_{\Gamma_R} (\partial\Phi^e/\partial n) S d\sigma. \quad (15)$$

Identity (10) represents the weak formulation of problem (1), (2), (9) and its solution $\Phi = (\Phi_i, \Phi_1, \Phi_2, \Phi_e) \in X$ will be called a weak solution of Problem 1. Arguing as in [27], on can easily show, that the introducing of the weak solution is admissible in the following sense: it satisfies all equations in (1) in the distribution sense, and also boundary conditions in (2) and (9) in the trace sense.

Using Hölder inequality and definition (7) for the norm $\| \cdot \|_X$ and (9), (10) we have

$$\left| \int_{\Omega_1} \mu_1 \nabla\Phi \cdot \nabla S d\mathbf{x} \right| \leq \|\mu_1\|_{L^\infty(\Omega_1)} \|\nabla\Phi\|_{\Omega_1} \|\nabla S\|_{\Omega_1} \leq$$

$$\leq \|\mu_1\|_{L^\infty(\Omega_1)} \|\Phi\|_X \|S\|_X,$$

$$\int_{\Omega_2} \mu_2 \nabla\Phi \cdot \nabla S d\mathbf{x} \leq \|\mu_2\|_{L^\infty(\Omega_2)} \|\nabla\Phi\|_{\Omega_2} \|\nabla S\|_{\Omega_2} \leq$$

$$\leq \|\mu_2\|_{L^\infty(\Omega_2)} \|\Phi\|_X \|S\|_X.$$

Besides, using (5), (6), we derive from (11), (12) and (15) that

$$\left| \mu_i \int_{\Omega_i} \nabla\Phi \cdot \nabla S d\mathbf{x} \right| \leq \mu_i \|\Phi\|_X \|S\|_X,$$

$$\left| \mu_e \int_{\Omega_e} \nabla\Phi \cdot \nabla S d\mathbf{x} \right| \leq \mu_e \|\Phi\|_X \|S\|_X, \quad (16)$$

$$\left| \int_{\Gamma_R} (T\Phi) S d\sigma \right| \leq \|T\Phi\|_{-1/2, \Gamma_R} \|S\|_{1/2, \Gamma_r} \leq$$

$$\leq C_T C_R^2 \|\Phi\|_X \|S\|_X, \quad (17)$$

$$|a_0(\Phi, S)| \leq (\mu_0 + C_T C_R^2) \|\Phi\|_X \|S\|_X,$$

$$\mu_0 = \max(\mu_i, \mu_e), \quad (18)$$

$$|\langle F, S \rangle| \leq (\|T\| \|\Phi^e\|_{1/2, \Gamma_R} + \|\partial\Phi^e/\partial n\|_{-1/2, \Gamma_R}) \|S\|_{1/2, \Gamma_R}$$

$$\leq (C_T C_R + C_R') C_R \|\Phi^e\|_{1, \Omega_e} \|S\|_X. \quad (19)$$

It follows from these estimates and (12) that forms $a(\mu_1, \mu_2; \cdot, \cdot)$, a_0 and F are continuous on X, and the following estimates hold:

$$|a(\mu_1, \mu_2; \Phi, S)| \leq (\|\mu_1\|_{L^\infty(\Omega_1)} + \|\mu_2\|_{L^\infty(\Omega_2)}) \|\Phi\|_X \|S\|_X \quad (20)$$

$$\|a_0\| \leq C_0, \ \|F\|_{X^*} \leq C_0 \|\Phi^e\|_{1, \Omega_e},$$

$$C_0 = \max[\mu_0 + C_T C_R^2, (C_T C_R + C_R') C_R]. \quad (21)$$

Here X^* is a dual of X with respect to space $L_0^2(B_R)$.

If, moreover, the condition (i) takes place then we have

$$\int_{\Omega_1} \mu_1 \nabla\Phi \cdot \nabla\Phi d\mathbf{x} \geq \mu_1^0 \|\nabla\Phi\|_{\Omega_1}^2,$$

$$\int_{\Omega_2} \mu_2 \nabla\Phi \cdot \nabla\Phi d\mathbf{x} \geq \mu_2^0 \|\nabla\Phi\|_{\Omega_2}^2,$$

$$a_0(\Phi, \Phi) = \mu_i \int_{\Omega_i} |\nabla\Phi|^2 d\mathbf{x} + \mu_e \int_{\Omega_e} |\nabla\Phi|^2 d\mathbf{x} -$$

$$- \int_{\Gamma_R} (T\Phi)\Phi d\sigma \geq \mu_0 \int_{\Omega_0 \cup \Omega_e} |\nabla\Phi|^2 d\mathbf{x} \ \forall \Phi \in X,$$

$$\mu_0 = \min(\mu_i, \mu_e).$$

It follows from these estimates and the definition of the norm (7) in space X that the bilinear form a_μ defined in (10) is coercive in X under condition (i) and, besides,

$$a_\mu(\Phi, \Phi) \geq \mu_* \|\Phi\|_X^2 \ \forall \Phi \in X,$$

$$\mu_* = \min(\mu_i, \mu_e, \mu_1^0, \mu_2^0). \quad (22)$$

We note that the bilinear form a_μ introduced in (10) defines a linear operator $A_\mu : X \to X^*$ acting by

$$\langle A_\mu \Phi, S \rangle = a_\mu(\Phi, S) \equiv a_0(\Phi, S) + a(\mu_1, \mu_2; \Phi, S), \tag{23}$$

while problem (10) is equivalent to operator equation

$$A_\mu \Phi = F. \tag{24}$$

As the bilinear form a_μ is continuous and coercive on X under condition (i), then from the Lax-Milgram theorem follows that the operator $A_\mu : X \to X^*$ is an isomorphism and the inverse $A_\mu^{-1} : X^* \to X$ to operator A_μ is also isomorphism. Let $C_\mu = \|A_\mu^{-1}\|$. It is clear by the Lax-Milgram theorem that $C_\mu \leq C_1 = (1/\mu_*)$. Using this estimate we derive that operator equation (24) has for any element $F \in X^*$ a unique solution $\Phi_\mu = A_\mu^{-1}(F) \in X$, for which the estimate $\|\Phi_\mu\|_X \leq C_1 \|F\|_{X^*}$ holds. Using this fact and the second estimate in (21) we conclude that for any field $\Phi^e \in H(\Omega_e)$ problem (10) has a unique solution $\Phi_\mu \in X$, and the following estimate holds:

$$\|\Phi_\mu\|_X \leq C_2 \|\Phi^e\|_{1,\Omega_e}, \quad C_2 = C_0 C_1. \tag{25}$$

We emphasize that constants C_1 and C_2 in (25) depend on $\mu_i, \mu_e, \mu_1^0, \mu_2^0$ and R but do not depend on functions μ_1 and μ_2 satisfying condition (i). Let us formulate the results obtained as the following theorem.

Theorem 1. *Let conditions (i), (ii) take place. Then for any pair $\mu = (\mu_1, \mu_2)$ we have:*

1) the operator $A_\mu : X \to X^*$ defined in (23) is an isomorphism and for the inverse operator $A_\mu^{-1} : X^* \to X$ the estimate $\|A_\mu^{-1}\| \leq C_1 \equiv (1/\mu_*)$ holds where constant μ_* is defined in (22);

2) for any external field $\Phi^e \in H(\Omega_e)$ problem (10) has a unique solution $\Phi_\mu \in X$, and the estimate (25) holds where the constant C_2 depends on $\mu_i, \mu_e, \mu_1^0, \mu_2^0$ and R but is independent of (μ_1, μ_2).

3. Formulation of the inverse problem. Applying the optimization method. Derivation of the optimality system

The main goal of this paper is analysis of the inverse problem arising while developing the design technologies of magnetic cloaking devices. This problem consists of finding unknown permeabilities μ_1 and μ_2 of inhomogeneous media filling Ω_1 and Ω_2 using given information about magnetic potential Φ in some subset $Q \subset B_R$. To achieve this goal we apply the optimization method. This approach is based on minimization of a cost functional which corresponds to the initial problem of designing approximate cloaking device. As a result the initial cloaking problem is reduced to studying corresponding control problem using the well-known methods of solving extremum problems. As a cost functional we choose one of the following:

$$I_1(\Phi) = \|\Phi - \Phi^d\|_Q^2 = \int_Q (\Phi - \Phi^d)^2 dx,$$

$$I_2(\Phi) = \|\nabla \Phi + \mathbf{H}^d\|_Q^2. \tag{26}$$

Here $Q \subset \Omega_i \cup \Omega_e$ is a bounded open subset, Φ^d (or $\mathbf{H}^d$) is a given in Q function (or vector-function). As controls we choose variable permeabilities μ_1 and μ_2. We will assume that the controls μ_1 and μ_2 are changed over certain sets K_1 and K_2. It is assumed that the following conditions hold.

(j) $K_1 \subset H_{\mu_1^0}^s(\Omega_1)$, $\mu_1^0 = \text{const} > 0$, $K_2 \subset H_{\mu_2^0}^s(\Omega_2)$, $\mu_2^0 = \text{const} > 0$, $s > 3/2$; $\alpha_0 > 0$.

Setting $K = K_1 \times K_2$, $\mu = (\mu_1, \mu_2)$ we define the operator $G : X \times K \to X^*$ by

$$\langle G(\Phi, \mu), S \rangle = \langle A_\mu \Phi, S \rangle - \langle F, S \rangle \equiv$$

$$a_0(\Phi, S) + a(\mu_1, \mu_2; \Phi, S) - \langle F, S \rangle \quad \forall S \in X \tag{27}$$

and rewrite the weak formulation (10) of problem 1 as $G(\Phi, \mu) = 0$. Let I is a weakly lower semicontinuous functional. Consider the following control problem:

$$J(\Phi, \mu) \equiv \frac{\alpha_0}{2} I(\Phi) + \frac{\alpha_1}{2} \|\mu_1\|_{s,\Omega_1}^2 + \frac{\alpha_2}{2} \|\mu_2\|_{s,\Omega_2}^2 \to \inf,$$

$$G(\Phi, \mu) = 0, \quad (\Phi, \mu) \in X \times K. \tag{28}$$

Here $\alpha_0, \alpha_1, \alpha_2$ are non-negative parameters which are used to control the relative importance of terms in (28). Setting $Z_{ad} = \{(\Phi, \mu) \in X \times K : G(\Phi, \mu) = 0, J(\Phi, \mu) < \infty\}$ we begin our analysis of problem (28) with proof of its solvability.

Theorem 2. *Let, under assumptions (ii) and (j), $\alpha_1 > 0$, $\alpha_2 > 0$ or $\alpha_1 \geq 0$, $\alpha_2 \geq 0$ and K_1, K_2 be bounded sets. Let $I : X \to \mathbb{R}$ be a weakly lower semicontinuous functional and a set Z_{ad} is not empty. Then control problem (28) has at least one solution $(\Phi, \mu_1, \mu_2) \in X \times K_1 \times K_2$.*

Proof. Denote by $(\Phi^m, \mu^m) \in Z_{ad}$, $\mu^m = (\mu_1^m, \mu_2^m)$, $m \in \mathbb{N} \equiv \{1, 2, \dots\}$ a minimizing sequence for the functional J for which the following relations hold:

$$a_0(\Phi^m, S) + a(\mu_1^m, \mu_2^m; \Phi^m, S) = \langle F, S \rangle \ \forall S \in X, \tag{29}$$

$$\lim_{m \to \infty} J(\Phi^m, \mu_m) = \inf_{(\Phi, \mu) \in Z_{ad}} J(\Phi, \mu) \equiv J^*.$$

By conditions of Theorem 2 we have

$$\|\mu_1^m\|_{s,\Omega_1} \leq c_1, \quad \|\mu_2^m\|_{s,\Omega_2} \leq c_2 \ \forall m \in \mathbb{N}. \tag{30}$$

Here and below c_1, c_2, c_3 are some constants which do not depend on m. It follows from (30) and Theorem 1 that $\|\Phi^m\|_X \leq c_3$. From this estimate and (30) we derive that there are weak limits $\mu_1^* \in K_1$, $\mu_2^* \in K_2$, $\Phi^* \in X$ of some subsequences of sequences $\{\mu_1^m\}$, $\{\mu_2^m\}$, $\{\Phi^m\}$. Using this fact and compactness of embedding $H^s(\Omega_k) \subset L^\infty(\Omega_k)$ at $s > 3/2$, $k = 1, 2$ we conclude that $\mu_1^m \to \mu_1^*$ strongly in $L^\infty(\Omega_1)$, $\mu_2^m \to \mu_2^*$ strongly in $L^\infty(\Omega_1)$, while $\Phi^m \to \Phi^*$ weakly in X.

Let us prove that $G(\Phi^*, \mu_1^*, \mu_2^*) = 0$, i.e. that

$$a_0(\Phi^*, S) + a(\mu_1^*, \mu_2^*; \Phi^*, S) = \langle F, S \rangle \ \forall S \in X. \tag{31}$$

To this end we pass to the limit in (29) as $m \to \infty$. It is clear that linear term $a_0(\Phi^m, S)$ passes to the

term $a_0(\Phi^*, S)$ as $m \to \infty$ while for the difference $a(\mu_1^m, \mu_2^m; \Phi^m, S) - a(\mu_1^*, \mu_2^*; \Phi^*, S)$ we have by (12)

$$|a(\mu_1^m, \mu_2^m; \Phi^m, S) - a(\mu_1^*, \mu_2^*; \Phi^*, S)| \le |a_1(\mu_1^m; \Phi^m, S) -$$

$$- a_1(\mu_1^*; \Phi^*, S)| + |a_2(\mu_2^m; \Phi^m, S) - a_2(\mu_2^*; \Phi^*, S)|. \quad (32)$$

Let us show that every of terms in the right-hand side of (32) vanishes as $m \to \infty$. In fact, taking into consideration (13), we have for the first term in (32):

$$|a_1(\mu_1^m; \Phi^m, S) - a_1(\mu_1^*; \Phi^*, S)| \le$$

$$\le \left| \int_{\Omega_1} \mu_1^*(\nabla\Phi^m - \nabla\Phi^*) \cdot \nabla S d\mathbf{x} \right| +$$

$$+ \left| \int_{\Omega_1} (\mu_1^m - \mu_1^*) \nabla\Phi^m \cdot \nabla S d\mathbf{x} \right| \quad \forall S \in X. \quad (33)$$

As $\Phi^m \to \Phi^*$ weakly in X then the first integral in the right-hand side of (33) tends to zero as $m \to \infty$ for any $S \in X$. Besides, it follows from the strong convergence $\mu_1^m \to \mu_1^*$ in $L^\infty(\Omega_1)$ that the second integral in (33) also tends to zero as $m \to \infty$. This means that the first term in the right-hand side of (32) tends to zero as $m \to \infty$. In a similar way one can show using (14) that the second term in the right-hand side of (32) tends to zero as $m \to \infty$. Therefore passing to the limit in (29) as $m \to \infty$ we arrive at (31). This means that $G(\Phi^*, \mu^*) = 0$ where $\mu^* = (\mu_1^*, \mu_2^*)$. As the functional $J(\Phi)$ is a weakly lower semicontinuous functional on $X \times K$ we derive that $J(\Phi^*, \mu^*) = J^*$. This proves the theorem.

At the second stage of the analysis of extremum problem (28) we derive an optimality system describing necessary conditions of extremum. For this purpose we make use of the extremum principle in smoothly-convex extremum problems [32]. Preliminarily we find the Fréchet derivative with respect to Φ of the operator $G : X \times K \to X^*$ defined in (27). It follows from linearity of the operator G with respect to Φ that the Fréchet derivative $G'_\Phi(\hat\Phi, \hat\mu)$ at every point $(\hat\Phi, \hat\mu) \in X \times K$ where $\hat\mu = (\hat\mu_1, \hat\mu_2)$ is defined by $G'_\Phi(\hat\Phi, \hat\mu) = \hat A \equiv A_{\hat\mu}$. Here operator $A_{\hat\mu}$ is defined by (23) at $\mu = \hat\mu$. Besides, it follows from (26) that

$$\langle (I')_\Phi(\hat\Phi), S \rangle = 2(\hat\Phi - \Phi^d, S)_Q = 2 \int_Q (\hat\Phi - \Phi^d) S d\mathbf{x},$$

$$\langle (I_2)'_\Phi(\hat\Phi), S \rangle = 2(\nabla\hat\Phi + \mathbf{H}^d, \nabla S)_Q \quad \forall S \in X. \quad (34)$$

Following [32] we introduce a Lagrange multiplier $\Psi \in X$ which will be referred to as an adjoint stage and consider the Lagrangian $\mathcal{L} : X \times K \times X \to R$ defined by the formula $L(\Phi, \mu, \Psi) \equiv J(\Phi, \mu) + \langle G(\Phi, \mu), \Psi \rangle_{X^* \times X}$. Denote by $\hat A^* \equiv G'_\Phi(\hat\Phi, \hat\mu)^* : X \to X^*$ the operator adjoint for operator $\hat A = G'_\Phi(\hat\Phi, \hat\mu) : X \to X^*$ defined by

$$\langle \hat A^* \Psi, S \rangle_{X^* \times X} \equiv \langle G'_\Phi(\hat\Phi, \hat\mu)^* \Psi, S \rangle_{X^* \times X} =$$

$$\langle G'_\Phi(\hat\Phi, \hat\mu) S, \Psi \rangle_{X^* \times X} = \langle \hat A S, \Psi \rangle_{X^* \times X} \quad \forall \Psi, S \in X. \quad (35)$$

It follows from linearity of operator G with respect to μ_1, μ_2 and from convexity of the set $K = K_1 \times K_2$ that the set $G(\Phi, K) = \{\mathbf{x}^* = G(\Phi, \mu) \in X^*, \mu \in K\}$ is a convex subset of X^* for any function $\Phi \in X$. As the operator $G'_\Phi(\hat\Phi, \hat\mu) \equiv \hat A$ is an isomorphism by Theorem 1, then from results of [32] the next theorem follows.

Theorem 3. *Let under assumptions (ii) and (j) the pair $(\hat\Phi, \hat\mu) \in X \times K$ where $\hat\mu = (\hat\mu_1, \hat\mu_2)$ be a solution of problem (28) and let functional $I(\Phi)$ be continuously differentiable with respect to state Φ in point $\hat\Phi$. Then there exists a unique Lagrange multiplier $\Psi \in X$ that satisfies the Euler-Lagrange equation*

$$a_{\hat\mu}(S, \Psi) \equiv a_0(S, \hat\Psi) + a(\hat\mu_1, \hat\mu_2; S, \hat\Psi) =$$

$$= -(\alpha_0/2)\langle I'_\Phi(\hat\Phi), S \rangle \quad \forall S \in X \quad (36)$$

and the minimum principle holds, which is equivalent to the following variational inequalities:

$$\alpha_1(\hat\mu_1, \mu_1 - \hat\mu_1)_{s, \Omega_1} + a_1\left(\mu_1 - \hat\mu_1, \hat\Phi, \hat\Psi\right) \ge 0 \, \forall\mu_1 \in K_1,$$
$$(37)$$

$$\alpha_2(\hat\mu_2, \mu_2 - \hat\mu_2)_{s, \Omega_2} + a_2\left(\mu_2 - \hat\mu_2, \hat\Phi, \hat\Psi\right) \ge 0 \, \forall\mu_2 \in K_2.$$
$$(38)$$

Direct problem (10), identity (36) which has the meaning of an adjoint problem for the adjoint state $\hat\Psi \in X$ and variational inequalities (37) and (38) constitute the optimality system. It describes the necessary conditions of an extremum for control problem (28). In particular case when $I = I_1(\Phi)$ we have by (34) that the Euler-Lagrange equation (36) has the form

$$a_{\hat\mu}(S, \Psi) \equiv a_0(S, \hat\Psi) + a(\hat\mu_1, \hat\mu_2; S, \hat\Psi) =$$

$$= -\alpha_0(\hat\Phi - \Phi^d, S)_Q \quad \forall S \in X. \quad (39)$$

Based on analysis of the optimality system we establish below sufficient conditions for the data which provide uniqueness and stability of solutions of problem (28) in particular case when $I(\Phi) = I_1(\Phi)$ (or $I(\Phi) = I_2(\Phi)$) with respect to small disturbances of function $\Phi^d \in L^2(Q)$ (or $\mathbf{H}^d \in L^2(Q)$) entering the cost functionals in (26).

4. Uniqueness and stability of optimal solutions

Denote by $(\Phi_1, \mu^{(1)}) = (\Phi_1, \mu_1^{(1)}, \mu_2^{(1)})$ a solution of problem (28) corresponding to given function $I(\Phi)$. By $(\Phi_2, \mu^{(2)}) = (\Phi_2, \mu_1^{(2)}, \mu_2^{(2)})$ we denote a solution of problem

$$J(\Phi, \mu) \equiv \frac{\alpha_0}{2}\tilde I(\Phi) + \frac{\alpha_1}{2}\|\mu_1\|_{s, \Omega_1}^2 + \frac{\alpha_2}{2}\|\mu_2\|_{s, \Omega_2}^2 \to \inf,$$

$$G(\Phi, \mu) = 0, \quad (\Phi, \mu) \in X \times K. \quad (40)$$

It is obtained from (28) by replacing functional $I(\Phi)$ with a perturbed functional $\tilde I(\Phi)$. We note that by Theorem 1 the following estimate holds for Φ_l, $l = 1, 2$:

$$\|\Phi_l\|_X \le M_\Phi \equiv C_2\|\Phi^e\|_{1, \Omega_e} \quad (41)$$

5

where C_2 is the constant defined in (25). Denote by $\Psi_l \in X$, $l = 1, 2$ Lagrange multipliers corresponding to solutions $(\Phi_l, \mu^{(l)})$. By Theorem 3 they satisfy

$$a_{\mu^{(l)}}(S, \Psi_l) \equiv a_0(S, \Psi_l) + a(\mu_1^{(l)}, \mu_2^{(l)}; S, \Psi_l) =$$

$$= -(\alpha_0/2)\langle I'_\Phi(\Phi_l), S \rangle \ \forall S \in X, \ l = 1, 2. \quad (42)$$

We set $\mu = \mu^{(1)} - \mu^{(2)}$,

$$\mu_1 = \mu_1^{(1)} - \mu_1^{(2)}, \ \mu_2 = \mu_2^{(1)} - \mu_2^{(2)}, \ \Phi = \Phi_1 - \Phi_2,$$

$$\Psi = \Psi_1 - \Psi_2, \ \Phi^d = \Phi_1^d - \Phi_2^d. \quad (43)$$

The following Lemma holds.

Lemma 1. *Let in addition to conditions (ii), (j) the triples $(\Phi_1, \mu_1^{(1)}, \mu_2^{(1)})$ and $(\Phi_2, \mu_1^{(2)}, \mu_2^{(2)})$ be solutions of problems (28) and (40), respectively. Let $\Psi_l \in X$, $l = 1, 2$ be the Lagrange multipliers corresponding to solutions $(\Phi_l, \mu_1^{(l)}, \mu_2^{(l)})$ and let the functionals I and $\tilde{I}$ be continuously differentiable with respect to the state Φ. Then the following estimate and inequality hold:*

$$\|\Phi\|_X \le C_1 C_s(\|\mu_1\|_{s,\Omega_1} + \|\mu_2\|_{s,\Omega_2})M_\Phi, \quad (44)$$

$$(\alpha_0/2)\langle I'_\Phi(\Phi_1) - \tilde{I}'_\Phi(\Phi_2), S \rangle \le -a(\mu_1, \mu_2; \Phi, \Psi_1 + \Psi_2) -$$
$$-\alpha_1\|\mu_1\|^2_{s,\Omega_1} - \alpha_2\|\mu_2\|^2_{s,\Omega_2}. \quad (45)$$

Proof. We subtract identity (10) written for $(\Phi_2, \mu_1^{(2)}, \mu_2^{(2)})$ from (10) written for $(\Phi_1, \mu_1^{(1)}, \mu_2^{(1)})$. Using notation (43) we obtain the following identity for the difference $\Phi = \Phi_1 - \Phi_2$:

$$a_0(\Phi, S) + a(\mu_1^{(2)}, \mu_2^{(2)}; \Phi, S) = -a(\mu_1, \mu_2; \Phi_1, S) \ \forall S \in X. \quad (46)$$

Using estimates (4), (20) and (41) we have

$$|a(\mu_1, \mu_2; \Phi_1, S)| \le C_s(\|\mu_1\|_{s,\Omega_1} + \|\mu_2\|_{s,\Omega_2})\|\Phi_1\|_X\|S\|_X \le$$

$$\le C_s(\|\mu_1\|_{s,\Omega_1} + \|\mu_2\|_{s,\Omega_2})M_\Phi\|S\|_X \ \forall S \in X. \quad (47)$$

Taking into account estimates (47) it follows from Theorem 1 applied to the linear with respect to the difference $\Phi = \Phi_1 - \Phi_2$ problem (46) that the estimate (44) holds for the solution Φ.

Now, we prove (45). Firstly, we set $\mu_1 = \mu_1^{(1)}$ in inequality (37) written for $\hat{\mu}_1 = \mu_1^{(2)}$, $\hat{\Phi} = \Phi_2$, $\hat{\Psi} = \Psi_2$ and then we set $\mu_1 = \mu_1^{(2)}$ in (37) written for $\hat{\mu}_1 = \mu_1^{(1)}$, $\hat{\Phi} = \Phi_1$, $\hat{\Psi} = \Psi_1$. Using (43) we obtain the inequalities

$$\alpha_1(\mu_1^{(2)}, \mu_1)_{s,\Omega_1} + a_1(\mu_1; \Phi_2, \Psi_2) \ge 0,$$

$$-\alpha_1(\mu_1^{(1)}, \mu_1)_{s,\Omega_1} - a_1(\mu_1; \Phi_1, \Psi_1) \ge 0. \quad (48)$$

Summing these inequalities we arrive at the following relation for the difference $\mu_1 \equiv \mu_1^{(1)} - \mu_1^{(2)}$:

$$a_1(\mu_1; \Phi_1, \Psi_1) - a_1(\mu_1; \Phi_2, \Psi_2) \le -\alpha_1\|\mu_1\|^2_{s,\Omega_1}. \quad (49)$$

In the same manner, we obtain the second inequality for the difference $\mu_2 \equiv \mu_2^{(1)} - \mu_2^{(2)}$:

$$a_2(\mu_2; \Phi_1, \Psi_1) - a_2(\mu_2; \Phi_2, \Psi_2) \le -\alpha_2\|\mu_2\|^2_{s,\Omega_2}. \quad (50)$$

We subtract identity (42) for $l = 2$ from (42) for $l = 1$ and set $S = \Phi$. We obtain

$$a_0(\Phi, \Psi) + a(\mu_1^{(2)}, \mu_2^{(2)}; \Phi, \Psi) + a(\mu_1, \mu_2; \Phi, \Psi_1) =$$

$$= -(\alpha_0/2)\langle I'_\Phi(\Phi_1) - \tilde{I}'_\Phi(\Phi_2), S \rangle. \quad (51)$$

Then we subtract identity (46) for $S = \Phi$ from (51) and obtain

$$a(\mu_1, \mu_2; \Phi, \Psi_1) - a(\mu_1, \mu_2; \Phi_1, \Psi) =$$

$$= -(\alpha_0/2)\langle I'_\Phi(\Phi_1) - \tilde{I}'_\Phi(\Phi_2), S \rangle. \quad (52)$$

Summing (52) with (49) and (50) we arrive at the desired inequality (45). The lemma is proved.

Relying on Theorem 4, we now establish sufficient conditions for the uniqueness and stability of the solution $(\hat{\Phi}, \hat{\mu})$ to the following control problem corresponding to the cost functional $I_1(\Phi) = \|\Phi - \Phi^d\|^2_Q$:

$$J(\Phi, \mu) \equiv \frac{\alpha_0}{2}I_1(\Phi) + \frac{\alpha_1}{2}\|\mu_1\|^2_{s,\Omega_1} + \frac{\alpha_2}{2}\|\mu_2\|^2_{s,\Omega_2} \to \inf,$$

$$G(\Phi, \mu) = 0, \ (\Phi, \mu) \in X \times K. \quad (53)$$

Setting $\Phi^d = \Phi_1^d - \Phi_2^d$ in addition to (43) we find in view of (34), that

$$\langle I'_1(\Phi_1) - \tilde{I}'_1(\Phi_2), \Phi \rangle = 2(\|\Phi\|^2_Q - (\Phi^d, \Phi)_Q). \quad (54)$$

By virtue of (34) and (54), identity (39) for Lagrange multiplyers Ψ_l, corresponding to the solutions (Φ_l, μ_l) and inequality (45) (for the differences Φ, μ_1, μ_2, Ψ entering into (43)) take the form

$$a_{\mu^{(l)}}(S, \Psi_l) \equiv a_0(S, \Psi_l) + a(\mu_1^{(l)}, \mu_2^{(l)}; S, \Psi_l) =$$

$$= -\alpha_0(\Phi_l - \Phi_l^d, S)_Q \ \forall S \in X, \ l = 1, 2, \quad (55)$$

$$\alpha_0(\|\Phi\|^2_Q - (\Phi^d, \Phi)_Q) \le -a(\mu_1, \mu_2; \Phi, \Psi_1 + \Psi_2) -$$

$$-\alpha_1\|\mu_1\|^2_{s,\Omega_1} - \alpha_2\|\mu_2\|^2_{s,\Omega_2}. \quad (56)$$

Set

$$M^0_\Phi = C_P M_\Phi + \max(\|\Phi_1^d\|_Q, \|\Phi_2^d\|_Q) \quad (57)$$

where C_P is a constant entering into Poincaré-Friedrichs inequality (8). The following main theorem is valid.

Theorem 4. *Let, in addition to assumptions (ii), (j), $K = K_1 \times K_2 \subset H^s_{\mu_1^0}(\Omega_1) \times H^s_{\mu_2^0}(\Omega_2)$ be a bounded set and let a triple $(\Phi_l, \mu_1^{(l)}, \mu_2^{(l)})$ be a solution of control problem (53) corresponding to a given function $\Phi_l^d = \Phi^d \in L^2(Q)$, $l = 1, 2$, where $Q \subset \Omega_i \cup \Omega_e$ is a nonempty open subset. We assume that the following conditions are satisfied:*

$$\alpha_1(1 - \varepsilon) > 4\alpha_0 C_1^2 C_s^2 M_\Phi M^0_\Phi,$$

$$\alpha_2(1 - \varepsilon) > 4\alpha_0 C_1^2 C_s^2 M_\Phi M^0_\Phi \quad (58)$$

where $\varepsilon \in (0, 1)$ is an arbitrary constant. Then the following stability estimates hold:

$$\|\mu_1^{(1)} - \mu_1^{(2)}\|_{s,\Omega_1} \le (1/2)\sqrt{\alpha_0/\varepsilon\alpha_1}\|\Phi_1^d - \Phi_2^d\|_Q, \quad (59)$$

$$\|\mu_2^{(1)} - \mu_2^{(2)}\|_{s,\Omega_2} \leq (1/2)\sqrt{\alpha_0/\varepsilon\alpha_2}\|\Phi_1^d - \Phi_2^d\|_Q, \quad (60)$$

$$\|\Phi_1 - \Phi_2\|_Q \leq \|\Phi_1^d - \Phi_2^d\|_Q, \quad (61)$$

$$\|\Phi_1 - \Phi_2\|_X \leq (1/2)C_1C_s(\sqrt{\alpha_0/\varepsilon\alpha_1} +$$
$$+ \sqrt{\alpha_0/\varepsilon\alpha_2})\|\Phi_1^d - \Phi_2^d\|_Q. \quad (62)$$

Proof. First, we derive the estimate of the Lagrange multiplier Ψ_l corresponding to the triple $(\Phi_l, \mu_1^{(l)}, \mu_2^{(l)})$, $l = 1, 2$. For this purpose, we turn to the problem (42) for $I(\Phi) = I_1(\Phi)$ which is equivalent to the following operator equation for the multiplier Ψ_l:

$$A_{\mu^{(l)}}^* \Psi_l = \alpha_0 f_l \in X^*, \ \langle f_l, S \rangle = -(\Phi_l - \Phi_l^d, S)_Q, l = 1, 2. \quad (63)$$

Here $A_{\mu^{(l)}}^*$ is the adjoint for the operator $A_{\mu^{(l)}}$ defined by $\langle A_{\mu^{(l)}}^* \Psi, \Phi \rangle = a_{\mu^{(l)}}(\Phi, \Psi) = \langle A_{\mu^{(l)}} \Phi, \Psi \rangle$ for all $\Phi, \Psi \in X$. We emphasize that $A_{\mu^{(l)}}^*$ is an isomorphism and for his inverse $(A_{\mu^{(l)}}^*)^{-1}$ the following estimate holds

$$\|(A_{\mu^{(l)}}^*)^{-1}\| \leq C_1. \quad (64)$$

It is easy to see using (57) and (8) that for all $S \in X$

$$|(\Phi_l - \Phi_l^d, S)_Q| \leq [\|\Phi_l\|_Q + \max(\|\Phi_1^d\|_Q, \|\Phi_2^d\|_Q)]\|S\|_X \leq$$
$$\leq [C_P\|\Phi_l\|_X + \max(\|\Phi_1^d\|_Q, \|\Phi_2^d\|_Q)]\|S\|_X = M_\Phi^0 \|S\|_X.$$

From this fact it follows that $\|f_l\|_{X^*} \leq M_\Phi^0$, and by estimate (64) applied to problem (63) with respect to Ψ_l, the following estimate holds for Ψ_l:

$$\|\Psi_l\|_X \leq C_1\alpha_0\|f_l\|_{X^*} \leq C_1\alpha_0 M_\Phi^0. \quad (65)$$

Combining estimates (4), (20), (44), (65) and the Young inequality $2cd \leq \varepsilon c^2 + (1/\varepsilon)d^2 \ \forall c \geq 0, d \geq 0, \varepsilon > 0$ at $\varepsilon = 1$, we derive using conditions (58) that

$$|a(\mu_1, \mu_2; \Phi, \Psi_1 + \Psi_2)| \leq$$

$$C_s(\|\mu_1\|_{s,\Omega_1} + \|\mu_2\|_{s,\Omega_2})\|\Phi\|_X(\|\Psi_1\|_X + \|\Psi_2\|_X) \leq$$
$$\leq 2C_1\alpha_0 M_\Phi^0 C_s(\|\mu_1\|_{s,\Omega_1} + \|\mu_2\|_{s,\Omega_2})[C_1C_s(\|\mu_1\|_{s,\Omega_1} +$$
$$+ \|\mu_2\|_{s,\Omega_2})M_\Phi] \leq$$
$$\leq 4\alpha_0 C_1^2 C_s^2 M_\Phi M_\Phi^0(\|\mu_1\|_{s,\Omega_1}^2 + \|\mu_2\|_{s,\Omega_2}^2) \leq$$
$$\leq \alpha_1(1-\varepsilon)\|\mu_1\|_{s,\Omega_1}^2 + \alpha_2(1-\varepsilon)\|\mu_2\|_{s,\Omega_2}^2. \quad (66)$$

Using estimate (66) we deduce from (56) that

$$\alpha_0\|\Phi\|_Q^2 \leq \alpha_0\|\Phi^d\|_Q\|\Phi\|_Q - \varepsilon\alpha_1\|\mu_1\|_{s,\Omega_1}^2 - \varepsilon\alpha_2\|\mu_2\|_{s,\Omega_2}^2. \quad (67)$$

From inequality (67) we obtain the estimate $\|\Phi\|_Q \leq \|\Phi^d\|_Q$, which is equivalent by (43) to estimate (61). Next, using given estimate and the inequality $\|\Phi^d\|_Q\|\Phi\|_Q \leq \|\Phi\|_Q^2 + (1/4)\|\Phi^d\|_Q^2$, which follows from the Young inequality at $\varepsilon = 1/2$, we derive from (67) that

$$\varepsilon\alpha_1\|\mu_1\|_{s,\Omega_1}^2 + \varepsilon\alpha_2\|\mu_2\|_{s,\Omega_2}^2 \leq$$

$$\leq \alpha_0\|\Phi^d\|_Q\|\Phi\|_Q - \alpha_0\|\Phi\|_Q^2 \leq \frac{\alpha_0}{4}\|\Phi^d\|_Q^2. \quad (68)$$

From inequality (68) we obtain estimates (59), (60) for norms $\|\mu_1^{(1)} - \mu_1^{(2)}\|_{s,\Omega_1}$ and $\|\mu_2^{(1)} - \mu_2^{(2)}\|_{s,\Omega_2}$, while the estimate (62) follows from estimates (44), (59) and (60). The theorem is proved.

In a similar way one can prove the stability of solutions of control problem

$$J(\Phi, \mu) \equiv \frac{\alpha_0}{2}\|\nabla\Phi + \mathbf{H}^d\|_Q^2 + \frac{\alpha_1}{2}\|\mu_1\|_{s,\Omega_1}^2 +$$

$$+ \frac{\alpha_2}{2}\|\mu_2\|_{s,\Omega_2}^2 \to \inf, \ G(\Phi, \mu) = 0, \ (\Phi, \mu) \in X \times K \quad (69)$$

corresponding to the second functional $I_2(\Phi)$ in (26).

Theorem 5. *Let, in addition to assumptions (ii), (j), $K = K_1 \times K_2$ be a bounded set and let a triple $(\Phi_l, \mu_1^{(l)}, \mu_2^{(l)})$ be a solution of control problem (69) corresponding to a given function $\mathbf{H}^d = \mathbf{H}_l^d \in L^2(Q)$, $l = 1, 2$, where $Q \subset \Omega_0 \cup \Omega_e$ is a nonempty open subset. Let $M_\Phi^0 = M_\Phi + \max(\|\mathbf{H}_1^d\|_Q, \|\mathbf{H}_2^d\|_Q)$ where M_Φ is defined in (41) and assume that conditions (58) take place. Then the following stability estimates hold:*

$$\|\mu_1^{(1)} - \mu_1^{(2)}\|_{s,\Omega_1} \leq (1/2)\sqrt{\alpha_0/\varepsilon\alpha_1}\|\mathbf{H}_1^d - \mathbf{H}_2^d\|_Q, \quad (70)$$

$$\|\mu_2^{(1)} - \mu_2^{(2)}\|_{s,\Omega_2} \leq (1/2)\sqrt{\alpha_0/\varepsilon\alpha_2}\|\mathbf{H}_1^d - \mathbf{H}_2^d\|_Q, \quad (71)$$

$$\|\Phi_1 - \Phi_2\|_Q \leq \|\mathbf{H}_1^d - \mathbf{H}_2^d\|_Q, \quad (72)$$

$$\|\Phi_1 - \Phi_2\|_X \leq (1/2)C_1C_s(\sqrt{\alpha_0/\varepsilon\alpha_1} +$$
$$+ \sqrt{\alpha_0/\varepsilon\alpha_2})\|\mathbf{H}_1^d - \mathbf{H}_2^d\|_Q. \quad (73)$$

Note that the stability of the solution of extremum problems (53) and (69) has been proved assuming that the parameters α_1 and α_2 are positive and satisfy (58). This means that the terms $(\alpha_1/2)\|\mu_1\|_{s,\Omega_1}^2$ and $(\alpha_2/2)\|\mu_2\|_{s,\Omega_2}^2$ in the expressions for the functional I_1 in (53) and I_2 in (69) have a regularizing effect.

5. Numerical algorithms

Optimality system (10), (36), (37), (38) derived above can be used to design efficient numerical algorithms for solving control problem (53) or (69). The simplest one (Algorithm 1) for the functional $I_1(\Phi)$ can be obtained by applying the fixed-point iteration method for solving the optimality system. The m-th iteration of this algorithm consists of finding unknown values Φ^m, Ψ^m, μ_1^{m+1} and μ_2^{m+1} for given μ_1^m and μ_2^m where $m = 0, 1, 2...$ by sequentially solving following problems:

$$a_0(\Phi^m, S) + a(\mu_1^m, \mu_2^m; \Phi^m, S) =$$
$$= \langle F, S \rangle \ \forall S \in X, \quad (74)$$

$$a_0(S, \Psi^m) + a(\mu_1^m, \mu_2^m; S, \Psi^m) =$$
$$= -\alpha_0(S, \Phi^m - \Phi^d)_Q \ \forall S \in X, \quad (75)$$

$$\alpha_1(\mu_1^{m+1}, \mu_1 - \mu_1^m)_{s,\Omega_1} + a_1((\mu_1 - \mu_1^{m+1})\Phi^m, \Psi^m) \geq 0$$

$$\forall \mu_1 \in K_1, \quad (76)$$

$$\alpha_2(\mu_2^{m+1}, \mu_2 - \mu_2^m)_{s,\Omega_2} + a_2((\mu_2 - \mu_2^{m+1})\Phi^m, \Psi^m) \geq 0$$
$$\forall \mu_2 \in K_2. \qquad (77)$$

For discretization and solving problems (74), (75) one can use open source software FreeFem++ (www.freefem.org) based on using finite element method. For discretization of (76), (77) it is comfortable to look for controls μ_1 and μ_2 as

$$\mu_1(\mathbf{x}) = \sum_{j=1}^N \lambda_j \varphi_j^{(1)}(\mathbf{x}), \ \mu_2(\mathbf{x}) = \sum_{j=1}^N \mu_j \varphi_j^{(2)}(\mathbf{x}), \ \mathbf{x} \in \Omega_k. \qquad (78)$$

Here $\varphi_j^{(1)}(\mathbf{x}) \in H^s(\Omega_1)$ and $\varphi_j^{(2)}(\mathbf{x}) \in H^s(\Omega_2)$ are non-negative basis functions, $\lambda_j \geq 0$ and $\mu_j \geq 0$ are unknown coefficients. In the particular case when Ω_1 and Ω_2 are divided into $2N$ sub-layers $\Omega_1^{(1)}, \ldots, \Omega_1^{(N)}$ and $\Omega_2^{(1)}, \ldots, \Omega_2^{(N)}$, and, besides, functions $\phi_j^{(1)}$ and $\phi_j^{(2)}$ are characteristic functions of sub-layers $\Omega_1^{(j)}$ and $\Omega_2^{(j)}$, $j = 1, \ldots, N$, respectively, the presentation (78) corresponds physically to replacing initial "continuous" magnetic shell by layered cloak. The letter consists of $2N$ sub-layers $(\Omega_1^{(j)}, \lambda_j)$ and $(\Omega_2^{(j)}, \mu_j)$, $j = 1, \ldots, N$, every of which is filled by homogeneous medium with constant permeability λ_j (or μ_j), $j = 1, \ldots, N$. Similar algorithm which is based on the strategy "optimize-then-discretize" (see [34]) can be used and for functional $I_2(\Phi)$.

Now we discuss another algorithm (Algorithm 2) which is based on the opposite strategy: "discretize-then-optimize". The idea of this algorithm consists of seeking unknown controls – permeabilities μ_1 and μ_2 in the form (78). There λ_j and μ_j are unknown coefficients which one should determine from the condition of minimum of the discrete analogue of functional $I_1(\Phi)$ (or $I_2(\Phi)$) in (26) which has the form

$$I_1(\lambda_1, \ldots, \lambda_N, \mu_1, \ldots, \mu_N) =$$
$$= \int_Q |\Phi(\lambda_1, \ldots, \lambda_N, \mu_1, \ldots, \mu_N) - \Phi^d|^2 d\mathbf{x}. \qquad (79)$$

Here $\Phi(\lambda_1, \ldots, \lambda_N, \mu_1, \ldots, \mu_N)$ is a solution of the direct problem (10) for the case when parameters $\mu_1(\mathbf{x})$ and $\mu_2(\mathbf{x})$ have the form (78). In such a case the discrete analogue of problem (53) takes the form

$$\frac{\alpha_0}{2} I_1(\lambda_1, \ldots, \lambda_N, \mu_1, \ldots, \mu_N) + \frac{\alpha_1}{2} \sum_{j=1}^N \lambda_j^2 +$$
$$+ \frac{\alpha_2}{2} \sum_{j=1}^N \mu_j^2 \rightarrow \inf, \qquad (80)$$

where $\lambda_j \geq 0, \mu_j \geq 0$, $j = 1, \ldots, N$ are sought for controls.

Problem (80) represents the finite-dimensional problem of conditional minimization which can be solved numerically using known methods of solution of discrete extremum problems. We note that for solving (80) it is comfortable to use the particle swarm optimization method (see
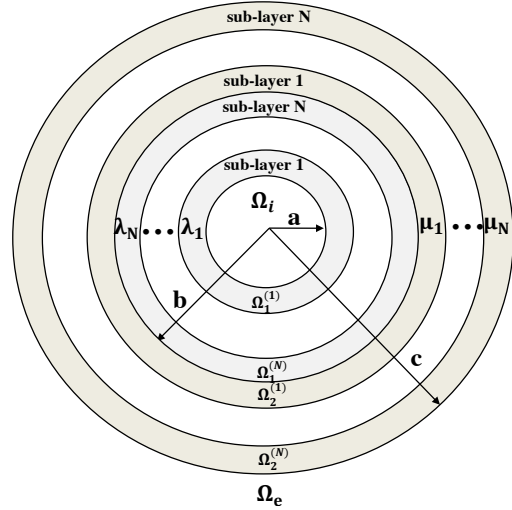
Figure 3: Geometry of $2N$-layered cloak

[33]) according to the scheme proposed in [34, 35, 36, 37] for the numerical solution of thermal cloaking problems for cylindrical and spherical bodies. The formal comparison of both algorithms shows that Algorithm 1 is more complicated and more expensive in terms of CPU time and memory space. This is due to the fact that Algorithm 1 is based on solving the optimality system (10), (36)–(38) which involves a coupled system of state and adjoint equations (10) and (36) together with two variational inequalities (37) and (38) for sought for controls.

6. Conclusion

In conclusion, we studied control problems for magnetic scattering model (1)–(3). These problems arise when optimization method is applied for solving cloaking problems for respective scattering model. The magnetic permeabilities μ_1 and μ_2 of the inhomogeneous media filling the layers Ω_1 and Ω_2 of the cloak play the role of controls. We studied some new properties of solutions of direct magnetic scattering problem, proved the correctness of this problem and solvability of general control problem (28). Besides, we derived the optimality system (10), (36)–(38) describing the necessary conditions of extremum. Based on analysis of the optimality system, we have established sufficient conditions for the initial data which provide the uniqueness and stability of optimal solutions for problems (53) and (69) with respect to small perturbations of functions $\Phi^d \in L^2(Q)$ or $\mathbf{H}^d \in L^2(Q)$ included in the respective cost functionals in (28). In the same manner, the stability of optimal solutions with respect to small perturbations of the external field Φ^e can be investigated.

Besides, we proposed two numerical algorithms for solving our cloaking problems. The first of them, based on the strategy "optimize-then-discretize", is obtained when the fixed-point iteration method is used for solving the

optimality system (10), (36)–(38) for the control problem under study. The second one which is based on strategy "discretize-then-optimize" consists of solving finite-dimensional problem (80). The particle swam optimization method can be used for this purpose.

Authors plan to devote a forthcoming paper to developing and studying the properties of the algorithms and to comparative analysis of results of numerical experiments performed using these algorithms.

Acknowledgement

References

[1] L.S. Dolin, On a possibility of comparison of three-dimensional electromagnetic systems with nonuniform anisotropic filling, *Izv. Vuzov Radiofizika* 4: 964–967, 1961.

[2] J.B. Pendry, D. Shurig, D.R. Smith, Controlling electromagnetic fields, *Science* 312: 1780–1782, 2006.

[3] U. Leonhardt, Optical conformal mapping, *Science* 312: 1777–1780, 2006.

[4] A. Alú, N. Engheta, Achieving transparency with plasmonic and metamaterial coatings, *Phys. Rev. E* 72: 016623, 2005.

[5] S.A. Cummer, D. Shurig, One path to acoustic cloaking, *New Journal of Physics* 9: 45–51, 2007.

[6] H. Chen, C.T. Chan, Acoustic cloaking in three dimensions using acoustic metamaterials, *Applied Physics Letters* 91: 183518, 2007.

[7] B. Wood, J.B. Pendry, Metamaterials at zero frequency, *J. Phys.: Condens. Matter.* 19: 076208, 2007.

[8] S. Guenneau, C. Amra, D. Veynante, Transformation thermodynamics: cloaking and concentrating heat flux, *Opt. Express.* 20: 8207, 2012.

[9] F. Yang, Z.L. Zhong Mei, T.Y. Jin, T.J. Cui, DC electric invisibility cloak, *Phys. Rev. Lett.* 109: 053902, 2012.

[10] S.V. Yampolskii, Y.A. Genenko, Magnetic cloaking by a paramagnet/superconductor cylindrical tube in the critical state, *Appl. Phys. Lett.* 104: 143504, 2014.

[11] T. Han, C.-W. Qiu, Transformation Laplacian metamaterials: recent advances in manipulating thermal and dc fields, *J. Opt.* 18: 044003, 2016.

[12] M. Raza, Y. Liu, E.H. Lee, Y. Yungui Ma, Transformation thermodynamics and heat cloaking: a review, *J. Opt.* 18: 044002, 2016.

[13] L. Kroon, K. Jarrendahl, Neutral shielding and cloaking of magnetic fields using isotropic media, *J. Phys.: Condens. Matter* 29: 035801, 2017.

[14] A. Sanchez, C. Navau, J. Prat-Camps, D.-X. Chen, Antimagnets: controlling magnetic fields with superconductor metamaterial hybrids, *New J. Phys.* 13: 093034, 2011.

[15] F. Gomory, M. Solovyov, J. Souc et al., Experimental realization of a magnetic cloak, *Science* 335: 1466–1468, 2012.

[16] F. Gomory, M. Solovyov, J. Souc et al., Supporting online materials for experimental realization of a magnetic cloak, *Science* 335: 1466–1468, 2012.

[17] G.V. Alekseev, V.G. Romanov, One class of nonscattering acoustic shells for a model of anisotropic acoustics, *J. Appl.and Ind. Math.* 6: 1–5, 2012.

[18] S. Xu, Y. Wang, B. Zhang, H. Chen, Invisibility cloaks from forward design to inverse design, *Science China Information Sciences* 56: 120408, 2013.

[19] G.V. Alekseev, *Invisibility problem in acoustics, optics and heat transfer*, Dalnauka, Vladivostok, 2016 [in Russian].

[20] B.-I. Popa, S.A. Cummer, Cloaking with optimized homogeneous anisotropic layers, *Phys. Rev. A*, 79: 023806, 2009.

[21] X.H. Wang, E.A. Semouchkina, A route for efficient non-resonance cloaking by using multilayer dielectric coating, *Appl. Phys. Lett.* 102: 113506, 2013.

[22] A. Mirzaei, A.E. Miroshnichenko, I.V. Shadrivov, Y.S. Kivshar, All-dielectric multilayer cylindrical structures for invisibility cloaking, *Scientific Reports*, 5: 9574. 2015.

[23] R.V. Brizitskii, A.S. Savenkova, Inverse extremum problems for Maxwell's equations, *Comput. Math. Math. Phys.* 50: 984–992, 2010.

[24] G.V. Alekseev, R.V. Brizitskii, The theoretical analysis of boundary control extremal problems for Maxwell's equations, *J. Appl. Ind. Math.* 5: 1–15, 2011.

[25] G.V. Alekseev, Cloaking of material objects by controlling the impedance boundary condition for Maxwell's equations, *Doklady Physics* 58: 482–486, 2013.

[26] G.V. Alekseev, Cloaking via impedance boundary condition for 2-D Helmholtz equation, *Appl. Anal.* 93: 254–268, 2014.

[27] G.V. Alekseev, V.A. Levin, Optimization method of searching parameters of an inhomogeneous liquid medium in the acoustic cloaking problem, *Doklady Physics* 59: 89–93, 2014.

[28] G.V. Alekseev, Stability estimates in the problem of cloaking material bodies for Maxwell's equations, *Comp. Math. Mathem. Phys.* 54: 1788–1803, 2014.

[29] G.V. Alekseev, Analysis and optimization in problems of cloaking of material bodies for the Maxwell equations, *Differential Equations* 52: 366–377, 2016.

[30] D.S. Anikonov, V.G. Nazarov, I.V. Prokhorov, Visible and invisible media in tomography, *Dokl. Math.* 56: 955–958, 1997.

[31] D.S. Anikonov, V.G. Nazarov, I.V. Prokhorov, Poorly visible media in X-Ray tomography, *Inverse and Ill-Posed Problems Series (VSP,Utrecht)* 38: viii+296, 2002.

[32] A.V. Fursikov, *Optimal Control of Distributed Systems: Theory and Applications*, American Mathematical Society, Boston, MA, USA, 2000.

[33] R. Poli, J. Kennedy, T. Blackwell, Particle swarm optimization: an overview, *Swarm Intel.* 1: 33–57, 2008.

[34] G.V. Alekseev, A.V. Lobanov, Yu.E. Spivak, Optimization and discretization in 2D problems of electromagnetic invisible cloaking, *CEUR Workshop Proceedings* 1623: 125–137, 2016.

[35] A.V. Lobanov, Yu.E. Spivak, Numerical analysis of problem of designing magnetic bilayer cloak, *Progress In Electromagnetics Research Symposium - Spring (PIERS)* 1362–1366, 2017.

[36] Yu.E. Spivak, Optimization method in static magnetic cloaking problems, *Progress In Electromagnetics Research Symposium - Spring (PIERS)* 1327–1331, 2017.

[37] G.V. Alekseev, V.A. Levin, D.A. Tereshko, Optimization analysis of the thermal cloaking problem for a cylindrical body, *Doklady Physics* 62: 71–75, 2017.

Optimization approach in axisymmetric problems of manipulating DC currents

Gennady Alekseev[1,2*], **Dmitry Tereshko**[1]

[1]Institute of Applied Mathematics, Far Eastern Branch of the Russian Academy of Sciences, Vladivostok, Russia
[2]School of Natural Sciences, Far Eastern Federal University, Vladivostok, Russia
*corresponding author, E-mail: `alekseev@iam.dvo.ru`

Abstract

Inverse problems associated with designing axisymmetric material shells for DC currents manipulating are studied. Applying the optimization method these inverse problems are reduced to corresponding control problems. A numerical algorithm based on the particle swarm optimization is proposed and the results of numerical experiments are discussed.

1. Introduction

In 2006 the transformation optics approach was proposed in [1, 2] to solve electromagnetic cloaking problems. Then this method has been firstly extended to acoustic cloaking [3, 4] and to cloaking thermal, magnetic, electric and another static fields [5, 6, 7, 8, 9, 10, 11, 12, 13]. This allowed to design metamaterial devices for manipulating DC currents such as invisibility cloaks, illusion devices and concentrators. But these devices usually adopted the analogue of transformation optics using complicated resistor networks to mimic inhomogeneous and anisotropic conductivities. Another and more general principle for DC currents manipulating based on the direct solution of electrical conduction equations using Fourier method has been proposed in [14]. However, the corresponding theory is valid under the strict limitations on the initial data which ensure the existence of an exact solution.

In this work we consider the problem of manipulating the dc currents in the general case when the theory developed in [14] is not applicable. To solve this problem we apply the optimization method described in detail in [15]. This approach is based on introducing the cost functional under minimization which adequately corresponds to the inverse problem of designing a device for manipulating DC currents. Beginning with the fundamental works by A.N. Tikhonov [16], this method is widely used when studying inverse problems of electromagnetism and heat and mass transfer (see [15] and references therein). As applied to cloaking problems, the optimization approach has given rise to a new cloaking strategy known as the inverse design strategy [17]. We mentioned the fist papers [18, 19] where cloaking problems were solved using numerical optimization methods (an iterative gradient method in [18] and a genetic algorithm in [19]). It should be mention papers [20, 21, 22, 23, 24, 25, 26, 27] where electromagnetic or acoustic cloaking problems are analyzed theoretically by applying an optimization method. Works [28, 29] are devoted to studying invisibility problem in X-ray tomography. Finally we note papers [30, 31, 32, 33] devoted to thermal cloaking problems. Optimization method for designing thermal cloaking shells was proposed and analyzed in [30, 33]. Numerical method based on particle swarm optimization was suggested for solving a thermal cloaking problems in [31, 32].

The purpose of this paper is the theoretical and numerical analysis of design problems of functional structures in the form of spherical shells to cloak material bodies in a stationary electric field. Keeping this goal in mind, the plan of our article is as follows. Based on the technical implementation conditions, the desired axisymmetric shell is divided into a finite number of layers, each of which is filled with a homogeneous isotropic material. As a result the manipulation problem under study is reduced to solving of respective finite-dimensional control problems. Constant conductivities of each layer play the role of controls in this control problem.

2. Mathematical model

Let us start with the statement of the general problem, considered in a three-dimensional cylindrical domain $D = \{\mathbf{x} \equiv (x, y, z) : -z_0 < z < z_0, \quad x^2 + y^2 < c^2\}$ with specified numbers $z_0 > 0$ and $c > 0$ (see Fig. 1). Let an external electric potential U^e be formed by two horizontal bases $z = \pm z_0$ with different values u_1 and u_2, and the lateral surface Γ of cylinder D be insulated. We assume that there is a material shell (Ω, σ) inside D. Here, Ω is a spherical layer $a < |\mathbf{x}| < b\}$, $b < c$ and σ is the electrical conductivity tensor of the inhomogeneous anisotropic medium filling the domain Ω. We assume also that the interior Ω_i: $|\mathbf{x}| < a$ and exterior Ω_e: $|\mathbf{x}| > b$ of Ω are filled with homogeneous media having (generally different) constant electrical conductivities: $\sigma_i > 0$ and $\sigma_e > 0$.

In this case, the direct conduction problem implies determination of a triad U of functions: u_i in Ω_i, u in Ω, and u_e in Ω_e, which satisfy the equations

$$\sigma_i \Delta u_i = 0 \ \text{ in } \ \Omega_i, \tag{1}$$

$$\text{div}\,(\sigma\,\text{grad}\,u) = 0 \ \text{ in } \ \Omega, \tag{2}$$

$$\sigma_e \Delta u_e = 0 \ \text{ in } \ \Omega_e, \tag{3}$$

and the boundary conditions

$$U|_{z=-z_0} = u_1, \quad U|_{z=z_0} = u_2, \quad \frac{\partial U}{\partial n}\Big|_\Gamma = 0. \quad (4)$$

The matching conditions are fulfilled at boundaries Γ_i and Γ_e of layer Ω, which have the form

$$u_i = u, \quad \sigma_i \frac{\partial u_i}{\partial n} = (\sigma \nabla u) \cdot \mathbf{n} \text{ on } \Gamma_i, \quad (5)$$

$$u_e = u, \quad \sigma_e \frac{\partial u_e}{\partial n} = (\sigma \nabla u) \cdot \mathbf{n} \text{ on } \Gamma_e. \quad (6)$$

As already mentioned, our goal is to analyze the cloaking problem for the model (1)–(6). Let us remain that inverse cloaking problem in the exact formulation consists in finding electrical conductivity tensor σ providing the following cloaking conditions [15]:

$$u_e = U^e \text{ in } \Omega_e, \quad \nabla u_i = 0 \text{ in } \Omega_i.$$

These conditions imply that electrical potential U must be equal to the external field U^e in Ω_e and its gradient ∇U must be equal to zero in Ω_i.

Firstly we will study some properties of solutions to direct problem (1)–(6). In spite of the different geometries (cylindrical and spherical) of the above-introduced domains D and $\Omega \subset D$, their common important property is that they are both axisymmetric. This property will be essentially used below, along with the following assumptions:

(i) tensor σ is diagonal in spherical coordinates r, θ, φ, and its diagonal components (radial, polar, and azimuthal conductivities) σ_r, σ_θ and σ_φ are independent of φ and satisfy the assumptions

$$\sigma_r \in L^\infty(\Omega), \ \sigma_r > \sigma_r^0 = \text{const} > 0,$$

$$\sigma_\theta \in L^\infty(\Omega), \ \sigma_\theta > \sigma_\theta^0 = \text{const} > 0, \ \sigma_\varphi = \sigma_\theta.$$

The condition $\sigma_\varphi = \sigma_\theta$ is widely used when analyzing three-dimensional problems of designing spherical functional devices. Moreover, in the particular case where the parameters σ_r, σ_θ, u_1 and u_2 are constant, $\sigma_i = \sigma_e = \sigma_0 = $ const) and the condition $2\sigma_r\sigma_\theta = \sigma_0^2 + \sigma_0\sigma_r$ is satisfied, problem (1)–(6) has an exact solution independent of φ:

$$u_i(r,\theta) = \frac{u_0}{z_0}\left(\frac{a}{b}\right)^{q(s)-1} r\cos\theta + \frac{u_1+u_2}{2} \text{ in } \Omega_i,$$

$$u(r,\theta) = \frac{u_0}{z_0}\left(\frac{r}{b}\right)^{q(s)-1} r\cos\theta + \frac{u_1+u_2}{2} \text{ in } \Omega,$$

$$u_e(r,\theta) = \frac{u_0}{z_0}r\cos\theta + \frac{u_1+u_2}{2} \text{ in } \Omega_e, \quad (7)$$

where

$$q(s) \equiv \frac{-1+\sqrt{1+8s}}{2}, \quad s = \frac{\sigma_\theta}{\sigma_r}, \quad u_0 = \frac{u_2-u_1}{2}.$$

The parameter $s = \sigma_\theta/\sigma_r$ characterizes the degree of anisotropy of the shell $(\Omega, \sigma_r, \sigma_\theta)$. In the particular case where $s = 1$ (provided that $\sigma_r = \sigma_\theta = \sigma_0$ so that the

entire medium filling the domain D is homogeneous and isotropic), formula (7) is transformed into the unified formula

$$U^e(z) = \frac{u_0}{z_0}r\cos\theta + \frac{u_1+u_2}{2} = u_0\frac{z}{z_0} + \frac{u_1+u_2}{2}, \quad (8)$$

which describes the external applied field $U^e(z)$, used to detect objects located in domain D. It follows from (7) and (8) that

$$u_e = U^e, \quad |\nabla u_e| = |\nabla U^e| = \frac{|u_0|}{z_0} \text{ in } \Omega_e,$$

$$|\nabla u_i| = \frac{|u_0|}{z_0}\mathcal{K}(s) \text{ in } \Omega_i, \quad \mathcal{K}(s) \equiv \left(\frac{a}{b}\right)^{q(s)-1}. \quad (9)$$

Then we introduce the quantity $\mathcal{M}(s) = 1 - \mathcal{K}(s)$, which was referred to as the cloaking efficiency of shell $(\Omega, \sigma_r, \sigma_\theta)$ at $s > 1$ in [15]. Obviously, $0 \le \mathcal{K}(s) \le 1$, $0 \le \mathcal{M}(s) \le 1$ at $s \ge 1$; and

$$q(s) \to 1, \ \mathcal{K}(s) \to 1, \ \mathcal{M}(s) \to 0 \text{ at } s \to 1;$$

$$q(s) \to \infty, \ \mathcal{K}(s) \to 0, \ \mathcal{M}(s) \to 1 \text{ at } s \to \infty.$$

Thus, the cloaking efficiency of the homogeneous anisotropic shell $(\Omega, \sigma_r, \sigma_\theta)$ described by formulas (7), increases with an increase in the anisotropy parameter $s = \sigma_\theta/\sigma_r$. In the limit at $s \to \infty$, we obtain an exact cloaking shell with maximum cloaking efficiency $\mathcal{M} = 1$. However, in the limit at $s \to 1$, we have a shell $(\Omega, \sigma_r, \sigma_\theta)$ with $\mathcal{M} = 0$.
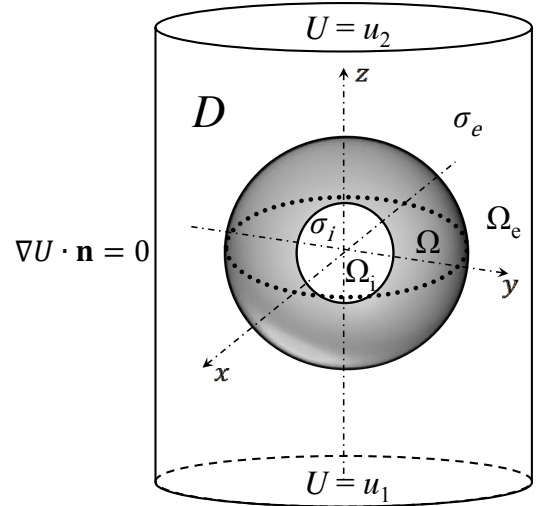

Figure 1: Geometry of the problem.

3. Optimization problems for layered shell

Let us now complicate the structure of the shell under consideration, assuming that $(\Omega, \sigma_r, \sigma_\theta)$ is a layered shell consisting of M concentric spherical layers Ω_j, $j = $

$1, 2, \ldots, M$. Each of these layers is filled with a homogeneous and (generally) anisotropic medium, described by constant conductivities $\sigma_{rj} > 0$ and $\sigma_{\theta j} > 0$, $j = 1, 2, \ldots, M$. The parameters σ_r and σ_θ of this shell are given by the formulas

$$\sigma_r(\mathbf{x}) = \sum_{j=1}^{M} \sigma_{rj} \chi_j(\mathbf{x}), \quad \sigma_\theta(\mathbf{x}) = \sum_{j=1}^{M} \sigma_{\theta j} \chi_j(\mathbf{x}). \quad (10)$$

Here, $\chi_j(\mathbf{x})$ is a characteristic function of layer Ω_j, which is equal to 1 inside of Ω_j and 0 outside of Ω_j.

We should emphasize that in the case of a layered shell, the inverse problems considered here become finite-dimensional, because they are reduced to determination of unknown coefficients σ_{rj} and $\sigma_{\theta j}$ (entering formula (10)), which form a $2M$-dimensional vector $\mathbf{s} \equiv (\sigma_{r1}, \sigma_{\theta 1}, \ldots, \sigma_{rM}, \sigma_{\theta M})$ having the sense of conductivity vector for respective M-layered shell. In the particular case of an isotropic shell, when $\sigma_{rj} = \sigma_{\theta j} = \sigma_j$, conductivities of layers will be described by a vector $\mathbf{s} = (\sigma_1, \sigma_2, \ldots, \sigma_M)$.

Using the optimization method, one can reduce inverse problems under study to the minimization of a certain quality functional J. To find the explicit form of functional J, we denote the solution to the direct problem corresponding to parameters $(\sigma_{r1}, \sigma_{\theta 1}, \ldots, \sigma_{rM}, \sigma_{\theta M})$ in Ω and to coefficients σ_i in Ω_i and σ_e in Ω_e by $U[\mathbf{s}] \equiv U(\sigma_{r1}, \sigma_{\theta 1}, \ldots, \sigma_{rM}, \sigma_{\theta M})$. It is assumed below that the vector $\mathbf{s} = (\sigma_{r1}, \sigma_{\theta 1}, \ldots, \sigma_{rM}, \sigma_{\theta M})$ belongs to the bounded set

$$S = \{ \mathbf{s} : m_r \leq \sigma_{rj} \leq M_r, \ m_\theta \leq \sigma_{\theta j} \leq M_\theta, \ j = 1, \ldots, M \}$$

for specified positive constants m_r, M_r, m_θ, M_θ, $j = 1, 2, \ldots, M$. Let our cost functions J_e, J_i and J are defined by

$$J_e(\mathbf{s}) = \frac{\|U[\mathbf{s}] - U^e\|_{L^2(\Omega_e)}}{\|U^e\|_{L^2(\Omega_e)}},$$

$$J_i(\mathbf{s}) = \frac{\|\nabla U[\mathbf{s}]\|_{L^2(\Omega_i)}}{\|\nabla U^e\|_{L^2(\Omega_i)}},$$

$$J(\mathbf{s}) = \frac{J_e(\mathbf{s}) + J_i(\mathbf{s})}{2}. \quad (11)$$

Below we will consider the following two problems:

$$J_e(\mathbf{s}) \to \inf, \quad \mathbf{s} \in S, \quad (12)$$

$$J(\mathbf{s}) = \frac{J_e(\mathbf{s}) + J_i(\mathbf{s})}{2} \to \inf, \quad \mathbf{s} \in S. \quad (13)$$

We refer to problem (12) as an external cloaking problem while problem (13) is a full cloaking problem.

Consider a particular case of a single-layer shell with constant parameters σ_r^*, σ_θ^* satisfying the condition

$$2\sigma_r^* \sigma_\theta^* = \sigma_0^2 + \sigma_0 \sigma_r^*.$$

A simple analysis in view of (9) shows that in this case the following relations hold:

$$J_e(\sigma_r^*, \sigma_\theta^*) = 0, \quad J_i(\sigma_r^*, \sigma_\theta^*) = \mathcal{K}(s^*),$$

$$J(\sigma_r^*, \sigma_\theta^*) = 0.5 \, \mathcal{K}(s^*), \quad s^* = \sigma_\theta^* / \sigma_r^*. \quad (14)$$

Here $\mathcal{K}(s^*)$ is the measure of visibility connected with the cloaking efficiency by the relation $\mathcal{K}(s^*) = 1 - \mathcal{M}(s^*)$. From here and from (14) follows that value $J_i(\sigma_r^*, \sigma_\theta^*)$ of the functional J_i as well as value $J(\sigma_r^*, \sigma_\theta^*)$ of the functional J characterizes the cloaking efficiency of the corresponding shell $(\Omega, \sigma_r^*, \sigma_\theta^*)$. The smaller values $J(\sigma_r^*, \sigma_\theta^*)$ correspond to higher cloaking efficiency of the shell $(\Omega, \sigma_r^*, \sigma_\theta^*)$ and vice versa. This fact is also true in the general case of M-layered shell with conductivity vector $\mathbf{s} \equiv (\sigma_{r1}, \sigma_{\theta 1}, \ldots, \sigma_{rM}, \sigma_{\theta M})$.

To solve problems (12), (13) we use an algorithm based on the particle swarm optimization (PSO) [34]. Within this method, the desired parameters determining the value of minimized functional J are presented in the form of the coordinates of the radius vector $\mathbf{s} \equiv (\sigma_{r1}, \sigma_{\theta 1}, \ldots, \sigma_{rM}, \sigma_{\theta M})$ of some abstract particle. A particle swarm is considered to be any finite set of particles $\mathbf{s}_1, \ldots, \mathbf{s}_N$. Within the particle swarm optimization, one sets the initial swarm position $\mathbf{s}_0^j$, $j = 1, 2, \ldots, N$, and the iterative displacement procedure $\mathbf{s}_j^{i+1} = \mathbf{s}_j^i + \mathbf{v}_j^{i+1}$ for all particles $\mathbf{s}_j$, which is described by the formulas (see [31])

$$\mathbf{v}_j^{i+1} = w\mathbf{v}_j^i + c_1 d_1 (\mathbf{p}_j^i - \mathbf{s}_j^i) + c_2 d_2 (\mathbf{p}_g - \mathbf{s}_j^i). \quad (15)$$

After each displacement we calculate the value $J(\mathbf{s}_j^{i+1})$ of the functional J for the new position $\mathbf{s}_j^{i+1}$, compare it to the current minimum value and, if necessary, update the personal and global best positions $\mathbf{p}_j$ and $\mathbf{p}_g$. In the end of this iteration process, all particles have to come at the global minimum point.

Here, $\mathbf{v}_j$ is the displacement vector; w, c_1 and c_2 are constant parameters; and d_1 and d_2 are random variables, which are uniformly distributed over the interval $(0, 1)$. Their choice was considered in more detail in [31, 34]. The subscript $j \in \{1, 2, \ldots, N\}$ in (15) denotes the particle number, and the superscript $i \in \{0, 1, \ldots, L\}$ indicates the iteration number.

4. Numerical results

In this section we discuss the results of using the proposed algorithm for designing single-layer and multilayer cloaking shells. The most time-consuming part is the calculation of the values $J(\mathbf{s}_j^i)$ of the functional J for the particle position $\mathbf{s}_j^{i+1}$ at different i and j values. This procedure includes two stages. At the first stage, the solution $U[\mathbf{s}_j^i]$ to direct problem (1)–(6) is calculated. To this end, we used the FreeFEM++ software package (www.freefem.org), designed for numerical solution of two- and three-dimensional boundary value problems by the finite-element method. After determining $U[\mathbf{s}_j^i]$, at the second stage we calculate the mean squared integral norms entering the definition of functionals J_e or J_i in (11).

In numerical experiments we assume that domain D and shell Ω are determined by the values

$$z_0 = 4 \text{ cm}, \ a = 1 \text{ cm}, \ b = 1.5 \text{ cm}, \ c = 4 \text{ cm}.$$
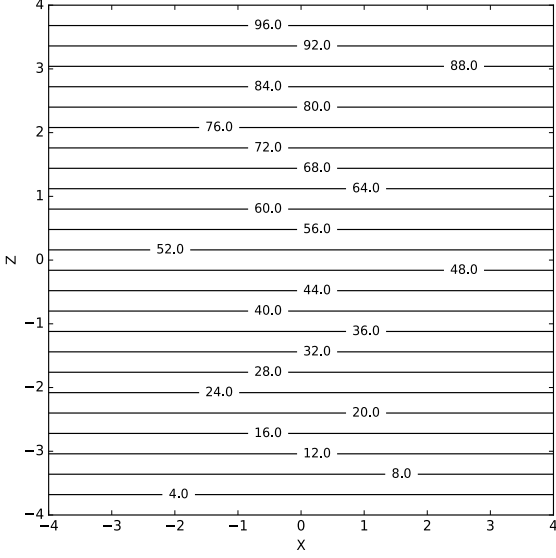
Figure 2: Equipotential lines for the external field U^e.

The role of the external field was played by the field U^e in (7) at $u_1 = 0$ V, $u_2 = 100$ V, which is characterized by straight equipotential lines $U^e = \mathrm{const}$, oriented perpendicular to the z axis (see Fig. 2). In view of the axial symmetry of the direct boundary value problem, its solution in spherical coordinates is independent of the angle φ. Therefore, an approximate solution was calculated in the cross section D_2 of the three-dimensional domain D by the $y = 0$ plane.

Let us note that field U^e in Fig. 2 corresponds to a homogeneous medium that fills the entire domain D. Placing an object with a different conductivity into this medium causes perturbation of the field U^e. To show this effect we assume that Ω_i is the aluminum ball with the electrical conductivity $\sigma_i = 3.8 \times 10^7$ S/m while the rest of the domain D is filled with the stainless steel ($\sigma_0 = 1.45 \times 10^6$ S/m). Solving the direct problem (1)–(6) we obtain the electrical potential U with equipotential lines shown in Fig. 3. Perturbation of the external field U^e indicates the presence of body (Ω_i, σ_i) in D. In order to suppress this perturbation we need to design a cloaking shell.

Firstly, we solve the design problem for a single-layer anisotropic shell $(\Omega, \sigma_r, \sigma_\theta)$ assuming that the background material in Ω_i and Ω_e is the stainless steel ($\sigma_i = \sigma_e = 1.45 \times 10^6$ S/m) while lower and upper bounds of the control set S are determined by

$$m_r = 1.0 \times 10^2 \text{ S/m}, \quad M_r = 1.25 \times 10^5 \text{ S/m},$$

$$m_\theta = 1.25 \times 10^5 \text{ S/m}, \quad M_\theta = 3.8 \times 10^7 \text{ S/m}.$$

Numerical solution of the minimization problem (12) with the help of PSO method gives after 50 iterations the following results:

$$\sigma_r^{opt} = 61725 \text{ S/m}, \ \sigma_\theta^{opt} = 1.77 \times 10^7 \text{ S/m},$$

$$J_e^{opt} = 2.5 \times 10^{-5}, \ J_i^{opt} = 1.1 \times 10^{-4}, \ J^{opt} = 6.8 \times 10^{-4}.$$

If we solve the problem (13) then we obtain the following optimal values of control parameters and cost functionals:

$$\sigma_r^{opt} = 57562 \text{ S/m}, \ \sigma_\theta^{opt} = 1.89 \times 10^7 \text{ S/m},$$

$$J_e^{opt} = 4.0 \times 10^{-5}, \ J_i^{opt} = 5.5 \times 10^{-5}, \ J^{opt} = 2.5 \times 10^{-5}.$$

Equipotential lines for corresponding field $U[\mathbf{s}^{opt}]$ are shown in Fig. 4. It can be seen that the electric potential $U[\mathbf{s}^{opt}]$ in Ω_e is close to the external field U^e, and it creates the illusion of the absence of the shell Ω for an external observer. It should be noted however that this high cloaking efficiency is achieved in both cases due to the high anisotropy of respective cloak $(\Omega, \sigma_r^{opt}, \sigma_\theta^{opt})$. It is characterized by anisotropy parameter $s^{opt} = \sigma_\theta^{opt}/\sigma_r^{opt}$ which is equal to 26 in the first case and to 85 in the second case.

Therefore our second group of tests concerns with designing multilayer cloak with isotropic layers. Let an even integer M denotes the number of layers of our cloak and σ_j is the electrical conductivity of the j-th layer, $j = 1, \ldots, M$. Setting $\mathbf{s} = (\sigma_1, \sigma_2, \ldots, \sigma_M)$ we define the set S as follows

$$S = \{\mathbf{s} : \sigma_{min} \leq \sigma_j \leq \sigma_{max}, j = 1, \ldots, M\}.$$

In our first test the lower bound corresponds to carbon ($\sigma_{min} = 1.0 \times 10^4$ S/m) and the upper bound corresponds to aluminum ($\sigma_{max} = 3.8 \times 10^7$ S/m). As in the previous case, the background material in domains Ω_i and Ω_e is the stainless steel ($\sigma_i = \sigma_e = 1.45 \times 10^6$ S/m).

Optimal values $\sigma_1^{opt}, \sigma_2^{opt}, \sigma_M^{opt}$ and corresponding values $Jopt$ of the cost functional J which were obtained by
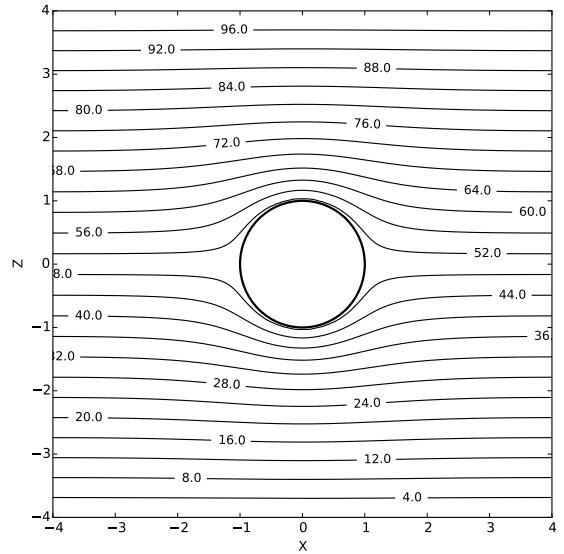

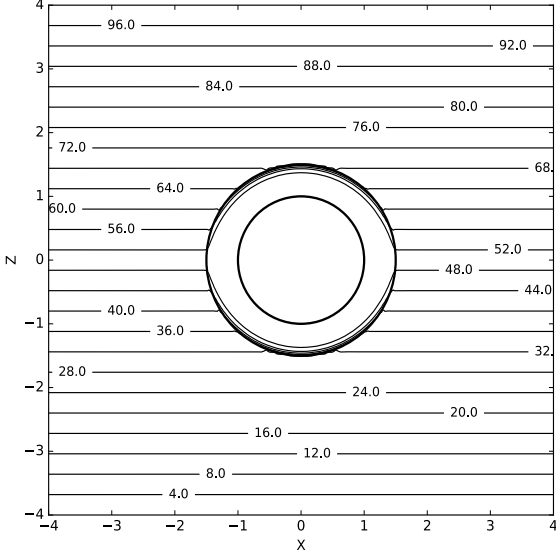Figure 3: Equipotential lines for an aluminum ball without a shell.

4

Figure 4: Equipotential lines for cloaking shell with a single anisotropic layer.

Figure 5: Equipotential lines for shell with two isotropic layers.

Table 1: Computational results for multilayer shells ($\sigma_{min} = 1.0 \times 10^4$ S/m, $\sigma_{max} = 3.8 \times 10^7$ S/m).

M	σ_1^{opt} [S/m]	σ_2^{opt} [S/m]	σ_M^{opt} [S/m]	$J(\mathbf{s}^{opt})$
2	1.0×10^4	4.3×10^6	4.3×10^6	2.4×10^{-2}
4	1.0×10^4	3.8×10^7	8.1×10^6	7.5×10^{-4}
6	1.0×10^4	3.8×10^7	1.1×10^7	9.6×10^{-5}
8	1.0×10^4	3.8×10^7	1.5×10^7	3.3×10^{-5}
10	1.0×10^4	3.8×10^7	1.7×10^7	2.9×10^{-5}

solving problem (13) using PSO are presented in Table 1 for five different scenarios corresponding to $M = 2, 4, 6, 8, 10$.

Analysis of numerical results for multilayer shell with isotropic layers showed very interesting fact, namely: the optimal values of all control parameters with odd indices coincide with $\sigma_1^{opt} = \sigma_{\min}$, i.e. they equal to the lower bound:

$$\sigma_1^{opt} = \sigma_3^{opt} = \ldots = \sigma_{M-1}^{opt} = \sigma_{\min} = 1.0 \times 10^4 \text{ S/m},$$

while all even controls except the last one coincide with σ_2^{opt}, i.e. they equal to the upper boundary $\sigma_2^{opt} = \sigma_{\max}$:

$$\sigma_2^{opt} = \sigma_4^{opt} = \ldots = \sigma_{M-2}^{opt} = \sigma_{\max} = 3.8 \times 10^7 \text{ S/m}.$$

Equipotential lines of corresponding field $U[\mathbf{s}^{opt}]$ for two-layer and four-layer shells are shown in Fig. 5 and Fig. 6, respectively. In both cases the electric potential $U[\mathbf{s}^{opt}]$ in Ω_e is close to the external field U^e shown in Fig. 4.

Analysis of Table 1 shows that the optimal value of functional J decreases with increasing the number of layers M and takes the value $J^{opt} = 2.9 \times 10^{-5}$ at $M = 10$. It corresponds to very high cloaking efficiency of the respective cloak $(\Omega, \mathbf{s}^{opt})$.

It should be noted that the results essentially depend on the bounds σ_{min} and σ_{max} of the control set S. In our second test the lower bound of the control set S corresponds to graphite ($\sigma_{min} = 1.2 \times 10^5$ S/m) and the upper bound corresponds to copper ($\sigma_{max} = 5.9 \times 10^7$ S/m). The background material in domains Ω_i and Ω_e is again the stainless steel ($\sigma_i = \sigma_e = 1.45 \times 10^6$ S/m). Computational results for second test are presented in Table 2.

As in the previous test the optimal values of all control parameters with an odd index coincide and equal to the
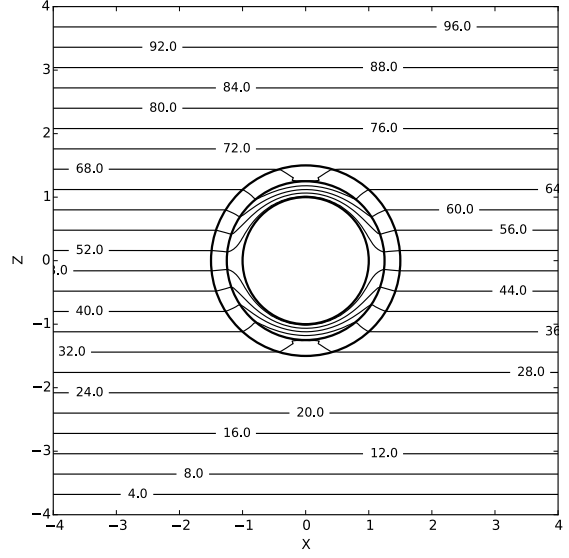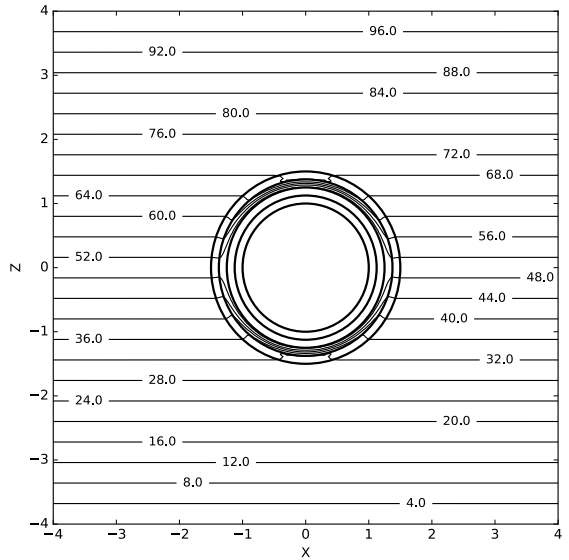

Figure 6: Equipotential lines for shell with four isotropic layers.

Table 2: Computational results for multilayer shells ($\sigma_{min} = 1.2 \times 10^5$ S/m, $\sigma_{max} = 5.9 \times 10^7$ S/m).

M	σ_1^{opt} [S/m]	σ_2^{opt} [S/m]	σ_M^{opt} [S/m]	$J(\mathbf{s}^{opt})$
2	1.2×10^5	5.9×10^7	5.9×10^7	1.1×10^{-1}
4	1.2×10^5	5.9×10^7	2.3×10^6	3.4×10^{-2}
6	1.2×10^5	5.9×10^7	5.8×10^5	1.3×10^{-2}
8	1.2×10^5	5.9×10^7	2.2×10^5	7.9×10^{-3}
10	1.2×10^5	5.9×10^7	1.2×10^5	5.1×10^{-3}

lower bound σ_{min} while all even controls except the last one take the maximum possible value which equal to upper bound σ_{max}. It is clearly seen that in this case the optimal values $J(\mathbf{s}^{opt})$ of the functional J for all M are greater than in Table 1. Thus for second choice of bounds σ_{min} and σ_{max} we obtained shell with a substantially lower cloaking efficiency.

In our third test the lower bound corresponds to carbon ($\sigma_{min} = 1.0 \times 10^4$ S/m) and the upper bound corresponds to copper ($\sigma_{max} = 5.9 \times 10^7$ S/m). The background material in domains Ω_i and Ω_e is again the stainless steel ($\sigma_i = \sigma_e = 1.45 \times 10^6$ S/m). Computational results for third test are presented in Table 3.

Table 3: Computational results for multilayer shells ($\sigma_{min} = 1.0 \times 10^4$ S/m, $\sigma_{max} = 5.9 \times 10^7$ S/m).

M	σ_1^{opt} [S/m]	σ_2^{opt} [S/m]	σ_M^{opt} [S/m]	$J(\mathbf{s}^{opt})$
2	1.0×10^4	4.3×10^6	4.3×10^6	2.4×10^{-2}
4	1.0×10^4	5.9×10^7	8.1×10^6	4.9×10^{-4}
6	1.0×10^4	5.9×10^7	1.1×10^7	6.1×10^{-5}
8	1.0×10^4	5.9×10^7	1.4×10^7	1.8×10^{-5}
10	1.0×10^4	5.9×10^7	1.8×10^7	1.6×10^{-6}

Analysis of Tables 1, 2 and 3 shows that the last choice of the bounds σ_{min} and σ_{max} gives the least optimal values J^{opt} of the functional J. Thus to obtain a shell with the highest cloaking efficiency it is necessary to choose the smallest possible value of the lower bound σ_{min} and the largest value of the upper bound σ_{min}.

Since the optimal values of all control parameters except the last one σ_M^{opt} are equal to the lower or upper bounds of the control set S, the designing a multilayer shell can be reduced to the one-parameter minimization problem for σ_M. As a result, we can use only three isotropic materials to construct a multilayer shell. Let us note that cloaking efficiency depends significantly on the materials of the shell. If the choice of materials is limited but we want to increase cloaking efficiency then we can use the geometric parameters of the shell (e.g. the thickness of the last sublayer) as additional controls.

5. Conclusions

In this paper we studied inverse problems arising when designing axisymmetric DC cloaking shells. Using the op-

timization method these inverse problems were reduced to corresponding control problems in which the electric conductivities play the role of controls. We proposed numerical algorithm based on the particle swarm optimization and discussed results of computational experiments. Optimization analysis showed that high cloaking efficiency of the shell can be achieved using either a highly anisotropic single-layer shell or a multilayer shell with isotropic layers. In the latter case the optimal values of all control parameters with odd indices coincide and equal to the lower bound of the control set while all even controls except the last one take the maximum possible value corresponding to upper bound. Using these results simplifies substantially technical realization of cloaks designed with the help of optimization method. In fact, it is enough to use three or only two different materials for obtaining high performance cloaks.

References

[1] J.B. Pendry, D. Schurig, D.R. Smith, Controlling electromagnetic fields, *Science* 312: 1780–1782, 2006.

[2] U. Leonhardt, Optical conformal mapping, *Science* 312: 1777–1780, 2006.

[3] S.A. Cummer, D. Schurig, One path to acoustic cloaking, *New J. Phys.* 9: 45, 2007.

[4] H. Chen, C.T. Chan, Acoustic cloaking in three dimensions using acoustic metamaterials, *Appl. Phys. Lett.* 91: 183518, 2007.

[5] B. Wood, J.B. Pendry, Metamaterials at zero frequency, *J. Phys. Condens. Matter.* 19: 076208, 2007.

[6] A. Sanchez, C. Navau, J. Prat-Camps, D.X. Chen, Antimagnets: controlling magnetic fields with superconductor-metamaterial hybrids, *New J. Phys.* 13: 093034, 2011.

[7] F. Gomory, M Solovyov, J. Souc et al., Experimental realization of a magnetic cloak, *Science* 335: 1466–1468, 2012.

[8] F. Gomory, M. Solovyov, J. Souc et al., Supporting online materials for Experimental realization of a magnetic cloak, *Science* 335, 1466–1468 (2012)

[9] S. Guenneau, C. Amra, D. Veynante, Transformation thermodynamics: Cloaking and concentrating heat flux, *Opt. Express* 20: 8207, 2012.

[10] F. Yang, Z.L. Mei, T.Z. Jin et al., DC electric invisibility cloak, *Physics Review Letters* 109: 053902, 2012.

[11] T. Han, T. Yuan, B. Li, C.W. Qiu, Homogeneous thermal cloak with constant conductivity and tunable heat localization, *Sci. Rep.* 3: 1593, 2013.

[12] T. Han, C.-W. Qiu, Transformation Laplacian metamaterials: Recent advances in manipulating thermal and dc fields, *J. Opt.* 18: 044003, 2016.

[13] M. Raza, Y. Liu, E.H. Lee, Y. Ma, Transformation thermodynamics and heat cloaking: a review, *J. Opt.* 18: 044002, 2016.

[14] T. Han, H. Ye, Y. Luo et al., Manipulating dc currents with bilayer bulk natural materials, *Advanced Materials* 26: 3478–3483, 2014.

[15] G.V. Alekseev, *Invisibility Problems in Acoustics, Optics and Heat Transfer*, Dalnauka, Vladivostok, 2016.

[16] A.N. Tikhonov, V.Ya. Arsenin, *Solutions of Ill-Posed Problems*, Halsted, New York, 1977.

[17] S. Xu, Y. Wang, B. Zhang, H. Chen, Invisibility cloaks from forward design to inverse design, *Sci. China Inf. Sci.* 56: 120408, 2013.

[18] B.I. Popa, S.A. Cummer, Cloaking with optimized homogeneous anisotropic layers, *Phys. Rev. A* 79: 023806, 2009.

[19] S. Xi, H. Chen, B. Zhang, B.-I. Wu, J.A. Kong, Route to low-scattering cylindrical cloaks with finite permittivity and permeability, *Phys. Rev. B* 79: 155122, 2009.

[20] R.V. Brizitskii, A.S. Savenkova, Inverse extremum problems for Maxwell's equations, *Comput. Math. Math. Phys.* 50: 984–992, 2010.

[21] G.V. Alekseev, R.V. Brizitskii, The theoretical analysis of boundary control extremal problems for Maxwell's equations, *J. Appl. Ind. Math.* 5: 1–15, 2011.

[22] G.V. Alekseev, Cloaking of material objects by controlling the impedance boundary condition for Maxwell's equations, *Doklady Phys.* 58: 482–486, 2013.

[23] G.V. Alekseev, V.A. Levin, Optimization method of searching parameters of an inhomogeneous liquid medium in the acoustic cloaking problem, *Doklady Phys.* 59: 89–93, 2014.

[24] G.V. Alekseev, Cloaking via impedance boundary condition for 2-D Helmholtz equation, *Appl. Anal.* 93: 254–268, 2014.

[25] G.V. Alekseev, Stability estimates in the problem of cloaking material bodies for Maxwell's equations, *Comput. Math. Math. Phys.* 54: 1788–1803, 2014.

[26] G.V. Alekseev, Analysis and optimization in problems of cloaking of material bodies for the Maxwell equations, *Differ. Equations* 52: 361–372, 2016.

[27] G.V. Alekseev, Yu.E. Spivak, Analysis of the 3D acoustic cloaking problems using optimization method, *J. Phys. Conf. Ser.* 722: 012002, 2016.

[28] D.S. Anikonov, V.G. Nazarov, I.V. Prokhorov, Visible and invisible media in tomography, *Doklady Math.* 56: 955–958, 1997.

[29] D.S. Anikonov, V.G. Nazarov, I.V. Prokhorov, *Poorly visible media in X-Ray tomography,* VSP, Utrecht, 2002.

[30] G.V. Alekseev, V.A. Levin, An optimization method for problems of thermal cloaking of material bodies, *Doklady Physics* 61: 546–550, 2016.

[31] G.V. Alekseev, V.A. Levin, D.A. Tereshko, Optimization analysis of the thermal cloaking problem for a cylindrical body, *Doklady Physics* 62: 71–75, 2017.

[32] G.V. Alekseev, V.A. Levin, D.A. Tereshko, The optimization method in design problems of spherical layered thermal shells, *Doklady Phys.* 62: 465–469, 2017.

[33] G.V. Alekseev, Analysis of a two-dimensional thermal cloaking problem on the basis of optimization, *Comput. Math. Math. Phys.* 58: 478–492, 2018.

[34] R. Poli, J. Kennedy, T. Blackwel, Particle swarm optimization: an overview, *Swarm Intel.* 1: 33–57, 2007.

Photonic integration from devices to sub-systems

Hot-Electron Photodetections by Planar Nanostructures

Cheng Zhang[1,2], Dong Ma[3,*], and Xiaofeng Li[1,2,*]

[1]College of Physics, Optoelectronics and Energy & Collaborative Innovation Center of Suzhou Nano Science and Technology, Soochow University, Suzhou 215006, China;
[2]Key Lab of Advanced Optical Manufacturing Technologies of Jiangsu Province & Key Lab of Modern Optical Technologies of Education Ministry of China, Soochow University, Suzhou 215006, China;
[3]School of Railway Transportation, Soochow University, Suzhou 215131, China.
*Corresponding Authors, E-mail: madong@suda.edu.cn (DM); xfli@suda.edu.cn (XL)

Abstract

There is an increasing interest in harvesting photoejected hot-electrons. However, the metallic nanostructures that excite surface plasmons to enhance photoemission of hot-electrons are complex with a high fabrication challenge. Here, we present two purely planar hot-electron photodetectors based on Tamm plasmons and microcavity, respectively. On resonance, the electric field is strongly increased in metal, leading to a high hot electron generation efficiency, a strong and unidirectional photocurrent and a photoresponsivity higher than that of the conventional nanostructured system.
KEY WORDS: Tamm plasmons; surface plasmons; microcavity; hot electrons

1. Introduction

Recently, there are vast attention on harvesting the energy carried by hot electron for various applications, e.g., photodetection, photovoltaics, etc. [1–3] The hot-electron photoconversion systems show a variety of benefits compared to the conventional semiconductor-based systems, including the high tunability on the resonance (into infrared band), the high energy concentration, the compatibility, and so on. Normally, the high-performance hot-electron photodetection relies strongly on the excitation of surface plasmons (SPs) from metallic nanostructures, which however are usually complex and challenging in fabrication. Planar systems which show a high compatibility with the current optoelectronic platforms and the ease of large-scale fabrication are highly desired. However planar systems without a delicate design always show the weak light-trapping capability. Advanced strategies which can substantially improve the optical performance of the planar systems are of great necessity for the application of hot-electron photoconversion devices.

In this study, we show two planar hot electron photodetector systems based on Tamm plasmons and microcavity, respectively [4, 5]. The former one integrates a distributed Bragg reflector with a metal/semiconductor/metal junction to strongly localize the incident light at the top metal and adjacent dielectric layers by exciting the Tamm plasmons. As a result, the top metal absorbs more than 87% of the incident light. The latter one sandwiches the transparent conductive oxide/ semiconductor/metal junction into two asymmetric Bragg reflectors and a transparent buffer layer. At the resonance, the electric field increases sharply and the absorption in metal reaches 92%, which is 21 times higher than that without the microcavity. In the two systems, the asymmetric absorption leads to a large unidirectional photocurrent with a photoresponsivity higher than the traditional systems based on surface plasmons. In addition, both of the planar systems show a narrow-band resonance with a high tunability, good resistance against the change of the incident angle, and the possibility for multiband photodetection.

References

[1] M. W. Knight, H. Sobhani, P. Nordlander, and N. J. Halas, Photodetection with active optical antennas, *Science*, 332: 702–704, 2011.

[2] C. Clavero, Plasmon-induced hot-electron generation at nanoparticle/metal-oxide interfaces for photovoltaic and photocatalytic devices, *Nat. Photon.*, 8: 95–103, 2014.

[3] T. P. White and K. R. Catchpole, Plasmon-enhanced internal photoemission for photovoltaics: theoretical efficiency limits, *Appl. Phys. Lett.*, 101: 073905, 2012.

[4] C. Zhang, K. Wu, Y. Zhan, V. Giannini, and X. Li, Planar microcavity-integrated hot-electron photodetector, *Nanoscale*, 8: 10323–10329, 2016.

[5] C. Zhang, K. Wu, V. Giannini, and X. Li, Planar hot-electron photodetection with Tamm plasmons, *ACS Nano*, 11: 1719–1727, 2017.

Polarization-insensitive 8-channel silicon DWDM Receiver

Chao Qiu[1], Yingxuan Zhao[1, 2], Aimin Wu[1*], Zhen Sheng[1], Haiyang Huang[1], Jun Li[1], Wei Li[1], Mingbin Yu[1] and Fuwan Gan[1]

[1]State Key Laboratory of Functional Materials for Informatics, Shanghai Institute of Microsystem and Information Technology, Shanghai 200050, China
[2]University of Chinese Academy of Science, Beijing 100049, China
*corresponding author, E-mail: `aiminwu@mail.sim.ac.cn`

Abstract

Both benefits and suffers from the large index contrast between Si and SiO_2, silicon photonics shows as a promising platform for next generation optical interconnections. By integrated a broadband silicon polarization-splitters and rotators (PSR) with arrayed-waveguide-gratings (AWG) and Germanium photodetectors (PDs, an integrated 8-channel silicon DWDM receiver is fabricated and polarization-insensitive operations at 10Gbps per channels is demonstrated.

1. Introduction

As a promising platform for next generation optical interconnection, silicon photonics has attracted a lot of attention because of the large index contrast between SiO_2 and Si layer which enables strong optical confinement and thus small device footprints, high integration density and low power consumption[Erreur ! Source du renvoi introuvable.Erreur ! Source du renvoi introuvable.]. However, the large birefringence lies in waveguides with strong optical confinement also poses great challenges to many applications, particularly for receivers. A polarization-diversity scheme has been proposed to address this issue[Erreur ! Source du renvoi introuvable.]. One of the key components in this scheme is polarization beam splitters (PBSs) and rotators (PSRs)[Erreur ! Source du renvoi introuvable.]. Tremendous efforts have been done in this field[Erreur ! Source du renvoi introuvable.,Erreur ! Source du renvoi introuvable.].

In this paper, an integrated silicon DWDM receiver is realized by combining a broadband PSR with silicon arrayed waveguide gratings(AWG) and Germanium photodetectors(PDs). Polarization insensitive operations at 10Gbps at all channels is demonstrated.

2. Device Structure and Operation Principle

Fig. 1 shows the microscope picture of the integrated silicon DWDM receiver. Input optical signal with random polarization states is coupled into the chip first with an inverse coupler, and then is split by a broadband silicon PSR into two TE modes. Two identical AWGs follow the PSR to realize the wavelength de-multiplexing, following with germanium photodetectors to realize optical-electrical conversion. The two polarization components are combined at PDs with waveguide-inputs from opposite directions. By combining the two output components from the PSR, polarization insensitive operations are realized.

Fig.2 shows the schematic of the broadband silicon PSR which comprise an adiabatic bi-level taper and a mode evolution coupler. The design is based on our previous work **Erreur ! Source du renvoi introuvable.**. The TE_0 mode passes through the device directly and outputs from the through port. For the TM_0 mode, it will be converted to the TE_1 mode first by the bi-level taper, and then coupled to the TE_0 mode in the cross port after passing through the counter-tapered coupler. To obtain a broad operation bandwidth, both the bi-level taper and mode-evolution counter-tapered coupler are optimized carefully.
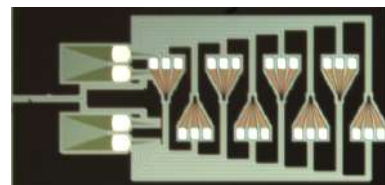
Figure 1: Microscope image of the integrated silicon DWDM receiver.
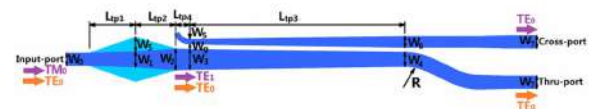
Figure 2: Schematic of the proposed PSR.

The 8-channel AWG is designed with a channel spacing of 3.2nm. 90nm/220nm bi-level tapers with its width linearly tapering from 0.45μm to 2.5μm were designed at the interface between arrayed waveguides and FPR region to reduce the modes mismatch loss. To reduce phase noises and sensitivity to fabrication errors, arrayed waveguides with a width of 1um are used in the array waveguide area. Arrayed waveguides with widths of 450nm were used at bends in order to maintain a small bending radius of 5μm.

The proposed device was fabricated through IME CMOS integrated silicon nano photonics process in

Singapore. SOI wafers with a top-silicon thickness(H) of 220 nm are used and a slab height(Hslab) of 90 nm is selected to be compatible with the standard fabrication process in the silicon photonic foundry.

3. Experiment Results

The measurement setup for the broadband PSR is shown in Fig. 3**Erreur ! Source du renvoi introuvable.**. The input polarization state was first set using a polarization-splitting prism with polarization controller (PC). After that, a straight silicon waveguide was used as a sample to align the output polarization plane with the input polarization. The output polarization state was set by tuning the linear polarizer system in the dashed box. For real samples, the polarization components of the output light were selected by rotating the polarizer correspondingly.

Figure 3: Experimental setup for on-chip PSR

Figure 4: (a)The measured spectra of the fabricated AWG;(b) The measured receiver photo response as a function of input wavelength for different input light polarizations.

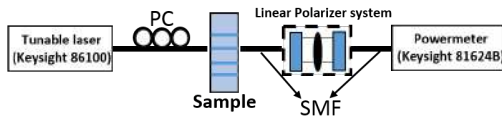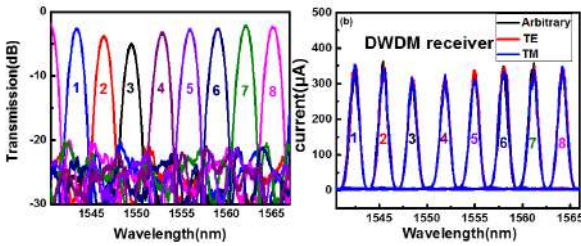Fig.4(a) shows the tested spectral for AWG. An insertion loss as low as 2.6dB and a crosstalk less than 18dB are obtained with the designed AWG. Fig.4(b) shows the tested results of the integrated DWDM receiver. Photocurrent responses of 8-channels with different input light polarization states including TE, TM and random polarization state were tested at wavelengths from 1540nm to 1565nm. A polarization-dependent loss between 1.2 and 1.8dB can be found. The responsivity of PDs is about 0.318A/W, including insertion losses from PSR and AWG. The dark current of PD is about 1.7μA.

Eye diagrams of eight de-multiplexed channels were finally measured with pseudorandom binary sequence (PRBS) signal at 10Gbps under the reverse bias of 2V. Input light with random polarization state was used in the test. The wavelength of each channel is also shown in Fig. 5.
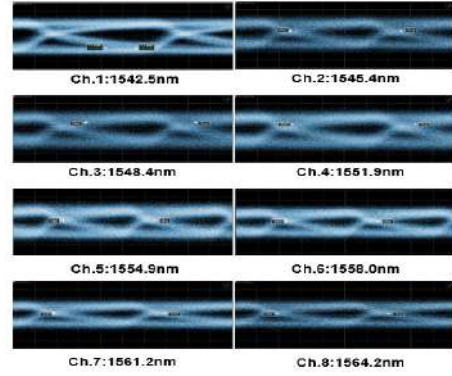
Figure 5: The measured 10 Gbps electrical eye diagrams of integrated DWDM receiver with random input polarization state.

4. Conclusions

A polarization-insensitive silicon DWDM receiver is demonstrated with 8-wavelength channels at 3.2nm spacing. The device includes a broadband silicon PSR based on bi-level taper and counter-tapered coupler, a 8-channel AWG and eight Germanium PDs. Operations at 10Gbps per channels is demonstrated.

References

[1] T. Baehr-Jones et al., Nature Photonics 6(4): 206-208, 2012.
[2] T. Tsuchizawa et al., IEEE IEEE Journal of Selected Topics in Quantum Electronics, 11:232-240, 2005.
[3] L. Chen, p. OW1C. 1,2013.
[4] Y. Ding et al., Opt. letters 38(8):1227-1229, 2013.
[5] J. Wang et al., Opt. Express, 22(23):27869-27879, 2014.
[6] X. Chen et al., Chinese Optics Letters, 2016.
[7] L. Liu et al. Opt. letters, 36:1059-1061, 2011.
[8] J. Wang et al., Opt. Express, 22(8):9395-9403, 2014.

Silicon Photonic Integrated Circuits for High-speed Modulation and Polarization-independent Bandwidth-variable Filtering

Lei Zhang[1,2], Sizhu Shao[1,2], Haoyan Wang[1,2], Linchen Zheng[1,2], Hao Jia[1,2], Jincheng Dai[1,2], Jianfeng Ding[1,2], Xin Fu[1,2], and Lin Yang[1,2]

[1]State Key Laboratory on Integrated Optoelectronics, Institute of Semiconductors, Chinese Academy of Sciences, Beijing 100083, China
[2]College of Materials Science and Opto-Electronic Technology, University of Chinese Academy of Sciences, Beijing China
*corresponding author, E-mail: zhanglei@semi.ac.cn

Abstract

We report the design and experimental results of silicon optical modulators and filters. The optical modulators are based on Mach-Zehnder interferometers. We demonstrate 100Gbps on-off keying (OOK) and 50Gbaud 4-level pulse amplitude modulation (PAM-4) modulations. The optical filters are based on asymmetrical directional couplers and 2nd-order microring resonators. We show polarization-independent optical bandpass filtering with the 3dB bandwidth varying from 37.5 to 100 GHz.

1. Introduction

Silicon photonics has been considered as one of the most promising candidates for the next 400 GbE optical transmission platform. Silicon optical modulator and tunable filter are two key components enabling the manipulation of field information of a light beam and improving spectral efficiency of the network. Here we report silicon optical modulators based on Mach-Zehnder interferometers for OOK and PAM-4 modulation. We also demonstrate a silicon optical filter based on asymmetrical directional coupler (ADC) and microring resonators (MRRs) to enable polarization-independent and bandwidth-variable filtering.

2. Silicon optical modulators

Carrier-depletion silicon modulators are widely employed because the carriers in the diode move by the drift effect, resulting high intrinsic electro-optic bandwidth. Figure 1(a) shows the schematic of the silicon Mach-Zehnder optical modulator [1-6]. The multi-mode interference (MMI) couplers are employed for light splitting and combining. Thermal tuning region is integrated on the phase shifter to compensate the fabrication error and to set the working condition. Figure 1(b) shows the cross section of the phase shifter. The height and width of the waveguide is 220 nm and 400 nm, and the slab thickness is 70 nm. The p- and n-doping concentrations are 1×10^{18}/cm^3 and 8×10^{17}/cm^3, respectively. The p-type region is to the right of the middle of the core with an offset of 40 nm. Figure 1(c) shows the microscope images of the modulators.
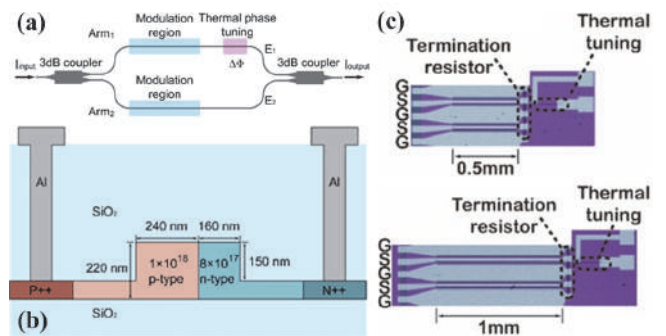
Figure 1: (a) Schematic of the silicon Mach-Zehnder optical modulator. (b) Cross section of the doped phase shifter. (c) Microscope images of the silicon optical modulators.

We drive the modulators to generate the optical OOK and PAM-4 signals. Figure 2 shows the eye diagrams of optical signals generated by the modulator with doped phase shifter length of 1mm and 0.5 mm. The OOK and PAM-4 optical signals generated by the 0.5mm modulators are measured to be up to 100 Gbps and 50 Gbaud, respectively.
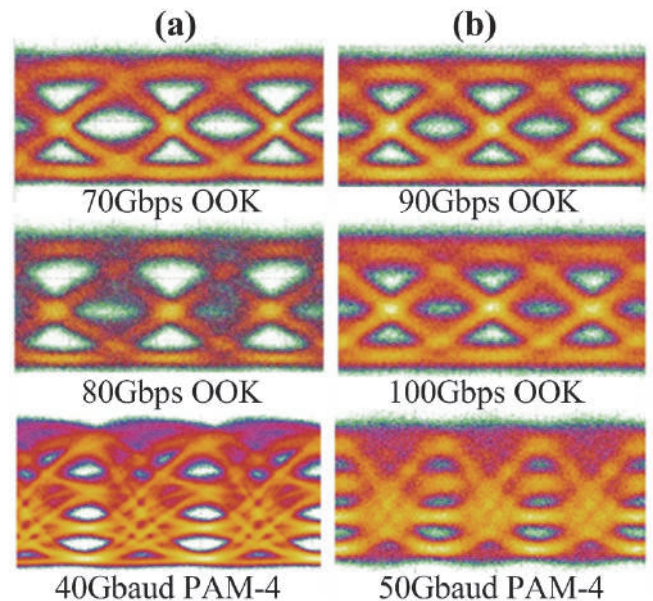
Figure 2: Eye diagrams of the silicon optical modulators with doped phase shifter of (a) 1 mm and (b) 0.5 mm.

3. Silicon optical bandpass filters

Optical bandpass filters with tunable central wavelength and adjustable bandwidth are essential to implement agile optical networks. Large free spectral range (FSR) is also desirable to allocate more WDM channels. Here we propose and demonstrate such an optical bandpass filter. As shown in Fig. 3(a), we employ polarization splitter and rotator (PSR) at both ends of the circuit to obtain polarization independence [7]. The PSR is based on asymmetrical directional coupler (ADC). For each optical filter in the two branches, we use two stages of 2nd-order MRRs with different radii to expand the FSR. We rely on the thermo-optic effect of silicon to tune the MRR. Each stage of the 2nd-order MRR is designed to have a flat-top response. The two flat-top responses of the two stages are intentionally slightly misaligned to adjust the bandwidth of the overall spectral response (Fig. 3(c)).
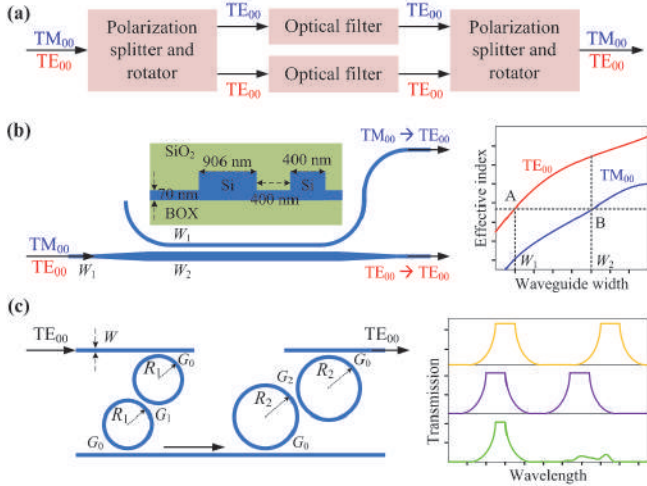
Figure 3: (a) Schematic of the optical filter. (b) Polarization splitter and rotator based on an asymmetrical directional coupler. (c) Optical bandpass filter based on cascading 2nd-order microring resonators.

As shown in Fig. 3(b), two orthogonal modes (TE$_{00}$, TM$_{00}$) are input at a narrow waveguide (W_1) and transformed to a wide waveguide (W_2). The width of the input waveguide and that of the narrow waveguide in the ADC (W_1) are both chosen to be 400 nm. The phase-matching condition is required to efficiently transform the optical energy of a mode in one waveguide to that of another mode in the adjacent waveguide [7]. Due to the width difference, the TE$_{00}$ modes in the two waveguides of an ADC have significantly different n_{eff}. Thus the TE$_{00}$ mode in the wide waveguide will keep propagating in it. In order to efficiently transfer the energy of TM$_{00}$ mode in the wide waveguide to the TE$_{00}$ mode in the narrow waveguide, W_2 is chosen to be 906 nm. We find the optimum the coupling length (Lc) to be 38 μm using the finite-difference time-domain (FDTD) simulations.

Figure 3(c) shows the schematic of the proposed tunable optical filter based on 2nd-order MRRs. Ring cavities in the 1st and 2nd stages have different radii of 7 μm and 10 μm, respectively. The output of the first stage acts as the input of the second stage. The gap spacing between the ring cavity and the straight waveguide G_0 is 200 nm for both stages. We

use the FDTD method to find the optimal value of the gap spacings between the two ring cavities (G_1 and G_2) to meet the maximally flat condition of second-order MRR [8]. The G_1 and G_2 are found to be 375 nm and 350 nm, respectively, for the two stages. All the four microring resonators have independent titanium nitride (TiN) heaters.
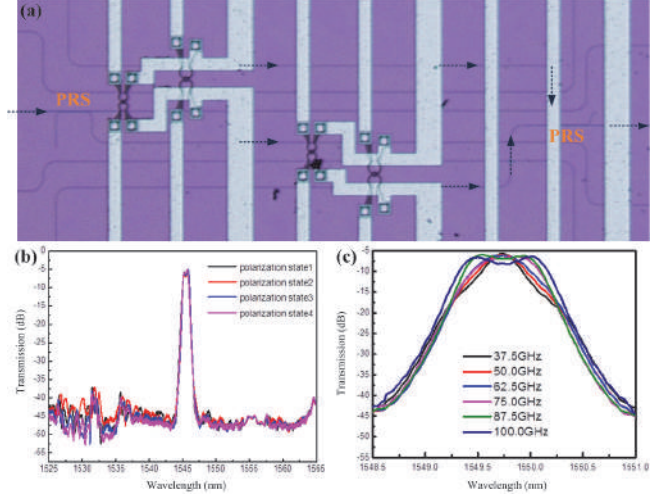
Figure 4: (a) Microscope image of the fabricated device. (b) Polarization-independent filtering responses. (c) The adjustment of the 3dB bandwidth.

The device is fabricated on an 8-inch silicon-on-insulator (SOI) wafer. The experimental results are shown in Fig. 4. We adjust the polarization states of the input light randomly and find negligible penalty on the transmission and low polarization-dependent loss (PDL) (Fig. 4(b)). The FSR is larger than 40 nm. Figure 4(c) shows the results of 3dB bandwidth adjustment from 37.5 GHz to 100 GHz with a step of 12.5 GHz via intentional misalignment of the two stages. The insertion loss varies from −5.44 dB for 37.5GHz bandwidth to −7.89 dB for 100GHz bandwidth.

4. Conclusion

We report high-speed traveling-wave silicon Mach-Zehnder modulators showing 100Gbps OOK and 50Gbaud PAM-4 modulations. We propose and demonstrate a polarization-independent optical bandpass filter with variable bandwidth (37.5 GHz to 100 GHz) and large FSR (> 40nm).

References

[1] J. Ding *et al*., Opt. Express 20 (3), 3209–3218 (2012).
[2] J. Ding *et al*., Opt. Express ss 20 (7), 7081–7087 (2012).
[3] S. Shao *et al*., Opt. Express, 25(19) 23003–23013 (2017).
[4] L. Zheng, *et al*., Opt. Lett., 42(11), 2213–2216 (2017).
[5] J. Ding *et al*., Opt. Lett., 42(8), 1636–1639 (2017).
[6] S. Shao *et al*., Opt. Commun., 407(15), 271–274 (2018).
[7] J. Wang *et al*., Opt. Express 22(4), 4137–4143 (2014).
[8] L. Zhang *et al*., J. Lightwave Technol. 35(24), 5347–5360 (2017).

Magnetoplasmonic Biosensors Based on Low Loss Magnetism Oxide Thin Films

Jun Qin[1,2], Tongtong Kang[1,2], Yan Zhang[1,2], Bo Peng[1,2], Longjiang Deng[1,2], and Lei Bi[*1,2,]

[1]National Engineering Research Center of Electromagnetic Radiation Control Materials, University of Electronic Science and Technology of China, Chengdu 610054, China
[2]State Key Laboratory of Electronic Thin-Films and Integrated Devices, University of Electronic Science and Technology of China, Chengdu, 610054, China
*corresponding author, E-mail: bilei@uestc.edu.cn

Abstract

Magneto-optical surface plasmon resonance (MOSPR) biosensors based on ferromagnetic metals such as Ni, Fe, Co show high sensing performance. However, the high optical loss of ferromagnetic metals compromise the performance of the device. In this presentation, we propose a MOSPR sensor based on low loss magnetism oxide thin films. The device is composed of Au/Ce:YIG/YIG/SiO$_2$/TiN multilayer thin films grown on silica substrates. Simultaneous transverse magneto-optical Kerr effect (TMOKE) and index sensitivity enhancement have been obtained, originated from the hybridization of waveguide mode in dielectric layer and SPR mode on gold surface. We experimentally demonstrate a high figure of merit (FOM) 964 ± 150 RIU^{-1} and low limit of detection (LOD) 4.13×10^{-6} RIU at wavelength 650 nm, which is 17.8 folds and 16 folds higher compared to standard Au SPR, respectively.

1. Introduction

MOSPR devices, where are ferromagnetic material is incorporated to the near field of a plasmonic nanostructure, has been widely studied due to their high figure of merit, low limit of detection for biosensing applications. Ferromagnetic metals such as Fe [1], Ni [2], and Co [3] are widely used for MOSPR sensors due to the strong magneto-optical effect and simplicity of fabrication. However, the high free electron concentration of the ferromagnetic metals brings about high optical loss, which compromises the device sensing performance. Compared to the ferromagnetic metals, dielectric magnetism oxides such as Bi or Ce doped Y$_3$Fe$_5$O$_{12}$ show strong magneto-optical effect and low optical loss in the visible to near infrared wavelength. Furthermore, the dielectric can support waveguide mode, which provide more design ideas for high FOM MOSPR biosensors. Here, we experimentally and theoretically demonstrate a high FOM magnetoplasmonic biosensor based on low loss magnetism oxide. Through properly design the structure parameters of the metal-insulator-metal (MIM) sandwich structure, we can achieve the coupling of MIM mode and SPR mode in our device. The strong

coupling leads to simultaneous TMOKE and surface sensitivity enhancement, which achieve a high theoretical FOM 39600 RIU^{-1} at wavelength of 650 nm. We also experimentally demonstrate a high FOM 964 ± 150 RIU^{-1} at the same wavelength, which is about 17.8 folds higher than standard Au SPR sensors. Another key property, limit of detection (LOD), is also measured by our home-made setup which reaches 4.13×10^{-6} RIU. The LOD of our MOSPR sensor is 16 folds lower compared to Au SPR sensor measured on the same setup.

2. Simulation and experiment results

The schematic of our device is shown in Fig. 1a. The device stack is Au/Ce:YIG/YIG/SiO$_2$/TiN thin films grown on both-side-polished silica substrates. A silica prism with index-matching oil (n=1.45) is used to excite MIM or SPR modes in the device. The magnetic field is perpendicular to the incident plane with p polarized incident light, *i.e.* the TMOKE geometry. In order to confirm the thickness of each layer, we measure the scanning tunneling electron microscope (STEM) of the cross section of our device, shown in Fig. 1b. The thickness of each layers are TiN 43 nm, SiO$_2$ 8 nm, YIG 53 nm, Ce:YIG 45 nm, and Au 14 nm, respectively. A prism coupling system has been used to measure the bulk sensing of the MIM device. The sensing solutions with index from 1.33 to 1.37 are the mixture of water and glycerinum with mass ratios of 0%, 7%, 15%, 22% and 30%. From Fig. 1c, a maximum FOM 964 ± 150 RIU^{-1} is obtained with index 1.33. Compare to the theoretical FOM of SPR sensor, the MIM MOSPR sensor shows a 17.8 folds enhancement. Next, in Fig. 1d, we measure the signal to noise ratio, which can extract the LOD of our device. The LOD of the MIM MOSPR and SPR devices are 4.13×10^{-6} RIU and 6.79×10^{-5}, respectively. The MOSPR device shows 16 times enhancement of the LOD compared to the SPR device. In theory, we optimize the thickness of Au and Ce:YIG to obtain the maximum FOM, as shown in Fig. 1e. The optimized thickness of Au and Ce:YIG are 10 nm and 48 nm with a large FOM of 39600 RIU^{-1}. We simulate the dispersion relation of the device, show in Fig. 1f. We clearly see two coupled modes

with large Rabi splitting as the deep blue area shows. The two black dash lines are the dispersion curve for independent MIM and SPR modes, which have a cross over, corresponding to the mode hybridization. Hence, the high FOM is result from the hybridization of MIM and SPR modes, which improves the TMOKE and sensitivity simultaneously.

3. Conclusions

In summary, we have designed and fabricated a novel MOSPR biosensor based on low loss magnetism oxides. A high FOM of 964 ± 150 RIU^{-1} is experimentally obtained at wavelength 650 nm. The high FOMs is originated from the WG-SPR hybrid mode excited by the prism coupling. Our work provides the new ideas for high performance magentoplasmonic biomedical sensing based on low loss magnetism oxides.

References

[1] D. Regatos, D. Fariña, A. Calle, A. Cebollada, B. Sepúlveda, G. Armelles, and L. M. J. Lechuga, Au/Fe/Au multilayer transducers for magneto-optic surface plasmon resonance sensing, *J. Appl. Phys.* 108: 054502, 2010.

[2] N. Maccaferri, K. E. Gregorczyk, T. V. de Oliveira, M. Kataja, S. van Dijken, Z. Pirzadeh, A. Dmitriev, J. Akerman, M. Knez, and P. Vavassori, Ultrasensitive and label-free molecular-level detection enabled by light phase control in magnetoplasmonic nanoantennas, *Nat. commun.* 6: 6150, 2015.

[3] B. Caballero, A. García-Martín, and J. C. Cuevas, Hybrid Magnetoplasmonic Crystals Boost the Performance of Nanohole Arrays as Plasmonic Sensors, *ACS Photonics* 3: 203-208, 2016.
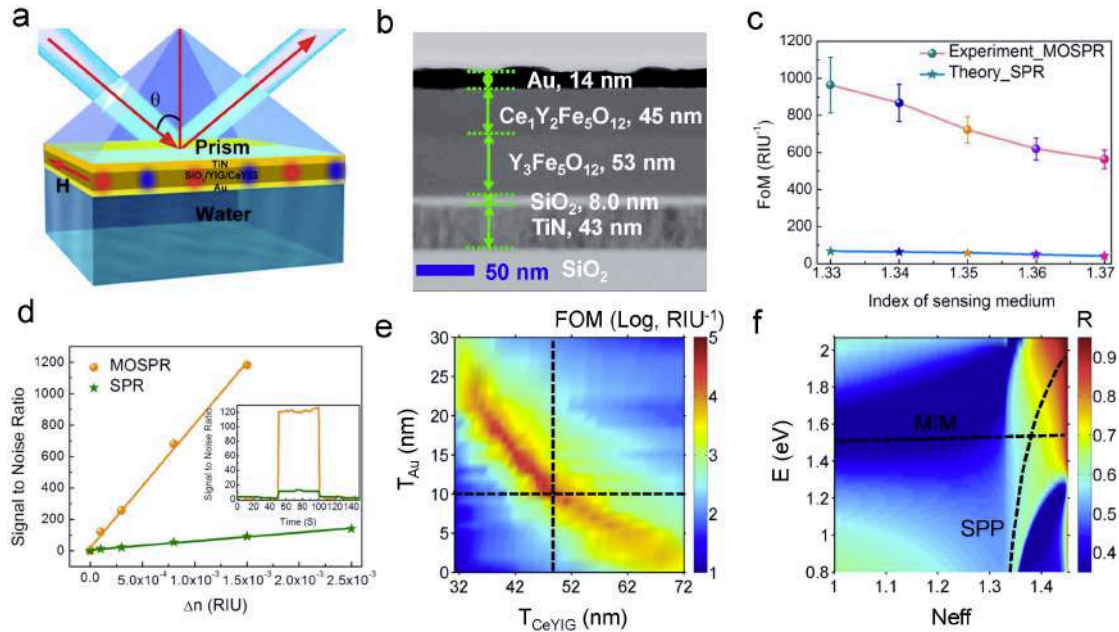
Figure 1: (a) Schematic of the MOSPR device. (b) The cross section STEM image of the fabricated device. (c) Experimental FOM as function of the sensing solution indices. (d) Measured signal to noise ratio as function of sensing medium index variation for both the MOSPR and SPR devices. The inset shows the real time SNR variation as changing the sensing medium index by 1×10^{-4}. (e) Optimized structure parameters of Au and Ce:YIG thickness with a maximum FOM of 39600 RIU^{-1} is obtained at Au 10 nm and CeYIG 48 nm, respectively. (f) Calculated dispersion relation of the MOSPR device, showing the hybridization of MIM and SPR modes.

Silicon-organic Hybrid Waveguide for High Performance Photonic Integrated Devices

Xiuyou Han[1*], Sicheng Yang[1], Linghua Wang[2], Shuhui Bo[3], Zhenlin Wu[1], and Mingshan Zhao[1]

[1]School of Optoelectronic Engineering and Instrumentation Science, Dalian University of Technology, Dalian 116024, China
[2]Fujian Institute of Research on the Structure of Matter, Chinese Academy of Sciences, Fuzhou 350002, China
[3]Key Laboratory of Photochemical Conversion and Optoelectronic Materials, Technical Institute of Physics and Chemistry, Chinese Academy of Sciences, Beijing 100190, China
*corresponding author, E-mail: xyhan@dlut.edu.cn

Abstract

This paper reports the recent work in our group about the silicon-organic hybrid waveguide for improving the performance of silicon photonic integrated devices. The athermal silicon-on-isolator (SOI) based microring resonator and arrayed waveguide grating are realized by overlaying organic polymer with negative thermal-optic coefficient on the SOI waveguide. The electro-optic modulator with wide bandwidth and low half-wave voltage is implemented by filling organic polymer with high electro-optic coefficient in the slot of SOI waveguide.
Key Words: Silicon-organic Hybrid Integration, Microring Resonator, AWG, Electro-optic Modulator.

1. Introduction

Photonic integration is becoming the main stream of photonic technology and has many applications in next-generation optical networks, optical interconnects, coherent transceivers, and microwave photonic signal processing system, etc. Silicon photonics is currently the most promising technology to realize large scale photonic integration, leveraging mature high-yield CMOS fabrication and offering the poetential of photonic-electronic co-integration on the same chip [1].

A lot of silicon-on-isolator (SOI) based photonic integrated devices have been demonstrated, such as microring resonstor (MRR), arrayed waveguide grating (AWG), optical true time delay line, polarization rotator, etc. However, since silicon has a quite large thermo-optic (TO) coefficient (dn/dT=1.8×10⁻⁴/°C), external heaters or coolers have to be employed to stabilize the chip temperature. This element takes extra space and consumes extra power. Organic polymer, as a promising photonic material with molecule-level designable property, has a large negative TO coefficient, which can be utilized to counterbalance the SOI waveguide core's positive TO coefficient [2, 3].

On the other hand, the electro-optic modulator (EOM) with wide bandwidth and low half-wave voltage is desired for optical fiber communication system, optical controlled phase array antenna system and photonic based satellite payload. However, second-order nonlinearities are absent in bulk silicon due to inversion symmetry of the crystal lattice. Hence, current silicon-based modulators have to rely on free-carrier depletion or injection in p–n, p–i–n or metal-oxide-semiconductor structures. This leads to various tradeoffs when realizing fast and energy-efficient devices with small footprint. The organic polymer can achieve a very high electro-optic (EO) coefficient by dispersing EO chromophore in a polymer matrix[4]. By filling EO polymer material in the slot of SOI waveguide, the EOM with high bandwidth and low half-wave voltage can be realized.

In this paper, the recent work in our group about the silicon-organic hybrid (SOH) waveguide for improving the performance of silicon photonic integrated devices is addressed. In Section 2, the athermal SOI based MRR and AWG is presented. In Section 3, the work of the EOM by filling EO polymer in the silicon slot waveguide is described. Finally, a conclusion is given in Section 4.

2. Athermal SOI waveguide devices

MRR, with the multiple function and compact size, is a key unit for the large scale integration photonic circuits. However, the resonant wavelength of MRR based devices is sensitive to the temperature, which is a great obstacle in real applications. By overlaying a polymer cladding on SOI waveguides, the athermal MRR can be realized [2]. The operational principle can be explained as follows.

The temperature dependence of the resonant wavelength of MRR can be expressed as

$$\frac{d\lambda_m}{dT} = \left(\frac{1}{L}\cdot\frac{dS}{dT}\right)\frac{\lambda_m}{n_{eff}} = \left(n_{eff}\cdot\alpha_{sub} + \frac{dn_{eff}}{dT}\right)\frac{\lambda_m}{n_g}, \quad (1)$$

where λ_m is the resonant wavelength, n_{eff} is the effective index of waveguide, S is the optical length defined as $S=n_{eff}L$, α_{sub} is the substrate expansion coefficient, n_g is the group index of waveguide. The athermal condition is achieved when Eq. (1) equals to zero. Normally silicon is used as substrate and the thermal expansion coefficient of Si is on the order of 10^{-6} (α_{sub} =2.6×10⁻⁶/°C); dn_{eff}/dT depends on the TO coefficient of the core material and cladding material. According to the TO coefficient of the core silicon of 1.8×10⁻⁴/°C and the cladding polymer of -(1~3)×10⁻⁴/°C, athermal SOI waveguides can be achieved by optimizing the

waveguide structures.

The standard SOI structure with a height of 220 nm is used for designing the athermal waveguides. Polymer PSQ-LH with a large TO coefficient of $-2.4\times10^{-4}/°C$ and low loss at 1550 nm is chosen as the cladding material. The narrow SOI waveguides as shown in Fig. 1 (a) are fabricated by deep UV lithography with standard CMOS fabrication technology. Fig.1 (b) shows the measured transmission spectra of a MRR for temperatures from 10°C to 50°C. By linear fitting of one resonant wavelength at different temperatures, the wavelength temperature dependence $d\lambda/dT$ is extracted. As shown in Fig.1 (c), the wavelength temperature dependence of the 350 nm-width MRR is reduced from 54.2 pm/°C to -4.9 pm/°C after overlaying a polymer PSQ-LH.
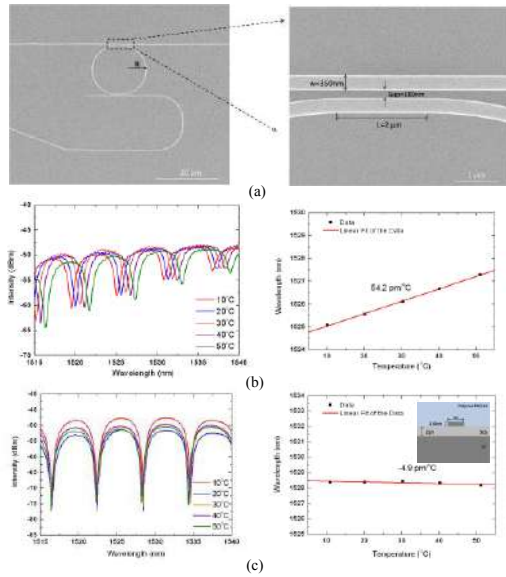

Figure 1: (a) SEM pictures of fabricated SOI MRR. Transmission spectra of MRR at different temperatures (b) before and (c) after overlaying a polymer.
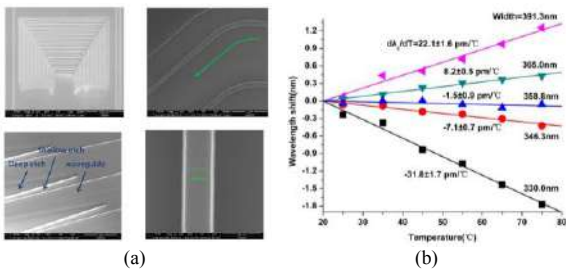
Figure 2: (a) SEM pictures of critical parts of fabricated SOI AWG. (b) Temperature dependence of the peak wavelength after polymer overlay for different waveguide widths.

The athermal SOI based AWG with polymer PSQ-LH as cladding is also designed and fabricated[3]. Considering the fabrication of SOI waveguide by the deep UV lithography and inductively coupled plasma–reactive ion etching, the trapezoidal waveguide model is chosen to design the athermal AWG. Fig. 2 (a) shows the SEM pictures of the critical parts of the AWG. Fig. 2(b) shows the temperature dependence of the peak wavelength of one of the AWG central channels with narrowed arrayed waveguide overlaid with polymer PSQ-LH. The lowest temperature dependence was obtained for a waveguide width of 358.8 nm, where the temperature dependence of the filter peak wavelength was

successfully reduced from above 65.4 pm/°C to -1.5 pm/°C, i.e., more than 1 order of magnitude lower than that of the normal SOI AWGs.

3. Silicon-organic hybrid electro-optic modulator

SOH waveguide combines the advantage of CMOS compatible fabrication of silicon waveguide and the high EO coefficient and low dielectric constant of organic polymer [4]. Fig. 3 (a) shows the slot waveguide cross section of EOM filled with EO polymer. From the simulated results, it can be seen that the optical field and the microwave field are both confined in the slot region, which can enhance the electro-optic modulation effect and improve the performance of bandwidth and $V_{\pi}{\cdot}L$. Fig. 3(b) and (c) give the confinement factor of optical field with different slot widths and different waveguide widths.
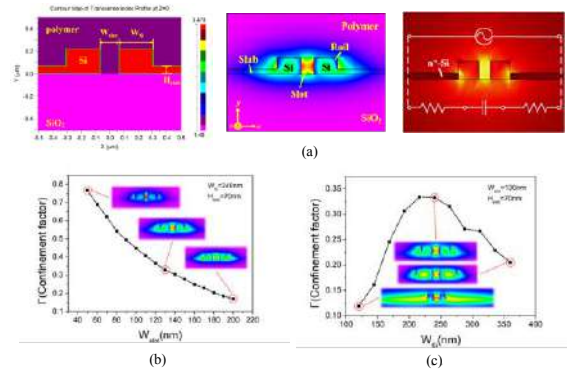
Figure 3: SOH waveguide based EOM. (a) Cross section of slot waveguide filled with polymer and simulated optical and microwave fields; Confinement factor of optical field with (b) different slot widths and (c) different waveguide widths.

4. Conclusions

SOH waveguides for athermal SOI devices and EOM have been presented, which shows the potential to improve the performance of silicon based photonic integrated circuit.

References

[1] J. E. Bowers, et al, Recent advances in silicon photonic integrated circuits, *Proc. of SPIE*, 9774, 977402, 2016.

[2] J. Teng, et al, Athermal silicon-on-insulator ring resonators by overlaying a polymer cladding on narrowed waveguides, *Optics Express*, 17, pp.14627-14633, 2009.

[3] L. Wang, et al, Athermal AWGs in SOI by overlaying a polymer cladding on narrowed arrayed waveguides, *Applied Optics*, 51, pp. 1251-1256, 2012.

[4] Y. Yang, et al. Enhanced electro-optic activity from the triarylaminophenyl-based chromophores by introducing heteroatoms to the donor, *J. of Materials Chemistry C*, 3, pp. 5297-5306, 2015.

Electromagnetics

Dynamic Control of a split ring resonator via pneumatic levitation

Xutao Tang[1], Iryna E. Khodasevych[2], and Wayne S. T. Rowe[1]

[1]School of Engineering, RMIT University, Melbourne, Australia
[2]School of IT & Engineering, Melbourne Institute of Technology, Melbourne, Australia
*corresponding author, E-mail: wayne.rowe@rmit.edu.au

Abstract

A pneumatically levitated azimuthally rotating split ring resonator system is proposed to provide dynamic tunability. A single split ring resonator is placed on a levitation platform controlled by pneumatic force. Changes in orientation of the split ring due to the continuous spinning motion relative to a second static split ring forms a broadside coupled resonator with dynamically swept resonant frequency. The speed and acceleration of the frequency sweep can be controlled by the applied pneumatic pressure and the interchangeable platform design. The contactless pneumatic levitation concept and corresponding dynamically tunable resonant frequency results are validated by both simulations and measurements.

1. Introduction

The implementation of a split ring resonator (SRR) as a key electromagnetic (EM) component in microwave devices, transmission line structures, metamaterials and metasurfaces has seen rapid expansion over the past few years. The SRR consists of a conductive wire loop with a small gap between each end. The position of the gap, and hence the mutual orientation of the SRR in the incident EM field causes variance in its resonant frequency. This property can be utilized to design tunable RF components such as a frequency configurable antenna [1, 2]. However in this technique the tunability of the RF component is limited by the static orientation of the printed split rings. Dynamically changing the orientation of the SRR will provide a swept resonant frequency akin to scanning systems such as radar and sensors. Traditional methods of frequency tuning involve adding active components into the SRR gap (e.g. [3]), requiring extra electronic components and bias line not native to the structure of SRR, causing potential interference to operation. Pneumatic structure have also been proposed, however may be susceptible to alignment tolerances [4, 5].

A contactless platform controlled by pneumatic force is proposed to change the orientation of an SRR relative to an incident EM wave. This approach is designed to encounter less EM interference than traditional tuning methods as the SRR is manipulated solely by air and no metallic bias/control line are required. The levitation platform restricts the movement of the SRR to azimuthal rotation only, therefore the resonant frequency sweep results from the orientation of the spinning SRR in the incident EM wave relative to a static broadside coupled SRR.
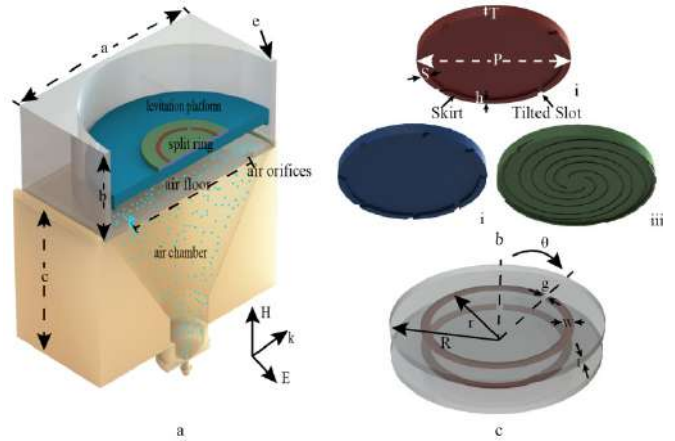
Figure 1: (a) Pneumatic levitation platform schematic cross section (b) Three levitation platforms designs (c) Split ring resonator configuration.

2. Pneumatic levitation concept

Fig. 1(a) shows a cross-section of the pneumatic levitation platform. Air is delivered from a tube at the base of the structure and is temporarily stored in the air chamber. The retarded air is well distributed in the cone-shaped chamber, and air flows through eighteen evenly spaced 0.65 mm diameter air orifices on the air floor layer of the structure in a circular geometry. This enables the levitation platform to be lifted by uniform air pressure across its bottom surface.

Fig. 1(b) depicts the underside of three levitation platform designs. The skirt is designed to trap air and create an air pressure difference above and below the platform. The air escaping from underneath the levitation platform flows through the small gap between the side of the platform and wall of the outside confinement structure in Fig. 1(a). This creates a laminar flow, securing the platform axially in the center. A rotational momentum is created by an even number of angular slots were symmetrically cut on the skirt to provide new paths for air flow, and spin the platform on its axis. The slots are cut at 45 degrees to the tangent of the circle. Polymethyl methacrylate (PMMA) is used as the building material for the levitation structure due to its optical transparency (to observe operation) and easy machinability. Fabrication of the pneumatic levitation platform was performed with a micro-miller (CPM 4030-Isel) to ensure precision.

The SRR is secured on to the top surface of the levitation platform, hence the orientation/location of the gap will be

synchronized with the platform. A schematic of the SRR is given in Fig. 1(c). A 0.508 mm thick Rogers RT/duriod 5880 substrate with relative permittivity ε_r = 2.2 and loss tangent δ = 0.0009 was used, and the SRR trace is chemically etched in 17 μm thick copper cladding.

3. Experimental results and discussions

An experimental set-up used to quantify the dynamic transmission response of the pneumatically levitated SRR with different applied air pressures. An air pump is used to create the initial air pressure, which is connected to a tank large enough to convert the pulsed air generated by pistol based pump to smooth, linear air pressure. A valve attached on top of the tank controls the pressure level contained in the tank. A pressure meter detects the static pressure parallel to the outlet of the tank as the air is delivered via a tube to a small hole in a WR-284 rectangular waveguide located directly below the levitation structure. Exhaust holes are placed above the levitation module to regulate the pressure inside the waveguide. By controlling both the air pump and valve on the tank, levitation of the platform can be achieved and the spinning speed can be controlled and the dynamic transmission response is recorded by the vector network analyzer.

The spinning speed of the different levitation platforms was determined by analyzing the experimental transmission results. According to the Bernoulli's principle:

$$\frac{v^2}{z} + gz + \frac{p}{\rho} = \text{constant} \tag{1}$$

where v = fluid flow speed at the chosen point, g = acceleration of gravity, z = elevation, p = static pressure, and ρ = density of the fluid, the total pressure applied to the levitation platform is the sum of the static and dynamic pressure. By injecting more air from the tank, the total pressure applied to the levitation platform increases, and the static pressure counter-balances the weight of the platform. The extra pressure converts to rotational momentum as it escapes through the open angular slots around the skirt. The more pressure that is applied to the system, the more angular momentum it produces; therefore the faster the platform rotates. All three levitation platforms rotate faster as the pressure increases and decelerate when the pressure is further increased due to variable air curtain accumulated. The structures require a different minimum pressure in order to commence rotation and have a distinct sensitivity to the applied pressure.

ANSYS HFSS was used to predict the resonant response of the coupled SRRs as a result of the pneumatically induced spinning motion. Static simulations and dynamic measurements are shown in Fig. 2(a) and (b) respectively and show good congruence. Experimentally, the resonance of the coupled SRR can be dynamically tuned over 2.68 GHz to 2.38 GHz as the top ring rotates from 0° to 180°, with the results reversing from 180° to 360°.
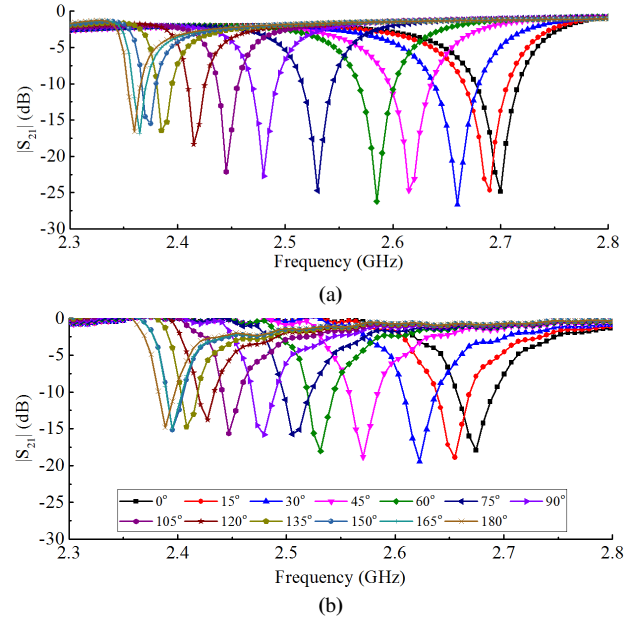
Fig. 2. $|S_{21}|$ of the coupled SRRs at a different rotation angle θ from 0° to 180° (a) simulation (b) measurement.

4. Conclusions

A novel pneumatic levitation system is presented as a means of dynamically controlling the relative rotation of broadside coupled SRRs. A frequency sweep due to the orientation change of SRRs is demonstrated, with control over the spinning speed using pneumatic force and platform design. This contactless air controlled system can minimize the EM interference introduced by traditional frequency tuning methods requiring metallic structures or bias lines in frequency scanning systems like radar/sensing applications.

References

[1] S. Sam, L. Sungjoon, Electrically Small Eighth-Mode Substrate-Integrated Waveguide (EMSIW) Antenna With Different Resonant Frequencies Depending on Rotation of Complementary Split Ring Resonator, *IEEE Trans. on Ant. & Prop.* 61: 4933-4939, 2013.

[2] C. Guclu, J. Perruisseau-Carrier, O. Civi, Proof of Concept of a Dual-Band Circularly-Polarized RF MEMS Beam-Switching Reflectarray, *IEEE Trans. on Ant. & Prop.* 60: 5451-5455, 2012.

[3] I. V. Shadrivov, S. K. Morrison, Y. S. Kivshar, Tunable split-ring resonators for nonlinear negative-index metamaterials, *Optics Express* 14: 9344-9349, 2006.

[4] I. E. Khodasevych, I. V. Shadrivov, D. A. Powell, W. S. T. Rowe, A. Mitchell, Pneumatically switchable graded index metamaterial lens, *Applied Physics Letters* 102: 31904, 2013.

[5] I. E. Khodasevych, W. S. T. Rowe, A. Mitchell, Reconfigurable fishnet metamaterial using pneumatic actuation, *Progress In Electromagnetics Research B* 38: 57-70, 2012.

Accurate Bi-static RCS Measurement for Scaled Object using Noise Illuminated W-band Radiometer

Ki In Kim[1], Ji Mi Jeong[2], Yong Hoon Kim[1,2*],

[1]School of Mechanical Engineering, Gwangju Institute of Science and Technology, Gwangju, Korea
[2]millisys Inc., Gwangju, Korea
*Corresponding author, E-mail: yhkim@gist.ac.kr

Abstract

This paper is proposed the new type of RCS measuring method and system for scaled objects. Unlike any other conventional radar-based RCS measuring system using wideband transmitter-receiver i.e network analyzer, in the large RF chamber, the proposed method uses W-band radiometer receiver with noise illumination and X-Y scanner which is compact and easy operation in small size room. The measured RCS accuracy for reference metal object of rectangular plate, cylinder and sphere is smaller than 1.0 dB in the azimuth scan angle of +/-5 degrees.

1. Introduction

The RCS (Radar Cross Section) is the fictional area produced by an echo of the incident radar signal from the target and this reflection and scattering quantity is very important for the "stealth" platform design like fighter, battle ship and armored moving vehicle. In this paper, we have proposed new type RCS measuring method and system using millimeter-wave radiometer for scaled targets. The advantage of this proposed system shows high sensitivity and visualization for the measurement of scattering from the platform, therefore, one can not only identify the reflection signal as RCS, but also measure the very weak interference signal between complex geometry structure, and easy operation at small laboratory room.

2. RCS measurement using microwave radiometer

Microwave radiometer [1] measures the brightness temperature T_B including emissivity of the target and reflectivity from illumination source as following equation (1) and (2). The radiometer converts the received noise like signal P_{target} to voltage as "brightness temperature" i.e. radiometer measures the brightness temperature for the target and this is the proportional with the echo signal, can be determined the RCS of the target considering emissivity and conductivity of target.

$$P_{target} = KT_B B , \qquad (1)$$

$$T_B = \varepsilon T_{obj} + \rho T_{source} , \qquad (2),$$

where P_{target} is the received thermal power, K is Boltzmann's constant, B is radiometer bandwidth, T is

temperature of object and illumination source, respectively. ε is emissivity, ρ is the conductivity. The RCS of target σ_{target} can be define as followings;

$$\sigma_{target} = \frac{P_{target}}{C_f} \qquad (3),$$

where C_f is the calibration factor and it is the function of wavelength, and geometric factor .

3. W-band radiometer for RCS measurement

3.1.1. RCS measuring system

The RCS measuring system is bi-static type with illumination source and high gain radiometer receiver. The receiver part consist of lens, metallic reflector, feed antenna, low noise amplifier, bandpass filter, square law detector and DC amplifier [2][3] as shown in Fig. 1 and Fig.2.
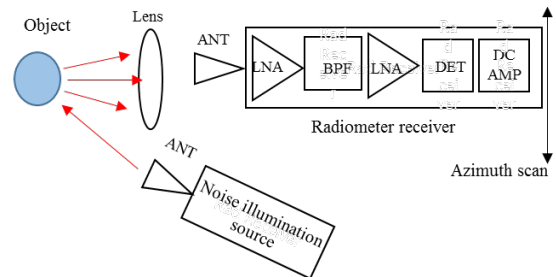

Figure 1: Geometry of bi-static RCS measuring system
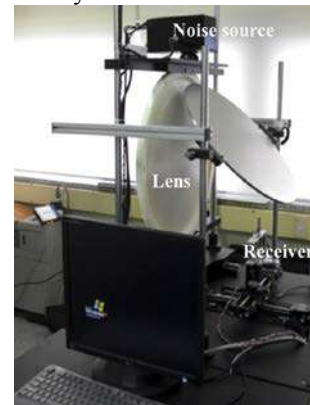
Figure 2: Photo of RCS measuring system with noise illumination. (by courtesy millisys Inc.)[4]

3.1.2. Noise source for illumination

The noise source is built using a high gain amplifier, with waveguide terminator at input port and connected an isolator for good output matching. To adjust the illuminated power level, a variable attenuator of 30 dB is mounted on output port of noise source.

3.2. RCS for reference targets

To verify the proposed concept of RCS measurement, first, we have measured the RCS for reference targets with sphere, cylinder, and rectangular plane plate of 30 mm, 60 mm, respectively. The reference targets can be simulated accurately based on the theory and this result is compared with the measurement result. The simulation and measurement RCS results are shown in Fig. 3 for 30 mm, and 60 mm size case, respectively. The accuracy of RCS is smaller than 1.0 dB in azimuth scan angle +/- 5 degrees.
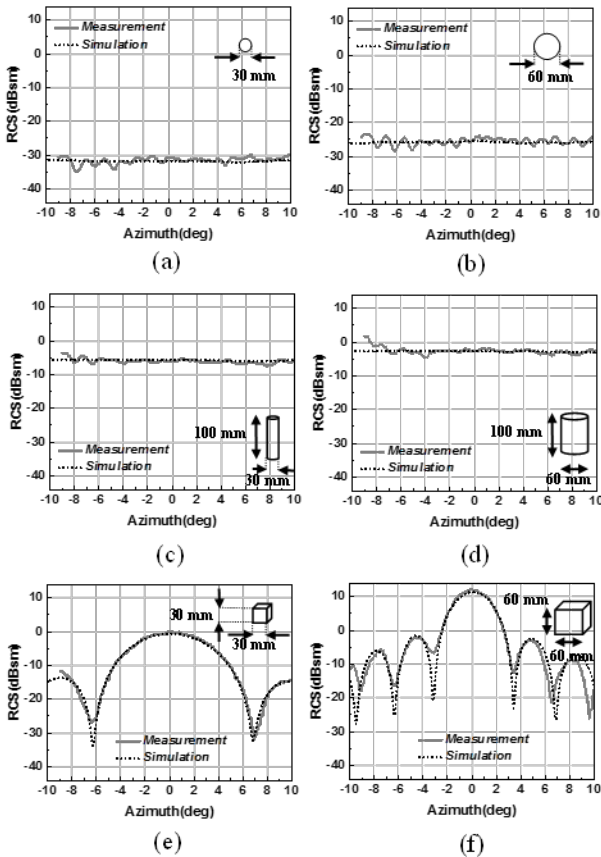
Figure 3: Measured and simulated RCS of metallic spheres, cylinders, and plane squares plate with noise illumination.

3.3. RCS for model airplane

After verify the RCS with the reference targets, the scaled target of model airplane is measured. The model is made by plastic, but we have painted over the surface with good conductive metal spray. The RCS image for differential view angle for model airplane are shown in Fig. 4. The RCS result of model airplane is also good compare with the simulation.
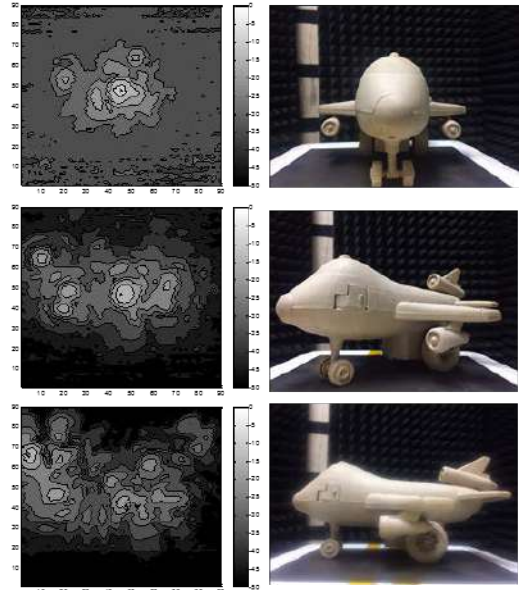
Figure 4: Photo of RCS measuring system.

4. Discussion and Conclusions

The RCS accuracy is very important in the measuring system and through our experiments, we have understand that is depended on the accuracy for the modeling of simulation target and precise experiment, especially, exact alignment between target and electrical center of lens antenna in vertical, horizontal position, and in target height.

5. Conclusions

We have propose first time, as authors know, new type of bi-static RCS measuring system using microwave radiometer for scaled target. This proposed system can be used for quick stealth platform design in small size space.

References

[1] F.T.Ulaby, R.K.Moore, A.K.Fung, *Microwave Remote Sensing*, Addison-Wesley Publishing, ch. 4, 1981.

[2] W-G Kim, N-W Moon, M. K Singh, H-K Kim and Y-H Kim, Characteristic analysis of aspheric quasi-optical lens antenna in millimeter-wave radiometer imaging system, *Applied Optics*, Vol.52, No.6, pp.1117-1225, Feb. 2013

[3] W.-G. Kim, N.-W. Moon, H.-K. Kim and Y.-H. Kim, Linear polarization sum imaging in passive millimeter-wave imaging system for target recognition, *PIER (Progress in Electromagnetics Research)* Vol. 136, pp.175-193, Jan., 2013.

[4] http://www.millisys.com

Kron-Branin modelling for Multilayer PCB with SMA connectors

Zhifei Xu[1], Blaise Ravelo[1]

[1]Normandy University UNIROUEN, ESIGELEC, IRSEEM,
Technopole du Madrillet, Avenue Galilée, BP 10024, F-76801 Saint Etienne du Rouvray, France

Abstract

Abstract: This paper develops an equivalent Kron-Branin (KB) model for the SMA connector and multilayer interconnect structure. The structure under study consists of SMA combined with two port terminations on a six-layer PCB structure. The KB equivalent graph is established to compute S-parameters, the results are compared to a full wave 3D simulation tool.

1. Introduction

With the increase of signal data rate, the interconnect discontinuity effects are playing a key role on the printed circuit board (PCB) performance [1]. Interconnect discontinuity needs to be analyzed during the PCB design phase. The discontinuities between, vias, SMA connector and PCB traces can affect the signal integrity (SI) in high speed signal transmission [1-2]. In this paper, the feasibility study of the unfamiliar Kron-Branin (KB) modelling [3] to multilayer PCB with SMA connector is elaborated.

2. Kron-Branin (KB) modelling methodology

2.1. Structure description

The structure under study shown in Fig. 1, inspired from [2], consists of two SMAs mounted vertically on a 6-layer PCB Cu-metallized and with dielectric relative permittivity ε_r=4.4 and height h=3.8 mm. The two interconnects with metallization thickness t=35 μm and width w=0.5 mm are connected by a blind via. The interconnects are placed on layer 3 and 4. Layers 1, 2, 3, 4 and 6 are signals layers. Layer 5 is a ground plane. Ports 1 and 2 are terminated by 50 Ω resistive impedance.

Figure 1: (a) Geometry of SMA connector and (b) Cross section of the structure under study.

Figure 2: Perspective view of the structure understudy.

2.2. KB modelling

2.2.1. SMA and via models

The part of SMA on the top layer can be considered as a coaxial cable with length to 9.52 mm, the inner dielectric substrate is Teflon with ε_r=2.1. The central pin can be represented as the inductance effect. From top to bottom layer except layer 5, at layer 5 the central pin will generate capacitive effects as showed in Fig. 3. The via is modelled by LC lumped π – network representing the pads and via hole [3].

Figure 3: (a) SMA model in Figure 2 and (b) via model

2.2.2. KB equivalent topology

The KB modelling starts with structural segmentation analysis, the basic elements constituting the graph are:

- $R_{1,2}$=50 Ω are the resistive loads connected to the ports on the interconnects,
- Via is modelled by LC lumped π – network,
- Interconnects are parametrized by their characteristic impedance $Z_{1,2}$ and propagation constant $\theta_{1,2}$, the internal sources e_m with $m = \{1,2,3,4\}$ indicate the Branin's coupling sources. Based on these primitive segments, the KB equivalent topology is established.

Figure 4: KB equivalent topology of the structure shown in Fig. 1

2.3. Analytical equations

The branch impedance tensor can be easily established based on the impedance on each branch of the topology, the inner matrix in (1) represents the branch impedance of various parts of the topology.

$$Z_{ab\_branch} = \begin{bmatrix} [Z_{sma1}] & & & & \\ & [Z_{PCB}] & & & \\ & & [Z_{via}] & & \\ & & & [Z_{PCB}] & \\ & & & & [Z_{sma2}] \end{bmatrix}_{(1)}$$

The analytical implementation of Kron's method needs to change the branch into the mesh space to extract the mesh current I.

$$\left[I^n(j\omega) \right] = \left[Z_{\mu\upsilon\_mesh}(j\omega) \right]^{-1} \left[E_{\mu\_mesh}(j\omega) \right] \quad (2)$$

From branch space to mesh space, the connection matrix (space change matrix) based on the relation between branch current and mesh current (3)-(4) is obligatory.

$$\begin{matrix} i_1 = 1I_1 + ... + 0I_{11} \\ \vdots \\ i_{17} = 0I_1 + ... + 1I_{11} \end{matrix} \Rightarrow C = \begin{bmatrix} 1 & 0 & 0 & 0 & 0 \\ 0 & 1 & 0 & 0 & 0 \\ 0 & 1 & 0 & 0 & 0 \\ 0 & 0 & 1 & 0 & 0 \\ 0 & 0 & 1 & 0 & 0 \\ 0 & 0 & 0 & 1 & 0 \\ 0 & 0 & 0 & 1 & 0 \\ 0 & 0 & 0 & 0 & 1 \end{bmatrix} \quad (3)$$

The mesh impedance can be obtained, same for the sources. Then, by combining (2) and (4), the mesh current can be extracted and applied to do analysis.

$$Z_{\mu\upsilon\_mesh} = C' Z_{ab\_branch} C$$
$$E_\mu = E_b C_m^b \quad (4)$$

3. Validation results

The structure was designed in CST MWS. The SMA connector model was imported from Molex$^@$. The simulation was performed with 50 million mesh cells on a workstation with about 6 hours. The results comparison from DC to 5 GHz is shown in Fig. 5. The KB modelled S-parameters are rather in good correlation with ADS and CST simulations with differences caused by the interconnects parametrization.

Figure 5: S parameter comparison

4. Conclusions

An unfamiliar modelling of multilayer PCB integrating SMA connectors is developed. The detailed description of the model and obtained results will be added in the final version of this paper.

Acknowledgements

References

[1] F. Jun, Y. Xiaoning, J. Kim, B. Archambeault, and A. Orlandi, "Signal integrity design for high-speed digital circuits: Progress and directions," *IEEE Trans. Electromagnetic Compatibility*, vol. 52, no. 2, pp. 392-400, May 2010.

[2] A. Ciccomancini Scogna, "Signal integrity analysis and physically based circuit extraction of a mounted SMA connector," *Interference Technology*, *EMC Design & Software*, pp. 1-5, 2008.

[3] Z. Xu, Y. Liu, B. Ravelo and O. Maurice, "Modified Kron's TAN Modeling of 3D Multilayer PCB", *Proc. of 11th Int. EMC Compo 2017*, St. Petersburg, Russia, 4-8 July 2017, pp. 242-247.

Kron-Branin modelling for Multilayer PCB with SMA connectors

Zhifei Xu[1], Blaise Ravelo[1]

[1]Normandy University UNIROUEN, ESIGELEC, IRSEEM,
Technopole du Madrillet, Avenue Galilée, BP 10024, F-76801 Saint Etienne du Rouvray, France

Abstract

Abstract: This paper develops an equivalent Kron-Branin (KB) model for the SMA connector and multilayer interconnect structure. The structure under study consists of SMA combined with two port terminations on a six-layer PCB structure. The KB equivalent graph is established to compute S-parameters, the results are compared to a full wave 3D simulation tool.

1. Introduction

With the increase of signal data rate, the interconnect discontinuity effects are playing a key role on the printed circuit board (PCB) performance [1]. Interconnect discontinuity needs to be analyzed during the PCB design phase. The discontinuities between, vias, SMA connector and PCB traces can affect the signal integrity (SI) in high speed signal transmission [1-2]. In this paper, the feasibility study of the unfamiliar Kron-Branin (KB) modelling [3] to multilayer PCB with SMA connector is elaborated.

2. Kron-Branin (KB) modelling methodology

2.1. Structure description

The structure under study shown in Fig. 1, inspired from [2], consists of two SMAs mounted vertically on a 6-layer PCB Cu-metallized and with dielectric relative permittivity ε_r=4.4 and height h=3.8 mm. The two interconnects with metallization thickness t=35 μm and width w=0.5 mm are connected by a blind via. The interconnects are placed on layer 3 and 4. Layers 1, 2, 3, 4 and 6 are signals layers. Layer 5 is a ground plane. Ports 1 and 2 are terminated by 50 Ω resistive impedance.

Figure 1: (a) Geometry of SMA connector and (b) Cross section of the structure under study.

Figure 2: Perspective view of the structure understudy.

2.2. KB modelling

2.2.1. SMA and via models

The part of SMA on the top layer can be considered as a coaxial cable with length to 9.52 mm, the inner dielectric substrate is Teflon with ε_r=2.1. The central pin can be represented as the inductance effect. From top to bottom layer except layer 5, at layer 5 the central pin will generate capacitive effects as showed in Fig. 3. The via is modelled by LC lumped π – network representing the pads and via hole [3].
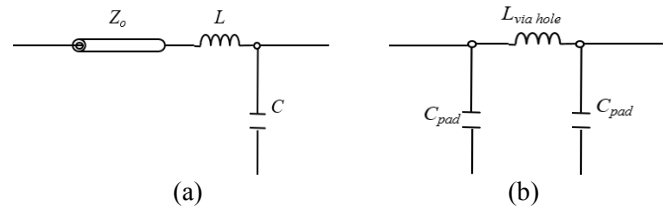

Figure 3: (a) SMA model in Figure 2 and (b) via model

2.2.2. KB equivalent topology

The KB modelling starts with structural segmentation analysis, the basic elements constituting the graph are:

- $R_{1,2}$=50 Ω are the resistive loads connected to the ports on the interconnects,
- Via is modelled by LC lumped π – network,
- Interconnects are parametrized by their characteristic impedance $Z_{1,2}$ and propagation constant $\theta_{1,2}$, the internal sources e_m with $m = \{1,2,3,4\}$ indicate the Branin's coupling sources. Based on these primitive segments, the KB equivalent topology is established.
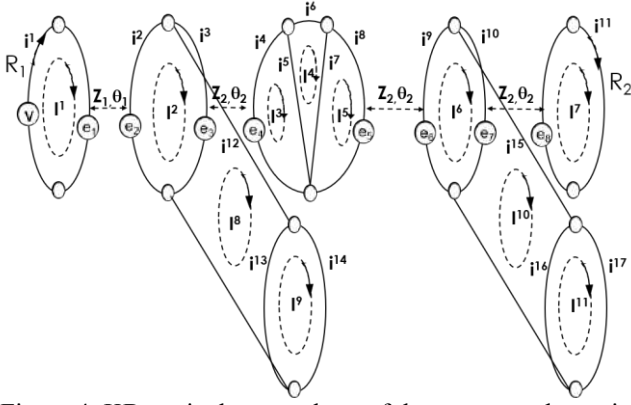
Figure 4: KB equivalent topology of the structure shown in Fig. 1

2.3. Analytical equations

The branch impedance tensor can be easily established based on the impedance on each branch of the topology, the inner matrix in (1) represents the branch impedance of various parts of the topology.

$$Z_{ab\_branch} = \begin{bmatrix} [Z_{sma1}] & & & & \\ & [Z_{PCB}] & & & \\ & & [Z_{via}] & & \\ & & & [Z_{PCB}] & \\ & & & & [Z_{sma2}] \end{bmatrix}_{(1)}$$

The analytical implementation of Kron's method needs to change the branch into the mesh space to extract the mesh current I.

$$\left[I^n(j\omega) \right] = \left[Z_{\mu\nu\_mesh}(j\omega) \right]^{-1} \left[E_{\mu\_mesh}(j\omega) \right] \quad (2)$$

From branch space to mesh space, the connection matrix (space change matrix) based on the relation between branch current and mesh current (3)-(4) is obligatory.

$$\begin{matrix} i_1 = 1I_1 + ... + 0I_{11} \\ \vdots \\ i_{17} = 0I_1 + ... + 1I_{11} \end{matrix} \Rightarrow C = \begin{bmatrix} 1 & 0 & 0 & 0 & 0 \\ 0 & 1 & 0 & 0 & 0 \\ 0 & 1 & 0 & 0 & 0 \\ 0 & 0 & 1 & 0 & 0 \\ 0 & 0 & 1 & 0 & 0 \\ 0 & 0 & 0 & 1 & 0 \\ 0 & 0 & 0 & 1 & 0 \\ 0 & 0 & 0 & 0 & 1 \end{bmatrix} \quad (3)$$

The mesh impedance can be obtained, same for the sources. Then, by combining (2) and (4), the mesh current can be extracted and applied to do analysis.

$$Z_{\mu\nu\_mesh} = C' Z_{ab\_branch} C$$
$$E_\mu = E_b C_m^b \quad (4)$$

3. Validation results

The structure was designed in CST MWS. The SMA connector model was imported from Molex@. The simulation was performed with 50 million mesh cells on a workstation with about 6 hours. The results comparison from DC to 5 GHz is shown in Fig. 5. The KB modelled S-parameters are rather in good correlation with ADS and CST simulations with differences caused by the interconnects parametrization.

Figure 5: S parameter comparison

4. Conclusions

An unfamiliar modelling of multilayer PCB integrating SMA connectors is developed. The detailed description of the model and obtained results will be added in the final version of this paper.

Acknowledgements

References

[1] F. Jun, Y. Xiaoning, J. Kim, B. Archambeault, and A. Orlandi, "Signal integrity design for high-speed digital circuits: Progress and directions," *IEEE Trans. Electromagnetic Compatibility*, vol. 52, no. 2, pp. 392-400, May 2010.

[2] A. Ciccomancini Scogna, "Signal integrity analysis and physically based circuit extraction of a mounted SMA connector," *Interference Technology, EMC Design & Software*, pp. 1-5, 2008.

[3] Z. Xu, Y. Liu, B. Ravelo and O. Maurice, "Modified Kron's TAN Modeling of 3D Multilayer PCB", *Proc. of 11th Int. EMC Compo 2017*, St. Petersburg, Russia, 4-8 July 2017, pp. 242-247.

Research on EMP Environment of SG-III Facility

MengCui1[1,2], Jin Han Bing[1,2] ,Jiang Yuansheng[1,2], Xuzhiqian[1,2],Zheng Wanguo[3]

[1] Department of Engineering Physics, Tsinghua University, Beijing, China, 100084
[2] Key Laboratory of Particle & Radiation Imaging, Ministry of Education, Beijing, China, 100084
[3] Laser Fusion Research Center, China Academy of Engineering Physics, Miangyang 621900, China
*Meng Cui, E-mail: mengcui@tsinghua.edu.cn

Abstract

In the high power laser-target matter interaction process within the high power laser facility, the movement of hot electron can excite high power electromagnetic pulse with electric field amplitude up to 10,000 V/m and frequency of GHz level. The measurement research and numerical simulation of the EM environment in high power laser facility SG III is introduced in this paper.

1.   Introduction

Electromagnetic pulse (EMP) has been found during the interaction of laser pulses and solid targets, which may cause electromagnetic interference problems, such as interfering or damaging electronic equipment and diagnostics and data loss.

For example, in experiments of Titan short-pulse laser facility, researchers observed high-level EMP with a broad frequency up to GHz[1]. Energetic electrons are produced in laser p lasma interaction, and a small fraction of these electrons escape the target. It is believed that escaping electrons are the main source of EMP [1,2], the gamma ray radiate EMP is smaller then this one.

2 Numerical Simulation with PIC method

2.1   Simulation of Laser-Plasma Interaction Producing Hot Electrons

The generation of EMP involves many complicated physical mechanisms and hasn't been understood clearly. It's suggested that transient current carried out by escaped electrons or target polarizationcould be important EMP contributions. Besides, the time scale of EMP generation is from fs to ns level, and the spatial scale is from the magnitude of μm to the magnitude of m. So to simulate the whole process is difficult to achieve.

In this paper, EMP related to electrons emission is studied. Considering main physical effects, the whole process is divided into three stages for analysis and the physical model is illustrated in Figure 1. Electrons of plasma get accelerated by absorbing the energy of laser pulses and become energetic. The hot electrons produced in the laser focal spot expand in all directions, some of which are ejected from the target in vacuum. The separation of positive charge and negative charge forms a strong electrostatic field on the target surface confining further emission of electrons. Major part of electrons ejected from the target are decelerated and then accelerated reversely back to the target under the electrostatic field. Only a small part electrons are energetic enough to overcome the potential barrier, escape from the target and propagate to the chamber, which could be called escaped electrons. The escaped electrons flow in the vacuum chamber and strike the chamber wall inducing large transient current and giant EMP. The simulations are based on the physical model and divided into three steps, as shown in Figure2 .
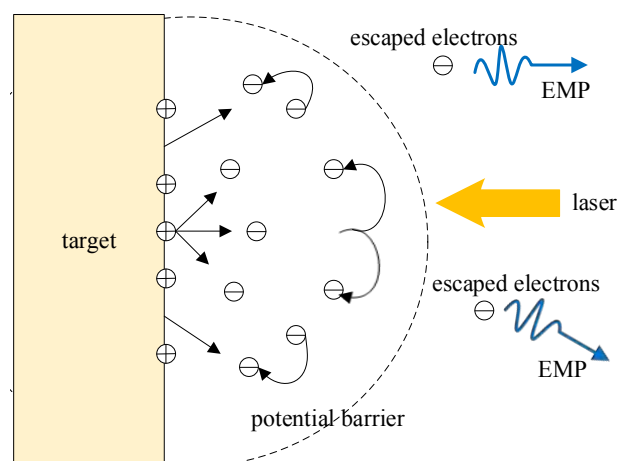

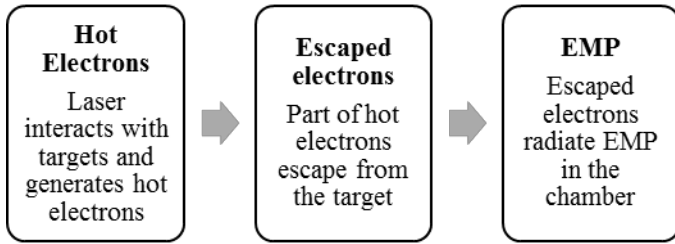Figure 1: Physical model of EMP generated by the laser-target interaction

Figure 2. The steps of simulation

2.2 Simulation of EMP radiated by escaped electrons

It's widely accepted that escaped electrons is the main source of EMP, but exact mechanism remains unclear yet. Analytical and experimental results demonstrated that the movement of the electrons in the target chamber and the transient current induced by electrons hitting the target wall contribute to the generation of EMP [3, 4]. In this section, given the number of and the energy of escaped electrons obtained from Section 3, EMP associated to electrons emission is simulated. A 2D-EMPIC code, which is a two dimension PIC code for EMP calculation, is developed for the simulation.

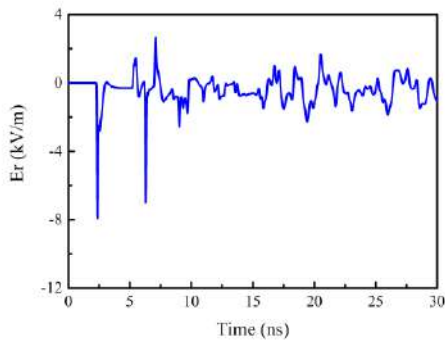Simulation result of EMP in target chamber is in figure3.

Figure 3: Electric field in time domain

3   Measurement Results

We developed magnetic field sensor and an electric field sensor, based on the Mobius loop model and the equivalent charge distribution method. They play an important role in high power laser EMP environment measurement. The environment of   target chamber and target room are measured using these two kind of sensors. Figure 4 shows the result in target room.
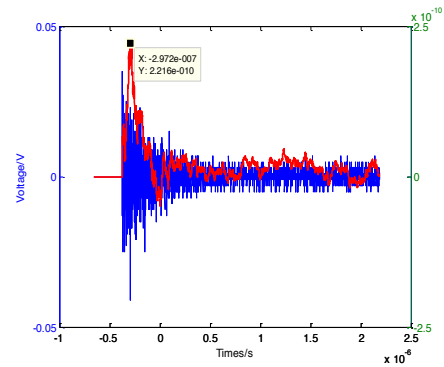
Figure 4: EMP measured in target room

4   Conclusion

The EMP environment is accordance with the format of the power density of high power laser, the target and the interaction format of the laser-target kind. The amplitude of electric field in target chamber is about 10kV/m and the amplitude of electric field in target room is about kV/m when there is window on the chamber. All electric equipment in these areas must be designed specially in order to increase the EMC level.

References

[1] C. G. Brown, E. Bond, T. Clancy, S. Dangi, D. C. Eder, W. Ferguson, etal., "Assessment and Mitigation of Electromagnetic Pulse (EMP) Impacts at Short-pulse Laser Facilities," Sixth International Conference on Inertial Fusion Sciences and Applications, Parts 1-4, vol. 244, p4-8,2010.

[2] J. L. Dubois, F. Lubrano-Lavaderci, D. Raffestin, J. Ribolzi, J. Gazave, A. C. L. Fontaine, et al., "Target charging in short-pulse-laser–plasma experiments," Physical Review E, vol. 89,013102-1-15, 2014.

[3] F. N. Beg, A. R. Bell, A. E. Dangor, C. N. Danson, A. P. Fews, M. E. Glinsky, et al., "A study of picosecond laser–solid interactions up to 1019 W_cm−2," Physics of Plasmas, vol. 4, p447-452, 1997.

[4] M. G. Haines, M. S. Wei, F. N. Beg, and R. B. Stephens, "Hot-Electron Temperature and Laser-Light Absorption in Fast Ignition," Physical Review Letters, vol. 102, 045008-1-4, 2009.

Information Content of Images

S. L. Vesely[1], C. A. Dolci[2] S. R. Dolci[3] A. A. Vesely[3],

[1]ITB-CNR, Milan, Italy
[2]Politecnico di Milano, Italy
[3]Milan, Italy
*corresponding author, E-mail: `sara.vesely@cnr.it`

Abstract

Extraction of information from images is often hampered by the ineffective definitions of information content as well as by the growing image storage capabilities and by the multifarious processing algorithms themselves. Sometimes it is suggested that some duality/reciprocity principle of physics may help encapsulate useful imaging parameters. In our opinion for imaging purposes geometry is a better background than optimization. We compare the customary duality concepts with the corresponding projective notion, and identify nonlinear features with the "useful parameters".

1. Introduction

Nobody would deny that human beings acquire a great deal of information on the external world through the eyes. Still, although the informal interpretation of seen images depends on the way they form, the link between the visual information they carry and the process by which the received signals get their spatial appearance is seldom scrutinized.[1] Informally, electromagnetic lenses and mirrors are deemed "to collect all rays from the points of an object into the corresponding points on a plane" rather that "to shape a received signal into a spatial manifestation of the outer world". To spell the core problem, no fundamental distinction is made between image formation by a vitreous sphere and rendering of a given picture by whatever algorithm can be easily implemented on a computer. Often, a similarity relationship between things and their icons is taken for granted. Moreover, the observed patterns are believed to be quite independent from the carrier frequency and received band-pass of the lighting, exactly as if the imaged things had been known beforehand in their entirety. In everyday life this is mostly acceptable, because the viewed scene is integrated with other sensations and with previous experience. However, settling for pattern recognition schemes and disregarding implementation of antennas design doesn't necessarily advance exploratory surveys. Indeed, when looking into a microscope, or at a radar picture of another planet, effects beyond similitude transformation can creep in and go unnoticed. Vignetting and Moiré are examples of linear effects, but now and then distortions and effects due to active, perhaps new responses also occur. Finally, although an underlying structure is needed to appreciate information, this is rather scattered over the raw data than encoded in the theoretical laws passed down. Thus, whenever data not complying with the trusted interpretation are filtered out, something is lost. Censoring undecided data is allowed in the first step of analysis, and perhaps within a highly speculative theoretical framework. Taking it over in technical applications and in innovation as well entails the risk of withering the scientific approach altogether. Anyway, it tends to level out the differences between *image* and *representation of a theoretical structure* or process, making modern image reconstruction techniques a hybrid handling of data. In contrast, we propose to interpret raw images according to geometry as a logical-deductive system in Euclid's own sense. We believe that that geometrical encoding of raw images may help distinguish between features dependent from observations conditions and active responses of matter by logical means,[1] and may in turn enrich scientific theories. Finally, antennas design could go beyond the actual constraints if a logical underpinning of geometric transformations allowed "to see with different eyes" and to transform images so one can avail of experience. We trace projective duality with this purpose in mind.

2. Forms of the Matter and their Volumes

The conception that the form of matter is a primary property amalgamated with some other properties is very old, and rests on image recognition. The extra qualification is glossed over, that the *hylomorphic doctrine* doesn't suppose the substance to be homogeneously distributed throughout its volume, as it is explicitly stated within the mechanics of continuous bodies. In natural philosophy the primary properties pertain to the things per se, while the secondary ones are not universal, and in addition depend on the specific circumstances under which they are perceived. During the genesis of exact sciences, the reductionist assumption was made, that the secondary properties can be derived from the primary ones, that thus assume a more fundamental role. In an attempt to achieve independence from the perceptual experience by reducing the secondary properties to attributes of the things, Locke went back to the atomic philosophy of Democritus, and tried to merge it with the Aristotelian doctrine. A formidable task, if one bears in mind that Aristotle

---

[1] The significance of disentangled non-linearities should be disclosed by means other than the purely optical ones.

himself had rejected Democritus' ideas. In Locke's times, the concept of form was still not severed from the space occupied by a material body. Rather, while causes were divided into formal and material,[2] form and substance were considered inseparable components of matter. In addition, doubts were cast on the possibility to exhaust our space. In fact, the existence of imponderable fluids filling up the space proved difficult to dismiss. It took a while to conceive that the form can be dissociated from the volume it occupies and moved like a bare reference frame through an emptied region of space. Newton shaped mechanics as a dualistic theory by sharply separating the two independent mechanistic principles of matter and motion. He himself tackled the matter-motion dualism by assuming that even solid bodies are rare and porous. Since he believed that the matter of all things is ultimately composed of unobservable, immutable, hard particles, while the forces shape the observed forms as well as the hierarchical structure of the world from the tiniest to astronomical scales,[3][2] for his immediate descendants matter altogether vanished into short-ranged mutual attractions and repulsions. In Faraday's times, a notion of chemical activity mingled with immaterialism came to the fore, and henceforth duality started to concern the space and its fields.

3. Force Fields

Some theories of electricity and magnetism, starting with Ampère's one, do without fields and refer back to the ontological meaning of "physical space" Plotinus had given to Euclid's geometry. Admitting that such Euclidean void space exists, the Newtonian disposition to move in it is evoked only at the locations of material bodies, i.e. at a distance. Incidentally, precisely this argument was used from Newton's peers to underline that he himself didn't tie the force to the extension, but rather to matter. Here we delve into the birth of the notion of field and into its dual relationship with space.

3.1. Origin of the field concept

The electromagnetic origin of the concept of field has been recounted a number of times. Knowledge about the effect loadstone has on small iron pieces within reach of its magnetic action is long-standing. As time went by, it was realized that even the capacity of a conductor is affected by neighboring conductors. To explain *electrical switch-on and -off surges*,[4] Faraday endeavored without success to make visible the electrotensive state of the di-

electric medium surrounding electrified bodes. Finally, he assumed that an electrified body does influence dielectric bodies within reach of its electric action nevertheless.

Maxwell felt that Faraday had grasped some very important new features, and pleaded for keeping them. Those features are the induced surges, the unclosed current loops, the inclusion of optics as an integral part of electromagnetism, and its spatial underpinning. Not long before, though, Lagrange had developed analytical mechanics. With pretty good justification, he had banished the informal graphical explanations of motion in space, especially those deliberately provided to substantiate the discipline of mechanics. Clearly, Faraday's visualization of surges by means of lines of force in space was in defiance of the Lagrangian formalism. At a glance, the same goes for Maxwell's mathematical framing of the *lines of induction*. In 1856, he cautiously pointed out that Lord Kelvin had applied Fourier's theory of heat conduction in uniform media to the electrostatic attraction at a distance by analogy, notwithstanding the fact that heat is supposed to proceed by nearby action between contiguous parts.[5] Incidentally, the frequency bandwidth of the surges was thus hinted at in the context of heat diffusion. Maxwell then drew from Euler's hydrodynamics of continuous media, and introduced the line of induction as a line passing through any point of space, such that it represents the direction of the acting force. To account for intensity, he considered an imaginary, incompressible fluid, variable in inverse proportion to the section of a tiny tube coaxial to a given line of induction. The acting force is thus translated into uniform motion through surfaces of a continuum whole possessing no inertia, but slowed down by a force proportional to velocity.[6] Forces satisfying the inverse square law allow arranging the tubes so as not to leave any interstice. And it turns out to be possible to lay down graphically the mathematical theorems of Gauss, Green and Stokes, unencumbered with matter.

In 1864, being dissatisfied with the above incompressible fluid analogy, and with the other mechanisms devised by him for the purpose of coupling electric and magnetic matters in a way that uniquely defines either kind of action, Maxwell took the step of subsuming Faraday's electromagnetic induction phenomena under the general principles of mechanics, i.e. Lagrangian mechanics including thermodynamics. He wrote down his electromagnetic laws first, and then embraced the space-agnostic reductionist Lagrangian specification to identify forces and induction. His compliance with the immaterialist tendency roughly consists in having produced mathematical equivalences between the physical quantities localized on bodies and those ascribed to the surrounding medium. Before we proceed further, we

---

[2] Besides the formal and material causes, there were the efficient and final causes, that aimed at stating the origin and the purpose of the objects. Transmutation of matter was admitted until the emergence of modern science, Newton included.

[3] Apparently, in those times, inanimate matter had to behave passively, while activity was reserved for the spirit.

[4] In our opinion, the pivotal point is whether a surge signals a direct electric coupling of the involved bodies, or whether it is a process primarily going on in the space in between. In times gone by, when activity was ascribed to the spirit, the controversial point was the ability of passive masses to exert forces on one another.

[5] Lord Kelvin's reprint of 1854 is titled: "On the uniform motion of heat in homogeneous solid bodies, and its connection with the mathematical theory of electricity". In the present case the linear motion of heat is described by $\rho c_p \frac{\partial T}{\partial t} - k \frac{\partial T}{\partial x} = 0$, with ρ mass density, c_p specific heat capacity, k thermal conductivity. The analogy is between the lines of motion of the heat and the electrostatic force. Maxwell was cautious because in the electrostatic case nothing is described as flowing.

[6] The kinematics of a Newtonian liquid's flow concerns states (of motion) characterized by a constant ratio of shear/deformation rate.

wish to underline that in the emerging field theory the field was naively conceived to exist, and to be well defined at all times and at every point of the "physical space". Even in the less naive case of it being conceived as a spatially extended property deprived of whatever truly material substance, the rigidity constraint was overwhelmingly important for its spatial underpinning. Judging by the field equations, there is no hint that the time dependent electric and magnetic induction lines in space don't intertwine into a single whole, whether the test body stands still or not.

3.2. Interpretations of the field

On the one hand the mathematics involved in solving Maxwell's system of partial differential equations is more demanding than that for finding Newtonian trajectories, and calls for some kind of visualization of the solutions. On the other hand, it is not clear just what physical thing is being mathematically described, and consequently what should be visualized. The requirement to form a mental image of the physics involved at each step in the computations marks the birth of *mathematical physics*. To Maxwell, his decision of subsuming his field theory under the general principles of dynamics meant not to lose sight of the underlying dynamical processes. He provided the field with energy that resides in it – and perhaps so much as constitutes it – in the form of motion and strain, on a par with mechanical systems. At the same time he sharply separated the field from matter. We highlight two outcomes in particular: (i) all manifestations of the electromagnetic field are through matter. If the field isn't dragged by the charged particles, a matter-field type of dualism is faced; (ii) the fields are specified at each point in a region of space while energy, and the possibility of transferring it as light and heat, are assigned to the configuration of the system as a whole. In pursuing the spatial features of the energetic processes, Poynting studied the settling of the field energy after slow motions, and found an energy flux perpendicular to the moving electrical and magnetic tubes of force. As funny as it sounds, although heat diffusion processes had been proposed since 1807,[7] as of 1884 *energy propagation* was yet unprecedented. A moment's thought will show that it is not clear in what space energy propagates. In the next paragraph we'll dust off the geometry-based representations of force fields in statics. We anticipate that, unlike Newton's force $\boldsymbol{F} = \frac{d^2\boldsymbol{x}}{dt^2}$,[8] the static field of force came to be supported by synthetic geometry. This is not true of Lagrange's principle of virtual works, that is nonetheless based on the static notion of force, i.e. that measurable by a dynamometer. Neither it is true of Hamilton's theory of rays and wavefronts, that is set in symplectic geometry, a representation specifically devised for it. The latter geometry can allow visualization of the algorithm but no independent check of its soundness.

    Going back to the outcomes (i) and (ii) highlighted

above, the main manifestations of the electromagnetic field consist of warming, jerky motions, light flashes, or a picked up muddle, unless the latter can be decoded as a received signal. Since already Faraday linked electricity and magnetism to light, let's consider the pattern formed by a light beam seeping through the small hole of a pinhole camera. The extent of the neighborhood packed within the collimated, seeping, light beam is evaluated differently according to whether we consider the intensity distribution on the opposite side of the box, rather then the subject of the picture. The picture carries information on a spatially extended environment, however in no way it itself can be called a spatially extended signal. Indeed, a pinhole camera does not form images extended in space, while human eyes undeniably do. Lenses and mirrors too are capable of shaping the received images into spatial forms. This is the sense in which the electromagnetic signals can carry spatial content, the information on which can apparently be decoded by some types of antennas. In this context it is appropriate to recall that lenses and mirrors (as well as the eyes) also can form a diffraction image of a flat object or another image, which is called the *dual image*, and which in fact contains the same information as the former image. This means that spatial information may be gained by performing some geometric transformations, which depend on the detector used, and can be stored as geometric information.

4. Statics at the Crossroad of Calculus and Geometry

With Maxwell's unification of the electric and magnetic fields, the need for a consistent system of units of measure came to the fore in mathematical physics. Differently from mathematics, the latter discipline appeared especially tailored for catching the correspondence of equations with real structures. Writing in terms of physical magnitudes, as a feature, was believed to prevent from formulating wild statements, and helped tell apart equations based on physical grounds from all the others. In discussing how fundamental magnitudes can be chosen within the program of geometrization of physics, Tolman was thus led to impart to geometry one magnitude (length).[3] Since it is undisputed that geometry is a branch of mathematics, perhaps by speaking of physical magnitudes he meant graphic statics, instead. That distinction matters, for in projective geometry there is a *duality principle*,[9] while there is none in the graphical methods of statics. For trusses, *reciprocal diagrams* of form and force were developed according to Euclidean rules, and were applied to masonry to get information on the static equilibrium load of structures built from lumped masses. Within the fully reductionist framework originated by Lagrange, statics, along with kinematics and dynamics, make up the three sub-branches of analytical mechanics. However, structural engineering design has a different background. We clarify this topic below.

---

[7] The proposer, Fourier, wrote a mathematical theory that was valid regardless of whether heat was stuff or motion.

[8] The Newtonian field of force cannot be represented in physical space, because it is bound to the second derivative of position.

[9] The principle of duality consists in the interchangeability of the roles of *point* and *plane* in projective theorems.

4.1. Reciprocity between force and structure in statics

At a difference with mechanics and electromagnetism, graphic statics is first and foremost a nomography. Graphical methods in structural engineering stem from empirical construction concepts,[4] and were favored by technicians before the mathematical theory of elasticity brought applied mechanics and structural behavior together under a single umbrella, by the early 1900s.

In 1864 Maxwell was possibly the first to conceive that reciprocal diagrams can help to rationalize the graphic computation of the stresses on load-bearing and structural members of frames. The point of departure of rationalization consisted in arranging the forces in succession and drawing a so called *polygon of forces*, rather than calculating the parallelograms of concurrent forces two by two, by displacing each of them along its line of action. Under equilibrium conditions the relevant polygon is closed. Since, owing to its construction, the force polygon breaks away from the skeleton of the frame, it is desirable to have two separate, but linked diagrams (Fig. 1).
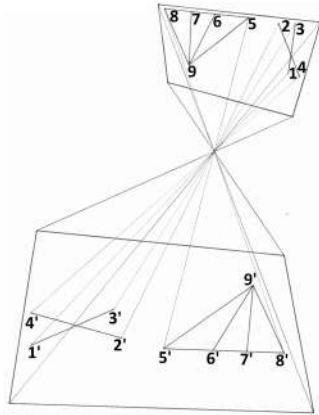

Figure 1: An example of geometric link between two 2D diagrams

To establish a link, Maxwell stated that "two figures are reciprocal when the properties of the first relative to the second are the same as those of the second relative to the first".
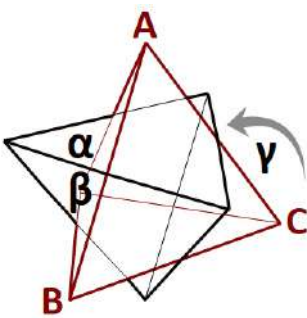

Figure 2: Corresponding vertices and faces of two linked dual tetrahedrons. These are self-dual

He meant that, when the joints of a rigid truss are represented by the edges of a given diagram, the loads applied on those edges are represented by a second diagram such that the first diagram results by applying reciprocation once more. To get an idea, think of an Eulerian polyhedron (in 3D space, Fig. 2). It is a geometric solid satisfying the formula $F + V = E + 2$, where F, V and E are the numbers of faces, vertices and edges respectively. It can be "dualized" by swapping vertices and faces. In principle, those reciprocal diagrams (in 2D) can be obtained by orthographically projecting a couple of mutually dual polyhedrons on one of their bases.[10] In the plane two simplicial

complexes result. Moreover, a "star-polygon conversion" is so arranged that the force diagram can be guessed at a glance from the truss. In 1870 Maxwell picked up the more straightforward *polar duality* of Poncelet as a construction method for linking reciprocal diagrams (in 2D), instead. His construction availed of a paraboloid of revolution as "self-conjugate quadric" (in 3D).

4.1.1. Relationship between projective duality and reciprocity

Without going into much detail, we recall how in the Erlangen program (1872) Klein linked the theory of invariant quadratic forms to the group of projective transformations of space into itself, thus establishing a bridge between algebra and geometry. A quadratic form $F(x_1, x_2, x_3, x_4) = 0$ written in homogeneous coordinates x_i, $i = 1, ..., 4$, and in canonical form, becomes the shorthand logogram for a special quadric locus, the *self-conjugate quadric*. This is the invariant locus of the transformation. If the variables in the algebraic quadratic equation F are real, the transformation is *real*. In that case only, the quadric can be classified according to the so-called *index of inertia*,[11] i.e. the modulus of the difference between the number of positive and negative signs in the equation. The transformation types can be grouped accordingly. Klein distinguished four irreducible transformation subgroups depending on the reality of the supporting geometric figure, i.e. on the possibility of constructing the corresponding invariant geometric loci. If all four squares have the same sign, the support of the self-conjugate quadric is not constructible and the transformation is of the *elliptical* type (1). If three signs are equal, there are constructible self-conjugate geometric figures, that consist of either a round (2) or a ruled (3) quadric. In the latter two cases the transformations are called *hyperbolic*. In the last type of invariant transformation (4) the difference of the signs in the expression of the quadric is nil, and the system of quadrics takes the name *null system*. Given that in all cases the elements point and plane of projective space transform into their dual elements (plane and point respectively), the transformation called duality is defined differently for type (4). The elliptical transformations (1) and the hyperbolic (2) and (3) are polar. Poncelet showed for hyperbolic constructions that points not lying on the special self-conjugate quadric don't belong to their dual plane, and vice versa. The same applies to lines. By contrast, the kind of duality in the null system (4) is involutionary, i.e. all points are conjoint with their associate planes. In addition, every point and every plane are associated with a flat pencil of self conjugated lines conjoint with it. Since Plücker, the forms associated with the null system are traditionally expressed in line coordinates rather than of point. Type (4) duality was developed in Möbius' book *die Lehre der Statik* (1837) to reduce the forces acting on a

---

[10] The dualizing operation associated with reciprocal diagrams consists

of the transformation of the first polyhedron into the second.

[11] Projective forms have *no coefficients*. When a section of the quadric can be drawn, it is used for the construction of the rest of the figure. This conic is selected as self-conjugate.

rigid body. The null system conceived by him is in 3D, so that graphics drops out by definition.[12]

4.1.2. Further development of reciprocity in graphic statics

The name *graphische Statik* was coined about 1865 by Culmann, who aimed at re-establishing graphic statics based on a logical-deductive system. The same reason was behind Cremona's later (1872) modification of Maxwell's reciprocity in accordance with the mathematics developed by Möbius. Specifically, Cremona took advantage of the peculiar point-plane correlative[13] relationship occurring in projective systems of lines (4). He translated the idempotence of duality into a valid operation for 2D graphic statics, with the bonus that the Maxwell-Cremona's reciprocal diagrams, consisting in replenished funicular polygon[14] and force polygon, also allow taking a couple into account. Clearly, notwithstanding the congruity of the modification with Möbius' definition of the null system, projective geometry cannot substantiate the graphic computations of stability conditions. In fact, the point-plane duality principle is utterly contradicted by 2D Euclidean graphics. In addition, projective geometry is incompatible with the notions of parallelism and measure. Accordingly, Cremona maintained the term reciprocity for the idempotent Cartesian operation.

4.1.3. The geometry of space called null system

To put the null system in the right light, let's recall that projective geometry was first formalized in von Staudt's book *Die Geometrie der Lage* ten years after Möbius work on statics (1847). In 1871 Klein observed that the null system of graphic statics can be subsumed under Plücker's *projective linear complex*. When speaking about duality in the previous paragraph we assumed the formalization step as already accomplished. Now, let's fill that gap by briefly introducing the linear complex. According to Plücker, four coordinates are needed to describe lines in 3D space, and each complex of lines is made up of heaps of lines. Just like a 2D manifold of $\mathbb{R}^3$ in Cartesian point-coordinates (x, y, z) is expressed by the equation $\varphi(x, y, z) = 0$, so a spatial construction of lines can be defined by the form $F(p_1, p_2, p_3, p_4, p_5, p_6) = 0$ in line coordinates p_α ($\alpha = 1, \cdots, 6$), aside from the fact that the coordinates are homogeneous. Linear complexes can be defined as sets of ∞^3 lines touching a skew cubic curve once. They can also be defined by incidence by a linear function of lines

$$\pi(p_\alpha) = ap_1 + bp_2 + cp_3 + dp_4 + ep_5 + fp_6 = 0.$$

In the latter case, if the lines (a, b, c, d, e, f) are aligned, i.e. all cut one line, $ad + be + cf \equiv 0$. The set $\pi(p_\alpha) = 0$ of all lines meeting this requirement is called *special linear complex*. Otherwise, $ad + be + cf \neq 0$.[15]

To exhibit the duality of type (4) in the general case, let's express the p_α in terms of homogeneous Cartesian point-coordinates (x, y, z, t) as[16]

$$p_1 = xt_0 - tx_0, \ p_2 = yt_0 - ty_0, \ p_3 = zt_0 - tz_0,$$
$$p_4 = zy_0 - yz_0, \ p_5 = xz_0 - zx_0, \ p_6 = yx_0 - xy_0.$$

If $P_0 = (x_0, y_0, z_0, t_0)$ is kept fixed

$$\pi(x, y, z, t) = x(at_0 + ez_0 - fy_0) + y(bt_0 - dz_0 + fx_0)$$
$$+ z(ct_0 + dy_0 - ex_0) - t(ax_0 + by_0 + cz_0)$$

is the equation of a plane containing P_0 in homogeneous point-coordinates. Vice versa, given a plane in general position $\pi(x, y, z, t) = Ax + By + Cz + Dt$, the condition that a point P lies on it is given by

$$\begin{pmatrix} 0 & -f & e & a \\ f & 0 & -d & b \\ -e & d & 0 & c \\ -a & -b & -c & 0 \end{pmatrix} \begin{pmatrix} x \\ y \\ z \\ t \end{pmatrix} = \begin{pmatrix} A \\ B \\ C \\ D \end{pmatrix}.$$

Since by hypothesis the determinant is $(ad + be + cf)^2 \neq 0$, the relationship is one to one, and exhibits exactly the statement of the kind of duality (4). Projective collineations (homographies) are geometric transformations conceptually akin to rigid motions in Euclidean space. Cartesian point coordinates can do collineations. However, the point-plane duality principle cannot be kept that way, hence point coordinates aren't particularly appropriate either for representing the projective space, or for exhibiting correlative transformations (duality) analytically. We saw that real duality transformations are linked to a quadric locus. In fact, constructions of projective space can be generated by transformations.[17] That's used to construct figures.[18] Fig. 3a gives a glimpse of the projective construction of the null system. Take a point A belonging to a plane α. Call A the pole of α, its polar plane. If a point $B \neq A$ also lies in α, there is a plane β, with $B \in \beta$ cutting α along the line $g : A, B \in g$. Call the line polar line. On the other hand, if $C \notin \alpha$, then α and γ are incident with a line g', called the reciprocal polar of g. If P is displaced on g', its plane π rotates about g. For the linear complex, all transversals incident with g and g' belong to a ruled surface. Although ruled surfaces of higher order can be constructed by availing of the two fixed lines met by all the lines common to two linear complexes (the directrices) [5], idempotent duality doesn't extend beyond quadrics.

---

[12] When the supports of the invariants are projected on the plane, there we find nothing corresponding to a projective null system (4).

[13] The term correlation refers to the transformation of an element into its dual element in the same projective space. Correlative relationship is slightly more general than duality (see Fig. 3). Different authors used different terms.

[14] The concept of the funicular polygon as a line of thrust is due to Hooke: "As hangs the flexible line, so but inverted will stand the rigid arch." It provides a geometric interpretation of the equilibrium of forces that aren't concurrent.

[15] In this case the bilinear equation can be put in the more symmetrical notation
$$\overset{\circ}{p}_4 p_1 + \overset{\circ}{p}_5 p_2 + \overset{\circ}{p}_6 p_3 + \overset{\circ}{p}_1 p_4 + \overset{\circ}{p}_2 p_5 + \overset{\circ}{p}_3 p_6 = 0.$$ The invariant complex of lines is formed taking all $\overset{\circ}{p}$. The set of lines p incident with a preset line $\overset{\circ}{p}$ is algebraically represented by homogeneous point coordinates x_α on a hyperquadric of $\boldsymbol{P}^5(\mathbb{C})$.

[16] Plane coordinates would do as well leading to similar equations.

[17] The link between space and transformations is peculiar for synthetic projective geometry. In Euclid's (synthetic) geometry motion is not allowed, which leaves the so-called superposition method dangling.

[18] As transformations can be expressed algebraically, the bad practice of representing the space in the same vein has caught on.
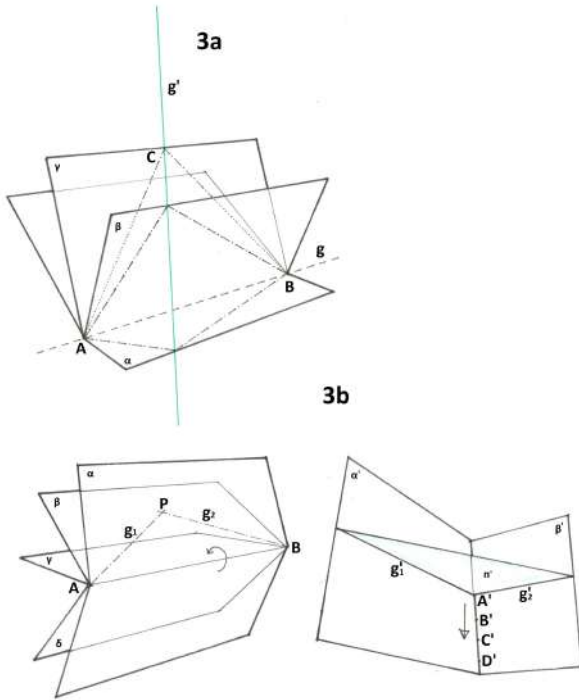
Figure 3: a) Null system. If the pole moves along a line, its polar plane rotates around an axis. b) A general correlative relationship can be split into a collineation and a duality.

Now let's briefly comment on the null system of statics. Möbius' aim was to obtain a spatial equivalent of the parallelogram law of forces. In want of a respectable vector calculus, he deployed the correlative relationship of the ruled space to extend the composition of forces and couples to space in a geometric guise. While within graphic statics, in keeping with Maxwell's rationalization, his developments lead to refinements of the reciprocal diagrams, within synthetic projective geometry (a mathematics) there is no need to introduce a dual space. In fact, the correlative transformation of the space in itself is on a par with all *finite* collineations. The distinction between collineations and duality was introduced, so to speak, for physical reasons: while collineations of the space in itself were equated with mechanical displacements, such as screws, correlations got no equivalent motion. Finally, in connection with the geometric representations of motions in mechanics it was posited that a correlation performed right before a collineation can give a geometric account in a dual space of the forces involved.

Totally counter to what Culmann tried to put forth, projective geometry as is cannot do statics. Euclidean-looking rules must be obtained by shifting the improper elements to infinity, as already mentioned in the piece about Cremona's reciprocal diagrams. Once (i) orthogonal coordinates are in place, (ii) a dual space is defined, and (iii) the decision is made on how to describe the couple acting on a body by means of the cross product, then the p_α can be rewrit-

ten in non-homogeneous coordinates as a force $\boldsymbol{F}$ on the unit mass with components: $X = x - x_0$, $Y = y - y_0$, $Z = z - z_0$, and a torque with respect to the origin O of the coordinate frame $\boldsymbol{M} = \boldsymbol{r} \times \boldsymbol{F}$, where $\boldsymbol{r}$ is the radius vector to the application point of the force. With this expedient the Euclidean "physical space" sprayed with matter turns out to be the reciprocal space of the field. Nowadays, the dual space is linked to frequency/energy.

4.1.4. The fate of Plücker's space of lines

In 1871, Klein staked a claim for Plücker's geometric approach to the mechanical doctrine. An almost correct, yet restricted statement. Plücker's analytical formulation of the ruled space was aspiring to a general geometry competing against algebra, rather than to a graphic mechanics. The "new geometers" sought to logically distinguish the geometry of position from that of Euclid and also to adopt a symbology alternative to the algebraic one. Generally they indicated with letters a, b, etc the classes of geometric elements instead of sets of numbers, and resorted to algebraic symbols to indicate the geometrical transformations to be performed on them. Plücker himself managed to abstract from individual geometric elements by identifying whole classes of geometric figures, such as complexes and congruences, by means of mathematical expressions. He dedicated the last years of his life to analytic representation of the "new geometry" (1868) by the *line element*. In fact, the point-plane duality associated with the definition that the point has no parts has the curious consequence that a dual plane of a point is indivisible, i.e. differs from the concept of analytic plane. Thus, Plücker picked the projective line that, given either as a ray or as an axis, is collectively self-dual.[19] Klein was aware of the profitability of the linear element when pursuing the analytical representation in Cartesian coordinates.[20] In the meantime, however, the line element was replaced with the algebraic notion of free vector, and the problem of vector division was faced. Lagrange's distrust of the identification of physical and Euclidean spaces was overcome by the geometrical interpretations of complex numbers and of the first hypercomplex number systems. The need also began to appear to standardize the various vector notations, so as to replace the normal specification of coordinates with a more concise notation. The new geometry was about to be relinquished altogether by the algebraic generalization of the old geometry. The old (Euclidean) geometry itself was framed in abstract terms, too. Nowadays, as a consequence of the development of field theories both instances, void space and forces, are avoided.

---

[19] Considered collectively the straight line is self-dual, but taken in a specific construction it is either a ray or an axis.

[20] In fact, the geometry of position is a synthetic geometry construable by means of the ruler, and could spare all analytical representations. If the goal is a bare mathematical interpretation, geometric function theory defines its elements, such as complexes, congruences, and the like as invariants of the point-plane transformations. That way, *one* function corresponds to *one* construction, as in the given example.

The former is introduced as an algebraic structure,[21] and its content (matter) relies on explanatory constructs, and is subsumed under the heading of materials science, a multi-disciplinary, multiscale subject area connected with chemistry, physics and engineering. Within physics, matter and motion are fitted together by equipping matter-related concepts with magnitudes, and by representing their properties by suitable mathematical objects pertaining to some algebraic structure. The resulting monistic theory is presented as a dynamics induced by a field.
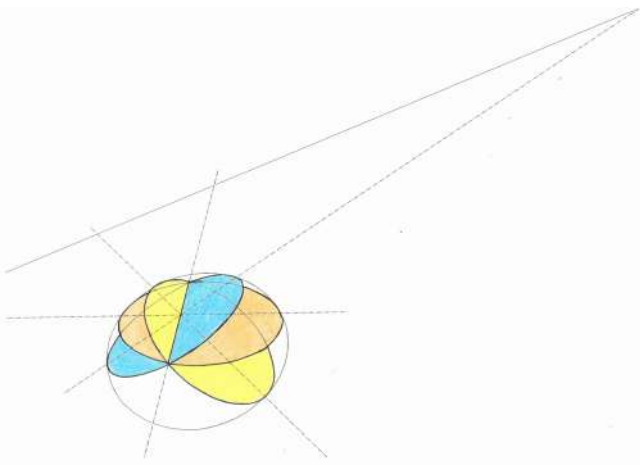
5. Transformations with a Fixed Quadric

Figure 4: A hyperbolic correlation. The points lie on a line external to the fixed quadric, their planes inside it.

By restricting to real projective transformations of space, Klein distinguished four subgroups. In the previous paragraph we dealt in more detail with the null system (4), but in principle *Poncelet's polarities* (1), (2) and (3) allow constructions according to the same principle (Fig. 4). Although duality is indeed no deal breaker within synthetic geometry, it is the reason behind Plücker's choice of the line element, and behind the dropping of correlations after him.
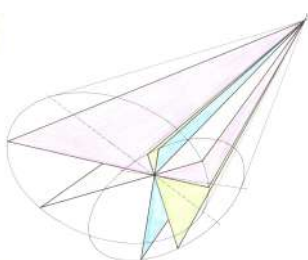
Figure 5: Bundles with same axis.

Once the elements point and plane get each a different invariant dimension, one has hard times with dual constructions. For now, let's thus forget about correlations, and show some examples of collineations of a bundle of planes in the projective space $\mathbb{P}^3$, instead. The planes of the bundle aren't terminated, but we cut them along a conic "level curve", in accordance with Klein's partitioning of real projective transformations. To show the pictures graphically, we pro-

jected them from 3D space to a Euclidean 2D, but holography would allow showing 3D images. And the eyes would do as well.

The bundle can be transformed keeping the same axis (Fig. 5), keeping a fixed plane (Fig. 6), or in more general ways (Fig. 7). Taking into account that synthetic projective geometry considers (Euclidean!) quadrics the same as planes, general collineations don't preserve the axis of the bundle (Fig. 8).
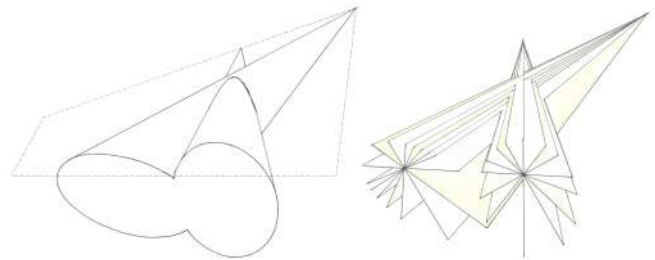
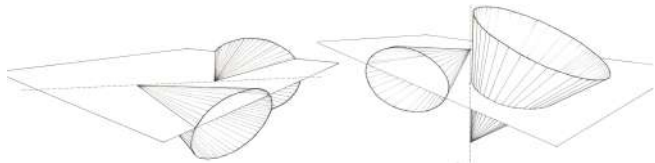Figure 6: Bundles on the same plane.

Figure 7: General bundles.

While there is no such thing as a plane section of the null system, excluding the general transformations (Fig. 8) flat sections across polar dualities can be drawn. Next we 'll deal with Klein's real collineations on the plane, and show where the conic level curves come from.
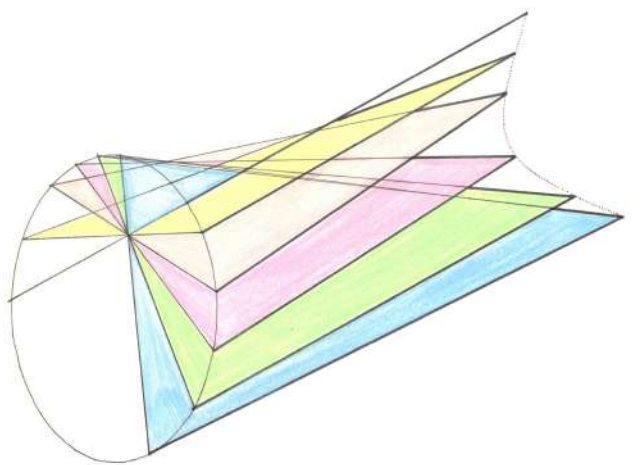
Figure 8: General transformation.

---

[21] Except for the general theory of relativity, space is a device for representing motion.

5.1. Real collineations

In linear algebra, projective collinear transformations of the whole space in itself are written in point coordinates as substitutions as $\sigma\xi_i = a_i x_1 + b_i x_2 + c_i x_3 + d_i x_4$. The index range is $i = 1, \cdots, 4$, $\sigma \in \mathbb{Q} \setminus \{0\}$ is an arbitrary proportionality constant, and the determinant of the substitution is $D \neq 0$. Three linear centro-affine transformations having the form $X_k = \frac{\xi_k}{\xi_4} = \frac{a_k x_1 + b_k x_2 + c_k x_3 + d_k x_4}{a_4 x_1 + b_4 x_2 + c_4 x_3 + d_4 x_4}$, ($k = 1, \cdots, 3$) were associated with the above four substitutions for representation purposes. After putting $\xi_4 = 1$, The variables X_k are often called affine coordinates of the space $A\mathbb{R}^3$– a vector space deprived of the origin marked as $(0, 0, 0)$. The projective coordinates giving rise to the X_k, that can be written as $(x_1 : x_2 : x_3 : x_4)$(excepting the quadruple of values $(0 : 0 : 0 : 0)$) are correspondingly attributed to the real projective space $\mathbb{P}^3$. As already mentioned, the reason for attributing to the space the same coordinates used to define transformations is that the projective space can be generated by transformations. Yet, while synthetic geometry allows constructing as many 3D tilings of space as one please, analytically, the projective space is an abstract space that cannot itself be displayed visually. Algebraic representation problems aside, the determinant of

$$\begin{pmatrix} (c_{11} - I) & c_{12} & c_{13} & c_{14} \\ c_{21} & (c_{22} - I) & c_{23} & c_{24} \\ c_{31} & c_{32} & (c_{33} - I) & c_{34} \\ c_{41} & c_{42} & c_{43} & (c_{44} - I) \end{pmatrix} \begin{pmatrix} x_1 \\ x_2 \\ x_3 \\ x_4 \end{pmatrix} = 0$$

gives a fourth degree polynomial in I, that helps characterize the linear projective transformations of the real space $\mathbb{P}^3$. Since $D \neq 0$, according to the fundamental theorem of algebra, there are always four roots, that can be real or complex numbers, ∞ included. Those roots leave the coordinates unchanged, thus defining four fixed points of the transformation.[22] Klein based his algebraic grouping criterion of the real projective transformations according to the types (1), (2), (3) and (4) on the above determinant, anticipating the eigenvalue equation.

5.1.1. Invariant conics

In algebra, homogeneous linear substitutions in n variables (here $n \leq 4$) that give rise to a group of finite order have one or more absolute invariant Hermitian forms of the bilinear type $f(u, x) = u_1 x_1 + u_2 x_2 + u_3 x_3 + u_4 x_4 = 0$, involving x and its conjugate coordinates u_k.[23] If the group is irreducible there is but one Hermitian form.

To simplify matters we restrict the discussion to flat projections. According to Klein, the $\mathbb{R}$-forms in homogeneous

point coordinates $x_1^2 + x_2^2 \pm x_3^2 = 0$ can be interpreted as the invariant conic of the elliptic (1) and hyperbolic (2) cases. In case the eigenvalue equation has three real roots (2), let's rewrite it as $x_1^2 + (x_2 + x_3)(x_2 - x_3) = 0$. Putting $\sigma y_2 = x_1$, $\sigma y_1 = x_3 + x_2$, $\sigma y_3 = x_3 - x_2$ one transforms it with respect to a tangent triangle $y_2^2 - y_1 y_3 = 0$. This triangle is shown as ABC in the diagram of Fig. 9.
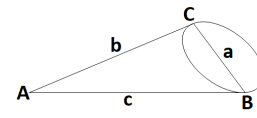

Its three sides represent possible translational motions (transformations). Also the rim of the conic represents translations. They are either from C to B, or from B to C, but not across those points.

Figure 9: Real conic and tangent triangle.

The case of coincident roots cannot be traced back to this. Nevertheless, the motions are of the same type. They are called hyperbolic motions.[24] In other words, the straight line a is like the ellipse. Vice versa, rotations are as linear as the motions on a line.

In the other cases, i.e. when either the conic is not traceable (1), or two roots of the eigenvalue equation have complex values (2) (Fig. 10), the transformations are interpreted as rotations.
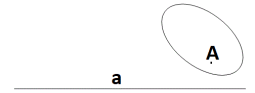

Figure 10: Real conic with two imaginary tangents.

In Klein's book *Vorlesungen über nicht-euklidusche Geometrie* many of those invariant primitive forms are drawn for both cases in Fig. 11. The resulting geometric bundles have been known for a long time. Within Euclidean geometry they are called Apollonian circles and, when both bundles are put together as orthogonal circles, they form the basis for bipolar coordinates in the plane. We notice that there is only one self invariant conic, from which the other "circles" derive. Arrows mark the mutual directions
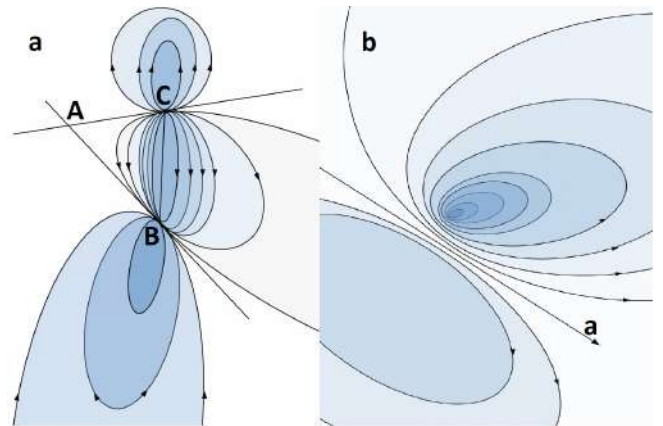
Figure 11: Some invariant conics for the hyperbolic (a), and elliptic (b) cases.

---

[22] A unique quadric is defined by five fixed points, not all lying in a plane.

[23] If a bilinear form is symmetric, i.e. $f(v, w) = f(w, v)$, with $v, w \in V$, then $f(v + w, v + w) = q(v) + 2f(v, w) + q(w)$ is a binary quadratic form. Although it can be difficult to diagonalize a matrix representation, it is easy to show that, by writing $a_0 v^2 + 2a_1 vw + a_2 w^2 = 0$, and requiring that $a_1^2 = a_0 a_2$, the latter form can be transformed into a perfect square $(\sqrt{a_0}\, v + \sqrt{a_2}\, w)^2$.

[24] In the context of the projective models of non-Euclidean geometries, the conic shown is interpreted as limit circle of hyperbolic geometry. At a difference with projective geometry, a metric is defined on non-Euclidean spaces. Correspondingly, it is also introduced in their projective models.

of the lines on those drawings. However, as the projective plane is an abstract, non-orientable and one-sided surface, the "level curves" traced on it belong to the drawing, and represent rather one complex analytic function than a set of coordinates.

5.2. Plücker's reciprocity versus Poncelet's duality

Plücker's conception of the linear complex in the 1860s was his mature effort to analytically represent the projective geometry of space. On the opposite, in the late 1820's he got the idea of line coordinates in a desire of dealing with Poncelet's style dual graphical constructions by a handy analytical method. Now, at a difference with Euclid, Poncelet and the majority of his peers conceived of geometry in the "observed space". Synthetic geometry proofs required to draw the figures on sheets of paper either by projection, or by cut, whatever seemed more appropriate for the specific case. Consequently, an overwhelming importance was accorded to the $3D \rightarrow 2D$ central projections with respect to the transformations of the space in itself. And this, in turn, did a great disservice to Poncelet's point-plane polar duality. In the special case in which Poncelet's hyperbolic
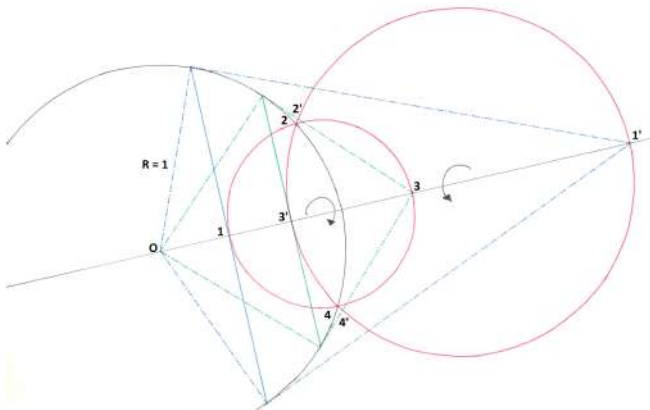

Figure 12: Inversion on a circle. $R = 1$ is the radius of the circle.

correlation (2) shown in Fig. 4 reduces to the perspective of a sphere, which is the self-corresponding circle shown in black in Fig. 12, a line through 1 corresponds to point $1'$. If the distances of those points from the origin O are x and x' respectively, it is $xx' = R^2 = 1$. This is the statement of the Euclidean transformation by reciprocal radii. It can be carried out for whatever geometric figure, which here is shown on circles.

Plücker's analytical formulation of his principle of reciprocity is set in the Cartesian plane, between a point of coordinates (x_0, y_0) and a line $ux_0 + vy_0 = -1$ *incident with it*, rather in agreement with his later choice for the null system (4) than with Poncelet's hyperbolic polar duality. His condition is satisfied for points $2' = 2$ and $4' = 4$ on the self-corresponding circle, in our case.

As a consequence of his setting, the young Plücker did

not express Poncelet's duality analytically. The meaning of his conic is not compatible with the polar transformations of space (1), (2) and (3). Instead, he contemplated all geometric figures as loci of either points, or tangents. He wrote bilinear expressions such as $ux + vy = \mp 1$ in non-homogeneous coordinates, and his reciprocity is obtained by imposing complete symmetry between coordinates of points (x, y) and of lines (u, v). That is not the same of Poncelet's duality, where the dual of a constructed figure is obtained by the dual construction, not by the dual coordinates. In sum, Plücker's reciprocity refers to the fact that the same geometric locus can have at least two different analytical representations, one by point coordinates, and one by line coordinates (in two different coordinate frames). Again, if one is aware of the implication that the definition of the line either as a linear set of points, or as an element, has on the dimension of a submanifold, and of the impact that the difference between the projective plane and the Cartesian one has on ordering, the fact that the given analytical representation changes the entire game will come as no surprise.

Finally, the important theorem of Desargues on triangles was reduced to a postulate in the plane, and 3D projective geometry was subsumed under the central projection that is obtained from a point in 4D, outside the space. The latter is an alternative to the generation of the projective space by means of transformations, that consists in simply adding one more orthogonal dimension. As regards transformations in the plane, nowadays, if the point of general homogeneous coordinates (x_1, x_2, x_3) is subjected to a collineation T, its image (x'_1, x'_2, x'_3) is given in vector form by $\boldsymbol{x}' = T(\boldsymbol{x}) = A\boldsymbol{x}$, where A is a regular 3×3 matrix. Writing the coordinates of the image point out, it is $x'_j = a_{j1}x_1 + a_{j2}x_2 + a_{j3}x_3$, $(j = 1, 2, 3)$. As anticipated when it was told that Hermitian invariant forms were associated to quadrics, u_j and x_j are considered contragredient coordinates in $u'_1 x'_1 + u'_2 x'_2 + u'_3 x'_3 = 0$. Denoting by A_{ij} the cofactors, and by $|A|$ the determinant of A, u'_j is obtained by multiplying u_j with the inverse conjugate matrix $u'_j = \frac{A_{j1}}{|A|}u_1 + \frac{A_{j2}}{|A|}u_2 + \frac{A_{j3}}{|A|}u_3$, whereas $x_j = \frac{A_{1j}}{|A|}x'_1 + \frac{A_{2j}}{|A|}x'_2 + \frac{A_{3j}}{|A|}x'_3$ is recovered by multiplying with the inverse matrix $(A)^{-1}_{ij}$.[25]

6. Complex Projective Space

We just had a look at many ways of dealing with the projective transformation of the space in itself, called duality. Plücker, Poncelet, and their peers were trying to choose how to best adapt transformations to a visualizable space. Yet competition generated a tendency to expand on each touched topic, and to search right off for physical applications especially for validation, without paying too much attention to formal aspects. It all ended by the end of the 19th century. This becomes apparent when dealing with

---

[25] In coordinate free language the indices of the dual variable are raised, u'^j. As homogeneous coordinates are defined up to a factor, they are seldom encountered when dealing with manifolds.

the complex projective space. Although complex numbers were not directly linked to measurements, that space was dealt with since the very beginning. At least two different conceptions can be unraveled: (i) von Staudt was busy with the projective representation of imaginary numbers; (ii) Klein was busy with the analytical definition of the projective space over the field of complex numbers. Here, we are interested in task (ii). When the transformations are complex, even if the motions are invariably interpreted as rotations, or as periodic motions if it sounds better, the problem of determining their irreducible groups is somehow elusive. We saw that for real transformations a projection of the drawn invariant quadrics looks like a set of level curves of a 3D object, as viewed from a special point. If the coefficients in the algebraic expressions defining the transformations are complex numbers, the $\mathbb{C}$-forms are no longer reducible according to Klein's index of inertia, as in the real case, and other linear functions like integral transforms could be involved in the transformations of space. Without prejudice to the fact that the same variables expressing transformations should describe the spatial figures, perhaps in the abstract $\mathbb{P}^3$ space, functionals on $\mathbb{C}$ take the place of the specific functions.

Due to the turn taken by analytical projective geometry, and to its merging with algebra, the synthetic projective space was expected to remain pretty the same, whether the transformations were real or not. Of course, as $\mathbb{P}^3$ is tied to transformations, it needs to match complex transformations, and to be defined over $\mathbb{C}$ in this case. But, as long as one deals with constructions one never attains the general space, for figures are always particular examples. Thus, only formalization brought about a great deal of change. In this context, indicating with V any representation of the projective group on space $\mathbb{C} \times \mathbb{C} \times \mathbb{C} \times \mathbb{C} = \mathbb{C}^4$, the abstract projective space $\mathbb{P}(V)$ and its subspaces are defined naturally by the representation of V as a complexified manifold of finite dimension 4 (Stein manifold). Hence, one deals with a real differentiable manifold of dimension 2×4 with an invariant structure for linear fractional transformations, that has the topology of $U(1)$.[26] To analyze perturbed

motions in quantum mechanics, the analytic representation of vector spaces in a division ring was extended to the field of invariant rational functions V^* by taking the limit of arrays $(z_1 : z_2 : \ldots : z_n : z_{n+1})$ to the completely continuous (vollstetig) sequences $n \to \infty$. This abstract vector space, called representation space, ceases to coincide with its dual space, as in the case of projective constructions. The considerations regarding the definition domains were placed during the development of spectral theory for self-adjoint operators. While it would be interesting to build the synthetic projective space as a function space, it is tricky to do so according to latest developments. In that case, the dual space is a vector space of linear functions, and the (Poncelet) dual of a figure would be expected to coincide with the image of the figure by the canonical isomorphism. In a sense, we may say that infinite dimensional spaces can at most be isomorphic to their dual.[27]

6.1. Dualism in quantum physics

The need for complex numbers and dual spaces surfaced in quantum physics. There it is built in the formalism of quantum mechanics, mainly on the operator calculus and on the probability interpretation of its outcomes. Its distant originator, Hamilton, reworked the classical Lagrangian formalism to pinpoint the analogy between Newtonian mechanics and ray optics, that in mechanical terms are very swiftly propagating fields.[28] Although Synge stresses that Hamilton's geometrical optics is by no means a theory of the formation of images, as it is supposed to be according to the name eikonal, the geometry he uses has a visualizable representation. After Hamilton the phase space is reworked using canonical variables, i.e. those putting on the same footing the generalized canonical coordinate q and its conjugate momentum p,[29] and letting the pair $\{q, p\}$ be the representa-

---

[26] A manifold of n dimensions is a connected Hausdorff space with a topology of open U_j. Let's denote by (U_j, ψ_j) a complete family of charts (i.e. an atlas), where ψ_j is a homeomorphic mapping of U_j on a ball $\sum_{k=1}^{p_j}(t_k^j)^2 < 1$, where t_k^j are local or uniformizing coordinates, and by p_j the topological dimension of element U_j. In the current case, since the group is $U(1)$ (not to be confused with open neighborhoods U_j), complex differential geometry deals with the same objects as algebraic geometry. All projective complex manifolds are actually algebraic (Chow's theorem). One has $t_k^j \in \mathbb{R}$ and $p_j = n \ \forall j, k$, where n is the homogeneous dimension of the whole complex manifold; further, all the inverse functions of ψ_j are analytic functions of these coordinates on the manifold $\cup_J U_j$. Consequently, by denoting a point of the projective space by P, $\forall P \in \cup_J U_j$ the manifold with the quotient topology representing $\mathbb{P}(V)$ is homeomorph to a (2n+1)-dimensional Cartesian space, $\mathbb{P}^n(\mathbb{C}) = \frac{S^{2n+1}}{U(1)}$, ($S^{2n+1} = \{(z_0, \cdots, z_n) \in \mathbb{C}^{n+1} \mid \sum x_k x_k^+ = 1\}$ is a (n+1)-sphere) and its atlas is smooth. The representation of the projective group is a group homomorphism $G_P \to PSL(V, \mathbb{C}) = \frac{GL(V, \mathbb{C})}{\hat{\mathbb{C}}}$, where $\hat{\mathbb{C}}$ is the normal subgroup that consists of the multiplications of vectors of the vector space V for elements of $\mathbb{C} \setminus \{0\}$. However, if a vector space is not defined in $\mathbb{R}^k$ it may lack the canonical base, that is, the canonical

mode of expressing its hyperplanes as coordinates. We also wish to note that the theory is applied to group representations, but not to the representations of the projective space itself, which is not Euclidean by definition.

[27] The theorem: a vector space V has the same dimension as its dual V^* if and only if it is finite dimensional is valid if the vector space has no extra structure, in particular if no notion of convergence is introduced. To have the same infinite dimension means having cardinally equivalent basis sets. The theorem is also valid for algebraic vector spaces. The algebraic dual V_{alg}^* is the set of all linear (not necessarily continuous) maps $\varphi : V \to K$ from the vector space V to the field K where it is defined. Thus $\varphi \in V_{alg}^* \subset K^V$ (the functionals do not form a basis in the algebraic sense). On topological vector spaces there is however a notion of continuity, and thus the topological duality defines a topological dual space V_{top}^* of all continuous linear functions (with the topology of V_{top}). In the latter spaces the Riesz representation theorem holds. But, if $S(\mathbb{R})$ is the space of functions of rapid decrease, and $S^*(\mathbb{R})$ is the space of distributions that are topological duals of $f \in S(\mathbb{R})$, clearly $S^*(\mathbb{R})$ contains also distributions that are not functions, and the infinite dimensional vector space $S(\mathbb{R})$ has a smaller dimension than its topological dual. The theorem is proven by Jacobson *Lectures in Abstract Algebra: II. Linear Algebra*.

[28] Motions of electromagnetic waves, by the same token, can be interpreted as a signal transformation producing a received signal. Usually, however, that motion is conceived in mechanical terms.

[29] For one particle, in Cartesian coordinates, q is its position, and $p = m\dot{q} = \frac{\partial L}{\partial \dot{q}}$ is its kinetic momentum. For n degrees of freedom, the switch $\dot{q}_i \to p_i$ ($i = 1, \cdots, n$) between Lagrangian and Hamiltonian approaches involves a Legendre transformation.

tive point of the system in the 2n-dimensional phase space. In quantum mechanics the pursuit of Hamilton's analogy between the dynamical systems and the optics of rays and surfaces orthogonal to them – call them *ray-surface combinations* – prevails over the alternative Lagrangian formulation given by Dirac, which uses contact transformations,[6] and results in the *dualism of matter*. The dualism results from the quantum mechanical need of parceling out the phase space into cells of the size of Planck's constant h. In fact, Heisenberg's uncertainty principle states that the value of the product of the root mean square fluctuations of the observables be $\Delta q \Delta p \geq \frac{h}{4\pi}$, whether that indeterminacy summarizes a primary quality of matter or a secondary one (a property bound to our knowledge of it). Let the state of a quantum system be specified by a function of state $\Psi(\widehat{q}, \widehat{p})$ of the selfadjoint operators $\widehat{q}_i$ and $\widehat{p}_i$. If q is an exact value, p is the Fourier transform of $\tilde{\psi}(q, -\frac{ih}{2\pi}\frac{\partial}{\partial q})$, indeed.[30] Yet, the $q \to p$ connection with the Fourier transform is misleading since, due to its probability interpretation, quantum mechanics doesn't share with graphic statics any easy form-force like reciprocity.

7. Duality of Images

Images differ from all representations discussed so far in one respect. Unlike the graphical and geometrical approaches – our mind's eye, the "transformations" of optical images, don't involve forms in the first instance but rather *received signals*. Signals don't possess any preset geometric form, they are raw data that can be detected in widely diverse contexts besides by direct observation. In addition, observed signals depend on the "electromagnetic properties" of bodies, that can hardly be severed from the perceptual experience. Moreover, a different context of acquisition quite often doesn't boil down to a mere magnification of the original context. At least the amount of detail changes, leading in fact to a magnification of the information gained (channel capacity), possibly with structural alterations of the information content (knowledge). In other worlds, electromagnetic images are phenomena in need of an interpretation, and if anything their geometric constructions can be recognized as a convenient interpretation according to the relevant geometry. The geometric space refers to received images, without attributing any material properties to the void space. Just because geometry is a mathematical construct,[31] it has no information linked with it. The modeled "physical thing" is the ethereal image (to distinguish it from its support), and the information bearing extension is in the individual shot, that provides cues on the relationship between forms, once they have been recognized.

Abbe showed that, when a thing is observed under the microscope, its diffraction limited image and its diffraction pattern encapsulate the same amount of information. More

precisely, the same thing can be visualized in either way, and each can be recovered from the other one. The textures of both images are interwoven to such an extent that vignetting one of them alters the overall roughness of the dual one. The Fourier transform is found to analytically describe simple images under monochromatic lighting. Calling this feature duality, the $image \Leftrightarrow diffraction\ pattern$ transformation can be modeled by way of the geometric construction of the same name. We showed that the dual construction is subsumed under the transformations of the projective space in itself. More in general, the information content of the linear part of an image is independent of geometric transformations.[32] Besides duality, projective geometry accommodates other general transformations of space in itself. Projective geometric constructions may serve as a logical framework of whatever received signal, provided that it can be transformed to exhibit its spatial content. That way, different transformations of the same signal can be generated and compared, while still storing only the information detected by the antenna. The constructions then visualize the projective geometric space devoid of any unit of measurement.

Finally, whether information on a specific signal is fully captured by geometric reasoning or not often depends on lighting conditions, beyond the linearity of the receiver. As for the receivers, at one end there are optical techniques exploiting whatever nearly linear detection, such as fringe analysis, holography and photoelasticity.[33] At the other end, there are more sensitive non-linear acquisition techniques based on resonance, that overtly benefit from on/off responses. Images of on/off responses depend on the way the picture is taken. They can provide additional information about the effect the exposure to radiation has on a possibly living specimen only if the data aren't subordinated to statistics. Spectral analysis of chemical elements as well as the very first (quite unprocessed) radar and magnetic resonance imaging pictures pertain to the latter kind. We stress that in both cases the only information directly accessed is the visual one, and that if quantitative information about material properties, such as density, hardness, or chemical composition, can be inferred at all, it doesn't stem from the geometrical framework, but is rather inferred from the observed nonlinear variations, and needs to be supplemented by measurement of another type.

8. Conclusion and Outlook

We briefly sketched how graphical aids and computations came about in mechanics over a long period of time, and compared the techniques based thereon with the later possibility of taking durable pictures in nearly whatever electromagnetic frequency range. In our opinion a merging of all the known theories of matter will allow no rational characterization of materials, neither will the interpreta-

---

[30] Within this context a de Broglie wavelength $p = mc = \frac{h\nu}{c}$ is also attributed to a particle.

[31] We recall that Euclid distinguished between cosmology and geometry, and build the latter on logic as a hypotetico-deductive discipline.

[32] The parts of the received signal that depend on excitation or images of sources are non-linear, and depend on the mode of visualization.

[33] While the collapse of a bridge is not reversible, a movie of the collapse is.

tion of the electromagnetic information available on them if based only on a geometrical approach. However, the latter can help to frame experiments. Nowadays the imaging techniques access the information based on electromagnetic stimulation of bodies directly, and deliver it as received signal. In our opinion, to really exploit that information one has to renounce the old mechanical interpretation of pictures, and develop antennas for image reception besides geometric modeling and scientific computation. Summing up, independently on the mechanical understanding, there is a spatial content in the electromagnetic field, which can be supported by a geometry as a logical-deductive system. There is also a respectable synthetic geometry of space – the geometry of position. This was used to represent general fields of force (including the electromagnetic field). In addition, however, naturalism artists used geometry to model their artifacts. For those reasons it could be improved with the aim of supporting the interpretation of the linear electromagnetic reception.

References

[1] R. Held, et. al., The newly sighted fail to mach seen with felt, *Nat. Neurosci.* 15(5): 551–513, 2011.

[2] J. E. McGuire, Body and void and Newton's De Mundi Systemate: Some new Sources, *Arch. Hist Exact Sci.* 3(3): 206–248, 1966.

[3] R. C. Tolman, The measurable quantities of physics, *Phys. Rev.* 9(3): 237–253, 1918.

[4] P. Block, M. DeJong, J. Ochsenfeld, As hangs the flexible line: Equilibrium of masonry arches, *N. N. J.* 8(2): 13–24, 2006.

[5] J. Plücker, Théorie génerale des surfaces réglées, leur classification et leur construction, *Ann. Mat. Pur. Appl.* 1: 160–169, 1867.

[6] D. A. M. Dirac, The Lagrangian in quantum mechanics, *Phys. Z. Sowjetunion* 3(1): 64–72, 1933.

Structure-Function Relationship and Neuroimaging

S. L. Vesely[1*]**, A. A. Vesely**[2]**, S. R. Dolci**[2]**, M. E. Vesely**[2]**, and C. A. Dolci**[3]

[1]ITB–CNR, Segrate, Italy
[2]Milan, Italy
[3]Politecnico di Milano, Milan, Italy
*corresponding author, E-mail: `sara.vesely@cnr.it`

Abstract

Recently, computationally expensive iterative image reconstruction techniques and sophisticated processing methods are deployed to map the structure and function of the human brain non-invasively. Multiscale representations are available for the visual representation of the local neural activity. Perhaps, by doing so the difference between the imaged brain functioning and that of a computer is expunged. In fact, understanding brain activity is not so much a matter of evolutionary ecology, but rather of clarifying in which sense it fits natural laws.

1. Introduction

In the context of the upcoming confluence of nanotechnology with biotechnology, info-technology and cognitive sciences, the consistence of the structure-function relationship becomes a topical issue. According to a widely held opinion, multiscale approaches to materials design will enable the bottom-up construction of life-inspired structures with new emergent properties, and capable of performing desired functions.[1] Those approaches are supposed to bear just enough information at different levels of resolution and complexity to allow enforcing hybridization, biomimetics and integration hierarchically along several length scales. Speaking of neuroimaging, the gap between computer and brain bears on both, structure and function. In nature, proper functioning is somehow related to an adapted structure, while apparently man-made machines can perform any complex task, provided that exact and unambiguous instructions are supplied. Thus, it may be argued that one thing is to combine molecules bottom-up by exploiting the principles of nature, and quite another thing is to combine them so that the bulk product can perform any narrowly prescribed task. As a matter of fact, modeling, as well as imaging, tend to wipe out the differences. To clarify, a bomb explosion and a video thereof can carry about the same amount of visual information, which is by no means all the information.

2. Form-Function Relationship

The form-function relationship can be traced back to the doctrine of Aristotle (hylomorphism). A few examples are known from natural philosophy, such as eye-sight, and wing-flight.[1] It doesn't apply specifically to the brain-mind combination because then, the brain being perceived as inert, the cardiocentric theory was fashionable. Anyway, this "hypothesis driven" way of tackling living organisms influenced the course of scientific inquiry in biology. In physiology, prior to Darwin the form-function relationship had a teleological dimension. To wit, morphogenesis was thought of as a spontaneous generation driven by a crystallization process, or a type of self organization seldom overshooting fitness.[2] The fitness of the resulting shape was not distinguished from the mechanism of its action. Moreover, it was backed by observation and logical methods that disregarded the possibility of producing some new effects by means of experimental manipulations.

Nanotechnology apparently breaks with this cultural tradition. One strategy of inquiry in new materials consists in assuming that, even if they may violate the common (on Earth) natural processes, and possibly the physical laws passed down, as long as stuffs don't arise by accident, the explanation of their functioning cannot defy all logic. Yet, since both, the previous and the actual strategies of inquiry build on human logic and skills, there is the shifty danger of circular analysis expelling crucial data.[2] In facing unfamiliar situations extra care should be taken when "linearizing" observations with the aim at giving a step by step account of them. We briefly highlight some historical points impacting on our actual understanding of the structure-function relationship.

2.1. Optical microscopy in biology

First observations of microscopic features and cells are reported in Hooke's Micrography (1670). Yet, those microscopic evaluations were centered on the description of intriguing details, rather than on the explanation of their purpose. A cell theory was formulated around 1838 to interpret the tiniest tissue units whose structure could be discerned from microscope observations. Soon thereafter cell biologists started to pursue the link between the science of form and the intrinsic biological processes. To enhance visualization of cells components, staining techniques were also developed. Investigations pursuing basic causal/mechanical explanations of the observed biolog-

---

[1] In addition, form is inseparable from the stuff of each material tool.
[2] We are excluding direct theological explanations.

ical structures beyond the morphology were scanty before molecular biology caught on in the 1940s.[3] They began by observing the ultrastructure of fibrous proteins and collagen. Thus, for now, let's disregard the explanations of the fine points on the functioning of the most basic structures in living organisms, and let's focus on the shape of cells. Distortion of the images is already apparent at low magnification. Either one is willing to confer the form as a primary quality on things, or one believes that microscopes magnify the envelope of any tiny object point by point, perhaps apart from small shape distortions. In the latter case, Euclidean geometry leaves room for similitude but, for the purpose of basing the interpretation of images on it, there has to be more than similitude. Doing without geometry, perhaps no interpretative problems arise from traditional scientific explanations so long as the imaged shapes, that belong to the *optical response* indeed, can be identified with outer boundaries. Still, given that the morphology of organisms appears to be non-homogeneous on all known scales, the mechanical notion of form attributed to pieces of homogeneous matter is being extended well beyond the realm of mechanics.

When geometry is applied to the study of images obtained by linear optical instruments,[3] it only underpins "linear" transformations, indeed. Moreover, optical responses falling outside the gamut of imaging often arise from a non-linear behavior. We think that non-linear responses may affect the images. Among them we mention the effects of birefringence (double refraction), and optical rotatory power, i.e. the ability to rotate the polarization plane of light, owing to their historical importance. The detection of those small effects, after 1800, depends on the ongoing technical progress in the detection of optical signals. Both effects came to the fore when it was pointed out that, except for quartz, the main optically active media are organic compounds in the liquid phase. Pasteur discovered that tartaric acid ($C_4H_6O_6$) extracted from unripe grapes is optically active, while synthetic tartaric acid is racemic, and isn't. In this context, chiroptical phenomena[4] seem to mark bonding processes occurring in natural organic (living) substances.[4] Soon thereafter, Pasteur exhibited enantiomorphism as a subtle crystallographic difference associated with the optical power of solutions. Subsequently, attempts at determining the effect of crystallization on chiral molecules were started. After 1920 the biological function of proteins became related to their native folded tertiary structure, and structural biology initiated its structure-function program.[5] The program became devoted to the analysis of the DNA contained in the haploid cell of chromosomes, which for a while, especially after the elucidation of the DNA structure by Watson and Crick (1953), [6] was identified with the material base storing the information content on the development and functioning of the organisms.[5][7] Nowadays, the recombinant-DNA technol-

ogy, that uses yeast or bacterial vectors cells as a factory for the transgenic synthesis of human insulin, hormones, coagulants and the like, holds promise of also allowing the engineering of many new drugs and therapeutic agents. In contrast, the solid-phase chemical synthesis of active natural proteins keeps being challenging.[8][9] Once synthetic proteins mimicking the natural ones will be obtained, the difference between living organisms and new life-inspired structures will be expunged. In Fig. 1 below, we give an example of a stepwise explanation of digestion. In the light of the modern, more sophisticated theories it appears very rough. Nevertheless, comprehension of natural processes somehow always implies stepwise disassembling.
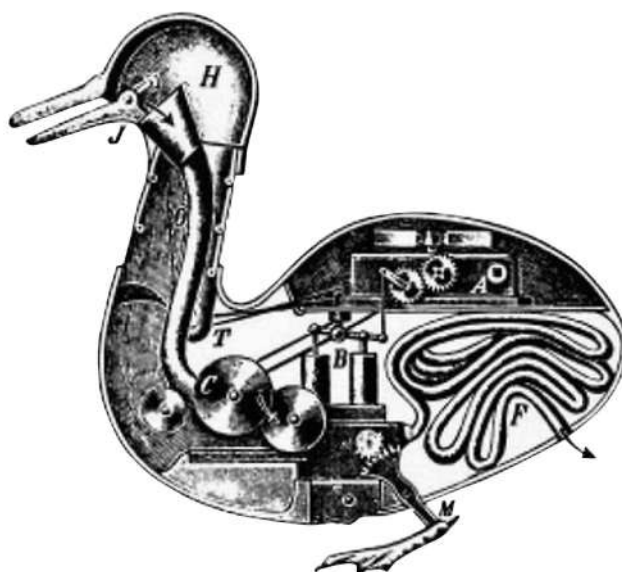

Figure 1: Duck of Vaucanson, showing the concept of bottom-up construction of living organisms other than humans in the 1700s. It gives a mechanical explanation of the digestive process, that was only partially understood by then.

2.2. Form-function in chemistry

The structural studies on molecules began at a relatively late stage.[6] Moreover, Mendeleev's table of the elements was endorsed by chemical analysis, synthesis, and function studies of inorganic salts performed by well-established methods. It led to formulating the electronic structure of the atoms rather then vice versa. For some time, following Lavoisier's system of chemistry, many scientists had repudiated the corpuscular conceptions of matter. We recall that during the 1800s, while Dalton's atoms, fitted with

---

[3] Abbe showed that for microscopy diffraction pattern and images are on equal footing.

[4] The two principal chiroptical phenomena are optical rotatory dispersion and circular dichroism.

[5] In the 1970s it was shown that the DNA in somatic cells also is com-

petent in the sphere of embryogenesis. Short thereafter the importance of the core histone proteins for the regulation of the gene expression during RNA transcription was pointed out.

[6] "Elective" affinity (Wahlverwandschaft) was among the first ideas pertaining to chemical reactions. Nowadays affinity is explained based on the valence bond theory (VB) of Heitler and London, while conformational analysis relies on molecular orbitals (MO).

size and weight, were rejected, thermodynamics laws were increasingly applied to inanimate chemistry. By dealing chiefly with equilibrium conditions, chemists could determine the stoichiometric coefficients that allow balancing many chemical equations. The idea that chemical reactivity is associated with the energy content of the reagents and reaction products gradually supplanted the notion of mutual attraction of substances, and led to the formulation of the law of mass action. The existence of that law doesn't mean that chemical reactivity was a well understood phenomenon.

2.2.1. Inorganic Crystals

Atoms and molecules apparently found their way into chemistry through crystallography. Haüy explained the crystallization out of an initial form of the germ. He spoke of a *molécule integrante*, a polyhedral shape around which the other molecules layer. Since he was only concerned with the physical structure and the static forces responsible for the gems' aspect, he didn't mull too much over the shape of the molecules themselves. Since the concept of chemical bond was quite alien, then, he also lacked a sharp distinction between mixtures and true compounds. In 1848, developing his mathematical theory of 14 regular crystal groups, Bravais assumed whole molecules to occupy a node in the crystal lattice. He held that their outer shell, that is now taken to be their hydration shell, is responsible for the overall crystal shape, while atoms are spheroidal or ellipsoidal in shape, like Dalton's.

The subjects related to the structure and orientation of small inorganic molecules were covered essentially by physicists. As Ewald remembers,[10] just before von Laue's discovery of single-crystal X-ray diffraction, people were studying double refraction and optical rotation (of solutions) to elucidate the relationship between the symmetry of the crystal lattice and that of its molecular constituents. In 1910, he himself was busy with calculations concerning the double refraction of light that results from electric dipoles oscillating in an ideal anisotropic lattice field. Albeit the story goes that one instance of compounds with the same composition, but showing a markedly different chemical behavior, belongs to the inorganic chemical synthesis,[7] stereochemistry, the subdiscipline of chemistry linking chemical reactivity to molecular structure, doesn't stem from crystallography. Rather, it plays a capital role in organic chemistry.

2.2.2. Relationship between structure and reactivity

Organic compounds are less stable and more prone to decomposition than the inorganic ones. Their analysis was cumbersome, and their synthesis raised such difficulties that their occurrence was connected with vital force. As just mentioned, Wöhler's synthesis of urea in 1828 is the first instance of an organic product artificially obtained from in-

organic reagents.[8] The reaction is explained as follows: (1) decomposition of lead cyanate by aqueous ammonia yields an ammonium cyanate solution, $Pb(OCN)_2 + 2NH_3 + H_2O \rightarrow PbO \downarrow + 2NH_4^+ + 2OCN^-$; (2) evaporation to dryness by warming in a water-bath causes isomerization of ammonium cyanate (NH_4OCN) to urea, $NH_4^+ + OCN^- \leftrightarrow NH_3 + CNCO \rightarrow H_2NCONH_2$.[9][11]

In 1830 Berzelius coined the term *isomerism* to relate the chemical properties of organic chemical compounds to their hypothetical structures – drawn on paper by their structural formulas – and initiated the structural theory of organic chemistry, as it were. The concept of molecular structure was only symbolic then, and relied on the functionalist conception. Van't Hoff even more than Kekulé contributed to the 3D extension of graphic representations by visualizing the tetravalent carbon atom as a tetrahedron (1874). Thereafter, if the effectiveness of chemical bonding was explained with steric effects, its modeling accuracy had to be inferred in retrospect from its explanatory power. Thus, a specific substituent, i.e. a functional group replacing a hydrogen atom in a hydrocarbon chain, could explain a hindered rotation. At a slow pace, in organic chemistry, too, the trend prevailed to regard theories as predictive tools. Only well after the refinement of optical methods in the 1880s chemists were moved into believing that the electromagnetic response bears evidence for the existence of individual mechanical structures from molecular size, and that pursuing matter organization at that level makes sense. After 1900, the interpretation of X-ray diffraction pattern of crystals according to the motto "small wavelengths are diffracted by small obstacles" corroborated that belief.[10] From WWII on, it is taken for granted that the chain of amino acids influences the local folding of the polypeptide chain as well as the overall three-dimensional structure of proteins. Nevertheless, the X-ray protein crystal analysis, which is considered the method for structure determination par excellence, is a hybrid prediction method that makes heavy use of computer simulations supplemented by sequence alignment scores, and of databases resources to evaluate the statistical significance. To assess the spatial organization of macromolecules, on the one hand, the source material needs to be integrated with conformational potential energy calculations, geometric algorithms, fluctuation models, and transition theories, that allow computers to render the images of the involved structures. On the other hand, with the breakthrough of the probabilistic interpretation of thermodynamics, form gradually dissolved into the information about the dynamical structure of the system under non-equilibrium constraints.[11] By relating the complexity of biological structures to their information content in-

---

[7] Stable silver (iso)cyanate (AgNCO) and detonant silver fulminate (AgCNO), led to a contention between Wöhler and von Liebig in 1825.

[8] Urea, like many other organic compounds, had been isolated much earlier.

[9] Urea is not produced by the same reactions in the liver of living beings.

[10] Form doesn't cause functioning by logical inference. Thus, stability and energy transfer calculations are required.

[11] In physics, the formulations of quantum mechanics are evolving from ontology to information.

formation theory overcomes the problem of distinguishing between structure and function. To restate it, in a rational world, the structure might encode all the information on the function, but in our irrational world we can think of recognizing some ultramicroscopic structure only after we gain some insight into the distinction between it and the small "spurious" effects of irradiation affecting the images.

3. System's Biology Approach

Bertalanffy's starting point in 1932 was the question about the applicability of the general principles of physics and chemistry to physiology. During that period the last vestige of teleological notions were reshaped borrowing either from mechanics or from cybernetics. Especially the II principle of thermodynamics became a pivotal point in the discussion of the extensibility of quantitative laws to biological systems. Like Prigogine and others, Bertalanffy took the energy flow as the driving quantity capable of explaining the principal features attributed to living systems, namely self-regulation, adaptation to external stimuli, ordering, reproduction and differentiation. He suggested the name *general system theory* for the new discipline, devised chiefly for the purpose of extending general principles to living systems. The biophysicists and physical chemists working in the domain of biology before 1953 – traditionally the starting year of the discovery of the DNA structure and function – tailored their mathematical models to suit some biological function, for instance morphogenesis, aside from all biological details.[12] To get an overview of the involved logical steps, they made use of physical analogies, thereby simplifying matters in a way unacceptable to most biologists.

Perhaps for that reason in the 2000s system theory was re-born as *systems biology* within the discipline of molecular biology. In its new role as bottom-up approach to living systems, it maintains its former features of managing biodiversity by pursuing simple general laws. It is concerned with a network composed of elements and relations, and its formal tools are differential equations, graph theoretical tools and cellular networks. Moreover, by maintaining independence from the concrete molecules taking part in the processes, it enables integration of various molecular network motifs at the level of the whole system. Finally, the development of computers in the interim allows handling complex networks of interaction, and cell signaling pathways.[12] Since computer simulation is conceived as the tool to manage detailed models of genetic and molecular networks, bioinformatics takes on a key role to the point where it doesn't matter whether data are experimental or computational. In brief, the understanding of the response properties of specific tissues and organs is based on their computer implementation, and draws upon what we already know about macromolecular reactions.[13] Clearly, the com-

putational conception of synthetic biology is by far less demanding with respect to a fully reductionist approach.

Neurobiology, likewise considers the general systems' strategy a method of choice for gaining information on the organization of the brain. Although its analysis focuses on the information content rather than on genome sequencing, there are bridges, such as neurogenomics, between it and bioinformatics.[13]

3.1. Physics of computation

The viability of idealizing assumptions is often indefinite. Since 1950, computational models were adopted to understand phenomena in some disciplines, including neuroscience. It makes sense to ask whether the form-function relationship is important, or the mind is in essence a computing machine, i.e. if its network structure can be modeled by machines. Information is represented by mathematical formulas and computation realizes a physical process.[14] The abstract and syntactic formality allows eliminating the "ghost in the machine". Taking a representational view of the mind, all brain functions are pooled under information processing in the broad sense. No precise mapping of the architecture of the nervous system is required to define the process of thinking with a language-like structure, since it can be analyzed at the neural network level. In the early days of the computer era people were interested in decoding conscious mental states, and tended to link metabolism especially to that brain activity. Neural networks have been developed as an alternative to classical theory of the mind, like von Neumann's centralized, sequential, and result-oriented architecture. At the network level a semantic content (distinct from the semantics of the natural language) is associated with the activation vectors. To model complex phenomena, recourse was taken to massively parallel distributed processing paradigms, and artificial neural networks, that are among the conceptually simplest yet difficult to grasp artificial intelligence (AI) techniques. Artificial neurons are endowed with a tiny amount of memory and the ability to exchange binary signals with given subsets of neurons, usually by layers (hidden units), thereby defining network topology and neurons' roles. According to the Church-Turing conjecture, an AI system works the same irrespective of the physical hardware which runs it. Going beyond binary computer science, a representation is a pattern of symbols that can emulate either the computer or the neural substrate.

As regards cognitive operations and neural codes, it is thought that the brain may provide a unique view of the relationship between energy and information. As the notion of computing engine is mathematically well characterized, it is expected that if an ultimate efficiency can be established for it, and AI is worth its name, that value can also be tentatively assigned to mental tasks. The worthiness

---

[12] The input signal driving a transition entails mutual information exchanged between the system and the input signal besides von Neumann entropy changes.

[13] In living organisms chemical reactions are expected to follow patterns different from single reactions occurring in cellular homogenates as

soon as compartmentalization becomes important. Until statistical inhomogeneities build up, the principles of non-equilibrium thermodynamics are supposed to explain energy driven self-assembly, and dissipative ordering processes.

of a computation could then be defined in terms of the energy dissipated in order to perform it, once powering up its Turing machine is excluded from the overall system's energy balance. Thermodynamics of computation traditionally looks for irreversible steps, drawing from a consideration by Maxwell on the extent to which a sharp-sighted tiny demon would be able to break the second law of thermodynamics. While Maxwell revolved around the tininess of the living observer, starting with Szilard in 1929 the question of breaking physical laws was resumed in connection with AI, and with the syntactic relations between symbols. An ideal gas can be seen as an oversimplification of a neural network. Indeed, in some types of neural networks, such as the self-organizing maps, topology is relaxed. To carry the similarity further, we might endow each neuron with attributes like mass, position, and velocity, as if it were a point particle. In addition, neurons need to exchange suitable messages so as to mimic elastic collisions. Following Shannon, we relate the amount of information with the entropy by $H = -\sum_{i=1}^{N} p_i \log_b p_i$, where p_i is the probability of occurrence of the ith character in the message string.[14] For binary codes $b = 2$. Yet, insofar as an equation is concerned, all mathematical transformations of it are equivalent (tautologies), in the sense that different mathematical expressions only differ subjectively. Thus, the ultimate value of the energy dissipated only for computation should be null. For dissipative systems, H is a lower bound. Beyond common machine learning algorithms, like linear or logistic regression, strategies for learning and intelligence could be implemented in thermodynamic computing systems by mimicking the physical intelligence.[15] While the link between energy and information may be established in this way, it is not integrable through many scales, for neurons are supposed to be highly integrated in a non-statistical fashion. Again, when speaking of energetic cost of information at a higher level a semantic content is added.

3.2. Spatial models

Rather than disassembling the brain into all its structures in the style of the phrenologists, the general systems theory endeavors to subsume functions like homeostasis and control, or like computing, learning and memory, into a manageable number of categories and identifies a level of abstraction appropriate for tracing them. Computer sim-

ulations are gaining ground because of the ever increasing amount of data to be processed, and also because of the expectation to find out some mechanism satisfying the requirement that the data show some understandable patterns.[16]. Especially in the marketing industry, it is supposed that a type of predictive intelligence of the above type can be observed in self-organized physical systems. Yet, from the outset, the application of system biology to the information processing by the brain was a bit less straightforward than information processing by biomolecular systems(see Fig. 2).
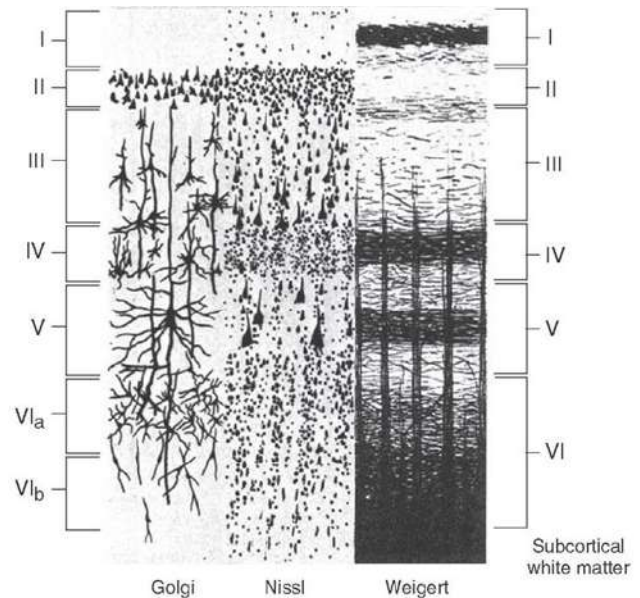

Figure 2: Hystological section through a granular cortical area from the pial surface to the subcortical white matter under the indicated staining conditions. The Golgi silver staining impregnates whole neurons. A Nissl basic dye stains nucleic acids mainly in cell bodies. Weigert-like type of staining is used for myelin sheets. I. Molecular layer; II. External granular layer; III. External pyramidal layer; IV. Internal granular layer; V. Internal pyramidal layer; VI. Polymorphic layer.

Going back to the overall form-function relationship, this has been pursued in two ways, either by explaining the molecular basis of the biological activity, or by exploring compartmentalized cellular structures. According to Capurro et al. the term "information" can be traced back to the knowledge of the form.[17] In fact, theoretical neuroscience faces mainly compartmentalization of structures and functions. The brain is a complex system, whose development is genetically organized, and whose functionality emerges during embryogenesis and childhood. For a short time saltatory conduction of the action potential was regarded as the cornerstone to uncover the function of the mind. It is at the origin of the classic computer-brain analogy, that bears on the encoding, transmission, storage and retrieval of information. Knowledge about neurotransmis-

---

[14] We recall that the entropy S is not itself a statistical notion. It was introduced to account for the direction of heat transfer between two contiguous bodies at different temperatures. It is such that $dS = \frac{\delta Q}{T}$ is a state function, and for isotherm processes it is linked to the system's internal (U) and free (F) energies by $\Delta F = \Delta U - T\Delta S$. Shannon's entropy is formally analogous to Gibbs' statistical entropy $S_G = -k_B \sum_{i=1} p_i \log_e p_i$ (for statistically independent degrees of freedom.) Here, the sum runs over all microstates i in the ensemble, and p_i is a multiplicity factor interpreted as the *a priori* probability of the ith microstate. Now, Gibbs' S_G is not a function of some microscopic dynamic magnitudes pertaining to the system, and only has significance in the thermodynamic limit, when Boltzmann's constant $k_B \approx 1.38 \times 10^{-23} m^2 kg s^{-2} k^{-1}$ relates S_G with temperature measurements (in kelvin units). In contrast, since in Shannon's entropy formula $-\log_2 p_i$ replaces the monotonic decreasing function $-\log_e p$ the physical meaning is lost.

sion at the level of the functional unit is based on electro-physiological measurements that led to the (already non-linear) Hodgkin-Huxley model of the neural events.[18] It assumes that the electrical stimulation is an allowed input (message), and that transmission occurs like in vivo (the message is correctly encoded). To extend causality from electrophysiological preparations involving an individual neuron to higher brain functions, we need to start from the above "simple process", and establish contact with stages of higher complexity, capable of accounting for the living brain's functions. Neural network modeling started in the 1970s as a consequence of Rall's pioneering work on the electrical properties of neurons. It modeled the effect of synaptic integration on neural excitability.

The mind is but an aspect of brain functioning. For example, while computation is mainly a cortical activity, learning and memory are activities under cortical control, but located in the hyppocampal region of the limbic system. For another example, by fractionation several kinds of neurons have been isolated, which have led to investigate the immunochemistry of synaptic proteins, and the glia-neurons interface. Recent studies of the latter interface show that in the neural hypothalamus (Fig. 3) – a part of the limbic system containing a number of small nuclei – the glia-neurons interactions have homeostatic and regulatory function.
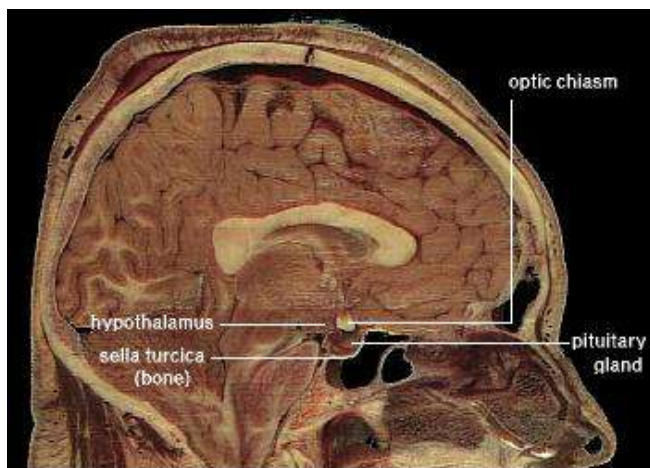
Figure 3: Anatomical location of the hypothalamus, a structure belonging to the limbic system (from Wikipedia).

Multiscale modeling is developed in neuroscience as a means to account for the fact that the brain includes many different and interlaced structures. An amount of already available biological knowledge on the cerebral functions is incorporated into the data in proceeding from the neuron to the neural network. To define a functional state large scale neural networks rest on emergency. Yet, in some quarters a lack of data to be able to cope with simulations is admitted.

4. Imaging Information

In basic cognitive neuroscience research the brain is studied according to psychological criteria, and the mental states are assumed to carry along beliefs, desires and attitudes, besides knowledge and thoughts. The computer metaphor became outdated with the emergence of neural networks, whose underlying paradigm is the parallel distributed network processing. The pattern of activation of elements corresponds to the flow of activation in the net. Implementing those networks, both the mechanism and the structure can be addressed according to location, thus granting the link of specific cognitive functions to specific regions of the brain. When neural networks are combined with a multiscale approach, the stimulus field is parceled into small receptive entities, and the macroscopic representation of messages emerges in a statistical sense. These methods aim at a concept-based bridging of the gap between organization of mental processes and the statistical molecular processes underlying them. At the bottom, the latter are those accounted for by electrophysiological parameters belonging to neuronal populations, and by the chemical phenomena correlated with them. In the next step, data driven modeling is expected to allow correlating the neurobiological and the psychic functions. Finally, based on a restricted sample of tasks, and on picking out systematic relationships between brain organization at the cellular level and behavior, this analysis should lead to an understanding of the underlying mental architecture that supports cognitive functions.

Coming to medical imaging techniques, the neurological access to mental states is reached as a top-down approach. The theories of brain mechanisms are used to explain information processing subject to the same reductionist strategy as intelligence. Yet, none of the functional imaging techniques, such as positron emission tomography (PET), functional magnetic resonance imaging (fMRI), and recently magnetoencephalography (MEG) is capable of directly measuring the electrical and chemical processes that mediate brain function. Conventional approaches are multimodal, whereby networks are reconstructed independently for each modality – usually fMRI and electroencephalography (EEG) – and take place through structural equation modeling procedures and autoregressive models. The process from the input sensations to the production of the code is increasingly understood as the evolution of a dynamic system, that responds to an input and a set of constraints, and approaches the output as an equilibrium state. The output is the "best inference" according to the maximum entropy theorem. A consistent account of the self-organization – whose EEG correlate are the cortical synchronizations – is given in terms of general dynamical laws and the known principles of neurophysiology. In particular, fMRI images are believed to show, on the average over space and time, the haemodynamics locally accounting for the neural activity.[15] It has been proposed that, when the dynamic causal modeling is applied, fMRI responses should

---

[15] The rates of change in firing rates differ by several orders of magnitude from the hemodynamic adjustments.

be predictable from simulations of the underlying neuronal responses.[19]. The fine details on the connections between areas require specification of a prior anatomical model, that is known from tracer studies on primate brain. The model devised allows for arbitrarily complex, nonlinear relationships between the stimulus and the neuronal activity. However, owing to the fact that the fundamental concern is cortical circuitry and the ways in which information is elaborated by the brain, other characteristic traits of it are neglected. On one hand there are many possible definitions of activity, such as the average firing rate of the neurons, the synchronous spiking activity across the neuronal population, and the local field potential (LFP). On the other hand, a very large scale integration (VLSI) of the activity involved in the brain's thoughtful performance is necessary to dynamically explain the model by mimicking stipulated biological details. Reasonable assumptions are that the effects can be summed over time, and that the blood supply is directly related with the neuronal activity on a local basis. Notwithstanding Wiener's famous quote: "Information is information, not matter or energy" the information content of neurobiological systems is being evaluated as if it could be directly inferred from energy changes, or as if it would "ride on the energetic flux". As a matter of fact, besides supporting the firing rate of local neuronal populations in response to attentional stimuli,[20] the blood supply supports brain activity in the task-free resting state (RSN),[21] as well as the activity of incoming fibres, interneurons, and inhibitory/excitatory synaptic activity in subcortical areas.[16][22] Furthermore, it supports the glia[23]. While neurons rely on oxydative glycolisis, and thus on oxigen consumption, it is known that astrocytes rely on non-oxidative glycolysis for the clearance of glutamate from the extracellular space, and for its conversion into the neurotransmitter glutamine. Presently, the average synaptic activity cannot be evaluated directly. Nevertheless, besides being related to oxygen consumption, the blood flow also depends on the glucose levels, and on other factors.[17]

Compared with the impact the first X-ray radiographs had on laypersons, subsequent medical imaging techniques were welcomed with less sensation. Since they need sophisticated acquisition techniques, and are very expensive, they never got off the healthcare environment. As a consequence the quite detailed magnetic resonance images were promptly compared with anatomy tables, and their power in diagnosing tumor formation and other illnesses, among which stands out multiple sclerosis, was tested. Magnetic resonance imaging (MRI) is sensitive to the anatomophysiological environment and chemical composition without the need of staining tissues. Contrast and brightness depend in a complicated way on tissue parameter, among which are diffusion and flow. In addition, there arise small distortions due to nearby tissues of different permittivity. Thus, differently from anatomical tables, the observed shapes and intensities, that are defined by the image acquisition parameters, already contain individual, i.e. nonrandom, functional information on living beings. These observations are being slowly retrieved when the exigences clearly require it. A comparison of Hooke's and modern microscope shots suggests that the very first progress possibly lies in acknowledging the innovative nature of the MRI technique and its features.

5. Conclusions

To this day, computerized approaches aim at integrating into a unique model haemodynamic patterns obtained by fMRI and standard measurements of evoked potentials deploying microelectrodes. If structure and function were mutually entailed by each other, multiscale methods would allow to simulate the brain's functional organization as a whole. Instead, in going from patch clamping to the functional MRI views of cerebral activity not only the scale changes, but in addition the types of measurement techniques are quite unrelated. Moreover, the diligence necessary to fine tune acquisition parameters reveals a difficulty in telling form from function of what appear like MRI anatomical snapshots. Under those conditions, until the conditions of contrast, brightness and distortion of the images are not cleared further, it may become difficult to disentangle observations from modeling assumptions, and the mechanisms behind conscious processes may approach the laws of thought.

References

[1] B. A. Grzybowski, W. T. S. Huck, The nanotechnology of life-inspired systems, *NNANO* 11(7): 585–592, 2016.

[2] N. Kriegeskoorte, W. Kyle Simmons, P. S. F Belgowan, C. I. Baker, Circular analysis in systems neuroscience: The dangers of double dipping, *Nat. Neurosci.* 12(5): 535–540, 2009.

[3] R. Olby, The macromolecular concept and the origins of molecular biology, *J. Chem. Educ.* 47(3): 168–174, 1970.

[4] S. M. Kelly, T. J. Jess, N. C. Price, How to study proteins by circular dichroism, *Biochim. Biophys. Acta* 1751: 119–139, 2005.

[5] G. B. Smejkal, The meaning of 'native', *Expert Rev. Proteomics* 10(5): 407–409, 2013.

[6] L. A. Pray, Discovery of the DNA structure and function: Watson and Crick, *NNANO* 11(7): 585–592, 2016.

---

[16] In their opinion fMRI data "reflect the input and intracortical processing of a given area rather than its spiking output."

[17] The basal glucose consumption in brain amounts to 20% of the glucose metabolized by the whole human organism. Thus, however high the goal-directed local energy consumption, the rise of whatever indicator bound to it, if any, can possibly be only marginal. In addition, it is difficult to quantify the contribution due to different cell types, and their different and correlated metabolism.

[7] N. C. Mullins, The development of a scientific specialty: The phage group and the origins of molecular biology, *Minerva* 10(1): 51–82, 1972.

[8] P. E. Dawson, S. B. H. Kent, Synthesis of native proteins by chemical ligation, *Annu. Rev. Biochem.* 69(7): 923–960, 2000.

[9] W. Hou, X. Zhang, C.-F. Liu, Progress in chemical synthesis of peptides and proteins, *Trans. Tianjin Univ.* 23: 401–419, 2017.

[10] P. P. Ewald, A review of my papers on crystal optics 1912 and 1968, *Acta Cryst.* A35: 1–9, 1979.

[11] G. B. Kauffman, S. H. Chooljian, Wöhler's synthesis of artificial urea, *J. Chem. Educ.* 56(3): 197–200, 1979.

[12] E. Fox Keller, *Making sense of life,* Harvard University Press, Cambridge (Mass), 2002.

[13] E. De Schutter, Why are computational neuroscience and systems biology so separate?, *PLOS Comput. Biol.* 4(5): 1–6, 2008.

[14] G. Dodig-Crnkovic, Significance of models of computation, from Turing model to natural computation, *Minds and Machines* 21: 301–322, 2011.

[15] R. L. Fry, Physical Intelligence and Thermodynamic Computing, *Entropy* 19(3): 107, 2017.

[16] H. Kitano, System biology: A brief overview, *Science* 295(5560): 1662–1664, 2002.

[17] R. Capurro, B. Hjörland, The concept of information, *ARIST* 37(8): 343–410, 2003.

[18] D. B. Tower, *The nervous system. Vol.3 Human communication and its disorders,* Raven Press, New York, pp. 81–96, 1975.

[19] K. J. Friston, K. H. Preller, C. Mathys, H. Cagnan, J. Heinzle, A. Razi, P. Zeidmaneh, Dynamic causal modelling revisited, *Neuroimage* 2017.02.045: 15 pp., 2017.

[20] K. J. Friston, Models of brain function in neuroimaging, *Annu. Rev. Psychol.* 56: 57–87, 2005.

[21] M. E. Raichle, Two views of brain function, *Trends Cogn. Sci.* 14(4): 180–190, 2010.

[22] N. K. Logothetis, What we can do and what we cannot do with fMRI, *NATURE* 453(12): 869–878, 2008.

[23] L. Hertz, Intercellular metabolic compartmentation in the brain: past, present and future, *Neurochem. Int.* 45: 285–296, 2004.

Antenna and Propagation

Transmission line with square modulation in time of the capacitance and/or inductance

José Gabriel Gaxiola Luna*, P.Halevi

Department of electronics
National Institute of Astrophysics, Optics and Electronics, Puebla, México
*corresponding author, E-mail: gxluna@inaoep.mx

Abstract

We studied wave propagation in a lumped transmission line with square modulation in time of the capacitances and/or inductances. Large band gaps in the propagation constant are obtained, although the case of equal, in-phase modulation is exceptional, with no gaps at all. Important to note, a finite resistance can be overcome with sufficiently strong modulation, resulting in no attenuation of the oscillations.

1. Introduction

A transmission line (TL) with capacitors that are periodically modulated in time can give rise to stop bands in the propagation constant β, rather than the frequency (as occurs for spatially periodic systems). This was demonstrated recently, theoretically and experimentally, employing nonlinear capacitances $C(V)$, the voltages V in all unit cells of the TL being modulated in tandem harmonically [1, 2]. In the present work we study theoretically the case of square modulation of $C(t)$ and, in addition, square modulation of the inductance $L(t)$ as well. Propagation in the corresponding effective medium, with harmonic dependence in time of the permittivity $\epsilon(t)$ and permeability $\mu(t)$, also resulted in β-gaps [3].

2. TL with square modulation of C(t) and /or L(t)

In our lumped, infinite, low-pass TL, the capacitance and inductance modulations are modeled as shown in Fig.1, with the strengths of modulations (m_C and m_L) also defined there. Note that $C(t)$ and $L(t)$ have equal (circular) modulation frequencies Ω ($= 2\pi/T$) and that the abrupt transitions occur simultaneously for both. However, they are not necessarily in phase: $C(t)$ can increase at the instants of time when $L(t)$ decreases, in which case the modulations would be out of phase. Our TL also includes a resistance R.

3. Calculation

Fig.1 suggests that the Kronig-Penney method, introduced a century ago as a toy model for calculating the first crystalline band structure [4] could be useful for the problem at
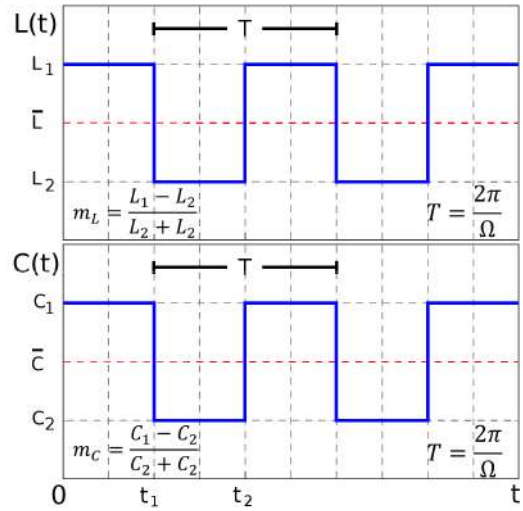
Figure 1: Identical, square modulation in time of the capacitance and/or inductance in every unit cell of the TL.

hand. Indeed, this method leads to a greatly simplified solution of Kirchhoffs laws, applied to our TL. It can be proved that the correct boundary conditions at the temporal interfaces are the continuities of the capacitor charge $Q(t)$ and the magnetic flux $L(t)I(t)$ through the inductors, where $I(t)$ is the current. The temporal periodicities of $C(t)$ and $L(t)$ imply that the Floquet-Bloch theorem must be satisfied:

$$Q(t+T) = Q(t)e^{-j\omega T} \tag{1}$$

with an analogous equation for the flux $L(t+T)I(t+T)$. Here ω is the frequency of the propagating wave. This leads to four homogeneous equations and a closed form solution of this eigenvalue problem:

$$-\frac{1 - m_L m_C}{\sqrt{(1 - m_L^2)(1 - m_C^2)}} sin\left(\omega_1 t_1\right) sin\left(\omega_2 t_2\right)$$
$$+ cos\left(\omega_1 t_1\right) cos\left(\omega_2 t_2\right) = cos\left(\frac{2\pi\omega}{\Omega}\right) \tag{2}$$

$$\omega_k = \frac{2sin\left(\frac{\beta a}{2}\right)}{\sqrt{L_k C_k}} \quad k = 1, 2. \tag{3}$$

This is an implicit dispersion relation (here, for simplicity, not including the resistance R) that relates the frequency ω and the propagation constant β. It is seen that it is periodic in ω, the period being Ω, and also in β, with period $4\pi/a$, where a is the size of the unit cell or lattice constant.

4. Numerical results for the dispersion relation

Eqs.(2) and (3) can be normalized, so we plot the reduced frequency ω/Ω versus the reduced propagation constant βa. The parameters are the modulations m_C and m_L. In Fig.2 we consider the case of purely capacitance modulation, with $m_L = 0$. This is a band structure with β pass-bands separated by β stop-bands. The nearest approach of the bands is at $\omega = (1/2)\Omega$, or $(3/2)\Omega$, etc, at which heights the band-widths and band gap-widths are defined. It is seen that the gaps strongly increase in size as the modulation is increased from $m_C = 0.35$ to 0.65. Also, the periodicity in ω is apparent and the group velocity vanishes at the border of the Brillouin zone $\beta = \pi/a$. In Fig.3 the capacitance and inductance are both modulated, equally in strength ($|m_C| = |m_L|$). For in-phase modulations (blue lines) there are no band gaps, while out-of-phase modulations (red lines) give rise to large gaps. The disappearance of the gaps in the first case can be understood from the equality of the impedances $\sqrt{L_1/C_1} = \sqrt{L_2/C_2}$ which essentially eliminates the temporal interfaces in Fig.1.

When eqs.(2) and (3) are generalized to allow for a finite resistance R, the frequencies ω_k become complex, and so does the propagation constant β, its imaginary part describing attenuation of the wave. While in general $Im(\beta a)$ increases with R, surprisingly, it can vanish for $\omega/\Omega = 1/2, 3/2, ...$ provided that the modulations are sufficiently strong (for a given R) or that the resistance is sufficiently weak (for given $m_{C,L}$). As seen in Fig.4, this happens in all cases except equal in-phase modulations, as can be expected.
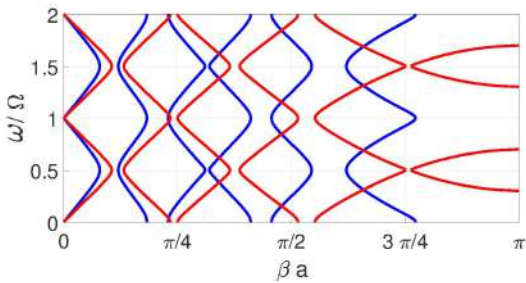
Figure 2: Normalized band structures for two values of the modulation m_C : 0.35 (red) and 0.65 (blue), with $m_L = 0$.

5. Conclusions

In comparison to harmonic modulation [1-3], the β-gaps for square modulation (Figs.2 and 3) are considerably larger. In fact, in the former case only the first gap is substantial,
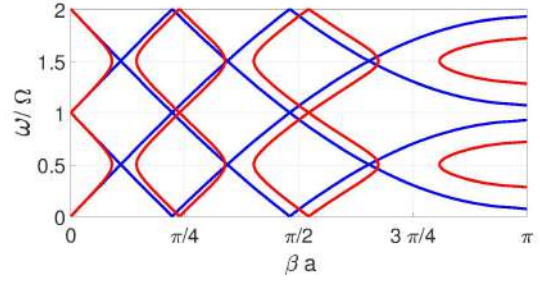
Figure 3: Band structures for equal modulations, $m_C = m_L = 0.35$, for in-phase (blue) and out-of-phase (red) modulations.
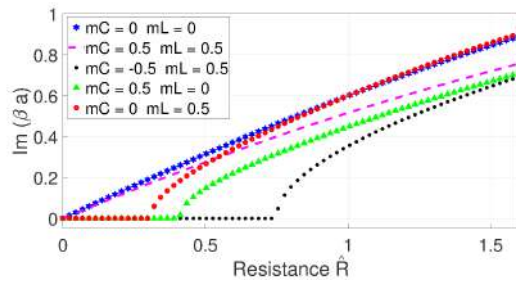

Figure 4: Attenuation coefficients for five cases of modulations vs. resistance.

while in the latter case higher order gaps can be larger than the first one. This suggests that square modulation is more appropriate for the investigation of temporally modulated systems. No band gaps exist when the wave impedance remains unchanged by the modulation, namely in the case of equal, in-phase modulations of the capacitance and inductance. Finally, a sufficiently strong modulation can overcome resistive effects, giving rise to *un*attenuated oscillations.

References

[1] J. R. Reyes-Ayona and P. Halevi, Transactions on Microwave Theory and Techniques **64**, 3449 (2016).

[2] J. R. Reyes-Ayona and P. Halevi, Appl. Phys. Lett. **107**, 074101 (2015).

[3] J. S. Martínez-Romero, O. M. Becerra-Fuentes, and P. Halevi, Phys. Rev. A **93**, 063813 (2016).

[4] C. Kittel. Introduction to Solid State Physics, Chapter 7 (Wiley and Sons, New York, 2005).

Wave propagation in a band-pass transmission line with periodically modulated capacitors

Alexander Gómez-Rojas[*]**, Uriel Algredo-Badillo and P. Halevi**

Department of Electronics,
Instituto Nacional de Astrofísica, Óptica y Electrónica (INAOE), Puebla, México
corresponding author, E-mail: agomez@inaoep.mx

Abstract

We study wave propagation in a band-pass transmission line whose capacitances are modulated in time periodically. Kirchhoff's laws lead to an eigenvalue problem with exotic solutions for the dispersion relation, depending on the ratio of the modulation frequency and resonance frequency of a unit cell. Simulations with modulation sources and a signal source confirm that the current wave contains multiple harmonics and that it travels a distance given by the product of the group velocity and time of propagation.

1. Introduction

In a recent study of wave propagation in a *low-pass* transmission line (TL) with periodically modulated capacitors the dispersion relation $\omega(\beta a)$ was found to exhibit pass-bands of the phase advance βa, separated by βa stop bands (rather than the usual frequency (ω) pass and stop bands) [1]. This and other interesting results motivated us to turn our attention to the periodically modulated band-pass TL. Similar ω-bands were also obtained in the effective-medium approximation with periodically modulated permittivity $\epsilon(t)$ and/or permeability $\mu(t)$ [2]. The capacitances in each unit cell of the TL can be modulated by means of (voltage-dependent) varactors or by generalized impedance converters (GICs) [3].

2. Band structure $\omega(\beta a)$

Each unit cell of the TL is composed of a dynamic capacitance $C(t)$, a resistance R, and two inductances L; neighboring cells are linked by a mutual inductance M (that can be replaced by the "T" model for $M < 0$). In order to derive the dispersion relation $\omega(\beta a)$ we remove the modulation source V_Ω and the wave source V_ω in Fig.2(a) and consider the TL to be infinite in length. The voltages induced by the two neighboring cells must include phase advance factors $e^{(\pm j\beta a)}$, where a is the size of the unit cell. The capacitances, being periodic in time (period $T = 2\pi/\Omega$, where Ω is the modulation frequency), can be expanded in a complex Fourier series:

$$\frac{1}{C(t)} = S(t) = \sum_r S_r e^{-jr\Omega t} \qquad (1)$$

Using Kirchhoff's laws, we derived a differential equation for the charge wave $Q(t)$ flowing through the capacitors. This equation is solved by the Floquet-Bloch theorem, stating that the charge oscillation itself is modulated periodically in Ω:

$$Q(t) = e^{j\omega t} \sum_n Q_n e^{-jn\Omega t} \qquad (2)$$

These substitutions convert the differential equation into an eigenvalue equation for the Fourier coefficients of the charge Q_n:

$$\sum_n \big\{ (\omega - r\Omega)S_{r-n} + [jR(\omega - n\Omega) $$
$$-2[L + M\cos(\beta a)](\omega - n\Omega)^2 \delta_{rn}]\big\}Q_n = 0 \qquad (3)$$

The indeces r and n run through all integers, so this is an infinite number of equations for the infinite number of unknowns Q_n. The periodicity of our TL in both time and space is here transformed, respectively, into periodicity of ω and βa. The requirement that the determinant of the coefficients vanish relates ω to βa, thus establishing the dispersion relation for the waves in the TL. It is convenient to define the following normalized quantities:

$$\hat{\omega} = \frac{\omega}{\Omega},\ \hat{\Omega} = \frac{\Omega}{\omega_0} = \Omega\sqrt{\frac{L}{S_0}},\ \hat{M} = \frac{M}{L},\ \hat{R} = \frac{R}{\sqrt{S_0 L}} \quad (4)$$

For simplicity, we assume that the modulation is harmonic, namely

$$\frac{1}{C(t)} = S(t) = S_0 + 2S_1\cos(\Omega t) = S_0[1 + m\cos(\Omega t)] \quad (5)$$

where $m = 2S_1/S_0$ is the modulation strength.

The parameter $\hat{\Omega}$ is the ratio of the modulation frequency Ω and the resonance frequency ω_0 of a unit cell; the dispersion $\omega(\beta a)$ depends crucially on its value. In Fig.1 we show a few selected cases of an extensive atlas. Each figurine renders just a single period Ω in ω and a single period 2π in the phase advance βa.
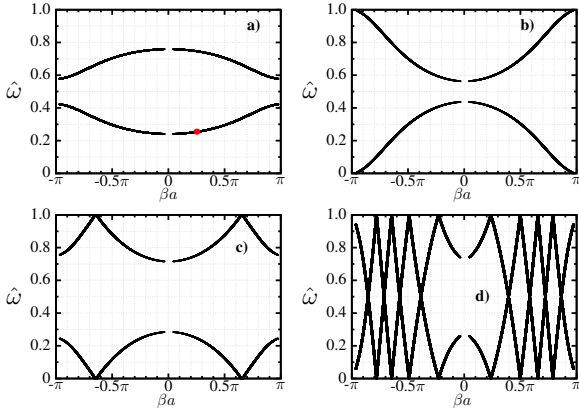
Figure 1: Frequency ω versus phase advance βa for several values of the parameter $\hat{\Omega} = \Omega/\omega_0$ with (a) $\hat{\Omega} = 2.4$, (b) $\hat{\Omega} = 1.0$, (c) $\hat{\Omega} = 0.798$, (d) $\hat{\Omega} = 20.1$.

In Fig.1 $M > 0$; the corresponding dispersion for $M < 0$ is obtained simply by a shift π of βa. In addition to these features that exist even in the ideal case, there is a signature effect of the finite resistance $\hat{R}$: small gaps in βa that appear near $\beta a = 0$ and $\pm\pi$. These gaps can be shown to be proportional to $\sqrt{\hat{M}}$.

3. Simulations

We proceed with simulations based on a realistic description of the band-pass TL in Fig.2(a), now incorporating both sources V_Ω that modulate the capacitors and a signal source V_ω. In Fig.2(b) we show the behavior of the current as function of time in one unit cell of the TL. We can observe a rapid oscillation of period $T = 1$ ns (corresponding to the modulation frequency $\Omega/2\pi = 1$ GHz and a slower oscillation of period 3 ns (corresponding to a propagating wave of frequency $\omega/2\pi = 0.333$ GHz). This is what can be expected from the Floquet-Bloch theorem, eq.(2). The corresponding Fourier transform, Fig.2(c), demonstrates that several harmonics $|\omega - n\Omega|$
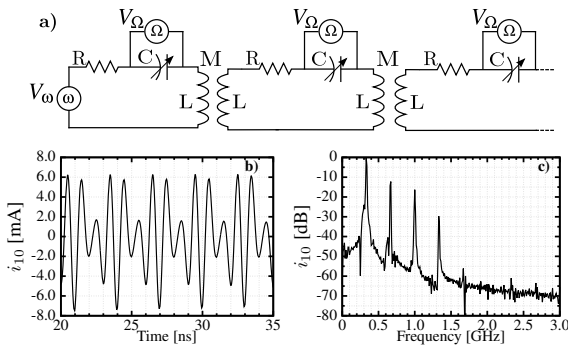
Figure 2: (a) Band-pass transmission line with sources V_Ω that modulate the capacitors and sources V_ω of the propagating wave. (b) Simulation of the current $I(t)$ in the unit cell $N = 10$. (c) Fourier transform of $I(t)$ in (b).
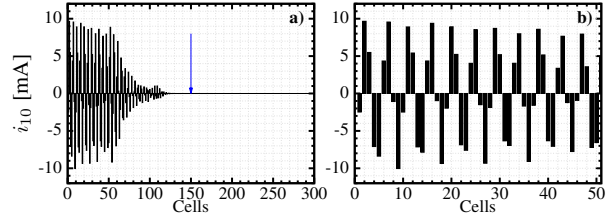
Figure 3: (a) Simulation of the current amplitude in a TL with 300 unit cells, 300 ns after launching a wave of reduced frequency $\hat{\omega} = 0.244$. (b) Zoom of the first 50 cells, confirming that the wavelength is $\lambda = 10a$. This simulation corresponds to the point $(\hat{\omega}, \beta a)$ indicated by a red dot in Fig.1(a)

have been significantly excited. This is explained by both the large modulation $m = 0.6$ and the small resistance parameter $\hat{R} = 0.01$ selected.

In Fig.3(a) we simulate a current wave $t = 300$ ns after it was launched. A reduced frequency $\hat{\omega} = 0.244$ was selected, to which there corresponds a wavelength $\lambda = 2\pi/\beta = 10a$ according to the dispersion relation in Fig.1(a), see red dot pointing at chosen $(\omega, \beta a)$ point. The group velocity $v_g = d\omega/d(\beta a)$ at this point is about 5×10^8 unit cells/s, thus the wave front can be expected to have reached the cell # $v_g t = 150$, in reasonable agreement with Fig.3(a). The zoom in Fig.3(b) beautifully confirms that the wavelength is indeed 10 unit cells, with rapid variations of the current from cell to cell.

4. Conclusions

A band-pass transmission line gives rise to exotic dispersion relations $\omega(\beta a)$. These depend qualitatively on the parameter $\hat{\Omega} = \Omega/\omega_0$, namely the ratio of the modulation frequency and the LC resonance frequency of a unit cell. Resistive effects give rise to small, distinctive gaps in b. Finally, realistic simulations that include a signal source and a modulation source in every cell, confirm that the propagating wave incorporates numerous harmonics $|\omega - n\Omega|$ and that its propagation distance is proportional to the group velocity $d\omega/d(\beta a)$.

References

[1] J.R.Reyes-Ayona and P.Halevi, Appl.Phys.Lett. **107**, 074101(2015) and IEEE Trans.Microw.Theo.Tech.**64**,3449(2016).

[2] J.S.Martinez-Romero, O.M.Becerra-Fuentes, and P.Halevi, Phys.Rev.A **93**,063813(2016) and references therein.

[3] F. Yuan, CMOS Active Inductors and Transformers. Springer, 2008.

Microwave Propagation and Transmission within a Small Spacecraft for Replacing Wired Buses

— *Effects of Antenna Polarization* —

Miyuki Hirose and Takehiko Kobayashi

Wireless Systems Laboratory, Tokyo Denki University, Tokyo, Japan
E-mail: miyuki@mail.dendai.ac.jp

Abstract

Path gains and throughputs were measured within a small spacecraft for various antenna settings and polarizations. A use of ultra-wideband technology within spacecrafts has been proposed with a view to partially replacing wired interface buses with wireless connections. A series of microwave (wideband and ultra-wideband) measurement campaigns were conducted within the small spacecraft. Polarization configurations were found to produce almost no effect on average power delay profiles and substantially small effects on the throughputs.

1. Introduction

Since data buses used in manned spacecrafts are required to be tripled, the weight becomes further significantly heavy [1]. A use of wireless connections within the spacecrafts could contribute to: (i) reduction of cable weight and launching cost as a result, (ii) reduction in the cost of manufacture, and (iii) more flexibility in layout of spacecraft subsystems, and (iv) more reliable connections at rotary, moving, and sliding joints. Numerous studies have been conducted about UWB radio propagation [2,3]. In a spacecraft, narrowband (2.4 to 2.5 GHz) wireless links were numerically calculated and evaluated in [4]. A demonstration based on impulse radio-UWB was described in [5]. Narrowband wireless communication systems suffer flat fading in multipath environments, hence need a substantial amount of fading margin, and only yield a low data rate. The wideband nature of UWB signals yields less susceptibility to fading due to the greater resolvability of the multipath components [6]. Within actual spacecrafts, transmitting and receiving antennas may be installed at any position and at any orientation. In this paper, various combinations of antenna, setting, and polarization configuration were examined within a mechanical test model (MTM) of a small scientific satellite.

2. Measurement setup

An MTM of a small scientific satellite "INDEX" (launched in 2005) was used for the measurement, as shown in Fig. 1. The MTM was a rectangular parallelepiped, 430 mm long × 470 mm wide × 435 mm high, enclosed in flat honeycomb
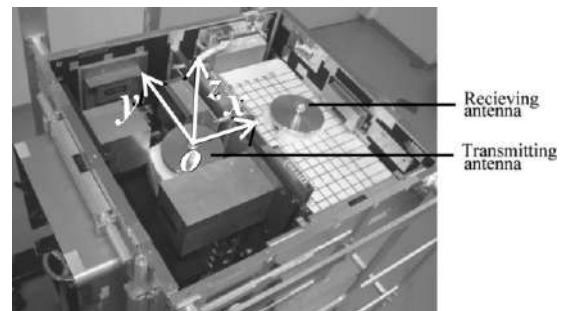
Figure 1: Inside of a spacecraft under test. The *x,* y, and *z* axes of the coordinate were parallel to the sides of the MTM, and the origin was located at the electric center of the transmitting antenna.
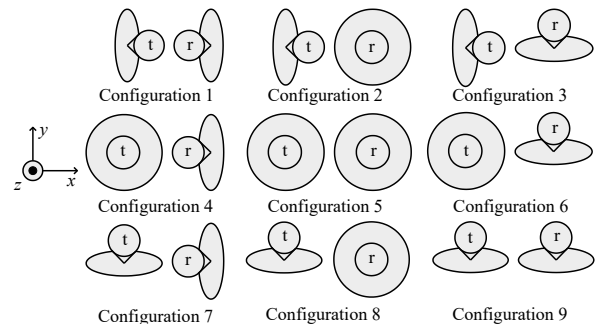

Figure 2: Polarization configurations for transmission (t) and reception (r).

panels made of aluminium, excluding its solar panels [6]. Its interior was divided into two nearly equal subspaces by a honeycomb partition having several openings. The transmitting and receiving antennas were omnidirectional, vertically polarized, low voltage-standing-wave-ratio UWB monopole antennas [7]. The feeding coaxial cables penetrated through the apertures on the sides. Frequency- (from 3.1 to 10.6 GHz) and time-domain propagation gains were measured with a microwave vector network analyzer. The antenna settings were either line-of-sight (LOS) or non-LOS (NLOS): they were located either in one of the subspaces (LOS) or across the partition (NLOS). The antennas were among the nine configurations depicted in Fig. 2: configurations 1 to 9 represent *xx, xy, xz, yx, yy, yz, zx, zy,* and *zz* polarizations, where the first and second letters denote transmitting and receiving polarizations, respectively. The distance between the antenna phase centers was 200

mm for all settings and polarization configurations.

3. Results

3.1. Propagation gains

Propagation gains ranged 60 dB for CW, from 3 dB for the full-band UWB in NLOS cases. The fading depth versus frequency bandwidth of polarization configurations at the deepest dead spots were derived from measured data, as shown in Fig. 3, where the center frequency was fixed at 6.85 GHz, and the 7.5-GHz-bandwidth propagation gain was set to the 0-dB reference. A bandwidth over 500 MHz was capable of reducing the fading depth to approximately 5 dB for the MTM.

3.2. Time domains

Examples of smoothed power delay profiles measured for the 9 configurations are presented in Fig. 4 where moving average was taken over 5 ns. Almost the same smoothed delay profiles were obtained at any setting and for any polarization configuration: no apparent effects of polarization configurations were observed in these heavy-multipath, metal-enclosed environments. The levels of the smoothed delay profiles for LOS typically exceeded 10 dB compared with those for NLOS.

3.3. Transmission performance

A commercially-available device of WiMedia [8] was used to measure link throughput. Its specifications are listed in [6]. The link throughputs were measured with use of a pair of WiMedia devices. Since the throughputs fluctuated typically ±4 Mb/s per trial, a number of trials (normally 35) were carried out to reduce the variation within ±1 Mb/s.

The delay spreads ranged respectively from 7.3 to 12.0 ns (LOS) and from 14.2 to 17.2 ns (NLOS) for 7.5-GHz bandwidth. The throughputs ranged

- 98.4 Mb/s for NLOS and 101.2 Mb/s for LOS in low-band UWB
- 100 Mb/s for NLOS and 102.8 Mb/s for LOS in high-band UWB.

Apparently LOS resulted in higher throughputs than NLOS, while no significant differences were observed between the low- and the high-band UWBs.

4. Conclusions

These studies conducted a series of propagation measurements which were carried out within heavy multipath environments. Wideband, ultra-wideband (from 3.1 to 10.6 GHz), and CW (6.85 GHz) propagation were measured and characterized within a small spacecraft. No dependence on the antenna locations and polarization configuration for transmission and reception was found for the average power delay profiles. The medians of the propagation gain for LOS were approximately 10 dB higher than those for NLOS. The delay spreads for LOS were notably shorter than those for NLOS. The throughputs for LOS were higher than those for NLOS, but the difference was less than 10%. No significant differences in the
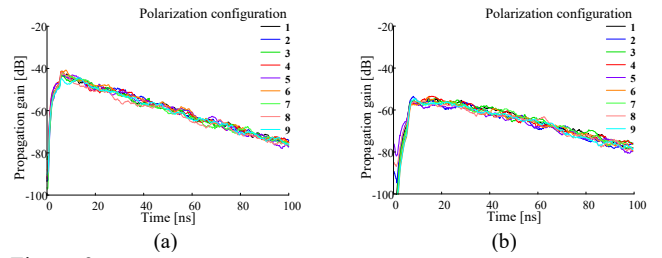

Figure 3: Average power delay profiles obtained at (a) Setting 3 (LOS) and (b) Setting 6 (NLOS) for nine polarization configurations.
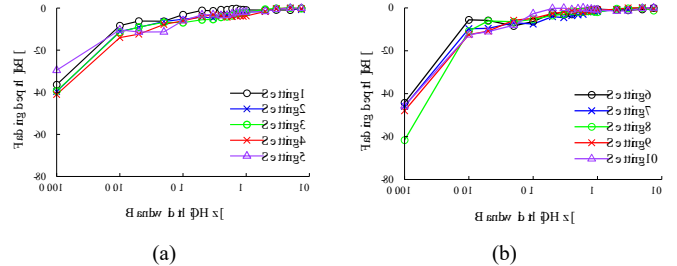

Figure 4: Fading depth versus occupied bandwidth of polarization configurations: (a) LOS and (b) NLOS cases.

throughputs were observed between the low- and high-band UWBs.

References

[1] R. Amini, G. Aalbers *et al*., "New generations of spacecraft data handling systems: less harness, more reliability," in *57th Intl. Astronautical Congress (AIAA 2006-448)*, Oct. 2006.

[2] A. Chandra *et al.*, "Frequency-domain in-vehicle UWB channel modeling," *IEEE Trans. Veh. Technol.*, vol. 65, no. 6, pp. 3929-3940, Jun. 2016.

[3] A. Sorrentino *et al*., "Propagation modelling and channel estimation: A comparison among different channel indicators in severe multipath environments," *Applied Computational Electromagnetics Society Symposium (ACES)*, Italy, 2017.

[4] Y. Herlem, A. Outay, and P.Pelissou, "Assessment of wireless link budget in a satellite by modelling techniques," in *2012 ESA Workshop on Aerospace EMC*, pp. 1-6, Venice, Italy, May 2012.

[5] Z. Li *et al.,* "A protocol designed for intra-spacecraft impulse radio ultra-wideband communications," in *Proc. IEEE Intl. Conf. Wireless for Space and Extreme Environments (WiSEE2014)*, Netherlands, Oct. 2014.

[6] T. Kobayashi and M. Hirose, "Wideband and ultra wideband radio propagation in heavy multipath environments," *IEICE Trans. Fundamentals*, vol. E98-A, no. 2, pp. 511-519, Feb. 2015.

[7] T. Taniguchi, A. Maeda, and T. Kobayashi, "Development of an omnidirectional and low-VSWR ultra wideband antenna," *International Journal on Wireless and Optical Communications*, vol. 3, no. 2, pp. 145-157, Aug. 2006.

[8] G. Heidari, WiMedia UWB − *Technology of Choice for Wireless USB and Bluetooth*, New York, John Wiley & Sons, 2008.

Exotic properties of Intrinsic Localized Modes (Discrete Breathers) in a transmission line in the microwave regime

A. Gómez-Rojas[*] and P. Halevi

Department of Electronics, Instituto Nacional de Astrofísica, Óptica y Electrónica (INAOE), Puebla, México 72840
*corresponding author, E-mail: agomez@inaoep.mx

Abstract

We have studied Intrinsic Localized Modes (ILM) or Discrete Breathers (DB) in a lumped, band-pass transmission line with nonlinear capacitors (varactors) that are periodically modulated in time. We found that is possible to create breathers that are localized at an impurity lattice site by increasing sufficiently the inductance or average capacitance in the unit cell at that site; the details of this process depend on the modulation amplitude. Also, for certain values of the modulation frequency, as well as values of the series resistance, multiple breathers can be created, only one of which coincides with the impurity site. Moreover, if two impurities are separated by eight or less cells, it is possible for a breather to appear in an intermediate host unit cell, rather than at the impurity sites themselves. Finally, for certain values of the modulation frequency, the system can evolve in time in such a way that new breathers pop up, while others cease to exist.

1. Introduction

More than three decades ago Sievers and Takeno [1] proposed that the interaction between nonlinearity and discreteness in a spatially periodic lattice can produce vibrations that are localized in space and periodic in time, known as Intrinsic Localized Modes or Discrete Breathers. Since that theoretical work the breathers have been extensively studied and found in systems as diverse as: granular crystals [2], superconducting Josephson unions [3], electric arrays [4], michromechanical arrays [5], antiferromagnets [6], optical waveguides [7], graphene [8], Bose-Einstein condensates [9], carbon nanotubes [10], and DNA [11].

The behavior of discrete breathers can be significantly affected by defects or impurities. The interaction between impurities and breathers has been investigated in various systems [12, 13, 14, 15]. In these studies it has been proven that a defect is essential to their creation, that they are robust, and that they can be easily generated over an ample range of initial conditions in granular crystals. Also, in MEMs, breathers can be created, destroyed, attracted, and repelled, as in electrical lattices, with an inductor, capacitor or resistor acting as an impurity. While these investigations are concerned with the formation, manipulation and interaction of breathers due to an impurity, these aspects have not yet been fully explored.

This paper is structured as follows. In the following section we briefly describe the transmission line studied. Then, in Sec. 3 we study the voltage $V_N(t)$ of a particular "defect unit cell" and its nearest neighbors due to small variations of its inductance or capacitance for two values of the driving voltage. In Sec. 4 we investigate the formation of multiple breathers as a consequence of variation of the modulation frequency. Sec. 5 concerns the interaction between two breathers, one of which was created at a site with an inductive impurity, the other at a capacitive impurity. Sec. 6 deals with a situation where attraction between two breathers results in their annihilation. Finally, in Sec. 7 we summarize our findings and present some possible directions for future research.
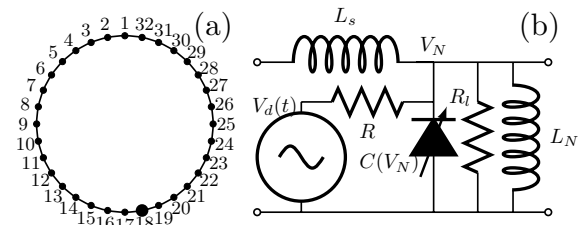
2. Transmission line

Figure 1: **(a)** Transmission line with non-linear varactors $C(V_N)$ fed by harmonic voltages $V_d(t) = V_d \sin(2\pi f_d t)$. The larger dot in cell 18 represents a defect unit cell, where either the inductance in parallel L_p or the average capacitance $\bar{C}$ is slightly different. **(b)** Unit cell where the inductance L_N has the same value L_p in all unit cells except the cell $N = 18$, where it has some increment δ_{L_p}. Our parameter values are: $L_s = 680 \ \mu$H, $L_p = 330 \ \mu$H, $R = 10$ kΩ, $R_l = 20$ kΩ, $\bar{C} = 788$ pF (Diode varactor NTE 618), $V_d = 4$ V.

In Fig. 1 we show a discrete (lumped), nonlinear, band-pass transmission line of 32 cells with voltage dependent capacitors (varactors) in each unit cell fed by uniform, harmonic modulation sources $V_d(t)$ (a model introduced by Palmero and collaborators [16, 17]). The capacitance and resistance models are defined in [16]. We have created an impurity by increasing the inductance only in cell 18 and we have studied the nodal voltages V_N experienced by the varactors in each of the 32 cells. All the voltages were obtained by numerical solutions of two coupled, non-linear
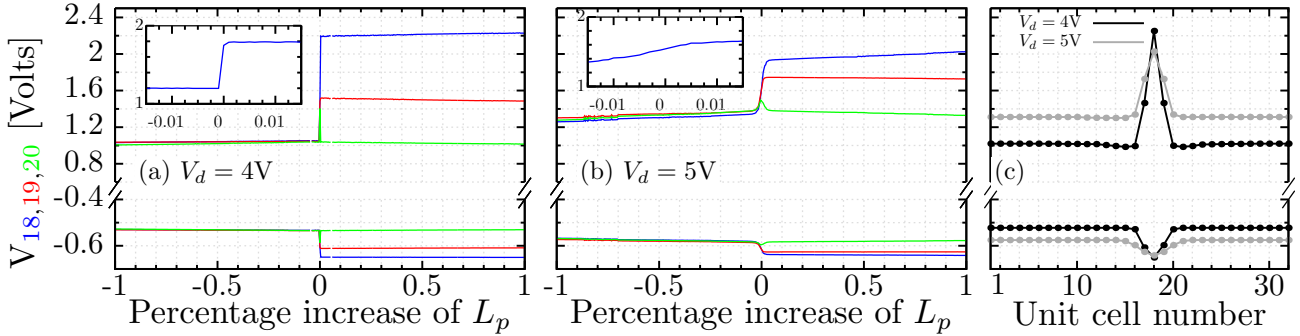
Figure 2: Nodal voltages $V_N(t)$ for the cells 18, 19 and 20 as function of the percentage increase of the inductance L_p in the cell 18 after a time $t = 250/f_d$. **(a)** For a modulation amplitude $V_d = 4$V it is possible to create a breather by increasing the inductance, following an abrupt transition of the voltage. **(b)** For $V_d = 5$V the transition around $\delta_{L_p} = 0$ is gradual and the voltage difference between cell 18 and its neighbors is smaller. The voltages reach saturation for $\delta_{L_p} > 3\%$. **(c)** Maximum and minimum voltages V_N in each of the 32 unit cells for an increase of 1% in the inductance L_p only in cell 18, corresponding to the cases **(a)** and **(b)**. These breathers have a width of about five cells. Parameters as in Fig. 1.

differential equations for V_N and the current i_{L_N} through the inductor L_N at least 250 periods $f_d t$ after the driving sources $V_d(t)$ have been switched on; this ensures that we are past the transitional period of the transmission line. The initial values (at $t = 0$) of all the $V_N(t)$ and $i_{L_N}(t)$ are 0.

$$C(V_N)\frac{dV_N}{dt} = \frac{V_d(t)}{R} - \left(\frac{1}{R} + \frac{1}{R_l}\right)V_N - I_D(V_N) + i_{L_N}$$

$$\frac{di_{L_N}}{dt} = \frac{1}{L_s}(V_{N+1} + V_{N-1} - 2V_N) - \frac{V_N}{L_N} \quad (1)$$

Here $L_N = L_p + (\delta_{L_p})\delta_{N,18}$, where δ_{L_p} is the increment of the inductance L_p (exclusively in the cell 18), and $\delta_{N,18}$ is a Kronecker delta. The $I_D(V_N)$ is the current through the N'th cell's diode.

3. Thresholds for creating a breather

In Fig. 2 we observe the voltages V_N obtained from numerical simulation of the successive (percentage) increase of the inductance L_p in a single unit cell (numbered "18") in a range of -1% (decrease) to 1%. All voltages were calculated at a time $t = 250/f_d$ after switch-on (at $t = 0$) of the modulation source. They are all symmetric with respect to cell 18, namely $V_{17} = V_{19}$, $V_{16} = V_{20}$, and so on. For both values of the chosen modulation amplitudes, $V_d = 4$V and $V_d = 5$V, if L_p is decreased (negative δ_{L_p}) the voltages remain unchanged in all the unit cells, so no breather is created. On the other hand, by increasing L_p with respect to the host values, breathers appear for both cases of V_d, as seen in Figs. 2(a) and (b). Fig. 2(c) shows the permanent maxima and minima of V_N in all the cells; note that only the voltages in cells 17-19 differ greatly from the host values. If a variation is performed in the opposite direction (from 1% to -1%), the same behavior is obtained, namely, the process is reversible. Moreover, we have verified that a perturbation of 0.1% of one of the parameters (f_d, V_d, R,

or R_l) leaves the breathers essentially unaltered. Also note that the amplitude of the breather for $V_d = 4$V is greater than for $V_d = 5$V.

For a modulation voltage $V_d = 3$V, the variation of $V_N(t)$ is qualitatively different from that graphed in Fig. 2. Here, there are 3 well differentiated regions: $\delta_{L_p} < -0.007\%$ where all the voltages of the 32 cells are equal (as for $\delta_{L_p} < 0$ in Fig. 2). Between this threshold and up to a second threshold ($\delta_{L_p} = 0.23\%$), unstable oscillations take place; the voltages oscillate chaotically at the impurity site and a few neighboring cells between their unperturbed values and final values provoked by the local perturbation. After this second threshold, the created breather is stable and remains unchanged even for very large impurity increases. Finally, it is also possible to produce a breather by altering the average capacitance $\bar{C}$ of the varactors, although the thresholds are larger in magnitude: a decrease of 0.2% (vs. 0.007% for the inductance) for the onset of chaotic oscillations and an increase of 6% for creating a breather.

4. Generation of multiple breathers

Now, we have varied the modulation frequency f_d in a wide range obtaining up to 6 breathers only between 267.8 and 365.5 kHz. A zoom between $f_d = 267$ to 276 kHz can be observed in Fig. 3. Here, there is an impurity of 10% in the average capacitance (instead of the inductance) in cell 18. The first breather appears in the perturbed cell 18 for $f_d = 267.9$ kHz, remains unchanged over a short frequency range up to $f_d = 260.03$ kHz where a second breather spontaneously emerges in cell 2 (no impurity site). As the frequency increases, the breather in cell 2 spontaneously divides into two breathers that are symmetrically located in the cells 7 and 29. However, they don't hold out for long, collapsing into a single breather in cell 2. After a short frequency range, again, there is a separation of the breather in cell 2 into two breathers in the same cells as be-
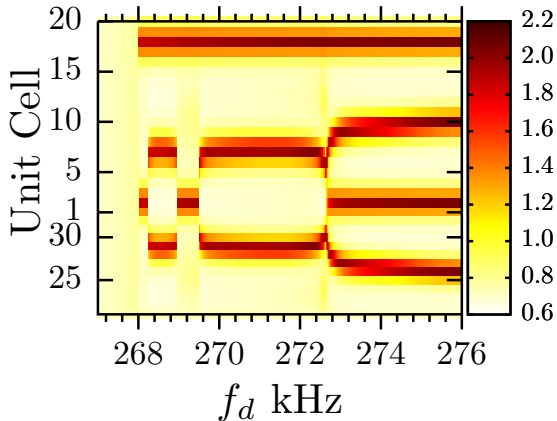
Figure 3: Spontaneous creation and collapse of breathers with increase of the modulation frequency f_d, from one to two, two to one, one to two again and then to three breathers. The values of the voltages V_N are indicated by their colour, according to the side bar. Parameters as in Fig. 1.
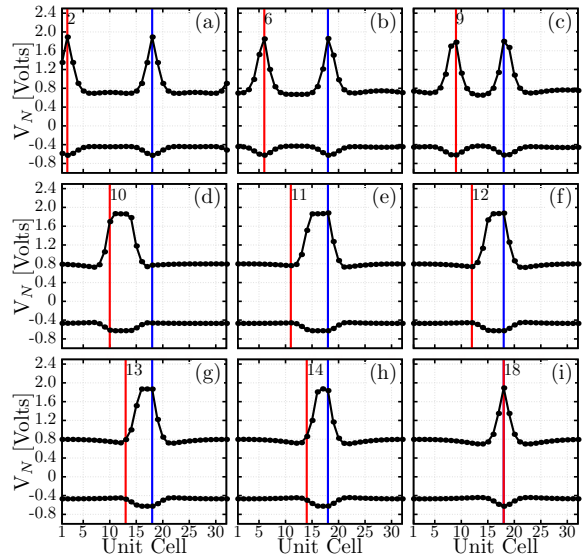

Figure 4: Interaction between a fixed inductive breather (blue line) and a mobile capacitive (red line) one. Breathers are created at both impurity sites if their separation is large enough, otherwise a single breather with a variable width is generated near the impurity located in cell 18. Parameters as in Fig.1.

fore. This whole process of division and collapse occurs in a short range of frequencies from $f_d = 268.2$ to 269.7 kHz. For further increase of f_d, the two breathers are attracted to each other and get close enough to create a breather in cell 2; then they are repelled to occupy new sites. This gives rise to four equidistant breathers. The process of division is repeated twice more (beyond the frequency range in Fig. 3), each time generating new breathers, until a total of six occupy symmetrical positions in the transmission line. The only breather that remains unchanged is the one generated in the impurity cell 18. The current i_{L_N} behaves completely analogously. If we apply the procedure in the reverse direction (gradually decreasing f_d) we obtain the same behavior, namely, the entire process is reversible.

Up to five breathers can also be produced by varying the resistence R of all cells from 2 to 10 $k\Omega$ with only a single inductive impurity ($\delta_{L_p} = 1\%$) in cell 18; no breathers are produced outside this resistence range. The breathers are created consecutively, namely, first one, then two, and so on; some of them are "onsite" (peaked at a single cell site), while others are "intersite" (with equal maximum amplitudes at two neighboring sites). The breather at the impurity site remains unaltered, while the other breathers change shape and place depending on the value of the resistance.

5. Breather interaction

We have simulated the interaction of two different breathers: one at a fixed site with 1% increase of L_p (blue line) and the other "mobile" with a 10% increase of its average capacitance $\bar{C}$ (red line) that is moved consecutively from cell to cell through the entire transmission line. For a large separation, as in Fig. 4(a), two independent, classically shaped identical breathers are created at the impurity sites. However, as the moving impurity approaches the cell 18 each breather "feels" the presence of the other and the line shapes

become slightly modified, see Fig. 4(b)-(c). When the separation of the impurities is less than or equal to eight cells, the two breathers collapse into a single wide one centered in the cell 12 (which is not an impurity site). If the impurity is moved to cell 11, the wide breather draws near to the cell 18 with slight change of shape, see Fig. 4(e). Subsequently, the width decreases as the mobile impurity progresses until it reaches the fixed impurity, see Figs. 4(e)-(i). At this value the breather amplitude is 5 cells wide. The situation is reversed symmetrically when the mobile impurity exceeds the cell 18. The behavior is analogous when both impurities are inductive and identical, except that for a separation of eight or less cells the resulting breather appears midway and alternates its shape between onsite and intersite as the moving impurity advances.

6. Attraction resulting in annihilation

Now, we have performed numerical simulations in time to study the temporal behavior of $V_N(t)$. For most modulation frequencies, a breather once created remains unaltered as time advances, but, for certain frequencies, exotic behavior occurs as shown in Fig. 5. As observed in the figure, during the first approximately 30 periods after switch-on the behavior of the voltages V_N is chaotic in all the cells. After this period, three breathers are created in the cells 6, 18 and 30, of which only the cell 18 is an impurity site. The others are symmetrically situated, but they are not equidistant, namely, the distance between the breathers in the cells 6 and 30 from the one in the cell 18 is the same ($B_{30} - B_{18} = B_{18} - B_6 = 12$), but not between the
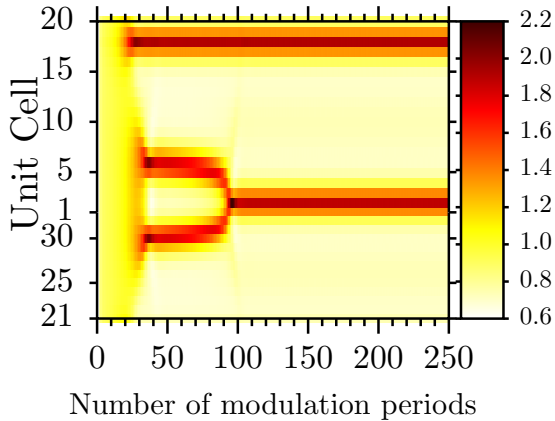
Figure 5: Exotic temporal behavior for $V_N(t)$ with fatal attraction after about 100 periods. Parameters as in Fig.1, with $f_d = 268.46$ kHz.

breathers in the cells 6 and 30 ($B_{30} - B_6 = 8$); here B_N denotes the location of the breather. As time goes on the breathers in cells 6 and 30 are attracted to each other until after 98 periods they collapse into a single breather in cell 2. From then on, the breathers remain unchanged. The entire spontaneous transition from three to two breathers lasts 20 periods. As in Fig. 4, the only unmodified breather is the one generated in the impurity cell 18. This same behavior occurs in frequency, only in the reverse direction, for frequencies in the range from $f_d = 269$ to 268 kHz. For two other frequencies f_d, a similar process of attraction between breathers occurs for different number of breathers, eliminating one of them in the process.

7. Conclusions

We found that a stable breather can be created in a modulated band-pass transmission line by sufficient increase of the inductance or average capacitance in a single, "defect" unit cell. The amplitude and shape of this breather depend on the modulation voltage, see Fig. 2. Up to five additional breathers can appear at host (non-impurity) sites when the modulation frequency or resistance is varied, as in Fig. 3. Two breathers at impurity sites can interact if they are separated at least nine unit cells, however they collapse into a single breather (at a host site) if the separation is eight or less cells. The width of this breather varies from 7 to 5 cells as the moving impurity moves along the transmission line, as seen in Fig. 4. Most exotic is the case of attraction resulting in annihilation, Fig. 5, where a breather disappears upon attracting two neighboring breathers close enough. All this suggests new questions such as: Is it possible to interpret this behavior in terms of interaction between currents and voltages? How are breathers attracted to each other? Is it possible to generalize this behavior to other systems? Does the exotic breather behavior reported here have analogies in other systems with non-linear lattices, such as granular crystals, micromechanical arrays, etc.? Most importantly, are our breathers robust and are

our findings supported experimentally?

References

[1] A. J. Sievers and S. Takeno, Phys. Rev. Lett. **61**, 970 (1988).

[2] S. P. Wallen, J. Lee, D. Mei, C. Chong, P. G. Kevrekidis, and N. Boechler, Phys. Rev. E **95**, 022904 (2017).

[3] C. Guarcello, K. Fedorov, D. Valenti, B. Spagnolo, and A. Ustinov, ArXiv e-prints (2015). arXiv:1501.04037.

[4] F. Palmero, J. Cuevas-Maraver, L. Q. English, and R. Chacón, ArXiv e-prints (2017), arXiv171000167P.

[5] M. Sato, Y. Sada, W. Shi, S. Shige, T. Ishikawa, Y. Soga, B. E. Hubbard, B. Ilic, and A. J. Sievers, Chaos **25**, 013103 (2015).

[6] L. Q. English, M. Sato, and A. J. Sievers, J. Appl. Phys. **89**, 6707 (2001).

[7] N. V. Alexeeva, I. V. Barashenkov, A. A. Sukhorukov, and Y. S. Kivshar, Phys. Rev. A **85**, 063837 (2012).

[8] G. T. Adamashvili and D. J. Kaup, Phys. Rev. A **95**, 053801 (2017).

[9] B. Opanchuk and P. D. Drummond, Phys. Rev. A **96**, 053628 (2017).

[10] Dmitriev, Sergey V. and Baimova, Julia A. and Korznikoza, Elena A. and Chetverikov, Alexander P., (2018). Nonlinear Excitations in Graphene and Other Carbon NanoPolymorphs. Springer International Publishing

[11] C. L. Gninzanlong, F. T. Ndjomatchoua, and C. Tchawoua, Chaos. **28**, 043105 (2018).

[12] G. Theocharis, M. Kavousanakis, P. G. Kevrekidis, C. Daraio, M. A. Porter, and I. G. Kevrekidis, Phys. Rev. E **80**, 066601 (2009).

[13] Y. Man, N. Boechler, G. Theocharis, P. G. Kevrekidis, and C. Daraio, Phys. Rev. E **85**, 037601 (2012).

[14] M. Sato, B. E. Hubbard, A. J. Sievers, B. Ilic, and H. G. Craighead, EPL (Europhysics Letters) **66**, 318 (2004).

[15] M. Sato, S. Yasui, M. Kimura, T. Hikihara, and A. J. Sievers, EPL (Europhysics Letters) **80**, 30002 (2007).

[16] F. Palmero, L. Q. English, J. Cuevas, R. Carretero-González, and P. G. Kevrekidis, Phys. Rev. E **84**, 026605 (2011).

[17] L. Q. English, F. Palmero, P. Candiani, J. Cuevas, R. Carretero-González, P. G. Kevrekidis, and A. J. Sievers, Phys. Rev. Lett. **108**, 084101 (2012).

The Radiation Characteristics of Three-Element Vivaldi Antenna Array which Elements are Located on The Edge of an Equilateral Triangle

Gevorkyan A.V.[1], Privalova T.Yu.[2]

[1] Department of Antennas & Radio Transmitters, Southern federal university, Taganrog, Russia
[2] Department of general physics, Southern Federal University, Rostov-on-Don, Russia

Abstract

Showed the results of the study of the radiation characteristics of a single Vivaldi antenna and this antenna in the composition of three-element antenna array on the edges of an equilateral triangle. It is shown that the composition of the antenna arrays this antenna for VSWR<3 has a large bandwidth (1.33-20 GHz) and the best form of the radiation pattern.

1. Introduction

It is known that the characteristics of single antennas and this antenna in the antenna arrays can vary significantly. This work is devoted to investigation of radiation characteristics of single Vivaldi antenna and this antenna in the composition of three-element antenna array whose elements are located on the sides of an equilateral triangle. Such antennas can be used in the development of multipolarization antenna arrays. This work is a continuation of studies of Vivaldi antennas located on different surfaces [1-4].

2. Antenna design

Fig.1a shows the design of a single Vivaldi antenna. Fig. 1b shows the design of three-element antenna array. The designation and numbering of the antenna array inputs is shown in Fig. 2.

This antennas implemented on a dielectric substrate Arlon AD300C with double-sided metallization.
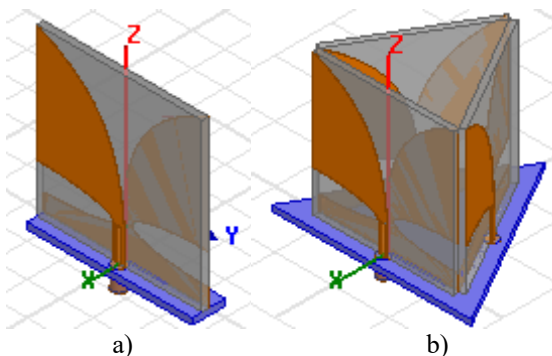
Figure 1: The design of: a) the single Vivaldi antenna; b) the three-element antenna array
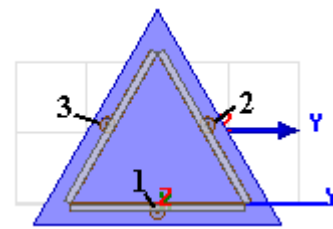
Figure 2: The view from the top on three-elements antenna

Numerical studies were conducted using the software package Ansoft HFSS [5]. Numerical studies were carried out in the frequency range from 1 to 20 GHz.

3. The radiation characteristics of antennas

3.1. Fig. 3 and 4 shows a comparison of the radiation characteristics of a single Vivaldi antenna (——) and this antenna in the composition of three-element antenna array (— —) with circular polarization. The circular polarization is implemented by the phase difference at the inputs of the antenna (from 1 to 3 inputs): 0; 120; 240°.
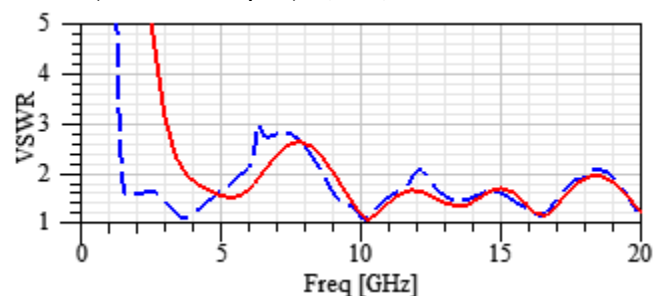

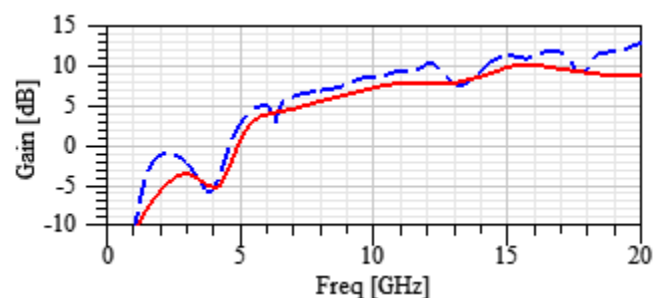Figure 3: Frequency dependence of VSWR

Figure 4: Frequency dependence of gain

From Fig. 3 it is seen that the single antenna has a VSWR<3 in the range from 3 to 20 GHz and three-element antenna array has a VSWR<3 in the range from 1.4 to 20 GHz. Gain (Fig. 4) of three-element antenna array more than gain of a single antenna, but on some frequencies there are decrease (6.5, 13.2 and 17.8 GHz).

3.2. Fig. 5 and 6 shows a comparison of the radiation pattern of this antennas on the frequency 5 and 15 GHz. In accordance with Fig. 1a and 1b, ——— – the yz-plane (for single antenna – E-plane) and — — – xz-plane (for single antenna – H-plane).

a)

b)
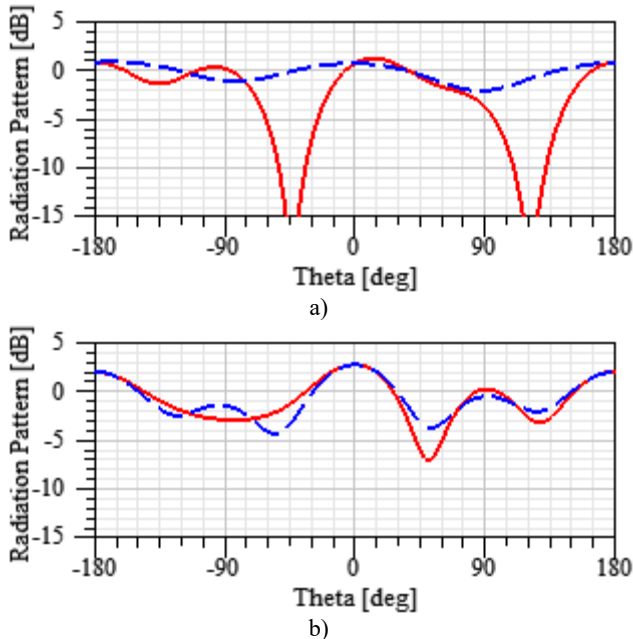
Figure 5: The radiation pattern on 5 GHz for: a) single Vivaldi antenna; b) three-element antenna array

a)

b)
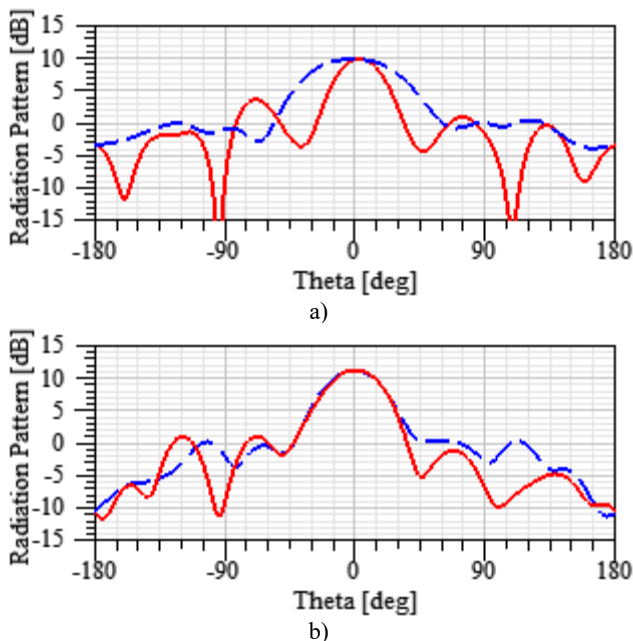
Figure 6: The radiation pattern on 15 GHz for: a) single Vivaldi antenna; b) three-element antenna array

From Fig. 5 and 6 it is seen that the radiation pattern of three-element antenna array has better form than the radiation pattern of a single antenna.

3.3. Figures 7-9 show the frequency dependence of VSWR, gain and transmission coefficient between antennas (S(1,2)=S(1,3)=S(2,3)) of a three-element antenna array for three values of the antenna width: 23 (———), 24.5 (— —) and 26 (---) mm.

From Fig. 7 it is seen that the increase of the antenna width leads to a small decrease in lower boundary (f_{low}) of the operating frequency band of the antenna. By level VSWR≤3 f_{low}=1.47 GHz for 23 mm of the antenna width and f_{low}=1.33 GHz for 26 mm. In this case the increase in the antenna width VSWR is reduced in the range of 6-9 GHz. The antenna array with 26 mm of the antenna width has VSWR≤3 in the frequency band 1.33-20 GHz.
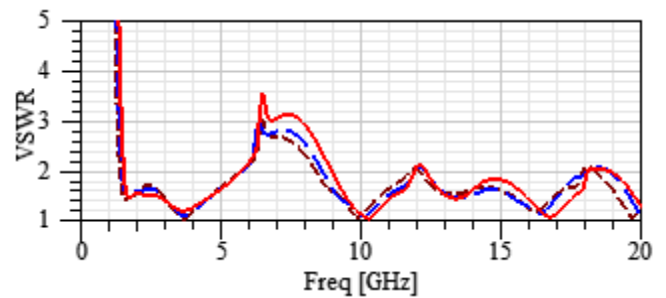

Figure 7: Frequency dependence of VSWR

Fig. 8 shows that increasing the antenna width leads to a slight increase in the gain. The levels of decrease in the range of 7-8 and 17.5-18.5 GHz reduced.
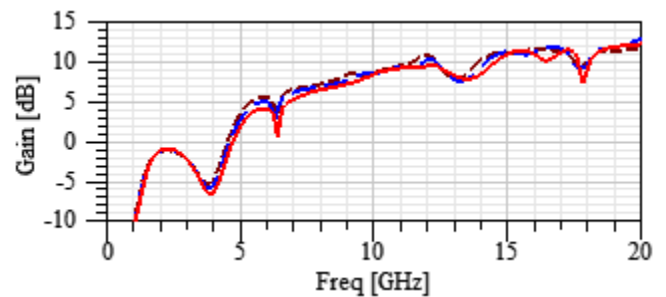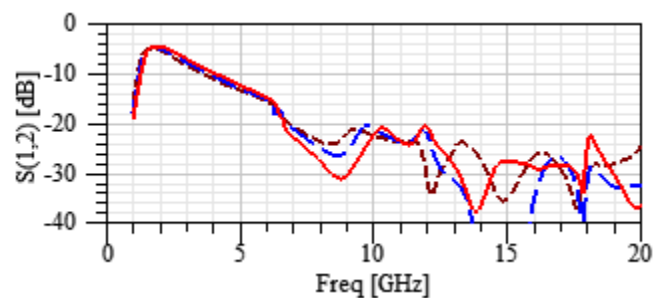

Figure 8: Frequency dependence of gain

Figure 9: Frequency dependence of transmission coefficient S(1,2)

From Fig. 9 it is seen that with increasing width of the antenna from 23 to 26 mm, the transmission coefficient between the antennas in the range 2-6,5 GHz is reduced to approximately 1 dB. At frequencies more than 7 GHz, the transmission coefficient between the antennas does not

2

exceed -20 dB at any of the investigated width of the antenna.

3.4. The previously discussed characteristics were obtained for the antenna array with circular polarization. The circular polarization is implemented by the phase difference at the inputs of the antenna (from 1 to 3 inputs): 0; 120; 240° (see Fig. 2). Fig. 10 shows the distribution of vector E for this case at different points in time.
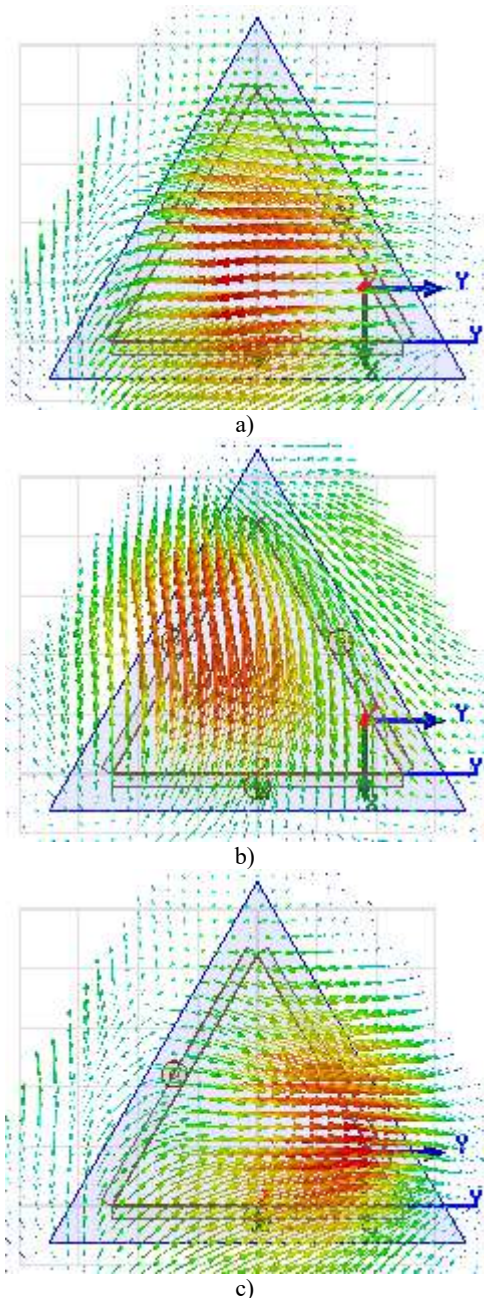

a)

b)

c)

Figure 10: The distribution of vector E for the antenna array with circular polarization at different points in time: a) 0 b) T/4 and c) T/2

Fig. 11 shows the angular dependence of the axial ratio for this case. In accordance with Fig. 1a and 1b, ——— – the yz-plane (for single antenna – E-plane) and — — – xz-plane (for single antenna – H-plane).

The analysis of graphs shows that in the sector of the angels ±29° the axial ratio is less than 3. The lowest value of the axial ratio is in the direction normal to the plane of the antenna (xy-plane – Fig. 1 and 2). This is corresponds for Theta=0°. Fig. 12 shows the frequency dependence of the axial ratio in this direction. Fig. 12 shows that in operating frequency band the axial ratio is less than 1.2.
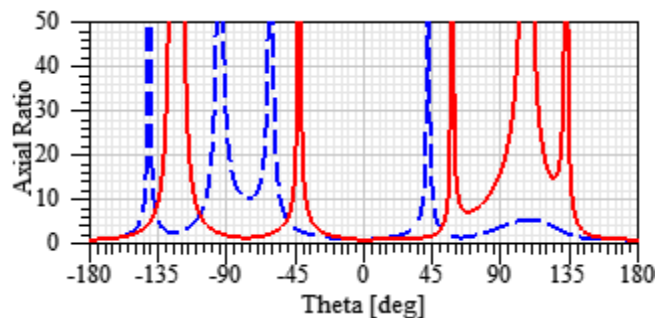

Figure 11: Angular dependence of the axial ratio

Figure 12: Frequency dependence of the axial ratio

To achieve linear polarization, the phase difference must be 0°. Fig. 13 shows the distribution of vector E for this case.
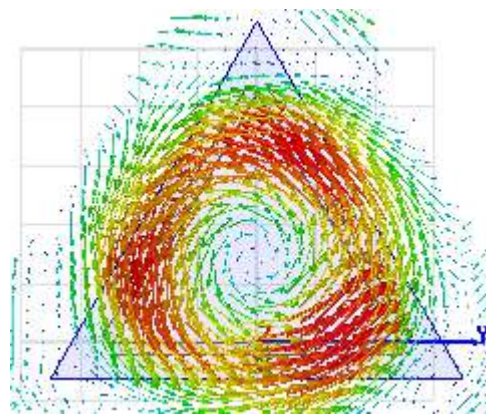

Figure 13: The distribution of the vector E for the antenna array with linear polarization

In this case, the radiation in the direction normal to the plane of the antenna (xy-plane – Fig. 1 and 2) is absent, and the radiation pattern of the antenna array has a conical form (see Fig. 14).
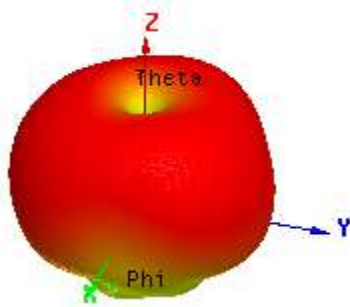
3

Figure 14: 3D radiation pattern (dB) on frequency 10 GHz

Fig. 15 shows the angular dependence of the axial ratio for this case. This figure shows that the axial ratio is greater than 5 on angles greater than ±10°.
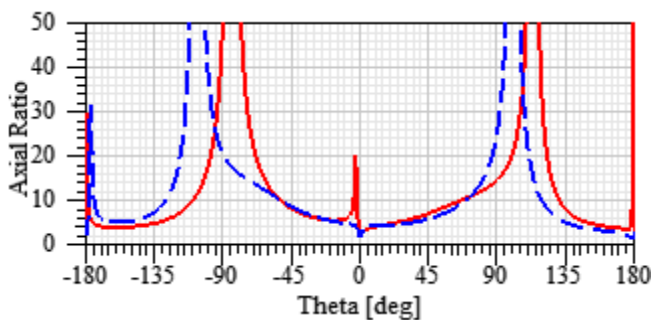

Figure 15: Angular dependence of the axial ratio

4. Conclusions

Studies have shown that the three-element antenna array has a wider wideband than a single antenna. The operating frequency band of the antenna array for VSWR≤3 is in the range 1.33-20 GHz. Three-element antenna array also has a better radiation pattern than a single antenna. By the design of this antenna can realize circular and line polarizations.

Acknowledgements

References

[1] Yukhanov Yu.V., Gevorkyan A.V., Privalova T.Yu. Radiation Characteristics Of Vivaldi Antenna On The Wedge Surface // IEEE International Symposium on Phased Array Systems and Technology (PAST). — 2016. — 6 p. DOI: 10.1109/ARRAY.2016.7832569.

[2] Yukhanov Yu.V., Gevorkyan A.V., Privalova T.Yu. Radiation Characteristics of Vivaldi Antenna on the Surface of the Wedge-Cylinder Adjunction // 5th Asia-Pacific Conference on Antennas and Propagation (APCAP 2016). — 2016. — P. 233–234. DOI: 10.1109/APCAP.2016.7843184

[3] Yukhanov Yu.V., Privalova T.Yu., Gevorkyan A.V. Radiation Characteristics of Vivaldi Antenna on the Cylindrical Surface // IEEE Radio and Antenna Days of the Indian Ocean (RADIO 2016). — 2016. — 2 p. DOI: 10.1109/RADIO.2016.7772005.

[4] Gevorkyan A.V., Yukhanov Yu.V., Privalova T.Yu. The radiation characteristics of the Vivaldi antenna located on a cylindrical surface // Progress in Electromagnetics Research Symposium (21-23 November 2017, Singapore). — 2017. — 6 p. DOI: 10.1109/PIERS-FALL.2017.8293426.

[5] Available: www.ansoft.com